



FACHBEREICH PHYSIK
BERGISCHE UNIVERSITÄT
GESAMTHOCHSCHULE WUPPERTAL

A Precise Determination of the Forward-Backward Asymmetry of b Quarks

The final DELPHI result for A_{FB}^b using inclusive charge
reconstruction and lifetime tagging

Dissertation zur Erlangung des Doktorgrades

von

Wolfgang Liebig

WUB-DIS 2003–10
Oktober 2003

Abstract

This thesis concerns a novel high precision measurement of the b quark forward-backward asymmetry at the Z pole, which has been performed on a sample of 3,560,890 hadronic events collected with the DELPHI detector at CERN's Large Electron Positron Collider in 1992 to 2000.

As part of the analysis technique, an enhanced impact parameter tag provides a high purity b sample. For event hemispheres with a reconstructed secondary vertex the charge of the corresponding quark or anti-quark is determined using a neural network tag which combines in an optimal way the full available charge information from the vertex charge, the jet charge and from identified leptons and hadrons. The probability of correctly identifying b quarks and anti-quarks is measured on the data themselves comparing the rates of double hemisphere tagged like-sign and unlike-sign events. The b quark forward-backward asymmetry is determined from the differential asymmetry, taking small corrections due to hemisphere correlations and background contributions into account. The results for different centre-of-mass energies are:

$$\begin{aligned} A_{FB}^b(89.449 \text{ GeV}) &= 0.0637 \pm 0.0143(\text{stat.}) \pm 0.0017(\text{syst.}) \\ A_{FB}^b(91.231 \text{ GeV}) &= 0.0958 \pm 0.0032(\text{stat.}) \pm 0.0014(\text{syst.}) \\ A_{FB}^b(92.990 \text{ GeV}) &= 0.1041 \pm 0.0115(\text{stat.}) \pm 0.0024(\text{syst.}) \end{aligned}$$

They correspond to an effective electroweak mixing angle of

$$\sin^2 \theta_{\text{eff}}^\ell = 0.23230 \pm 0.00054 .$$

Statistical correlations with other determinations of A_{FB}^b on the common data-sets are evaluated, and a combined DELPHI result:

$$A_{FB}^{0,b} = 0.0990 \pm 0.0029$$

obtained. It agrees with the results from other LEP experiments, and the combined value is interpreted in the framework of the Standard Model and beyond, taking into account also measurements at LEP 2 energies above the Z pole.

Kurzübersicht

Diese Arbeit beschreibt eine neuartige Präzisionsmessung der Vorwärts-Rückwärts-Asymmetrie für b-Quarks auf dem Z Pol. Die Messung basiert auf einem Datensatz von 3,560,890 hadronischen Ereignissen, die mit dem DELPHI Experiment am LEP Beschleuniger am CERN in den Jahren 1992 bis 2000 genommen worden sind.

Teil der hier verwendeten Analysetechnik ist ein aus der Impaktparameter-Methode weiterentwickeltes Auswahlverfahren für b-Quark Ereignisse, welches diese mit hoher Reinheit anreichert. Auf Ereignishemisphären, in denen ein sekundärer Vertex rekonstruiert werden konnte, wird dann die Ladung des initialen Quarks bzw. Antiquarks mit Hilfe eines neuronalen Netzes bestimmt. Dieses Netz verarbeitet in einer optimalen Weise alle zur Verfügung stehenden Ladungsinformationen aus dem Jet, dem Sekundärvertex und den Ladungen identifizierter Leptonen und Hadronen zu einer inklusiv rekonstruierten b-Quark Ladung. Die Wahrscheinlichkeit, das Ladungsvorzeichen richtig zu rekonstruieren, wird direkt auf den Daten bestimmt aus dem Verhältnis der Raten von gleich zu entgegengesetzt geladenen Hemisphärenpaaren. Die b-Quark Vorwärts-Rückwärts-Asymmetrie wird über die differentielle Asymmetrie gemessen, nachdem der Einfluß von Hemisphärenkorrelationen und Untergrundereignissen korrigiert worden ist. Das in verschiedene Schwerpunktsenergien klassifizierte Ergebnis ist

$$\begin{aligned} A_{FB}^b(89.449 \text{ GeV}) &= 0.0637 \pm 0.0143(\text{stat.}) \pm 0.0017(\text{syst.}) \\ A_{FB}^b(91.231 \text{ GeV}) &= 0.0958 \pm 0.0032(\text{stat.}) \pm 0.0014(\text{syst.}) \\ A_{FB}^b(92.990 \text{ GeV}) &= 0.1041 \pm 0.0115(\text{stat.}) \pm 0.0024(\text{syst.}) \end{aligned}$$

Die Werte für die Vorwärts-Rückwärts-Asymmetrie entsprechen einem effektiven elektroschwachen Mischungswinkel von

$$\sin^2 \theta_{\text{eff}}^\ell = 0.23230 \pm 0.00054 .$$

Die statistischen Korrelationen zwischen dieser und den vorangegangenen Messungen auf teilweise identischen Datensätzen werden ermittelt, so daß die DELPHI A_{FB}^b -Messungen zusammengefaßt werden können zu:

$$A_{FB}^{0,b} = 0.0990 \pm 0.0029 .$$

Dieser Wert stimmt mit denen anderer LEP-Experimente überein. Das gemeinsame Ergebnis von allen LEP-Experimenten wird daher im Rahmen des Standardmodells und weiterführender Theorien interpretiert. Zusätzliche Asymmetriemessungen bei LEP 2 Energien oberhalb der Z-Resonanz werden dabei beachtet.

Contents

1	Introduction	1
2	The theory	3
2.1	Theory of the electroweak interaction	3
2.2	Quantum chromodynamics	7
2.3	Standard Model parameters and phenomenology	8
2.4	Radiative corrections	10
2.5	Fermion pair production at LEP	13
2.6	Forward-backward asymmetries at LEP	14
2.7	The transition from quarks to stable particles	17
2.7.1	The parton cascade	18
2.7.2	String fragmentation	18
2.8	The properties of b- and c-hadrons	20
2.8.1	Oscillation in the $B^0 - \bar{B}^0$ system	23
3	The DELPHI experiment	26
3.1	The LEP collider	26
3.2	The DELPHI detector	28
3.2.1	The microvertex detector	30
3.2.2	The tracking detectors	31
3.2.3	Particle identification	33
3.2.4	Calorimeters	35
3.2.5	Muon detectors	36
3.3	Data acquisition	36
3.4	Event reconstruction	37
3.5	Simulation	38
4	Principles of the method to extract A_{FB}^b	40
5	The selection of Z decays to hadrons	42
6	The identification of b quark events	46
6.1	Lifetime tagging	46
6.2	Combined tagging	50
6.3	The b tagging efficiency in b and c events	57
6.4	The correction function	60
7	Inclusive charge reconstruction by BSAURUS	62
7.1	Neural Network techniques	62
7.2	Particle identification	65

7.3	The reference axis	67
7.4	Secondary vertex finding	68
7.5	Auxiliary Neural Networks	68
7.6	The hemisphere charge tagging Neural Network	70
7.6.1	The construction of the b-hadron flavour tags	70
7.6.2	The jet charge	71
7.6.3	The b charge tagging Neural Network	74
8	The measurement of the b quark forward-backward asymmetry	80
8.1	The method to extract the b asymmetry	80
8.2	Measured efficiencies and flavour fractions	82
8.3	Calculation of the charge identification probability	83
8.3.1	The probabilities to identify the b quark charge correctly	83
8.3.2	The correlations δ and β	86
8.3.3	The probabilities to identify the c quark charge correctly	90
8.4	The QCD correction	93
8.5	The fit of the b quark forward-backward asymmetry	96
8.5.1	The off-peak data sets	98
8.5.2	Combined results	99
9	Discussion of systematic uncertainties	103
9.1	Additional tests	109
10	The results and their interpretation	114
10.1	The results for the b asymmetry	114
10.2	The DELPHI combined b and c asymmetry results	115
10.3	Interpretation	118
11	Conclusions	127
A	The w_b calibration method	129
B	The χ^2 fit to the measured event rates	132
C	The DELPHI measurement of A_{FB}^b and R_b at LEP 2	134
C.1	Introduction	136
C.2	Track selection	136
C.3	event selection	136
C.4	Detector inefficiency during the 2000 data-taking	138
C.5	Identification of b quarks	138
C.6	The R_b measurement	139
C.7	The A_{FB}^b measurement	143
C.8	Interpretation	147
C.9	Conclusions	148
	List of Figures	150
	List of Tables	153
	Bibliography	155
	Acknowledgements	162

Chapter 1

Introduction

During the last century, the knowledge of the fundamental processes and structures in nature has grown with high speed, and in particular much faster than at any time before. One of the driving forces behind this development is the idea that the processes and structures under consideration should be described by a theory model, and that this model itself is predictive, i.e. can be verified by experiments. Often the somewhat aesthetic aim in developing such physical theories was finding a common formalism for seemingly different effects. This unification process is hoped to culminate in a single theory of everything, which should be able to describe all known particles and interactions at all energy and distance scales. During the last decades, modern physics has passed some important steps on the way of finding this grand unified theory.

The theoretical approach of unifying the electromagnetic and the weak interaction led to the prediction of very heavy gauge bosons, the W and Z bosons. Both indeed were discovered fifteen years later in 1983 at the laboratory of the European Organisation for Nuclear Research in Geneva, CERN. For the purpose of studying this “electroweak” interaction and the properties of its gauge bosons, CERN constructed the Large Electron-Positron Collider: a 27 km-circumference ring accelerator with several thousand scientists working at it, which has been the largest running machine so far. LEP was operated from 1989 until the end of 2000, providing several millions of electron-positron annihilation events to each of the four experiments ALEPH, DELPHI, L3 and OPAL. During its first phase the accelerator was run so that the Z boson could be created in resonance. The resulting high number of events allowed — among other very interesting physics topics — a precise determination of the Z boson properties and hence the fundamental parameters of the electroweak theory. By measuring more observables than the theory has free parameters, its predictions and hence its consistency could be verified within the same experiments.

Compared to the status before the start of LEP, the analysis of the LEP data has boosted the precision with which the electroweak parameters are known by often as much as a factor 1000. In the same way as the experiments increased the knowledge of the theory parameters, the electroweak theory became more and more predictive and the tests of its consistency very stringent. As a result, none of the tests has shown a significant discrepancy, so that the theory of the electroweak and strong interactions, the Standard Model, stands on more solid ground than ever. Some effects at the level of three standard deviations, however, have remained after the

closure of LEP. One of them showed up when comparing different measurements which determine the effective electroweak mixing angle. It is particularly visible between the two most precise measurements, the LEP b quark forward-backward asymmetry and the left-right polarisation asymmetry from the SLD experiment in Stanford. The electroweak mixing angle mainly puts the weak and electromagnetic coupling strength into relation and consequently plays a central role in the concept of unifying the two interactions. In addition, the effective mixing angle is indirectly related to the remaining unknown parameter in the Standard Model, the mass of the Higgs boson. It is therefore highly interesting to understand the situation of the mixing angle results, i.e. to decide if a statistical fluctuation or a hint at a new physical phenomenon is observed.

This analysis contributes significantly to increasing the precision with which the electroweak observables are measured, and in particular to investigating the situation that persists in the combination of the mixing angle results. It provides a very precise measurement of the b quark forward-backward asymmetry using the full data set from 1992-2000 taken by the DELPHI experiment in the energy range at the Z resonance. The method exploits sophisticated data analysis tools, which, in an inclusive way, select Z decays to b quarks with high purity and provide a means of identifying the charge sign of the b. The latter information is necessary to distinguish b quarks moving in either forward or backward direction from \bar{b} anti-quarks, so that the predicted asymmetry between forward and backward rates can be observed and verified. For a more detailed introduction to the method the reader may be referred to Chapter 4.

The analysis tools, especially the Neural Network method to identify the charge sign, were developed with steady feed-back from this analysis. The development process took place a few years after the data-taking, when the quality of the data processing made it possible and a better knowledge of the special properties of B hadrons was available. As a remarkable result, a significant improvement in the statistical precision of the asymmetry has been achieved with respect to the the previous measurement while using the same data set. The gain in precision in conjunction with an increased interest in excluding any experimental errors has required a broad application of self-calibration techniques and a comprehensive study of the remaining systematic uncertainties. The result is the by far most precise measurement of the b quark forward-backward asymmetry in DELPHI. Together with the other DELPHI and LEP measurements it provides an interesting contribution to the discussion of the electroweak observables.

Chapter 2

The Theory

The aim of particle physics is to study and understand the basic constituents of matter and the fundamental forces interacting between them. Four types of fundamental interactions can be observed in nature, termed electromagnetic, weak, strong and gravitational force. Although the mass of a particle is used to characterise it, the gravitational force related to it is extremely small compared to the other three forces. It cannot be detected in particle physics experiments and is hence neglected. Modern theory attempts to describe the phenomena related to the electromagnetic, weak and strong interaction by means of a relativistic quantum field theory which interprets an interaction as an exchange of force carrier particles. This has led to the Standard Model of particle physics, a gauge theory based on the mathematical framework of local $SU(3) \otimes SU(2) \otimes U(1)$ invariance. This symmetry is spontaneously broken, involving three distinct types of fields respectively particles: the gauge fields, the fermion matter fields and the Higgs field. The twelve different *gauge fields* correspond to the eight spin-1 bosons mediating the strong interaction, the gluons, and the four vector bosons of the electroweak theory (W^\pm, Z^0, γ). The *fermion fields* which describe quarks and leptons are two-component spinor fields as detailed in Table 2.1. They are grouped in three families of identical structure. By definition, leptons are only subject to the electromagnetic and weak forces while quarks take part in all three. The *Higgs field* is responsible for the elementary particle masses and will be explained in the context of the electroweak theory. Its associated particle, the Higgs boson, has not yet been discovered.

The unified electroweak theory (and some Quantum Chromodynamics) will be described in the next section, followed by the theoretical aspects of electron-positron annihilation at centre-of-mass energies around the Z resonance (91.2 GeV) and forward-backward asymmetries of quark final states in particular. Finally, as a measurement with heavy quarks also involves knowledge of the processes that lead to a stable final state, the fragmentation and the decay properties of heavy hadrons are discussed.

2.1 Glashow-Salam-Weinberg Theory of the Electroweak Interaction

Between 1960 and 1970 S.L. Glashow, A. Salam and S. Weinberg developed the electroweak theory [1], a unified theory of electromagnetism and weak force based on

	fermion families			Y	I	I_3	Q
leptons	$\begin{pmatrix} \nu_e \\ e \end{pmatrix}_L$	$\begin{pmatrix} \nu_\mu \\ \mu \end{pmatrix}_L$	$\begin{pmatrix} \nu_\tau \\ \tau \end{pmatrix}_L$	-1	1/2	1/2 -1/2	0 -1
	e_R	μ_R	τ_R	-2	0	0	-1
quarks	$\begin{pmatrix} u_i \\ d'_i \end{pmatrix}_L$	$\begin{pmatrix} c_i \\ s'_i \end{pmatrix}_L$	$\begin{pmatrix} t_i \\ b'_i \end{pmatrix}_L$	1/3	1/2	1/2 -1/2	2/3 -1/3
	$u_{i,R}$	$c_{i,R}$	$t_{i,R}$	4/3	0	0	2/3
	$d_{i,R}$	$s_{i,R}$	$b_{i,R}$	-2/3	0	0	-1/3

Table 2.1: The three families of fermions and their quantum numbers. (hypercharge Y , weak isospin I and electr. charge $Q = I_3 + \frac{Y}{2}$). Quantum numbers of antiparticles have reversed signs. The index i runs over the three colour states of QCD and the primed quarks d' , s' , b' denote states which are mixed with respect to the strong interaction eigenstates d , s , b .

the group $SU(2)_L \otimes U(1)$. It was extended to the hadronic sector via a mechanism suggested by S.L. Glashow, J. Iliopoulos and L. Maiani [2], which finally led to the concept of N. Cabibbo, M. Kobayashi and K. Maskawa for quark flavour mixing [3].

The crucial new phenomenological input [4] to electroweak theory is that the weak interaction does not respect reflection symmetry, or parity. Parity violation means that the interaction is different for the left-handed and for the right-handed components of the fermion fields. The gauge fields of $SU(2)_L$ are the triplet $W_\mu^{(1)}, W_\mu^{(2)}, W_\mu^{(3)}$, which exclusively couple to the left-handed fermion fields via a common coupling constant g_2 . Such a coupling has the spin structure of vector minus axial vector, $V - A$. In the Dirac algebra it is represented by a factor $1 - \gamma_5$, where γ_5 applied to a Dirac spinor, ψ , forms the axial vector part of the coupling. Hereby the left-handed components of the fermion fields form doublets while the right-handed ones are singlets under $SU(2)_L$ (indices L and R in Table 2.1). A singlet B_μ together with the coupling constant g_1 is assigned to the group $U(1)$, acting on the fields of both helicity states (L and R),

$$\psi_L = \frac{1 - \gamma_5}{2} \psi \quad \text{and} \quad \psi_R = \frac{1 + \gamma_5}{2} \psi \quad . \quad (2.1)$$

However, to comply with the massive gauge bosons observed in experiments, the W^\pm and Z bosons, the existence of a weakly interacting scalar field seems necessary: the Higgs field. It is a complex doublet written as

$$\Phi = \frac{1}{\sqrt{2}} \begin{pmatrix} \Phi_1 + i\Phi_2 \\ \Phi_3 + i\Phi_4 \end{pmatrix} \quad \text{with} \quad \Phi_0 = \frac{1}{\sqrt{2}} \begin{pmatrix} 0 \\ v \end{pmatrix} \quad \text{and} \quad v^2 > 0 \quad , \quad (2.2)$$

which has the very special property of a non-zero expectation value Φ_0 in vacuum. The coupling to the Higgs field spontaneously breaks the symmetry of the massless gauge fields $W_\mu^{(i)}$ with respect to isospin rotation. This symmetry breaking leads to non-diagonal mass terms

$$\frac{1}{2} \left(\frac{g_2}{2} v \right)^2 ((W^{(1)})^2 + (W^{(2)})^2) + \frac{v^2}{4} (W_\mu^{(3)}, B_\mu) \begin{pmatrix} g_2^2 & g_1 g_2 \\ g_1 g_2 & g_1^2 \end{pmatrix} \begin{pmatrix} W_\mu^{(3)} \\ B_\mu \end{pmatrix} \quad (2.3)$$

for the gauge fields in the Lagrangian energy density. The transformation from the gauge fields to the physical fields is realised via

$$W_\mu^\pm = \frac{1}{\sqrt{2}} (W_\mu^{(1)} \mp W_\mu^{(2)}) \quad (2.4)$$

and

$$\begin{pmatrix} Z_\mu \\ A_\mu \end{pmatrix} = \begin{pmatrix} \cos \theta_w & -\sin \theta_w \\ \sin \theta_w & \cos \theta_w \end{pmatrix} \begin{pmatrix} W_\mu^{(3)} \\ B_\mu \end{pmatrix} . \quad (2.5)$$

The rotational angle in Eq. 2.5 is the electroweak mixing angle θ_w , expressed by

$$\cos \theta_w = \frac{g_2}{\sqrt{g_1^2 + g_2^2}} , \quad \sin \theta_w = \frac{g_1}{\sqrt{g_1^2 + g_2^2}} . \quad (2.6)$$

In these fields the mass term Eq. 2.3 is diagonal, giving

$$m_A = 0 , \quad m_W = \frac{g_2 \cdot v}{2} , \quad m_Z = \frac{v}{2} \sqrt{g_1^2 + g_2^2} = \frac{m_W}{\cos \theta_w} . \quad (2.7)$$

The derivative in the full electroweak Lagrangian related to the spin-1 boson A, the charge operator, leaves the vacuum expectation value Φ_0 of the Higgs field in Eq. 2.2 invariant. Gauge fields coupled to unbroken symmetries do not acquire mass, and A can be identified with the massless photon. It couples to the charged fermions via the electric charge e , expressed here by the gauge couplings

$$e = \frac{g_1 \cdot g_2}{\sqrt{g_1^2 + g_2^2}} = g_2 \cdot \sin \theta_w = g_1 \cdot \cos \theta_w . \quad (2.8)$$

The charged weak current is mediated by W^\pm bosons. As a transformation of the $W_\mu^{(1,2)}$ gauge bosons of $SU(2)_L$, Eq. 2.4, the W^\pm bosons couple only to left-handed particles (and right-handed anti-particles). The Z boson turns out to be the carrier of the neutral weak current. Its couplings to fermions do not show a pure $(V - A)$ structure any more due to the mixed state of $W_\mu^{(3)}$ and B_μ . The Z coupling is therefore modified to

$$(v_f - a_f \cdot \gamma_5) . \quad (2.9)$$

The vector and axial vector coupling coefficients v_f and a_f depend on the fermion charges, Q_f , the three-components of the weak isospin, I_3^f , and the electroweak mixing angle, θ_w :

$$v_f = \frac{I_3^f - 2Q_f \sin^2 \theta_w}{2 \sin \theta_w \cos \theta_w} , \quad a_f = \frac{I_3^f}{2 \sin \theta_w \cos \theta_w} . \quad (2.10)$$

This interference between vector and axial vector coupling of fermions to the Z boson is the origin of the forward-backward asymmetry occurring in the $e^+e^- \rightarrow Z \rightarrow q\bar{q}$ process at LEP 1 energies.

Calculations in the Standard Model are expressed as a perturbative expansion in terms of the coupling constant, where the terms are represented by Feynman diagrams containing increasing numbers of fundamental vertices. The different types of fundamental electroweak vertices are shown in Fig. 2.1. The neutral current manifests itself as radiation of a photon or Z by a fermion as well as in the crossed processes, fermion pair production and annihilation. The mid diagram shows the charged current via radiation of a W^\pm boson, hereby changing the flavour, i.e. a charged lepton into its antineutrino and a quark into its isospin partner antiquark. Also, the coupling between gauge bosons is possible: the decay of a neutral boson into charged W bosons as observed at LEP 2 energies.

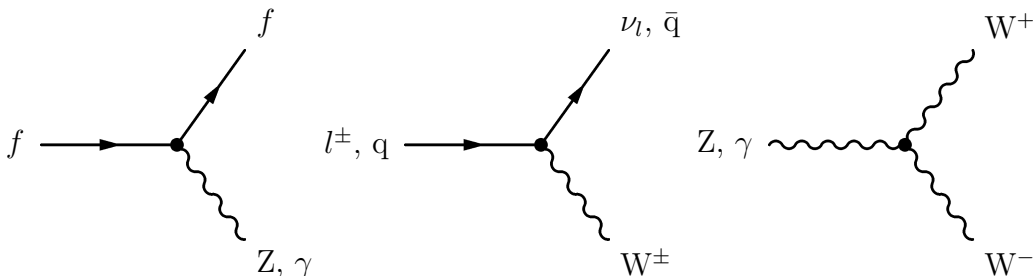


Figure 2.1: The fundamental Feynman graphs of the electroweak theory. From left to right is shown the neutral current, the charged current and the boson self-coupling.

The fermions spontaneously acquire mass as well; this time via a generic “Yukawa” interaction, $g_f \bar{\psi} \psi \Phi$. This type of interaction is not a gauge interaction, and the fermion masses are not predicted by the electroweak theory. Instead, they are determined not only by the scale of the electroweak symmetry breaking, v , but also by their Yukawa coupling to the Higgs field. This coupling, $g_f = m_f \sqrt{2}/v$, is arbitrary in the Standard Model. Here it should be noted that the Higgs couples most strongly to the heaviest particles.

Only the weak interaction is able to change a member of an isospin doublet to the corresponding partner within one family. As a consequence, the lighter quark in each family will be stable — like the neutrino in the case of the lepton doublets. However, stable particles with s or b quark content are not found in nature; instead, the decay of s quarks into d quarks is observed. The reason for that is the electroweak eigenstates d' , s' and b' not coinciding with the mass eigenstates, but forming a linear combination,

$$\begin{pmatrix} d' \\ s' \\ b' \end{pmatrix} = U \cdot \begin{pmatrix} d \\ s \\ b \end{pmatrix} . \quad (2.11)$$

The transformation matrix U is called Cabibbo-Kobayashi-Maskawa (CKM) matrix. It is not diagonal, and hence leads to transitions between quark generations in the charged current interaction. However, U is unitary, so that the neutral current part becomes diagonal in the mass basis, that is flavour-changing neutral currents do not exist. By redefinition of the quark fields, the nine real parameters of U can be reduced to four: three “rotational angles” and one CP -violating phase.

2.2 Quantum Chromodynamics

At about the same time in the 1960ies, M. Gell-Mann, Y. Ne'eman and G. Zweig derived the quark hypothesis from the ordinance of the more and more copiously discovered hadrons [5]. It implies that all strongly interacting particles consist of quarks, elementary particles carrying a new degree of freedom, *colour*. The hint at colour- $SU(3)$ for strong interaction came from the study of baryon spectroscopy and the idea of flavour- $SU(3)$, an approximate symmetry rotating the three light quarks u, d, s. From there it was known that for example the Δ^{++} particle consisted of (uuu) in an s -state, a system with spin z component $+\frac{3}{2}$. Its wave function is totally symmetric in space, spin and flavour (a seeming violation of the Pauli principle) so that complete antisymmetry in the colour state is required.

In Quantum Chromodynamics, $SU(3)_C$ is therefore selected as a gauge group, implying that quarks carry colour charge, which the eight gauge bosons of $SU(3)_C$, the gluons, couple to. The $SU(3)_C$ group is believed to be an exact gauge symmetry so that the gluons are massless. Its non-abelian structure makes the gluons themselves carriers of colour and allows self-coupling between differently colour-charged gluons, analogous to the ZW^+W^- and γW^+W^- vertices in the electroweak interaction. The three fundamental processes of QCD are shown in Fig. 2.2.

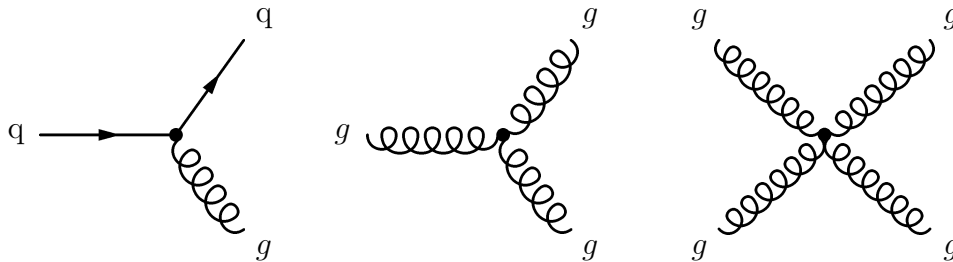


Figure 2.2: The fundamental Feynman graphs of QCD. From left to right they are the gluon radiation or quark pair production, and the self-coupling of three and four gluons.

The colour charge exists in three states, termed *red*, *green* and *blue*. A $SU(3)_C$ triplet consists of a red, green and blue quark of identical flavour; hence the strong interaction does not change flavour. The choice of $SU(3)_C$ is confirmed experimentally by many processes that directly measure the number of different existing colour charge states, N_c . A famous example is the measurement of the ratio R of the hadronic cross-section to the muon cross-section in e^+e^- annihilation,

$$R = \frac{\sigma(e^+e^- \rightarrow q\bar{q})}{\sigma(e^+e^- \rightarrow \mu^+\mu^-)} \quad . \quad (2.12)$$

It is directly proportional to N_c , and the data clearly indicate $N_c = 3$ [6].

However, experiments do not observe free colour-charged *partons*, i.e. quarks or gluons, but only colour-neutral bound states, the *hadrons*. The latter are classified in two groups, baryons and mesons. *Baryons* consist of three quarks, one in each colour state red, green and blue. In analogy to chromatics this forms a colour-neutral state. *Mesons* are made of a quark and an antiquark, so that colour and anti-colour add to

a neutral state. Baryons have half-numbered spins while mesons are hadrons with whole-numbered spins.

This non-observation of free colour-charged partons is related to two very striking properties of the dynamical behaviour of the strong interaction: confinement and asymptotic freedom. *Confinement* is a mechanism which encloses bound state partons in the space of the size of about a nucleus. Terms rapidly rising with distance in the potential between quarks make it energetically impossible to separate them. If quark pairs are created in high energy collision experiments and move apart in their centre-of-mass rest frame, the energy stored in the colour field is sufficient to create additional quark-antiquark pairs in a process called fragmentation, thus neutralising colour. Confinement also explains the short-range nature of nuclear forces, while exchange of massless gluons otherwise is long-range. By contrast, the *asymptotic freedom* allows the quasi-free movement at small distances respectively high energies.

This behaviour is expressed in the theory by an energy dependent coupling constant α_s , that rises rapidly with distance respectively with decreasing energy. Energy dependence is derived from renormalisation (see also Section 2.4), a technique to cancel divergences in the Feynman amplitudes of higher order perturbation theory by including them into the coupling “constant”. This *running coupling constant* has to solve the renormalisation group equation (RGE), which itself is a consequence of requiring the renormalisation process to be independent of the renormalisation scale μ . In next-to-leading order the RGE reads

$$\mu^2 \frac{d\alpha_s(\mu^2)}{d\mu^2} = -b_0\alpha_s^2 - b_1\alpha_s^3 + \mathcal{O}(\alpha_s^4) \quad (2.13)$$

$$\text{with } b_0 = \frac{33 - 2n_f}{12\pi}, \quad b_1 = \frac{153 - 19n_f}{24\pi^2}, \quad n_f = \text{nb. of flavours} .$$

Its most general solution is

$$\alpha_s = \frac{1}{b_0 \log \frac{\mu^2}{\Lambda^2}} - \frac{b_1 \log(\log \frac{\mu^2}{\Lambda^2})}{(b_0 \log \frac{\mu^2}{\Lambda^2})^2} + \mathcal{O}\left(\frac{\log^2(\log \frac{\mu^2}{\Lambda^2})}{\log^2 \frac{\mu^2}{\Lambda^2}}\right) . \quad (2.14)$$

Although the forward-backward asymmetry is the result of a purely electroweak process, a precise model for the running of α_s is needed in the correction for QCD effects in the measured asymmetry and in the simulation of hadronic final states.

2.3 Standard Model Parameters and Phenomenology

The Standard Model of electroweak and strong interaction features altogether 18 free parameters, i.e. parameters that are not predicted by theory but have to be determined by experiments and used as inputs to the model. They are the coupling constants α_s , g_1 , g_2 , six quark masses and three lepton masses, the four parameters of the CKM matrix and the masses of the Higgs and Z bosons, m_h and m_Z . It should be noted that the W mass, m_W , is not a free parameter but determined via Eq. 2.7. Instead of the couplings g_1 , g_2 the mathematically equivalent and much more precisely measured observables α_{QED} (the electromagnetic coupling) and G_F

(Fermi constant obtained from the muon lifetime τ_μ) are used as inputs. The number of parameters probably needs to be complemented by the neutrino masses and a corresponding mixing matrix [7]. But neutrino masses are too small to be detected directly and may have a different origin than the masses of the quarks and charged leptons, so this has not yet been fully implemented in the Standard Model.

The Standard Model has been firmly established by the enormous success in predicting new particles (c , b , t , W^\pm and Z) and by its ability to accurately describe the bulk of the present data. The existence of the Higgs boson and the parameters in the neutrino sector are the main open questions raised by the Standard Model, which have to be answered in the future. Still, there are aesthetic reasons why the gauge theory based on $SU(3)_C \otimes SU(2)_L \otimes U(1)$ is not considered as the final theory. They are mainly

- The *family problem*. The total number of families in the theory is neither predicted nor restricted. The sum of the electric charges in each family vanishes, which is not explained but turned out to be necessary for the construction of a renormalisable theory.
- The *fermion masses*, which are arbitrary parameters in the Standard Model. A more fundamental theory is expected to explain their very wide spectrum.
- The *grand unification*. $SU(3)_C \otimes SU(2)_L \otimes U(1)$ is not a unified theory, i.e. for each group factor there is a different coupling constant. In addition, there is no reason why the electric charge is quantised, as in Abelian QED there is no gauge boson self-coupling to fix the coupling constant.

Theories beyond the Standard Model thus try to unify the three forces by seeing $SU(3)_C \otimes SU(2)_L \otimes U(1)$ as the remnants of a larger, but simple group G , which is spontaneously broken at very high energies. All possible candidates for such a grand unified theory (GUT) suffer from the hierarchy problem, the need of having a very fine-tuned cancellation of the quadratic divergences in the mass correction terms of the scalar particles. The hierarchy problem is technically solved by supersymmetric GUTs (SUSY). They establish a relation between the previously independent three types of fields — the gauge, matter and scalar fields — by assigning a fermionic superpartner to each boson, and vice-versa. To agree with the non-observation of light superpartners, supersymmetry must be broken and the supersymmetric particles heavy. Models that assume a specific SUSY breaking process are able to express all the low-energy parameters in terms of a few free parameters at the GUT scale. The most prominent of these specific models, or scenarios, are minimal Supergravity (mSUGra), minimal Gauge Mediated SUSY Breaking (mGMSB), and minimal Anomaly Mediated SUSY Breaking (mAMSB). The specific models are much more predictive than the unconstrained SUSY, which makes no specific assumptions but uses a parameterisation of all SUSY-breaking terms instead. Further theories, which go beyond SUSY, replace the model of point-like particles by a theory of vibrating superstrings. Currently superstrings can not be verified or excluded by experiments.

2.4 Radiative Corrections

Based on the $SU(3)_C \otimes SU(2)_L \otimes U(1)$ group described above, the Standard Model predicts processes and observables by computing exchange amplitude matrix elements via the so-called Feynman rules. The matrix elements or probabilities of *all* graphs with identical initial and final state have to be added, thus leading to a perturbation expansion in orders of the coupling constant.

In principle, already the lowest order, the Born level, gives a meaningful quantitative prediction, which can be computed with relatively small effort. The experimental precision of the Z factories LEP and SLC (of order 0.1%) is such that the measurements are sensitive to one-loop effects and even higher orders — and the high quality of the fits to all data confirms the presence of these corrections strongly, thus establishing the Standard Model as a quantum field theory.

Radiative corrections, that is the above-mentioned virtual loops and higher-order corrections, have therefore to be taken into account in theory predictions. As a consequence, however, divergences appear in the Lagrangian. They are overcome by the method of dimensional regularisation, which introduces renormalised parameters and fields into the original Lagrangian, leading to non-divergent, finite results independent of regulator and renormalisation scale in the prediction of physical observables. Within a theory model, i.e. concerning the relation between the free parameters, the choice of the renormalisation scheme is relevant. In QCD often the so-called modified minimal subtraction scheme, \overline{MS} , is chosen because the absence of free fundamental particle states does not necessitate the choice of a specific mass scale in the renormalisation procedure. This is different for the electroweak corrections, where the *on shell* scheme is chosen instead. It uses the boson masses, m_W , m_Z and m_h , the fermion masses and the electron charge as experimentally determined parameters. One of its advantages is the possibility of treating weak and photonic corrections separately in first order perturbation theory. The different radiative corrections are summarised in the following; a more detailed description can be found in the “Z Physics at LEP 1” report [8].

QED radiative corrections

The QED radiative corrections comprise all Feynman diagrams with an emission of a real photon and with an internal photon loop. The QED corrections are calculated with very high precision and do not add to the sensitivity to the Standard Model parameters. However, in e^+e^- annihilation the corrections due to photon emission in the initial e^+e^- state (ISR¹) are particularly large:

- At energies above the Z peak, the emission reduces the centre-of-mass energy available to the e^+e^- system so that the annihilation reaction takes place at the Z peak, which is favoured due to its much higher cross-section. The total cross-section is thereby increased, and observables (such as the asymmetry) at a much higher centre-of-mass energy \sqrt{s} receive contributions from the effective lower energies $\sqrt{s'} < \sqrt{s}$.
- At a double beam energy which is just a few GeV above the Z peak, it is sufficient to include the ISR correction in the theory prediction while the correction

¹Initial State Radiation

also depends on the experimental set-up at LEP 2 energies of 130 GeV and more.

- At the Z peak the ISR correction still represents the main part of the QED correction, leading to a reduction of both cross-section and asymmetry of the order of 10%. The correction to the asymmetry due to final state radiation amounts to 0.17%, and the interference between both is negligibly small.

The QED corrections are calculated within the ZFITTER programme package [9]; the way how this is done and their effect on the asymmetry are discussed in a more detailed way in Section 2.6.

Weak radiative corrections

The second-order weak corrections are one-loop diagrams with an internal line formed by a fermion, a W or a Z. They can be divided into three groups: corrections to the Z/ γ propagator, vertex corrections and box diagrams. For each of them an example is shown in Fig. 2.3. What is particularly interesting in the first two graphs is that they

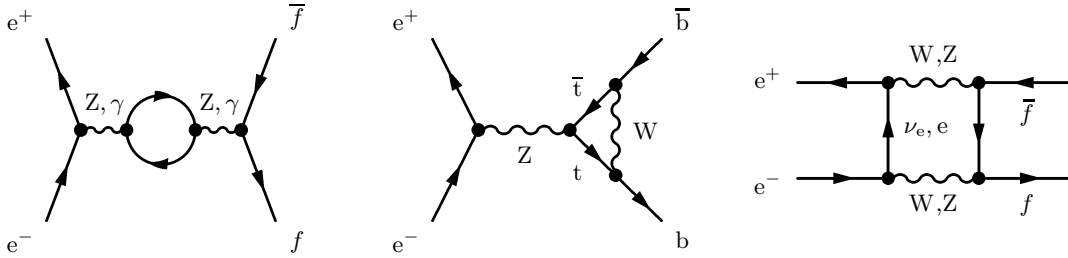


Figure 2.3: The principal Feynman diagrams of the weak radiative corrections: correction to the Z/ γ propagator, vertex correction and box diagram (from left to right).

include the appearance of virtual particles, which cannot be produced kinematically at LEP energies, such as the t quark and the Higgs boson. Contrary to the heavy quark suppression in QED vacuum polarisation, the corrections for the weak case are proportional to m_t^2 and hence large for the heavy t quark. The reason for this non-decoupling of heavy particles in the electroweak theory lies in the property of the spontaneous symmetry breaking that both gauge bosons and fermions are given mass by a common Higgs vacuum expectation value.

The close coupling between t and b quark within the electroweak isospin doublet enables a $t\bar{t}$ pair to be produced and later converted to a $b\bar{b}$ final state by W exchange. This process is displayed in Fig. 2.3 and leads to an additional m_t -dependent correction for $b\bar{b}$ final states. As a consequence, the first precision b quark measurements at LEP allowed a prediction of the (at that time unknown) t quark mass. Now it is the experimental error of its direct measurement that influences the interpretation of heavy quark results. For the Higgs boson mass, however, the corrections proportional to m_h^2 are cancelled out, leaving only logarithmic terms. Also the two-loop level radiative corrections are relatively insensitive to m_h , so that it is difficult to get a grip on the Higgs boson mass from fits to the electroweak precision data.

Box diagrams refer to the exchange of two massive bosons and become resonant only at LEP 2 energies near the WW and ZZ thresholds, at 161 GeV and above. Their

effect turns out to be negligibly small at the Z resonance, but is nevertheless included in the flavour-dependent form factors ρ_f (Eq. 2.20) [9, 10].

As indicated above, the on-shell scheme proposed by D.A. Ross and J.C. Taylor [11] uses e , m_W , m_Z , m_h and m_f as inputs. The derived quantity $\sin\theta_W$ then is not the same anymore if it is defined by the couplings (Eq. 2.6) or via the boson masses (Eq. 2.7). The choice of A. Sirlin [12] fixes the renormalised mixing angle in all orders of perturbation theory to

$$\sin^2\theta_W = 1 - \frac{m_W^2}{m_Z^2} . \quad (2.15)$$

The definition via the coupling constants, respectively the experimental inputs α_{QED} and G_F is then modified by a correction factor $(1 - \Delta r)^{-1}$ to

$$\sin^2\theta_W = \frac{1}{2} \left(1 - \sqrt{1 - \frac{4\pi\alpha_{QED}}{\sqrt{2}G_F m_Z^2} \cdot \frac{1}{1 - \Delta r}} \right) , \quad (2.16)$$

where $\Delta r = \Delta\alpha_{QED} - \cot^2\theta_W \cdot \Delta\rho + \Delta r_{\text{rem.}}$ contains the weak corrections: $\Delta\alpha_{QED}$ covers the QED vacuum polarisation, $\Delta\rho$ the vacuum polarisation contribution to the W and Z propagators while $\Delta r_{\text{rem.}}$ contains the vertex corrections and the $\ln(m_h^2/m_W^2)$ dependent effects due to the Higgs boson.

The weak corrections do not depend at all on the experimental set-up. Therefore they can be absorbed into the energy dependence of the electromagnetic coupling, the definition of an effective electroweak mixing angle and the re-definition of the Z couplings [13].

$$\alpha \longrightarrow \alpha(m_Z^2) = \frac{\alpha}{1 - \Delta\alpha} \approx 1.064 \cdot \alpha \quad (2.17)$$

$$\begin{aligned} \sin^2\theta_W \longrightarrow \sin^2\theta_{\text{eff}}^f &= \sin^2\theta_W + \cos^2\theta_W \cdot \frac{2\sqrt{2}G_F(m_t^2 - m_b^2)}{(4\pi)^2} \\ &+ \frac{\alpha}{4\pi} \left[\ln \left(\frac{m_h}{17.3 \text{ GeV}/c^2} + 1 \right) - 2 \right] + \text{h.o.} \end{aligned} \quad (2.18)$$

$$a_f \longrightarrow \bar{a}_f = \sqrt{\rho_f} \cdot a_f \quad (2.19)$$

$$v_f \longrightarrow \bar{v}_f = \sqrt{\rho_f} \cdot \frac{I_3^f - 2Q_f \sin^2\theta_{\text{eff}}^f}{2 \sin\theta_W \cos\theta_W} \quad (2.20)$$

This definition is termed the improved Born level, indicating that the structure of the tree level equations does not need to be modified. In the following it will be used as lowest order in the theory predictions.

QCD radiative corrections

Radiating gluons in the quark final state differs from photon final state radiation only by the strong coupling constant and its characteristics. However, as colour-charged particles the radiated gluons are subject to confinement and contribute to the hadron formation. The treatment of gluon radiation is therefore a part of the phenomenological models for the transition from quarks to hadrons (see Section 2.7.2), and is not combined with the other radiative corrections in the analytic theory prediction. The effects of gluon radiation on the asymmetry depend on the experimental set-up. Their correction is described later in Section 8.4.

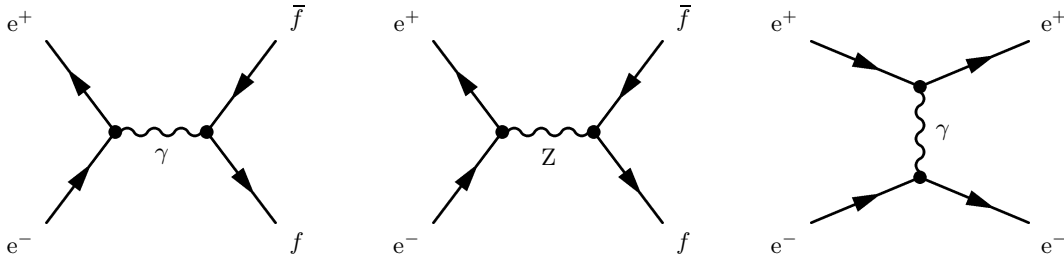


Figure 2.4: The Feynman diagrams for e^+e^- annihilation into fermions at energies close to the Z resonance. Directly at $\sqrt{s} = m_Z$, the Z exchange (middle) is by far the dominant channel. The reaction $e^+e^- \rightarrow e^+e^-$ receives a contribution from the t channel exchange (right diagram).

2.5 Fermion Pair Production at LEP

At an e^+e^- collider like LEP (see Section 3.1), fermion pairs are produced via the diagrams shown in Fig. 2.4. In particular, heavy quark final states can only be created by the s -channel exchange of a neutral gauge boson. The electroweak theory predicts the cross-section for the reaction $e^+e^- \rightarrow f\bar{f}$ at the improved Born level (and allowing for mass effects) to

$$\left(\frac{d\sigma}{d\cos\theta}\right)_f = \frac{2\pi\alpha^2}{4s} N_c^f \sqrt{1-4\mu_f} \cdot \left[G_1(s)(1+\cos^2\theta) + 4\mu_f G_2(s)\sin^2\theta + \sqrt{1-4\mu_f} G_3(s) \cdot 2\cos\theta \right] \quad (2.21)$$

$$\begin{aligned} G_1(s) &= Q_f^2 - 2v_e v_f Q_f \operatorname{Re}\chi_0(s) + (v_e^2 + a_e^2)(v_f^2 + a_f^2 - 4\mu_f a_f^2) |\chi_0(s)|^2, \\ G_2(s) &= Q_f^2 - 2v_e v_f Q_f \operatorname{Re}\chi_0(s) + (v_e^2 + a_e^2)v_f^2 |\chi_0(s)|^2, \\ G_3(s) &= \underbrace{-2a_e a_f Q_f \operatorname{Re}\chi_0(s)}_{\gamma\text{-exch.}} + \underbrace{4v_e a_e v_f a_f |\chi_0(s)|^2}_{\gamma\text{-Z interference}} + \underbrace{4v_e a_e v_f a_f |\chi_0(s)|^2}_{\text{pure Z exchange}} \end{aligned} \quad (2.22)$$

as a function of the variables

$$\begin{aligned} s &= \text{square of the centre-of-mass energy, } E_{\text{CM}}^2, \\ \theta &= \text{scattering angle (between incoming electron and outgoing fermion)} \end{aligned} \quad (2.23)$$

and the parameters

$$\begin{aligned} N_c^f &= \text{Number of colour degrees of freedom} = \begin{cases} 3 & \text{for quarks} \\ 1 & \text{for leptons} \end{cases}, \\ \mu_f &= \frac{m_f^2}{s}, \quad m_f = \text{fermion mass}. \end{aligned} \quad (2.24)$$

It uses the vector and axial vector couplings defined in Eq. 2.10 and 2.20 as well as the Z propagator,

$$\chi_0(s) = \frac{s}{s - m_Z^2 + im_Z\Gamma_Z}, \quad (2.25)$$

with the total decay width

$$\Gamma_Z = \sum_f N_c^f \frac{\alpha}{3} m_Z \sqrt{1 - 4\mu_f} \left(v_f^2 (1 + 2\mu_f) + a_f^2 (1 - 4\mu_f) \right) . \quad (2.26)$$

At $\sqrt{s} = m_Z$ the Z propagator (Eq. 2.25) becomes resonant so that the photon exchange and its interference with the Z exchange can be neglected. Eq. 2.21 is valid only for unpolarised incoming beams and for the sum of all polarisation states of the outgoing fermions. Furthermore, it is restricted to the case that the outgoing fermion is not an electron, as for electrons the t channel exchange, Bhabha scattering, has to be added (Fig. 2.4 on the right). For the analysis of Z decays to heavy quarks it forms a background contribution, that can be fully suppressed by selection cuts, and is therefore neglected in the following. Integration over all scattering angles yields the total cross-section at Born level,

$$\sigma_f(s) = \int_{-1}^1 d \cos \theta \left(\frac{d\sigma}{d \cos \theta} \right)_f = \frac{\pi \alpha^2}{4s} N_c^f \sqrt{1 - 4\mu_f} \left(\frac{8}{3} G_1 + 2\pi \mu_f G_2 \right) . \quad (2.27)$$

2.6 Forward-Backward Asymmetries at LEP

The angular dependence of the differential cross-section (emphasised by bold print in Eq. 2.21) has a contribution proportional to **cos θ** , which does not maintain the symmetry at $\theta = 90^\circ$ given by the incoming particle beams. This is parameterised by the *forward-backward asymmetry*

$$A_{\text{FB}} \equiv \frac{\sigma_{\text{F}} - \sigma_{\text{B}}}{\sigma_{\text{F}} + \sigma_{\text{B}}} , \quad (2.28)$$

where σ_{F} (σ_{B}) denotes the contribution to the total cross-section from a fermion moving to the forward (backward) direction with respect to the incoming electrons.

$$\sigma_{\text{FORWARD}} = \int_0^1 d \cos \theta \frac{d\sigma}{d \cos \theta} , \quad \sigma_{\text{BACKWARD}} = \int_{-1}^0 d \cos \theta \frac{d\sigma}{d \cos \theta} . \quad (2.29)$$

The big advantage of the asymmetry observable compared to the cross-section is its independence of the total event rate, while it provides the same sensitivity to the predictions of the electroweak theory.

Inserting the differential cross-section Eq. 2.21 into the asymmetry definition, Eq. 2.28, yields its dependence of centre-of-mass energy and fermion type,

$$A_{\text{FB}}(s, f) = \frac{3}{4} \cdot \frac{G_3(s, f) \sqrt{1 - 4\mu_f}}{G_1(s, f) + 2\mu_f G_2(s, f)} . \quad (2.30)$$

It is shown in Fig. 2.5 at the improved Born level for a wide range of centre-of-mass energies, and at the level of the full QED and electroweak corrections for the energy range close to $\sqrt{s} = m_Z$, which is relevant for this analysis.

The programme ZFITTER [9] was used to compute both diagrams in Fig. 2.5. It obtains the improved Born prediction directly from Eq. 2.30, hereby taking the effective couplings Eq. 2.17 to 2.20. ZFITTER then computes the QED-corrected observables

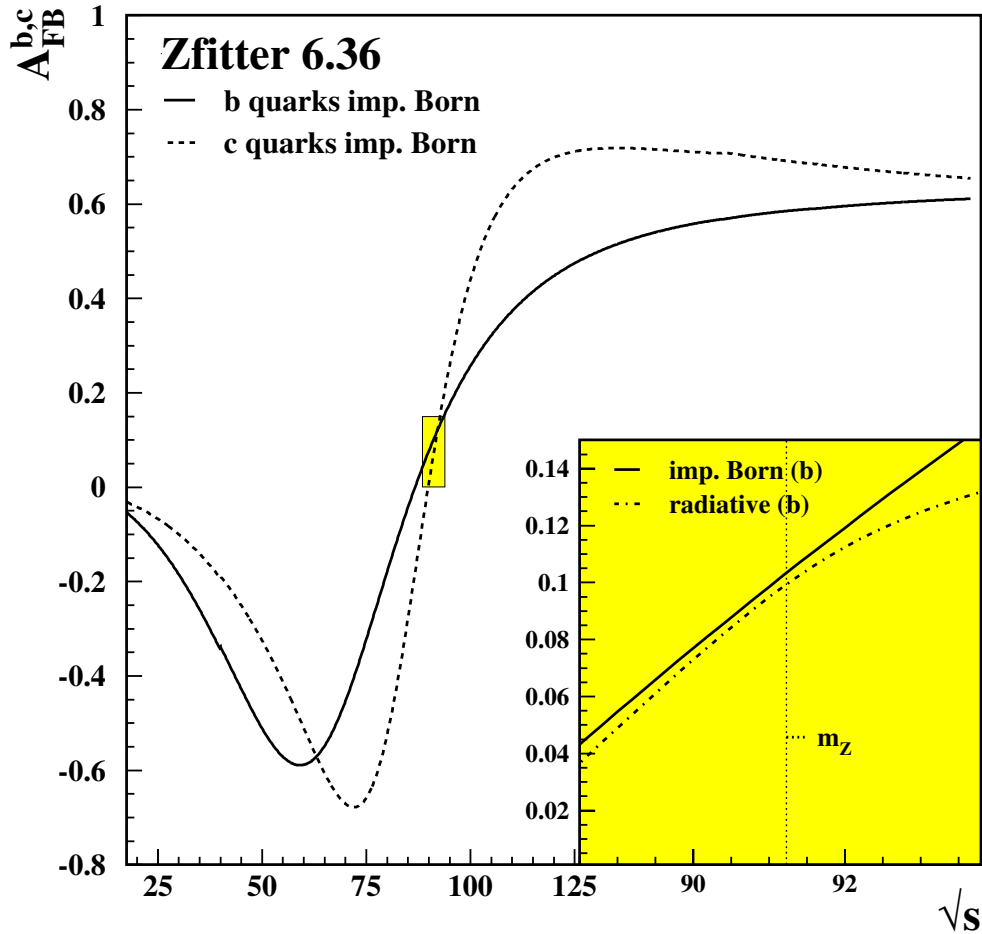


Figure 2.5: The forward-backward asymmetry as a function of the centre-of-mass energy. The large plot displays the improved Born calculation for b and c quarks. In the zoomed region around the Z resonance, a comparison between the improved Born and full QED corrected b quark asymmetry is given.

in a semi-analytic ansatz by folding the Born cross-sections $\sigma_{\text{TOT}} = \sigma_{\text{F}} + \sigma_{\text{B}}$ and $\sigma_{\text{FB}} = \sigma_{\text{F}} - \sigma_{\text{B}}$ with radiator functions:

$$\sigma_{\text{TOT,FB}}(s) = \int_{s_0}^s ds' \sigma_{\text{TOT,FB}}^{\text{Born}}(s') \cdot G_{\text{TOT,FB}}(s, s') \quad . \quad (2.31)$$

The latter describes photon emission up to an effective centre-of-mass energy $\sqrt{s'}$

$$s' = (1 - v)s \quad \text{using} \quad v = \frac{E_\gamma}{E_{\text{Beam}}} = 2 \frac{E_\gamma}{\sqrt{s}} \quad (2.32)$$

whose lower limit $\sqrt{s_0}$ is given either by the kinematic limit $4m_f^2$ or an experimental cut on $\sqrt{s'}$. The radiator functions, $G_{\text{TOT,FB}}(s, s')$, are discussed in detail in the ZFITTER manual [9]. At $\sqrt{s} = m_Z$, they are assumed independent of the observable under consideration (σ_{TOT} or σ_{FB}) and of the type of emission (ISR or FSR). The version of radiator functions implemented in ZFITTER is however applicable to the entire energy range of LEP 1 and LEP 2.

If the contributions to the differential cross-section are sorted according to the type

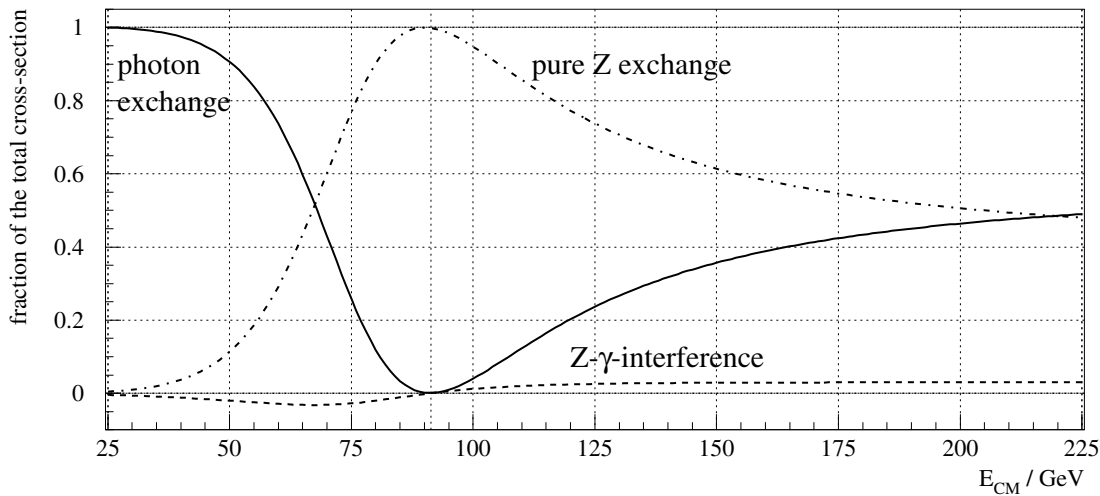


Figure 2.6: The relative contributions to the total hadronic cross-section resulting from the photon exchange, the Z exchange and the interference between the two diagrams (according to the equations in Section 2.5).

of coupling (such as in Eq. 2.22) instead of functions in θ it can be decomposed in three parts:

- terms proportional to Q_f^2 originating from the pure photon exchange,
- terms proportional to $|\chi_0(s)|^2$, which represent the pure Z exchange, and
- terms proportional to $Q_f \cdot \text{Re}\chi_0(s)$, which result from the interference between the two diagrams.

The energy dependence of the three distinct contributions to the total cross-section is displayed in Fig. 2.6. The term from the Z/ γ interference is strongly forward-backward asymmetric at energies above and below the Z resonance, and leads to the large values of up to 0.6 for A_{FB} in Fig. 2.5. The interference term hardly adds to the total cross-section, and vanishes at $\sqrt{s} = m_Z$ together with the pure photon exchange. As a consequence, A_{FB}^f at $\sqrt{s} = m_Z$ observes the parity-violating properties in the coupling of the Z to fermions directly. The *pole asymmetry* $A_{\text{FB}}^{0,f}$, which is A_{FB}^f at $\sqrt{s} = m_Z$ in improved Born calculation, can be expressed as the product of the fermion polarisation parameters,

$$A_{\text{FB}}^{0,f} = \frac{3}{4} \mathcal{A}_e \mathcal{A}_f \quad , \quad (2.33)$$

safely neglecting the fermion masses and the contributions from the photon exchange. The polarisation parameters,

$$\mathcal{A}_f = \frac{2v_f a_f}{v_f^2 + a_f^2} = \frac{2}{\frac{v_f}{a_f} + \frac{a_f}{v_f}} \quad , \quad (2.34)$$

depend solely on the ratio of the vector and axial-vector couplings. This ratio yields the effective electroweak mixing angle,

$$\frac{v_f}{a_f} = 1 - 4 |Q_f| \sin^2 \theta_{\text{eff}}^f \quad . \quad (2.35)$$

The particle properties and the electroweak mixing angle in the Standard Model are such that the \mathcal{A}_f values are close to 1.0 for b (and c) quarks. The sensitivity of the b quark asymmetry to \mathcal{A}_e is therefore much higher than that to \mathcal{A}_b , thus determining mainly the *leptonic* effective electroweak mixing angle, $\sin^2 \theta_{\text{eff}}^\ell$:

$$\mathcal{A}_q \frac{\partial \mathcal{A}_e}{\partial \sin^2 \theta_{\text{eff}}^\ell} \gg \mathcal{A}_e \frac{\partial \mathcal{A}_q}{\partial \sin^2 \theta_{\text{eff}}^q} . \quad (2.36)$$

As a consequence, the results from the forward-backward asymmetry of b and c quarks can be combined with lepton final state measurements to determine $\sin^2 \theta_{\text{eff}}^\ell$ with high precision, and to put constraints on the Higgs boson mass, which enters the effective mixing angle via higher order electroweak corrections. Although the Higgs boson mass dependence is only logarithmic (Eq. 2.18), $\sin^2 \theta_{\text{eff}}^\ell$ is still the most sensitive quantity to m_h in the Standard Model. For example, compared to the W mass it is

$$\frac{\delta \sin^2 \theta_{\text{eff}}^\ell}{\sin^2 \theta_{\text{eff}}^\ell} \approx 0.0023 \frac{\delta m_h}{m_h} \quad \text{versus} \quad \frac{\delta m_W}{m_W} \approx 0.0008 \frac{\delta m_h}{m_h} . \quad (2.37)$$

As the Higgs boson has not been discovered at LEP [14], this dependence provides an additional strong motivation for the LEP experiments to measure the b quark asymmetry with an optimal precision.

2.7 The Transition from Quarks to Stable Particles

The quark confinement discussed in Section 2.2 enforces the formation of colour-neutral hadrons out of the colour field of the primary quarks and possibly emitted gluons, so that the primary quarks cannot be observed directly. As a consequence, the final state consists of colour-neutral particles, that are grouped in jets pointing along the direction of the primary quark. To be able to test the theoretical predictions it is therefore necessary to simulate this final state by means of event generators. For this purpose, the process $e^+e^- \rightarrow \text{hadrons}$ is divided into four phases, as displayed in Fig. 2.7 for centre-of-mass energies close to m_Z .

The first phase, the annihilation of the e^+e^- pair and the subsequent creation of the initial quark pair, is a pure electroweak process and can be calculated according to Sections 2.1, 2.4 and 2.5. The *parton cascade* in phase II comprises QCD processes that can be calculated perturbatively, namely the emission of gluons with high energy, which lead to the creation of further $q\bar{q}$ pairs. The calculations in perturbative QCD are limited by a minimal momentum transfer of $\sim 1 \text{ GeV}/c$, beyond which the transition from the quasi-free partons to bound-state hadrons, the *fragmentation* process, has to be predicted by phenomenological models (phase III). Both parton cascade and fragmentation are explained in detail in the following Sections 2.7.1 and 2.7.2. In the last phase (phase IV), the decays of τ leptons and unstable hadrons determine the experimentally observable final state. Hereby it has to be taken into account that long-lived unstable hadrons can possibly decay during the detection process, that is in or in between sub-detectors. Details on the decays and transformations of hadrons with b and c quark content are given in Section 2.8.

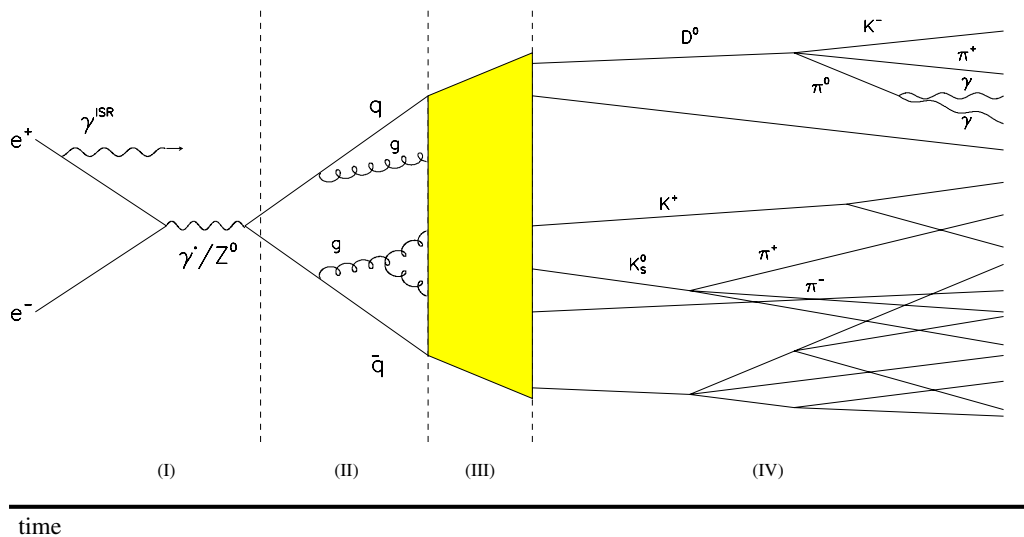


Figure 2.7: The transition $e^+e^- \rightarrow hadrons \rightarrow stable\ particles$, split into the four phases: pair production in e^+e^- annihilation, the perturbative formation of quarks and gluons, the analytically not accessible hadronisation and the final phase of decays of unstable hadrons.

2.7.1 The Parton Cascade

The hard gluon radiation after the initial quark production and the subsequent splitting into more quarks and gluons with high momentum transfer is the regime of perturbative QCD. It means the running coupling constant is sufficiently smaller than 1, so that the perturbative expansion converges. One way to obtain the probability for the resulting final state is therefore to compute it directly by means of *QCD matrix elements*. This can be performed up to the second order in α_s , resulting in a $qqqq$ or $qqgg$ final state and leaving a possible further splitting into more partons to the fragmentation model.

The other way consists of an iterative procedure like the *QCD cascade model*. It produces a quark-gluon shower by calculating the process of gluon emission or gluon splitting into partons in leading logarithmic approximation in an iterative way, which uses the split virtuality (i.e. squared momentum) as input to the next iteration. A cut-off parameter is used to keep off the non-perturbative region and to stop the iteration, preventing infrared divergences at low momenta. This model is implemented in the PYHTIA/JETSET simulation programme [15] used throughout this analysis.

2.7.2 String Fragmentation

At a momentum transfer of below $\sim 1\text{ GeV}/c$, the size of the strong coupling α_s does not allow of a perturbative calculation, hence the fragmentation has to be described by QCD-based phenomenological models. The *Independent Jet Fragmentation* approach was suggested as early as in 1972 [16] and became a wide-spread model with the R.D. Field and R.P. Feynman paper [17]. Lacking somewhat theoretical motivation as well as agreement with the data it is not used any more in today's models,

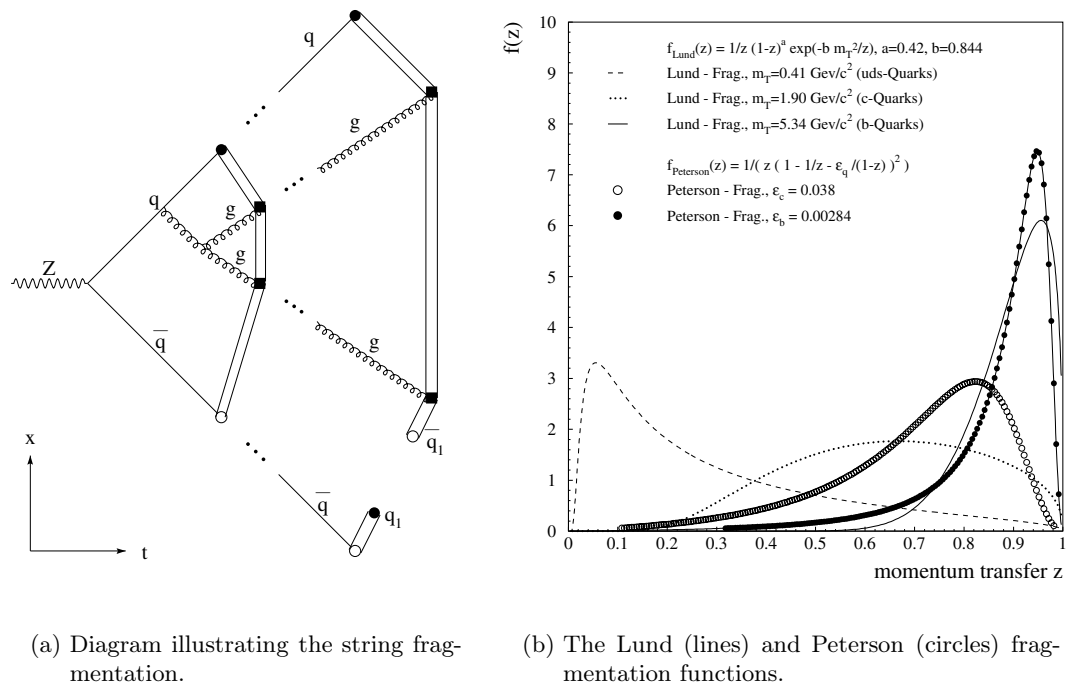


Figure 2.8: The string fragmentation.

but it did pass on to them the basic idea that the fraction of energy and longitudinal momentum contained in the fragmentation products,

$$z = \frac{(E + p_{\parallel})_{\text{hadron}}}{(E + p_{\parallel})_{\text{quark}}}, \quad (2.38)$$

follows a fixed distribution, a *fragmentation function*.

The Lund model of the string fragmentation is directly based on the concept of QCD confinement by assuming a colour flux tube stretched between the partons of phase II – see Fig. 2.8(a). Such a colour “string” is supposed to have a transversal extension of ~ 1 fm and a maximal energy density $\kappa \approx 1$ GeV/fm. The rapidly moving apart primary quarks and hard gluons stretch the string and hence increase the energy stored in it linearly with growing distance. The string can break apart, hereby producing new quark-antiquark pairs, if its energy attains their rest energy. This procedure is likewise illustrated in Fig. 2.8(a). It is then repeated iteratively for every sub-string between the initial and the newly created (anti-) quark, until the energy stored in the string is of the order of the light hadron masses.

The string fragments with the newly produced quark-antiquark pairs at their end form mesons as colour-neutral states. In order to produce also baryons, the string fragmentation model contains two additional mechanisms: diquark production and popcorn scheme. The former describes the appearance of a highly correlated baryon anti-baryon pair by simultaneous creation of a pair of quarks (a diquark) and a pair of anti-quarks. The popcorn scheme features an additional meson in the fragmentation chain between baryon and anti-baryon and seems necessary to explain the observation of baryon resonances with a total spin greater than $\frac{3}{2}$.

The breaking apart of the string is a quantum mechanical process, in which the newly produced virtual $q\bar{q}$ pairs tunnel out to their mass shell. The energy fluctuation by uncertainty principle needed to create the $q\bar{q}$ pair is not compensated by re-annihilation, but supplied by the energy in the colour field between them. For that purpose, the quark and anti-quark need to separate in space and shorten the colour string by a distance that equals the total energy of the quark pair, $2m_{\perp} := 2\sqrt{m_q^2 + p_{\perp}^2}$. The mass dependence in the resulting tunnelling probability,

$$\mathcal{P} \propto \exp(-\pi m_{\perp}^2 \kappa^{-1}) \quad , \quad (2.39)$$

directly explains the observed suppression of heavy quark production during the fragmentation phase,

$$d : u : s : c : b = 1 : 1 : \gamma_s : 10^{-11} : 10^{-100} \quad . \quad (2.40)$$

The transverse momentum (with respect to the string) must be compensated locally due to the one dimensionality of the colour string. Independent of the quark flavour, it is given by an exponential distribution,

$$f(p_{\perp}^2) \sim \exp\left(-\frac{p_{\perp}^2}{2\sigma_{\perp}^2}\right). \quad (2.41)$$

Hereby σ_{\perp} is a free parameter in the fragmentation model. As briefly mentioned in the introductory paragraph, the distribution of the longitudinal momentum fraction, z , is controlled by a fragmentation function. For light quarks, the Lund symmetric function is used [15]:

$$f(z) = N \frac{(1-z)^a}{z} \cdot \exp\left(-b \frac{m_{\text{hadron}}^2 + p_{\perp}^2}{z}\right) \quad . \quad (2.42)$$

Recently this function has also proved to be adequate for heavy quark fragmentation [18, 19]. The older versions of the simulation, which are used in this analysis, have the Peterson function implemented for heavy quarks [20]:

$$f(z) = \frac{N}{z \left(1 - \frac{1}{z} - \frac{\epsilon_q}{1-z}\right)} \quad . \quad (2.43)$$

γ_s , a , b and ϵ_q are internal parameters of the simulation model. The s quark suppression, γ_s , happens to be about 0.3. Both fragmentation functions are displayed in Fig. 2.8(b) for fixed values of the parameters. The Lund function shows a clearly softer spectrum for light quarks (u, d, s) than for heavy quarks. Compared to the Lund function, the Peterson function yields a harder spectrum for c quarks, but a somewhat softer one for b quarks.

This is the fragmentation model as implemented in the PYHTIA/JETSET generator. It necessitates a large number of free parameters — controlling transverse momentum, flavour, spin, baryon production etc. — that have to be tuned using real data if available, like the millions of Z events produced at LEP [21].

2.8 The Properties of b- and c-Hadrons

The heaviest quarks that were produced at LEP are b and c quarks. In combination with light quarks from fragmentation, they form different types of B-mesons (mesons

particle	$I(J^P)$	fraction [%]	mass [MeV/ c^2]	lifetime [ps]
B^+	$\frac{1}{2}(0^-)$	38.9 ± 1.3	5279.0 ± 0.5	1.65 ± 0.03
B_d^0	$\frac{1}{2}(0^-)$	38.9 ± 1.3	5279.4 ± 0.5	1.55 ± 0.04
B_s^0	$0(0^-)$	10.7 ± 1.4	5369.6 ± 2.4	1.49 ± 0.07
b-baryons	$0(\frac{1}{2}^+)$	11.6 ± 2.0	—	1.21 ± 0.05
Λ_b	$0(\frac{1}{2}^+)$	—	$5624. \pm 9.$	1.23 ± 0.08
D^+	$\frac{1}{2}(0^-)$	23.4 ± 1.6	1869.3 ± 0.5	1.051 ± 0.013
D^0	$\frac{1}{2}(0^-)$	$54.5 \pm .$	1864.6 ± 0.5	0.413 ± 0.003
D_s^+	$0(0^-)$	12.6 ± 2.6	1968.5 ± 0.6	0.496 ± 0.010
c-baryons		9.5 ± 2.3	—	—
Λ_c	$0(\frac{1}{2}^+)$	—	2284.9 ± 0.6	0.206 ± 0.012

Table 2.2: Properties such as quantum number, production fraction, mass and lifetime of the most important b- and c-hadrons in their ground state, from [22]. The baryon production fractions in $b\bar{b}$ and $c\bar{c}$ events are given for the admixture of all ground state b- and c-baryons. The c-hadron fractions are normalised to 100%, hence no measurement error is quoted for the D^0 fraction [24].

detecting and identifying all stable particles from the considered decay. Although this method yields a very pure set of high-quality $b\bar{b}$ or $c\bar{c}$ measurements, its efficiency is extremely limited. Especially in the case of b quark events, the *inclusive* reconstruction has proved not only to be feasible, but also to be much more powerful than the exclusive method. By exploiting the distinctive features in the properties of b- and c-hadrons, the inclusive approach yields a highly enriched set of b-hadrons with an additional strong charge correlation to the primary quark charge. It forms the basic prerequisite for measuring b quark forward-backward asymmetries.

Heavy hadrons are distinguished from those with pure light quark content by their special characteristics such as the kinematics of their production, their mass, lifetime and decay properties. A large fraction of the momentum of the initial heavy quarks is passed on to the subsequently formed b- or c-hadron; an observation that is reflected by the hard fragmentation function in Fig. 2.8(b) for b and c quarks in the string fragmentation model. Firstly, this results in a relatively long flight distance of the decaying hadron. Secondly, the high momentum, passed to the decay particles, increases the track rapidities (see Section 6.2) and creates the leading particle effect, which aids in identifying the quark charge. Excited hadron states decay rapidly via the strong interaction to the corresponding ground state, so that the location of their decay cannot be measured separately from the production vertex (i.e. the primary vertex for b-hadrons).

However the ground states of the heavy hadrons decay weakly, allowing a relatively long lifetime. The most common b- and c-hadron ground states and their lifetimes are listed in Table 2.2. In combination with their large mass and hence large momentum, the long lifetime often leads to a flight length of several mm and to a displaced decay vertex. A schematic illustration of a typical heavy hadron decay topology is given in Fig. 2.10. The possibly displaced decay vertex is called secondary vertex. It is on

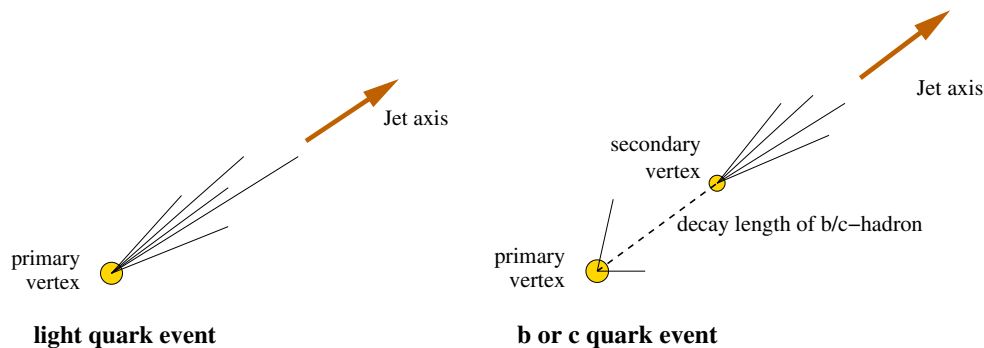


Figure 2.10: Schematic view of the topology of a light quark event (left) compared to an event with a primary b or c quark (right). Tracks from the fragmentation and a possible strong decay of excited B or D states originate from the primary vertex, while the particle trajectories from the heavy hadron decay point to the secondary vertex.

average separated from the primary vertex by 3 mm for B-mesons, 1.5 mm for D^0 -mesons and 4 mm for D^+ -mesons; a distance that can be detected by the powerful microvertex detectors used in the LEP experiments. An example for a real event with secondary vertices measured by the Vertex Detector can be found in Chapter 6 in Fig. 6.1. Apart from the heavy hadrons, only the Λ and the K_s^0 (see Fig. 2.9) have a similar average flight length, so that an observed secondary vertex and in particular the use of the reconstructed life time provides an excellent means of identifying b and c quark events with only low contamination from u, d and s quark events.

Another distinctive feature of b- and c-hadrons is their high mass (see Table 2.2) and consequently the high decay multiplicity. The relative mass difference between b- and c-hadrons of about a factor three is sufficiently large to be used also to separate b-hadrons from primary c-hadrons. The production and decay of secondary c-hadrons out of B decays is likewise controlled by the weak interaction, so that a cascade of secondary and tertiary vertices can be reconstructed and the separation between the processes $e^+e^- \rightarrow b\bar{b}$ and $e^+e^- \rightarrow c\bar{c}$ improved. An example of a B decay to D mesons is given in Fig. 2.11(a). In the semileptonic decay such as in Fig. 2.11(b), the decay lepton is created with high p and p_\perp and hence appears isolated in phase space. At LEP energies, this decay mode appears with a branching ratio of $10.59 \pm 0.22\%$ [6]. Reconstructing the lepton provides a clear signature for identifying not only b- and c-hadrons but also the charge of the primary quark.

2.8.1 Oscillation in the $B^0 - \bar{B}^0$ System

As seen in the previous section, the b quark charge can be identified by exploiting a correlation to the track charges in inclusively reconstructed b-hadron decays. In the case of neutral B-mesons, however, oscillations between particle and antiparticle dilute the charge correlation already before the decay. This mixing process exists for both neutral mesons, B_d^0 and B_s^0 . The leading order diagrams for the $B^0 - \bar{B}^0$ oscillation are displayed in Fig. 2.12.

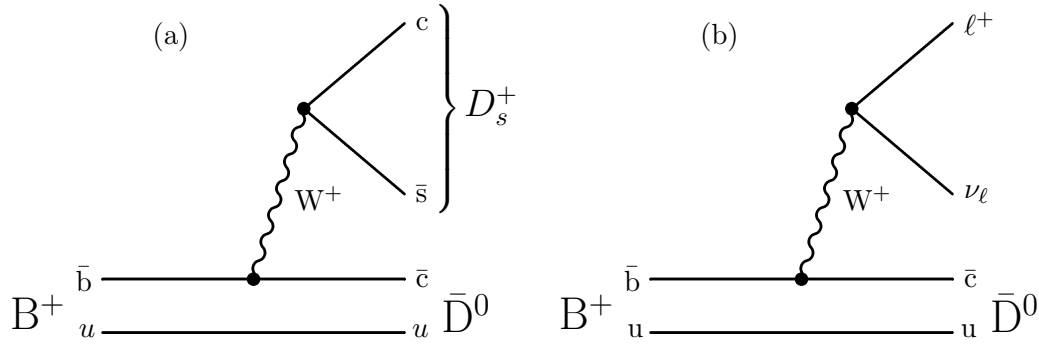


Figure 2.11: Two examples of the decay of a B^+ meson in the spectator model: a decay producing two D mesons and the semileptonic decay.

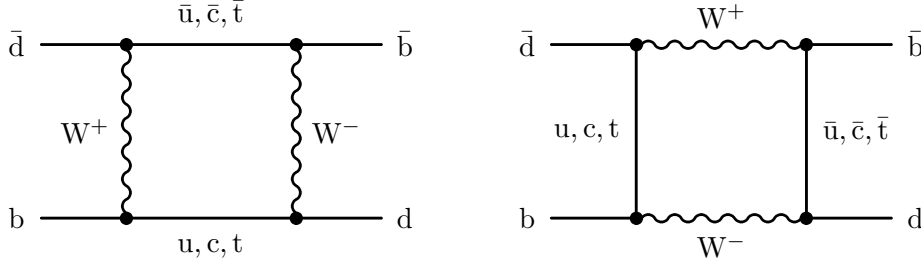


Figure 2.12: Feynman diagrams showing the $B^0 - \bar{B}^0$ oscillation.

Starting with a B_q^0 state at time $t = 0$, the probability to observe a \bar{B}_q^0 decaying at the proper time t can be expressed by

$$\mathcal{P}_{B_q^0}^{\text{mix}}(t) = \frac{1}{2\tau_B} \cdot \exp\left(-\frac{t}{\tau_B}\right) \cdot (1 - \cos(\Delta m_q \cdot t)) \quad (2.45)$$

while a B_q^0 is still observed with the probability

$$\begin{aligned} \mathcal{P}_{B_q^0}^{\text{nomix}}(t) &= \frac{1}{2\tau_B} \exp\left(-\frac{t}{\tau_B}\right) \cdot (1 + \cos(\Delta m_q \cdot t)) \quad , \quad (2.46) \\ &= \frac{1}{\tau_B} \exp\left(-\frac{t}{\tau_B}\right) \cdot \left(1 - \sin^2\left(\frac{\Delta m_q t}{2}\right)\right) \quad . \end{aligned}$$

Here τ_B denotes the B_q^0 lifetime and Δm_q the mass difference, $m_{B_q^0} - m_{\bar{B}_q^0}$, between the oscillating mass eigenstates. Effects from CP violation as well as a possible difference between the B_q^0 lifetimes of the heavy and light mass eigenstates are neglected. The time-integrated mixing probability, χ_q , then becomes

$$\chi_q = \int_0^\infty \mathcal{P}_{B_q^0}^{\text{mix}}(t) dt = \frac{x_q^2}{2(1+x_q^2)} \quad , \quad x_q = \Delta m_q \tau_B \quad . \quad (2.47)$$

The mass difference in the B_d^0 system is small, allowing both: time-dependent measurement aimed at a direct determination of Δm_d (Eq. 2.45) and time-integrated

measurement of χ_d (Eq. 2.47). The current world average for the total mixing probability is $\chi_d = 0.174 \pm 0.009$ [22]. Using the measured B_d^0 lifetime of

$$\tau_{B_d^0} = (1.56 \pm 0.04) \text{ ps} \quad , \quad (2.48)$$

the Particle Data Group [22] quotes a result for the mass difference of

$$\Delta m_d = (0.472 \pm 0.017) \text{ ps}^{-1} \quad . \quad (2.49)$$

Due to the apparently larger mass difference, only a time-dependent measurement is possible in the B_s^0 system, which leads to a lower limit on the mass difference of $\Delta m_s > 10.6 \text{ ps}^{-1}$ [22]. The total mixing probability is compatible with 50%, implying that no information on the primary quark charge can be deduced from the B_s^0 decay products.

Chapter 3

The DELPHI Experiment

This measurement is based on data taken between 1992 and 2000 with the DELPHI detector, one of the four experiments at the Large Electron Positron collider, LEP. The LEP collider at CERN provided e^+e^- annihilation reactions at centre-of-mass energies around 91.2 GeV and, after several upgrades, up to 209 GeV. CERN, the European Organisation for Nuclear Research¹, is a research facility for about 6500 scientists from 500 universities and from more than 80 countries.

3.1 The LEP Collider

LEP was conceived in 1976, shortly after the discovery of the J/ψ and the weak Neutral Currents, for the study of weak interactions [25]. In 1989 it started operating as a 26.67 km long ring accelerator in a tunnel 50-150 m underground, with the large general purpose detectors ALEPH, DELPHI, L3 and OPAL set up at four different collision points [26].

As illustrated in Fig. 3.1, the LEP ring was the last stage in a system of accelerators that made efficient use of already existing synchrotrons at CERN. Beams of electrons and positrons were created by an electron gun and a subsequent positron converter. Two linacs (LIL) accelerated them to 600 MeV before they were accumulated (EPA) in bunches. The bunches were further accelerated by the Proton Synchrotron (PS), used as a 3.5 GeV electron synchrotron, and the Super Proton Synchrotron (SPS) which served as a 20 / 22 GeV injector to LEP. There the bunches were collected and accelerated to the final beam energy, at which they were brought into collision. Radio frequency cavities provided the electric field that was needed for acceleration and for compensating the energy loss by synchrotron radiation. Due to their equal mass and opposite charge, electrons and positrons were conducted in opposite directions using the same beam pipe and the same bending magnetic fields and accelerating fields. With beam-beam bremsstrahlung and interaction with thermal photons limiting the bunch lifetime, collisions typically lasted for a few hours until the beams were dumped and the machine was re-filled.

A collider is mainly characterised by two parameters: beam energy and luminosity. As LEP accelerates electrons and positrons in opposite directions, twice the beam

¹The acronym CERN is from its original title, Conseil Européen pour la Recherche Nucléaire.

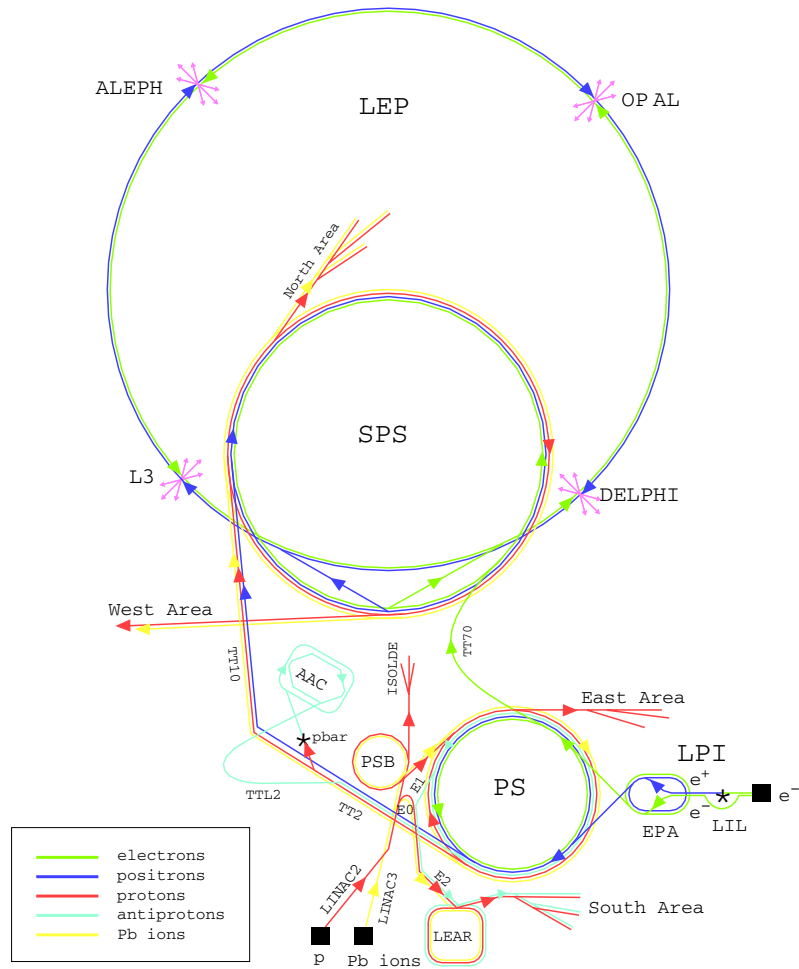


Figure 3.1: Schematic view of the CERN accelerator complex

energy is available as centre-of-mass energy for annihilation reactions,

$$\sqrt{s} = E_{\text{CM}} = 2 E_{\text{beam}} \quad . \quad (3.1)$$

The luminosity characterises the productivity of a collider and is given by

$$\mathcal{L} = f_{\text{circ.}} k \frac{N_{\text{bunch}}^+ N_{\text{bunch}}^-}{4\pi\sigma_x\sigma_y} \quad . \quad (3.2)$$

Hereby $f_{\text{circ.}}$ denotes the orbiting frequency of the N_{bunch}^\pm particles per bunch and k the number of bunches per beam. $4\pi\sigma_x\sigma_y$ is the collision cross-section. For any given process the product of cross-section and luminosity yields the reaction rate.

During the LEP 1 period (1989-1995) copper accelerating cavities were used to operate LEP at centre-of-mass energies around 91.2 GeV for Z boson physics [27]. Since the energy loss by synchrotron radiation rises with $(E_{\text{Beam}})^4$, increasing the centre-of-mass energy required superconducting cavities to be installed. This allowed LEP to operate at a maximum centre-of-mass energy of 209 GeV at the end of the LEP 2 period (1995-2000). At the start of each year in 1996-2000, short runs were performed at 91.2 GeV. The high reaction rate at the Z resonance was used to calibrate and align the detectors.

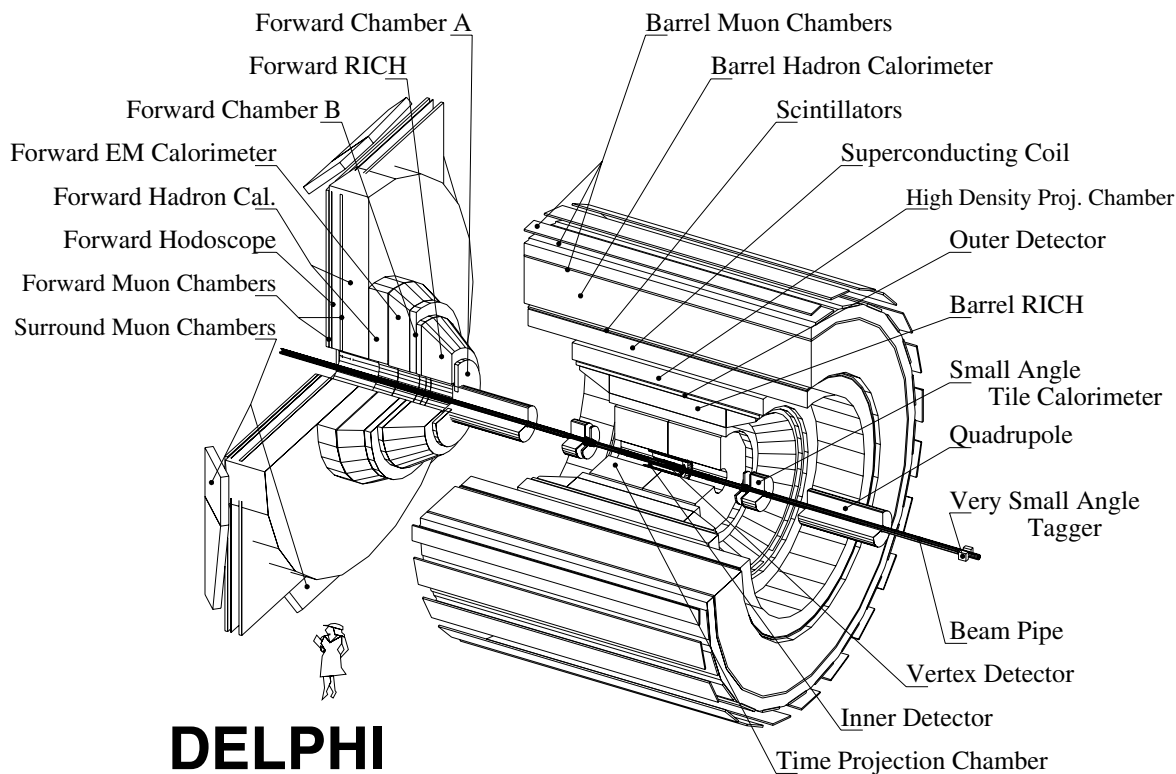


Figure 3.2: The Layout of the DELPHI detector

3.2 The DELPHI Detector

DELPHI stands for **D**etector with **L**epton, **P**hoton and **H**adron Identification. By combining different detector components and techniques, DELPHI was able to provide high quality three dimensional track reconstruction and particle identification over almost the entire solid angle [28, 29]. Another integral part of the design concept was a microvertex detector, which determined the position of the primary and possible secondary interaction points precisely. It is the key detector for measurements with heavy quarks as in this analysis.

The detector was structured into a barrel-like central part with concentric layers of sub-detector systems surrounding the beam pipe, and two end-caps that almost completely covered the open sides of the barrel region, as displayed in Fig. 3.2. The end-caps could be moved, giving maintenance access to all detector components.

The DELPHI structure favours a cylindric coordinate system (R, ϕ, z) for the description of its geometry, with the z axis defined along the direction of the incoming electrons. The polar angle θ to the z axis is preferably used to characterise forward and backward directions as well as different regions of acceptance.

The DELPHI detector sub-systems can be classified according to their different tasks.

- The microvertex detector measured tracks with high precision at close distance to the beam pipe, providing information on decays and lifetimes of short-lived particles.

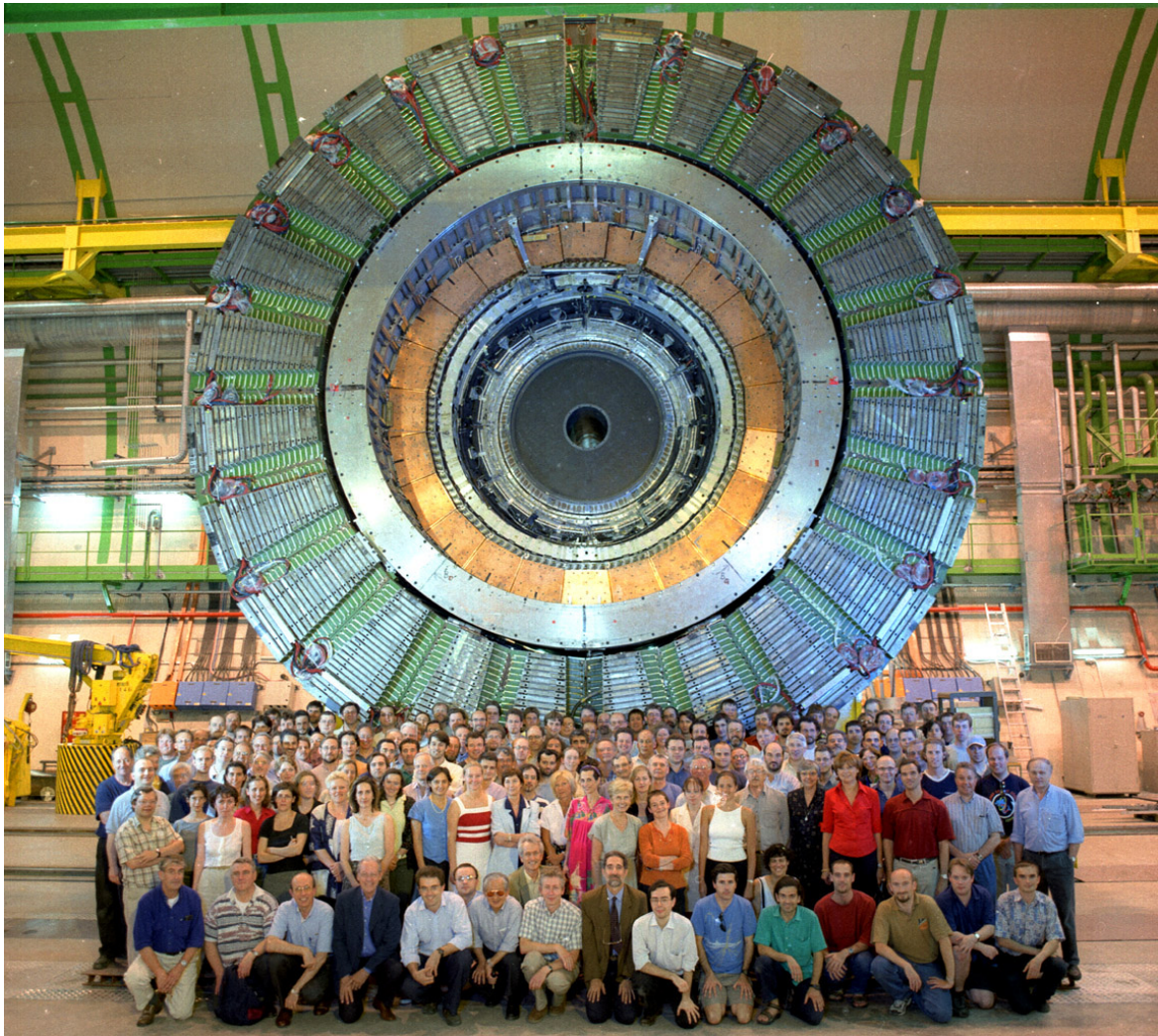


Figure 3.3: The DELPHI barrel with all cabling infrastructure removed, giving a direct view on the concentric layers of detector systems from TPC to HCAL. Picture taken on May 30th, 2001, from [30].

- Tracking detectors reconstructed charged particles inside a homogeneous magnetic field.
- Ring Imaging Cherenkov detectors made it possible to identify charged hadrons.
- Electromagnetic and hadronic calorimeters measured the particle energies.
- Track chambers outside the calorimeters provided muon detection.
- Dedicated calorimeters at very small polar angles measured the beam luminosity via bhabha scattering.

The different systems are explained in detail in the following. Only the combined data from all detector components facilitate a full event reconstruction with information on momentum, energy, charge, mass and secondary interactions of the observed

particles. The picture in Fig. 3.3 shows the large barrel detector components tightly fitting into each other.

3.2.1 The Microvertex Detector

Already in the design of DELPHI a silicon microstrip Vertex Detector (VD) was foreseen to be mounted in the space between the beam pipe and the first tracking chamber. After initial tests during the LEP pilot run in 1989, two layers of single-sided detectors were installed in 1990, which provided space points in $R\phi$ with very high precision. The 6×3 cm microstrip plaquettes had a read-out pitch of $50 \mu\text{m}$, yielding an effective resolution after alignment of $8 \mu\text{m}$ [31]. The plaquettes were arranged in modules that overlapped in ϕ by 12 – 13%, leading to full azimuthal coverage. This also provided redundancy so that a stand-alone geometrical alignment could be performed, which was the seed for the final alignment of the entire DELPHI experiment. High spatial resolution and good alignment of the vertex detector enabled a precise track extrapolation into the beam pipe, so that the primary vertex was well defined for each hadronic event, and decay vertices of short-lived b- and c-hadrons could be identified with a typical decay length of a few $100 \mu\text{m}$. Therefore powerful vertex detectors are crucial to heavy flavour physics.

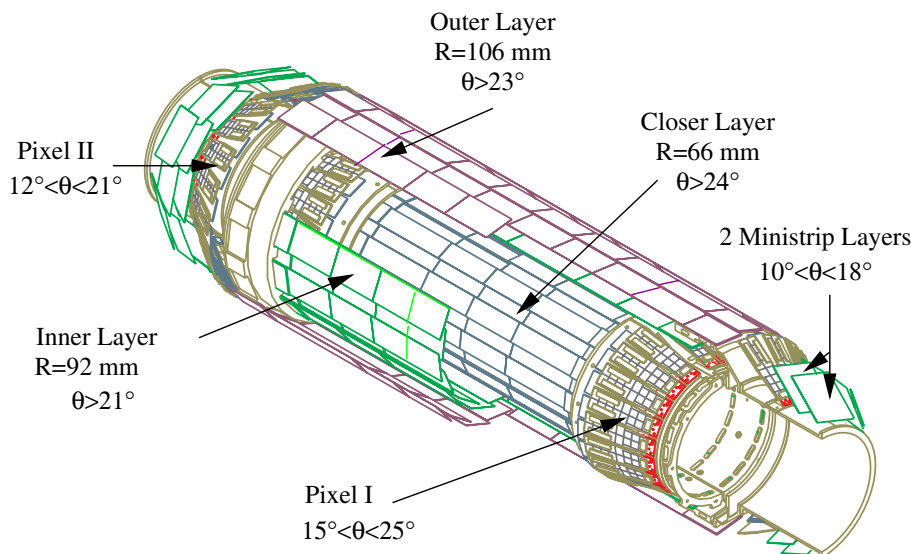


Figure 3.4: The DELPHI silicon tracker as installed in 1996-2000

During the 12 years of LEP running, the vertex detector has been upgraded several times in order to cope with the requirements of the physics programme in different LEP phases, like heavy flavour precision measurements in 1992-95 and a wide set of new LEP 2 processes demanding a larger angular coverage. When in 1991 experience with LEP operation had allowed a new beam pipe with reduced diameter, another layer of silicon detectors was installed even closer to the interaction point. This has led to a geometrical set-up with three layers termed “Closer”, “Inner” and “Outer” at average radii of 63 mm, 92 mm and 109 mm, which was left basically unchanged until the end of LEP [31]. For the years 1994 to 1995 the Closer layer was extended down to a polar angle θ of 25° , and double-sided silicon plaquettes in the Outer

	1991-93	1994-95	1997-2000
Closer	$-0.855 < \cos \theta < 0.855$	$-0.905 < \cos \theta < 0.905$	$-0.91 < \cos \theta < 0.91$
Inner	$-0.81 < \cos \theta < 0.805$	$-0.79 < \cos \theta < 0.80$	$-0.934 < \cos \theta < 0.934$
Outer	$-0.74 < \cos \theta < 0.74$	$-0.71 < \cos \theta < 0.72$	$-0.915 < \cos \theta < 0.915$

Table 3.1: The polar angle acceptance for the different VD set-ups [33].

and Closer shells provided also Rz measurements [32]. The readout pitch in the Rz plane changed for plaquettes with different angles to give the best resolution possible perpendicular to the track, varying between $10 \mu\text{m}$ and $25 \mu\text{m}$ for tracks of different inclination.

In 1996 the DELPHI vertex detector was fully replaced by the Silicon Tracker (SiT) as displayed in Fig. 3.4. It consisted of the barrel vertex detector doubled in length and the new Very Forward Tracker [31]. The already double-sided Closer shell was kept and the Outer shell re-used in the forward parts of the Inner layer, so that at least one $R\phi$ and Rz measurement could be obtained in an angular region of $21^\circ - 159^\circ$. In the Outer shell, where multiple scattering is less crucial, double sided read-out was realised by a simpler back-to-back solution. The single-sided middle part of the inner shell was the only part where the modules did not provide Rz information.

The VFT was a combination of ministrip and pixel detectors and covered the angular region of $11^\circ - 26^\circ$ and $154^\circ - 169^\circ$. Vertex reconstruction by means of precise extrapolation was impaired in this region by multiple scattering and a lower momentum resolution. Therefore the main aim of the VFT was the pattern recognition in the far forward region, for which a resolution of about $100 \mu\text{m}$ had proved sufficient. With a total sensitive area of 1.78 m^2 the DELPHI Silicon Tracker represented the largest silicon vertex detector at its time [34].

3.2.2 The Tracking Detectors

Trajectories of charged particles were reconstructed in DELPHI by a system of independent tracking detectors. They were embedded in a homogeneous magnetic field of 1.23 Tesla parallel to the beam axis, which was produced by a superconducting solenoid. This bent the trajectory of each charged particle into a helix whose radius is proportional to the momentum of the particle, revealing also its charge sign.

The Inner Detector (ID) enclosed the Vertex Detector and consisted of two components, the jet chamber and the trigger layers. The jet chamber was a high-resolution drift chamber divided into 24 azimuthal sectors, each of which measured $R\phi$ track coordinates from 24 axial wires at ascending radii. The trigger layers consisted of 5 layers of multiwire proportional chambers (MWPCs, 1989-1994) or straw tubes (1995-2000) and provided a rapid read-out.

DELPHI's principal tracking device was a Time Projection Chamber (TPC). TPCs are capable of detecting ionisation electrons in a large gas volume with a high spatial resolution by a special field configuration and a close monitoring of electron drift

times in the gas. By using also the pulse height information to measure the specific energy loss, dE/dx , it helps charged particle identification.

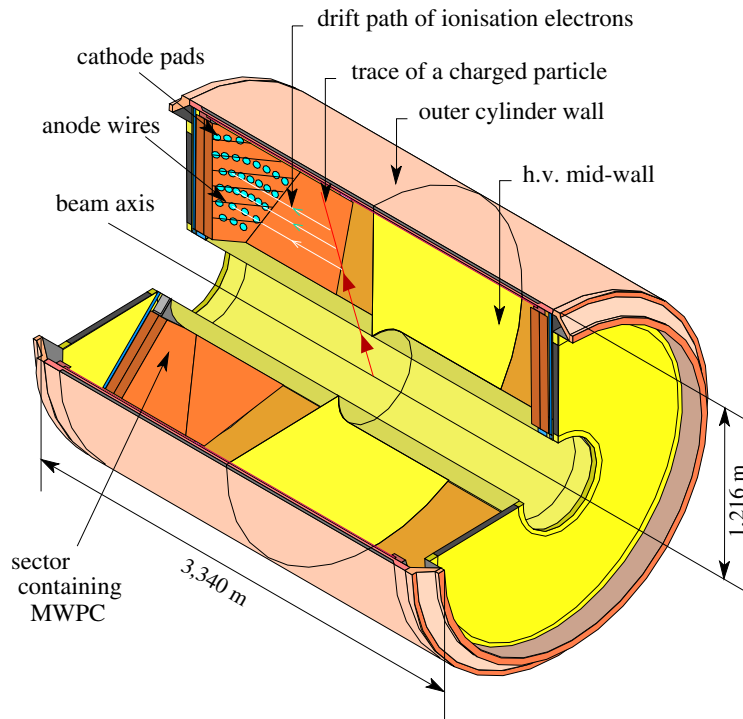


Figure 3.5: Schematic layout of the DELPHI TPC.

The DELPHI TPC was a cylindrical vessel of two times 130cm, divided in two by a cathode plane at $z = 0$. The layout of the TPC is illustrated in Fig. 3.5. The field cage between cathode and read-out planes produced a uniform drift field of 187 V/cm. Primary electrons created by the passage of charged particles drifted to either end of the cylinder, where they were amplified and read out by 6 azimuthal sectors. Each sector acted as a MWPC with 16 azimuthal rows of cathode pads. The pads were located 4 mm behind 192 sense wires, which provided the dE/dx measurement. The TPC measured points per particle trajectory between the radii 40 cm and 110 cm and in a polar angle range of 39° to 141° for a full trajectory, and 20° to 160° for at least three pad rows. The size of the TPC was constrained by the barrel Ring Imaging Cherenkov (RICH) detectors surrounding it.

Outside the RICH at a radius of 2m was a layer of drift tubes, the Outer Detector (OD). It ensured precise knowledge of the track position in the RICH and added to the momentum resolution by providing additional track curvature measurements at large distance from the primary vertex. A similar arrangement was realised in the end-caps, where the wire chamber detectors FCA and FCB were located on the front and back sides of the forward RICH. Several tracking detectors from the barrel and end-cap regions overlapped in polar angle, thus ensuring continuous coverage and some redundancy. The polar angle coverage of the innermost tracking detectors SiT, ID and TPC is illustrated in Fig. 3.6 for the upgraded DELPHI detector in 1996-2000. It shows the number of $R\phi$ and z coordinates as a function of polar angle.

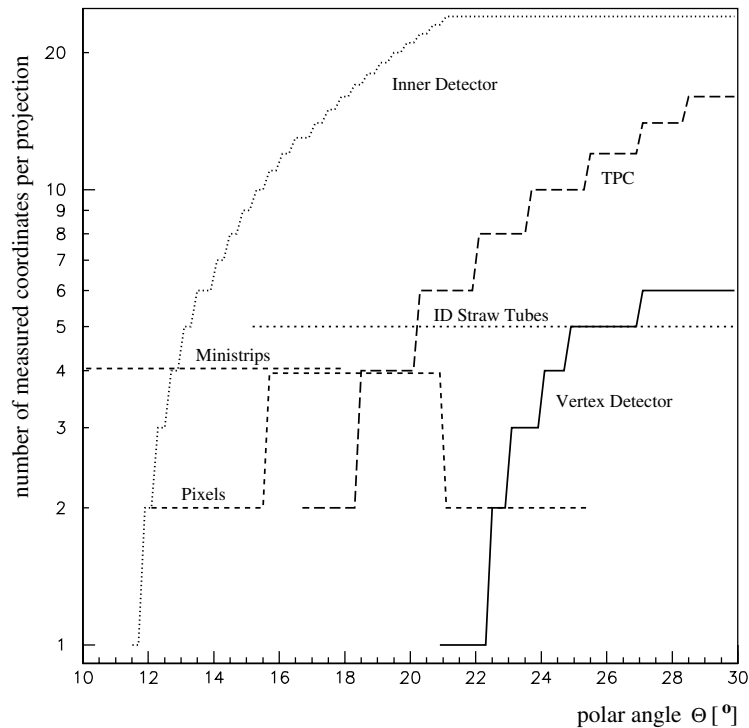


Figure 3.6: The polar angle acceptance of the innermost tracking detectors in the forward region [31].

3.2.3 Particle Identification

Charged hadrons like pions, kaons and protons were identified in DELPHI by Ring Imaging Cherenkov detectors in the barrel and the end-caps. While traversing a medium with a relative velocity $\beta = p/E$ faster than the local speed of light, charged particles emit photons in the ultraviolet spectrum. The presence of such Cherenkov photons and their angle to the particle trajectory, θ_c , determine its relative velocity by

$$\cos \theta_c = \frac{1}{\beta n} = \frac{1}{n} \sqrt{q + \frac{m^2}{p^2}} . \quad (3.3)$$

With the momentum (p) measured by the tracking detectors, this allows – in many cases - to identify the particle by its mass, m . Eq. 3.3 implies constraints on the momentum range for which particles can be identified, and hence the choice of the refractive index, n , i.e. of the medium itself. With $\cos \theta_c < 1$ the momentum is constrained to

$$p > \frac{m}{\sqrt{n^2 - 1}} , \quad (3.4)$$

below which no Cherenkov photons are emitted, still providing a veto against the particle hypothesis (m) under consideration. There is also a saturation angle $\cos \theta_c^{\max}$ that is reached for $\beta \rightarrow 1$, independent of the particle mass,

$$\cos \theta_c^{\max} \approx \frac{1}{n} . \quad (3.5)$$

It leads to an upper limit on the momentum, above which the sensitivity of the Cherenkov angle to the particle mass is not sufficient any more to distinguish the proton, kaon and pion hypotheses.

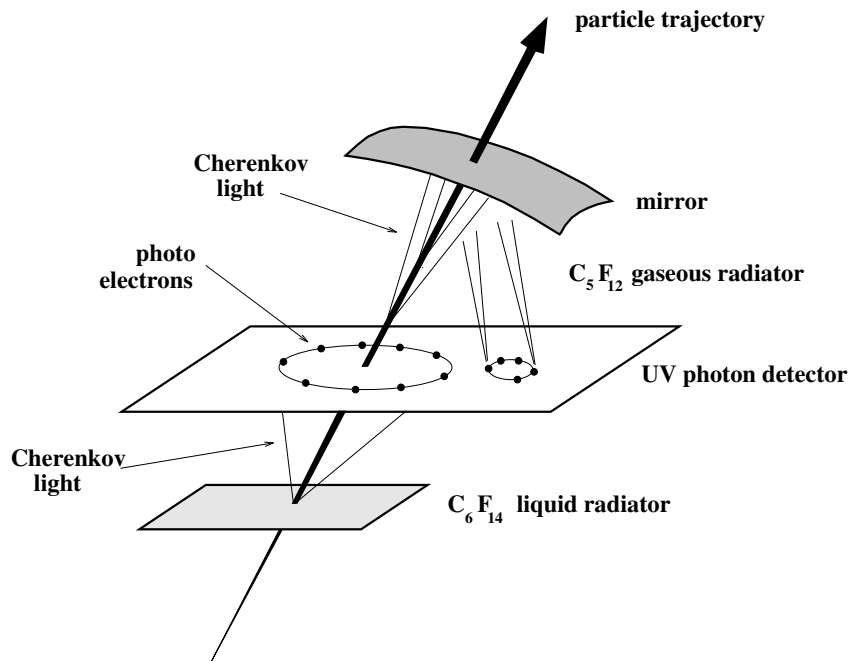


Figure 3.7: The operating principle of the DELPHI barrel RICH. The photons emitted in the liquid radiator are directly detected while the photons from the gas radiator are reflected back to the photon detector by means of focusing mirrors.

The DELPHI RICH detectors [35, 36] were therefore equipped with two different perfluorocarbon radiators: a liquid radiator consisting of C_6F_{14} with a refractive index of 1.283 to identify soft particles ($0.7 - 8 \text{ GeV}/c$) and a gaseous radiator of C_5F_{12} (C_4F_{10} in the end-caps) with $n = 1.00172$ to identify particles with momenta of 2.5 to $25 \text{ GeV}/c$. Projections of the Cherenkov light cones were detected using the time projection technique in quartz drift tubes which contained photo-ionising vapour. As illustrated in Fig. 3.7, the gas radiator is situated behind the drift tubes, so the light is reflected back to them with parabolic (spherical in the end-caps) mirrors at the outer wall of the RICH.

During the construction and startup period of the DELPHI detector, emphasis was laid on the operational availability of the barrel RICH, so that the forward RICH detectors started to contribute sufficiently to the data-taking much later than the barrel RICH. Even in the barrel RICH, the contributions from different types of radiators strongly varied during the data-taking. The RICH availability as a function of time has been implemented in simulation by removing the related detector response. In detail, the liquid radiator was fully removed from simulation for the years 1992 and 1993, when it still was hardly available. The forward RICH is not included in this analysis at all.

3.2.4 Calorimeters

The DELPHI experiment used several different calorimeter systems, such as the main electromagnetic and hadronic calorimeters for measuring particle energies, dedicated calorimeters for luminosity measurements and additional scintillators for fast trigger information and hermeticity. Detailed information regarding geometrical acceptance, depth and energy resolution is listed in Table 3.2.

Calorimeters reconstruct the energy of an incident particle by converting it into a shower of secondary particles. For electrons and photons this happens via elastic Coulomb scattering from nuclei in the converter material, while hadron calorimeters rely specifically on the hadron showers produced by inelastic hadronic interactions. Properties such as the signal height or the dimensions of the shower then give information about the particle energy, while the type of calorimeter under consideration helps in particle identification.

DELPHI's barrel **electromagnetic calorimeter**, the High-Density Projection Chamber (HPC), used a lead converter that was instrumented according to the TPC principle. This ensured a highly granular three-dimensional shower reconstruction. In each of the 6×24 HPC modules, 8 layers of lead wires in $R\phi$ were segmented into 41 partitions in z and hence induced the electromagnetic showers and also provided the drift field. Just like with the TPC, pad rows at the end of each module measured the radial and azimuthal coordinates while the z coordinate was calculated from the drift time. The forward electromagnetic calorimeter (EMF) used an arrangement of 4532 lead glass blocks in each end-cap. The Cherenkov signal was read out by phototriodes at the back of each block.

The **hadron calorimeter** (HAC) was formed by the magnetic return yoke, which was instrumented with plastic streamer tubes to detect showers produced by interactions between hadrons and the iron nuclei. It was made of 2×12 sectors in the endcaps and 24 modules in the barrel, each consisting of 20 layers of limited streamer tubes interleaved by 50 mm thick iron. Until 1995/6, the tubes were grouped into radial "towers" which were read out together by the same electronic channel.

A precise **knowledge of luminosity** is required for measuring absolute cross-sections. The integrated luminosity, $\int \mathcal{L} dt$, was obtained from the measured rate of small-angle Bhabha scattering events, a well understood QED process. Therefore additional electromagnetic calorimeters were installed in the very forward region, which served as luminometers. They were the Small Angle Tagger (SAT, until 1993) and later the Small angle Tile Calorimeter (STIC, 1994-2000) for a precise off-line luminosity determination, and the Very Small Angle Tagger (VSAT). The VSAT was installed beyond the LEP superconducting focusing quadrupoles at each side of DELPHI and provided information on the relative luminosity and beam background, which was transmitted online to the LEP control room. SAT and STIC used lead shells and plates interleaved with scintillating layers while the VSAT consisted of tungsten converters and silicon detectors.

Scintillators were used to obtain a very rapid signal on the passage of charged particles. They provided information to trigger the read-out of the rest of the detector as well as to reject cosmic muons which were not in synchronisation with the beam cross-over signal. They consisted of the Time Of Flight (TOF) and Forward Hodoscope (HOF) detectors and a scintillating layer at the position of the expected

calorimeter	geometric acceptance			depth	#s	readout granularity [°]		shower resol'n $\frac{\sigma_E}{E}$ [%]
	R [cm]	z [cm]	θ [°]			$\Delta\theta$	$\Delta\phi$	
HPC	208-260	≤ 254	≥ 43	$18X_0$	9	.1	1	6.4
EMF	46-240	284-340	10-36.5	$20X_0$	1	1	1	3.8
HAC	320-479	≤ 489	≥ 11	$6\lambda_I$	4	3	3.75	17
SAT	10-36	233-285	2.5-7.7	$28X_0$	8	.7	7.5	4.4
STIC	6.5-42	218-249	1.7-10.6	$27X_0$	49	.9	22.5	2.7
VSAT	$\sim 6-9$	770	0.3-0.5	$24X_0$	12			5.0

Table 3.2: The main characteristics of the DELPHI calorimeters: The electromagnetic calorimeters HPC and EMF, the hadron calorimeter and the luminosity monitors SAT, STIC and VSAT. #s denotes the number of samples taken alongside the shower. X_0 is the radiation length and λ_I the nuclear interaction length. The shower resolution is given for an energy of 45.6 GeV.

shower maximum in the HPC. Additional scintillators in the HPC gaps and the space between barrel and end-caps contributed to the hermeticity of the detector by identifying the presence of unreconstructed energy.

3.2.5 Muon Detectors

Muons with momenta above $\approx 2 \text{ GeV}/c$ were the only charged particles that were able to penetrate $\sim 110 \text{ cm}$ of HAC iron, hence they were identified by detecting them outside the iron. The DELPHI muon detectors consisted of three layers of drift chambers in the barrel (MUB) and two in the end-caps (MUF). Additional surround muon chambers (MUS) were added in 1994 to cover the gap at $\theta = 50^\circ$ between the barrel and the forward chambers. Muons were fully reconstructed by extrapolating measured tracks and comparing them to hits in the muon chambers.

3.3 Data Acquisition

The DELPHI trigger system, data acquisition and detector control systems are described in detail in [29] and references therein. The trigger system was able to cope with high luminosities and possibly large background rates by using four successive levels (T1 to T4) of increasing selectivity. The first two levels T1 and T2 acted synchronously to the Beam Cross Over signal (BCO), which occurred every 22 or 11 μs , depending whether LEP ran with 4 or 8 bunches per beam. The T1 level provided a rapid pre-trigger 3.5 μs after the BCO by ORing independent signals only from detectors with fast readout times such as ID, OD, FCA, FCB and the scintillator-based detectors. Once the drift time information from TPC, HPC and the muon chambers had been complete, their signals as well as the correlations between the detectors were included to form the second level trigger, 39 μs after the BCO. A positive T2 started the readout of the front-end electronics, with a readout time of about 3 ms, during which the detector was insensitive to new collisions. At a nominal luminosity

of $1.5^{31} \text{ cm}^{-2}\text{s}^{-1}$, the T2 rate was $\sim 5 \text{ Hz}$ while the resulting dead time due to T1 and T2 amounted to 3%. The successive levels of asynchronous software triggers, T3 and T4, were added in 1992 and 1994 respectively in order to further reduce the rate down to $\sim 1 \text{ Hz}$ after the machine luminosity had been increased. T3 used the same logic as T2 but with the full digitised and calibrated detector data, thus allowing tighter cuts. T4 was running a specialised version of the DELPHI event reconstruction software, DELANA [37], to further reduce the number of background events.

The data acquisition was organised in different stages as well, starting with independent partitions for each detector or half-detector. In a number of digitisation modules per partition, the data were stored in a 4-event front end buffer so that the dead time was kept low. From there the modules were read out, in case of a positive T2 decision, by software running in Fastbus Intersegment Processors and their data merged by the Local Event Supervisor (LES). The LES then provided the input to the Global Event Supervisor as well as to the local on-line monitoring software for each detector. If the event had passed T3, the Global Event Supervisor combined the information from all partitions and transferred it to a cluster of workstations where the T4 stage was run and data storage managed. The data acquisition, the quality of the data and the overall detector status were continuously monitored. The detector status was logged to the DELPHI geometry database, CARGO [38]. Such status information comprised low and high voltages, gas pressure distributions and temperatures.

3.4 Event Reconstruction

The raw data from the data acquisition were processed to identify and characterise the products of the e^+e^- interaction from the electronic measurements. This task was performed by the DELPHI Data Analysis Program (DELANA) using the data model and access routines from the Track Analysis and Graphics package (TANAGRA) [39]. After calibrations were applied to the digitised raw data (leading to TD TANAGRA banks), track elements (TE banks) were obtained by performing a local pattern recognition in the individual subdetectors, yielding e.g. TPC track segments or HPC clusters. The TEs were extrapolated over the entire detector and combined to track candidates (TS banks). Hereby track segments from the TPC as well as combinations of ID-VD, ID-VD-OD and ID-OD were used as different seeds. This allowed for low-curvature tracks that might have remained undetected in the TPC cracks and fully exploited the high VD granularity to improve track resolution close to the primary vertex. On the other hand, equivalent sets of track candidates appeared with a high number of multiply used TEs. The task of reducing these sets in an optimal way to a single consistent track fit was performed by the ambiguity processor [40]. It classified and sequentially removed any multiply used TEs while the thereby modified track candidates were re-fitted. A recursive algorithm evaluated the current set of tracks and, by removing equivalent sets, selected the optimal one (TK). In a last step, calorimeter clusters as well as muon and RICH information were associated to the fitted tracks. Unassociated calorimeter clusters were attributed to neutral particles.

The event reconstruction described above was the result of efforts taken in the years 1995/1996, which have led to a huge improvement in the reconstruction of complicated events and dense jets. It has been used for the (re-) processing of all DEL-

PHI data taken from 1992 to 2000. The data quality profits from better alignment procedures, from new algorithms like the ambiguity processor and from a better understanding of multiple scattering and energy loss in the Kalman filter track fit. As an example, the signal of exclusively reconstructed D^* mesons decaying into $D^0\pi^+$ with $D^0 \rightarrow K\pi\pi$ was increased by a factor of 2.4 [41]. Another benefit was the feasibility of inclusive analysis tools such as BSAURUS (Chapter 7), which exploits the capabilities of the DELPHI detector to their extreme.

The results from the DELANA processing were written to Data Summary Tape (DST), a data format that takes about 60 kB for a typical Z event instead of the 150 kB of initial raw data. Hereby a stream of Z decays was selected by very loose tags in order not to reject events that might have been accepted after more sophisticated post-DELANA corrections were performed. As a matter of fact, the information written to DST is still so complete that further corrections, like more up-to-date calibrations and high level identification algorithms, can be applied even at the DST level without a time-consuming full reprocessing. In addition, the efficiency, cleanliness and precision of the simulated data can be adjusted at this stage. This procedure is called DSTANA and results in an “extended ShortDST” format with a hadronic event size of about 20 kB [42]. It is the basis on which the analysis tools for determining the forward-backward asymmetry are run. The interpretation of all different data formats in the reconstruction and analysis chains and the transformation between them is fully based on the ZEBRA memory management system [43]. ZEBRA provides a machine-independent storage format and provides dynamic data structuring in Fortran 77, which lacks the pointer or reference data type needed for this data model.

3.5 Simulation

Simulated events in a high energy physics experiment are of great importance for the full understanding of the measurement results, and in particular its scrutinising, its interpretation and comparison to other results and to theory. So they are used for improving the analysis by checking and/or correcting for non-trivial detector and possibly also for physics effects. The interpretation and the study of systematic uncertainties demands a high quality of the simulation and a good agreement with real data. Finally, the combination with other experiments and the comparison to theory often needs corrections for detector effects such as acceptance and efficiency. Therefore, the predictions of the simulation in every observable should match the real data within the given precision [29], with the possible exception of the effect being studied.

The DELPHI simulation programme, DELSIM [44], consists of three main components: generator, tracking and detector response.

1. Depending on the primary physics process, a variety of external generators can be used, including hadronisation for quark final states. The JETSET generator [15] is most commonly used to model $e^+e^- \rightarrow Z \rightarrow q\bar{q}$ and hadronisation (see Section 2.7.2).
2. The particle four-vectors from the previous stage are tracked through the simulated detector, accounting for weak decays, curvature in the magnetic

field and various kinds of interaction with the detector material. The latter comprise ionisation energy loss, multiple scattering, the photoelectric effect, bremsstrahlung, delta ray emission, pair production, positron annihilation, Compton scattering, and nuclear interactions.

3. In a third step, the response of each component of the detector is simulated, using (like already in the second step) the same detector geometry and calibration constants from the CARGO database as for real data.

By producing a set of artificial electronic signals in the last step, the output of DELSIM closely models the real raw data produced by the data acquisition and can thus be processed directly by DELANA. The simulated and subsequently reconstructed events are stored in the same format as real data, and are further processed by the same analysis tools. At every step in the processing the full truth information on the underlying physical facts can be extracted, thus leading to the above benefits from simulation.

Chapter 4

Principles of the Method to Extract the b Asymmetry

The differential cross-section for b quarks from the process $e^+e^- \rightarrow Z \rightarrow b\bar{b}$, Eq. 2.21, can be expressed as :

$$\frac{d\sigma}{d\cos\theta} \propto 1 + \frac{8}{3} A_{\text{FB}}^b \cos\theta + \cos^2\theta \quad . \quad (4.1)$$

Hence the forward-backward asymmetry generates a $\cos\theta$ dependence in the production of b quarks. The back-to-back configuration of the two b-jets in the event, ideally, gives the axis along which the b quark and anti-quark moved apart, and consequently the value for $|\cos\theta|$. The plane perpendicular to this axis defines the two event hemispheres. The charge of the primary quark or anti-quark in a hemisphere is necessary to determine the orientation of the quark polar angle $\cos\theta$. This charge information is obtained separately for both event hemispheres using a hemisphere charge tag obtained by means of a Neural Network. The following chapters will explain in full detail the tagging techniques and the method to extract the b asymmetry so that the experimental results together with their systematic uncertainties can be discussed in depth. This chapter gives a brief introduction to the analysis in order to provide an overview of the essential features of the method and the way how they are used to obtain a high precision measurement.

The hemisphere charge Neural Network reconstructs the charge of a b hemisphere in an inclusive way, i.e. in a way that does not necessitate the explicit identification of the b hadron type and its decay products. By combining several variables with different sensitivities to the b quark charge into a single network output, it provides an optimal way of tagging the quark charge and yields a much higher rate of correctly tagged b quarks than any approach with only a single variable. Some of the input variables are themselves constructed by means of sophisticated Neural Network techniques so that charge observables can be exploited which by itself only have a weak dependence on the b charge.

In order to profit from the much improved b charge tagging fully, a self-calibrated method to extract the forward-backward asymmetry has been developed. The b quark charge sign is measured in event hemispheres with a reconstructed secondary vertex. The different possible combinations of negative, positive and untagged event

hemispheres define classes of single and double charge tagged events, with the double tagged distinguished into like-sign and unlike-sign. The forward and backward rates of single and double unlike-sign events provide sensitivity to the asymmetry. As the $b\bar{b}$ final state is neutral, one of the two hemispheres in like-sign events is known to be mistagged. By comparing the like-sign and unlike-sign rates of double hemisphere charge tagged events, it is hence possible to extract the probability of correctly assigning the b quark charge directly from the data.

A b-tagging variable constructed from lifetime information as well as secondary vertex and track observables provides an additional strong means of rejecting charm and light quark events in which a secondary vertex occurred. Separate event samples of successively enhanced b-purity are used in the analysis to allow for a statistical correlation between the b purity and the probability of correctly assigning the quark charge.

The asymmetry measurement as well as the self-calibration method rely on the good knowledge of the true b content and residual non-b background in the individual rates of differently charge-tagged events. Therefore the b efficiency in each rate is measured directly on the real data. For the most important background contribution, c quark events, additional calibration techniques are used: the c quark efficiency of the enhanced impact parameter tag is measured using a double tag method while the c charge tagging probability is calibrated on data by means of exclusively reconstructed D meson decays in the opposite hemisphere.

The b quark forward-backward asymmetry is determined from the differential asymmetry of the two samples of single tagged and unlike-sign double tagged events. The differential asymmetry is measured independently in consecutive bins of the polar angle and in the different b purity samples. Here small corrections due to residual background contributions and due to charge tagging hemisphere correlations are taken into account.

The description of the measurement is organised as follows. First a short summary of the hadronic event selection is given. In Section 6 the b event tagging used to obtain the high purity b quark sample is described in conjunction with the calibration of its efficiency. Chapter 7 details the charge tagging technique based on Neural Networks. Chapter 8 describes the self-calibrating method to extract the forward-backward asymmetry and the measurement of A_{FB}^b from the DELPHI data of 1992 to 2000. Chapter 9 discusses the systematic errors and additional cross-checks on the stability of the measurement. Finally the conclusion and interpretation are given in Chapter 10. Technical information on the self-calibration method can be found in the appendices at the end of the thesis.

Chapter 5

Selection of Z Decays to Hadrons

The measurement of the b quark forward-backward asymmetry is performed on all the DELPHI data taken from 1992 to 2000 at centre-of-mass energies close to the Z pole. In addition to the LEP 1 data in an interval of ± 0.5 GeV around the Z pole, the data taken at 2 GeV above and below as well as the LEP 2 calibration runs taken at the Z pole are included. The different years and centre-of-mass energies divide the data into nine sets which are analysed separately and compared to individually generated simulated data. The analysis makes full use of the information provided by the tracking system, the calorimetry, and the detectors for hadron and lepton identification. Of special importance is the Vertex Detector providing sensitivity to the properties of b-hadrons and enabling extra charge information, like the vertex charge, to be used in the asymmetry measurement.

For events entering the analysis nominal working conditions during data taking are required at least for the central tracking detector, TPC, for the electromagnetic calorimeters and for the barrel muon detector system. Nominal working conditions for the VD are guaranteed by the b-tagging algorithm, which rejects events that are not filed in the beam spot database mainly because of insufficient detector status. The operating conditions and efficiency of the RICH detectors varied widely for the different data sets. These variations are included in the corresponding simulated data samples.

Event hemispheres

The well-balanced topology of Z decays, in which the primary quarks ideally have opposite momenta and in which the resulting jets are arranged back-to-back, is parameterised by the definition of event *hemispheres*. In this analysis each event is split into two hemispheres by the plane perpendicular to the thrust axis [45]. The thrust axis, \vec{T} , is defined as the axis of projection, for which the sum of the longitudinal momenta of all charged and neutral particles reaches its maximal value. This maximum sum of the longitudinal momenta normalised to the sum of the absolute momenta is defined as thrust:

$$T = \max_{\vec{T}} \frac{\sum_{i=1}^N |\vec{p}_i \vec{T}|}{\sum_{i=1}^N |\vec{p}_i|} \quad . \quad (5.1)$$

In the limit of vanishing transverse momenta, the thrust value is close to 1, thereby characterising high-quality back-to-back topologies. By contrast, a thrust value of 0.5 is obtained for the limit of isotrop events, rendering the thrust axis arbitrary. The axis is always oriented in such a way that the angle between the incoming electron direction and the thrust axis itself, the polar angle $\theta_{\vec{T}}$, becomes less than 90° . The hemisphere to which the thrust axis points is defined as the forward hemisphere and the opposite one as the backward hemisphere. This definition of hemisphere is the basis for the measurement of the forward-backward asymmetry, but is also used in the event selection as well as the selection of b quarks.

Selection cuts

Apart from hadronic Z boson decays other events were recorded by the DELPHI detector which have to be excluded from the analysis. Such background events can be e^+e^- reactions with non-hadronic final states, like leptonic Z boson decays or two-photon events, which form the signal for other measurements. However, also reactions totally unrelated to e^+e^- collisions may happen, such as interactions of beam electrons with the remaining gas, or with the beam pipe wall or particles from the cosmic radiation crossing the detector. Hadronic Z boson decays are separated easily from the other kinds of event by their high number of charged particles, which can be traced back to the central interaction region.

For each event cuts are applied first to the measured particles to ensure good quality of the reconstruction. The selections are summarised in Table 5.1. The cut on the minimal momentum suppresses a large fraction of tracks produced in secondary interactions with the detector material. The constraint on the maximal impact parameters rejects tracks that do not originate from the primary vertex or any subsequent decay. Tracks that were measured by the forward tracking chambers, FCA and FCB, have a less well defined momentum and consequently a worse resolution when extrapolated to the primary vertex. They are not considered in this cut. The analysis tools for selecting b quark events and for reconstructing the b charge require tracks to have a certain number of hits in the VD in order to be used in the tagging algorithms. Such extra conditions or track quality flags are mentioned in the respective sections. In addition, for neutral clusters measured in the calorimeters the reconstructed shower energy had to be above 0.3 GeV for the barrel electromagnetic calorimeter (HPC, see Section 3.2.4) and the small angle luminosity calorimeters (STIC/SAT), and above 0.4 GeV for the Forward ElectroMagnetic Calorimeter (FEMC).

charged particle momentum	\geq	0.4 GeV/c
neutral particle energy		see text
length of tracks measured only with TPC	\geq	30 cm
polar angle	\geq	20°
uncertainty of the momentum measured	\leq	100 %
impact parameter ($R\phi$)	\leq	4 cm
impact parameter (Rz)	\leq	10 cm

Table 5.1: Cuts to select particles. Impact parameters are defined relative to the primary vertex.

multiplicity of charged particles in the event	≥ 7
multiplicity of charged particles in hemisphere	≥ 1
total energy of charged particles	$\geq 0.15 \times \sqrt{s}$
sum of energy of charged particles in hemisphere	$\geq 0.03 \times \sqrt{s}$
forward electromagnetic energy $E_{\text{FEMC}} := \sqrt{E_{\text{F}}^2 + E_{\text{B}}^2}$	$\leq 85\% E_{\text{beam}}$

Table 5.2: Selections for Z decays to hadrons. \sqrt{s} is the centre-of-mass energy, $E_{\text{F/B}}$ the total shower energy per FEMC side.

In a second step, Z decays to hadrons are selected as detailed in Table 5.2. The minimum number of charged tracks, i.e. the minimum charged multiplicity, rejects leptonic Z decays and events from cosmic radiation. Two-photon events as well as beam-gas or beam-wall interactions carry an energy usually far below the e^+e^- centre-of-mass energy. Hence such events can be suppressed by making a cut on the minimal charged energy at 15% of \sqrt{s} . In addition, background events that do not originate from e^+e^- collisions are often unbalanced and consequently can be further suppressed by the condition imposed on the charged multiplicity and energy per hemisphere (Table 5.2). Moreover, a negligible number of events with an unphysically high momentum particle are discarded.

year	data	simulation	$\langle\sqrt{s}\rangle$
1992	636401	1827321	91.280 GeV
1993	454895	1901060	91.225 GeV
1994	1303131	3260752	91.202 GeV
1995	416560	1206974	91.288 GeV
1996-2000	332944	971299	91.260 GeV
1993 peak-2	86601	269027	89.431 GeV
1993 peak+2	126648	339528	93.015 GeV
1995 peak-2	79989	268899	89.468 GeV
1995 peak+2	123721	385648	92.965 GeV

Table 5.3: Number of selected (data) and generated (simulation) Z decays to hadrons for the different years of data taking and different centre-of-mass energies.

In total 3.56×10^6 Z decays to hadrons are selected using data at mean centre-of-mass energies of 89.449 GeV, 91.231 GeV and 92.990 GeV (see Table 5.3). The data taking periods with centre-of-mass energies below and above the Z peak (called “peak-2” and “peak+2” in the following) are analysed separately. Data from these periods were taken in 1993 and 1995 together with the Z peak data sets so that the energy information obtained from LEP and stored in the DST has to be used to split the energy points. The splitting has been cross-checked by means of the reconstructed B energy obtained from the EB-Net output described in Section 7.5.

The remaining backgrounds due to $\tau\tau$, Bhabha, and $\gamma\gamma$ events as well as contributions from beam-gas or beam-wall interactions are estimated to be well below 0.5%.

They can be safely neglected after the subsequent selection of Z decays to b quarks with a reconstructed secondary vertex. The data are compared to 10.43×10^6 fully simulated hadronic decays using JETSET 7.3 [15] with DELPHI tuning of fragmentation, b production and decay parameters [21]. For the peak ± 2 energy points dedicated simulation has been produced with an appropriately modified centre-of-mass energy.

Simulation reweighting

Several parameters in the simulation concerning heavy hadron production and decays have not been exactly set to the present-day measured values. In order to use an event generator as uniform as possible over the different years, updates in the measured values have not been implemented in the generator when available. Instead, the simulated data have been reweighted in order to represent the measured composition and lifetimes of c- and b-hadrons and also other observables correctly. In detail, the following parameters have been taken into account:

- The measured composition and lifetimes of D^0 , D^+ and D_s^+ mesons as well as c-baryons as listed in Table 2.2 on page 22.
- The measured composition and lifetimes of B^0 , B^+ , B_s and b-baryons (Table 2.2).
- The rate of gluon splitting into $c\bar{c}$ ($b\bar{b}$) pairs according to the measured values given in Eq. 2.44.
- The D topological decay fractions into n charged particles. The simulation was reweighted so as to represent the fractions in Table 5.4. The decay rate for $K_{\text{short}}^0 \rightarrow \pi^+\pi^-$ of 0.68 was taken into account when the truth information about the number of D decay tracks was extracted from the simulation.

# of charged decay tracks	branching fraction [%]		
	D^+	D^0	D_s^+
0	—	5.1 ± 1.1	—
1	38.4 ± 2.3	—	37.0 ± 10.0
2	—	63.4 ± 2.4	—
3	54.1 ± 2.3	—	42.0 ± 15.0
4,6	—	31.2 ± 2.3	—
5	7.7 ± 1.5	—	21.0 ± 11.0

Table 5.4: Topological D branching fractions measurements from [23] used in the reweighting of the simulation.

In the case that an event is effected by one or several of those parameters with a need for reweighting, the weight of the simulated event is modified by a multiplicative correction for each concerned parameter.

Moreover, $B^0 - \bar{B}^0$ mixing was not implemented in the simulated data from 1992 and 1993. This situation cannot be rectified by a reweighting method, so that larger differences between data and simulation are expected for those years, making the use of calibrated observables indispensable.

Chapter 6

Identification of b Quark Events

As motivated in Chapter 2, the study of b and c quarks can be used for testing the electroweak sector of the Standard Model. The search for its possible violations or extensions, which might be best visible in the third generation particles, and gaining a better knowledge of the properties of heavy hadrons provide additional motivation for studying b quarks at LEP. It was therefore very important to develop a b-tagging algorithm that is capable of identifying b quarks with high efficiency while maintaining a high purity, i.e. a low background of light (uds) and c quark events. The b-tagging technique in DELPHI was mainly created for the measurement of R_b [46] and subsequently improved for other analyses. While doing so emphasis was laid on a good understanding and close monitoring of the algorithm in order to cope with the high precision achieved by the LEP 1 data. The resulting reliable selection of b jets again proved essential at LEP 2, when a Standard Model Higgs boson decaying predominantly to $b\bar{b}$ pairs was being searched for. A comprehensive write-up of the technique, its performance and application can be found in the DELPHI b-tagging report [47].

The b-tagging algorithms in DELPHI make extensive use of variables that are sensitive to the distinct features of b hadrons, which were already discussed in Section 2.8. The main tagging variable for reconstructing secondary vertices and selecting b-jets is based on the track impact parameters (see Section 6.1 for details). Section 6.2 discusses the so-called combined algorithm, which uses additional variables in combination with the impact parameter information to further improve the b-tagging performance. The Sections 6.3 and 6.4 describe a calibration procedure that finally leads to the b-tagging variable used in the measurement of the b asymmetry.

6.1 Lifetime Tagging

The lifetime tagging method based on impact parameters was originally proposed by the ALEPH collaboration [48] and is also implemented in the DELPHI b-tagging technique [49, 50]. The *impact parameter* (IP) of a track is defined as the minimal distance between the estimated primary interaction point and the particle trajectory extrapolated to the primary vertex region. Only particles that do not originate directly from the primary vertex are capable of having an IP which is significantly different from zero; hence IPs are sensitive to the long decay length of heavy hadrons.

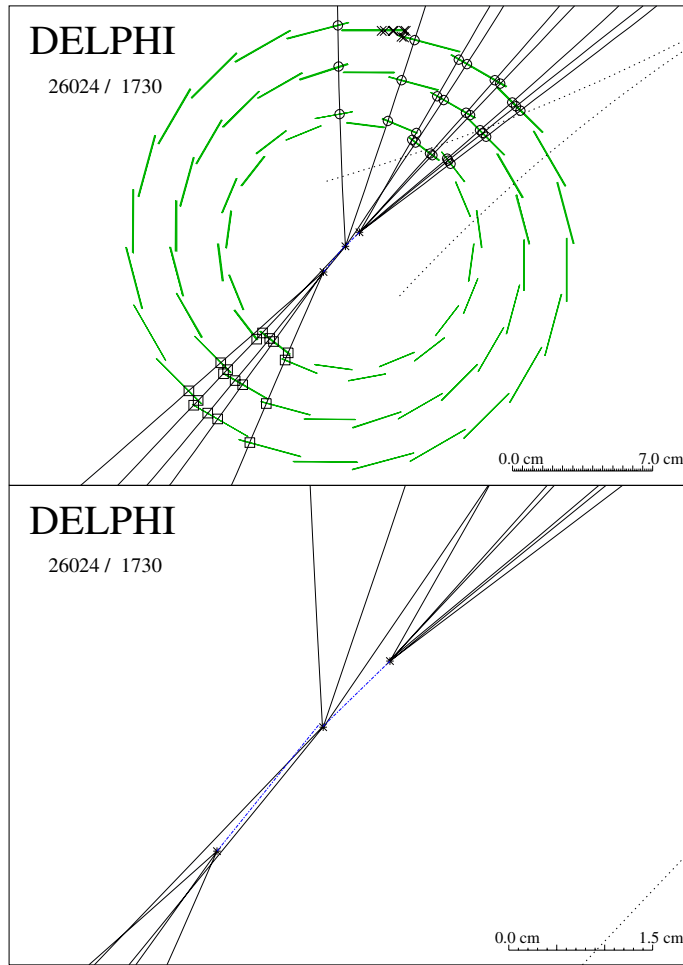


Figure 6.1: An $e^+e^- \rightarrow b\bar{b}$ event measured by the Vertex Detector and displayed in the $R\phi$ plane (upper plot). The zoom into the interaction region clearly shows the decay vertices of the two b-hadrons with a significant distance to the primary vertex.

They can be measured in DELPHI due to the high experimental resolution in the Vertex Detector and the resulting accuracy in the track extrapolation. Fig. 6.1 shows an $e^+e^- \rightarrow b\bar{b}$ event in the Vertex Detector with a long decay length for both b-hadrons and a clear separation between primary and secondary vertices. The relatively high number of tracks with a large transverse momentum with respect to the B direction is also characteristic of b-hadron decays.

Due to the different Vertex Detector resolution in the $R\phi$ and Rz components (see Section 3.2.1), due to the beam spot geometry and to some extent also due to historical reasons, the 3-dimensional information is separated into $R\phi$ and Rz components. Details of how the IPs are computed separately in the $R\phi$ and Rz planes are given in reference [47].

Lifetime sign

The *lifetime sign* of the IP plays an important role in selecting b-hadron decay tracks

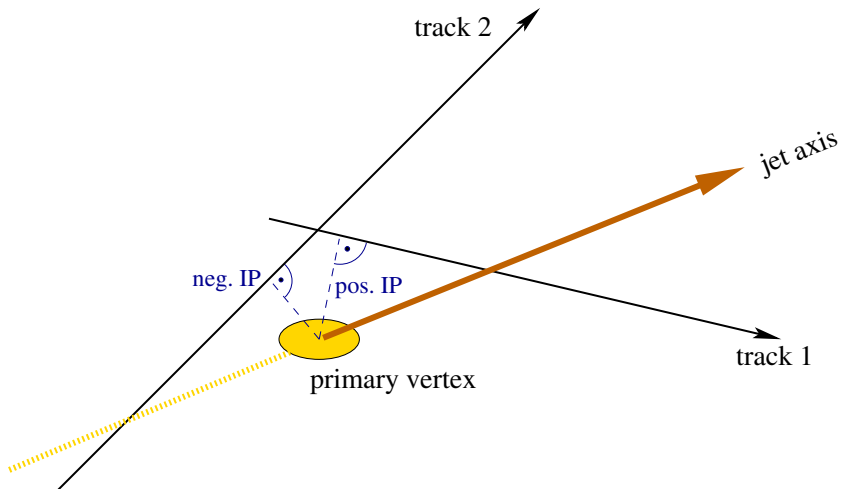


Figure 6.2: The definition of positive and negative impact parameters (IPs) for tracks which are extrapolated to the primary vertex region. Track 1 has a positive IP, while track 2 — seemingly originating from behind the primary vertex — is assigned a negative IP.

and in controlling the detector resolution at the same time. To define the sign, first the flight path of the long-lived hadron is computed. If its decay point, the secondary vertex, could be reconstructed (see Section 6.2), the direction from the primary to the secondary vertex yields the flight path; if not, the jet direction is taken. A track IP is defined as *positive* (*negative*) if the point of closest approach in space of the track to the estimated B flight path is upstream (downstream) of the primary vertex position. Fig. 6.2 illustrates the definition of the lifetime sign: In contrast to track 1, track 2 is extrapolated to a space behind the primary vertex and to a time before the primary annihilation. It is therefore most likely to come from the primary vertex, with the extrapolation accuracy distorted by detector resolution effects, including scatters in the detector material and wrong hit associations.

Beam spot and primary vertex

To evaluate the IP information further, its error must be determined. The error of the IP is composed of two components, the error of the track fit and the uncertainty of the primary vertex position. The primary vertex is reconstructed for each event using a set of selected tracks and the beam spot position. The beam spot is relatively stable in a fill, and is therefore computed from events with at least three tracks with VD hits over a time period of about 20 minutes. A fit to the three-dimensional position is performed as well as to the size in x and z . Due to the absence of synchrotron radiation orthogonal to the bending radius in LEP, the beam position in y can be maintained with very high precision, so that the size, $\sigma_y \lesssim 10 \mu\text{m}$, is smaller than its positioning error and therefore not fitted for. The average LEP beam spot size in x is $\sigma_x \simeq 150 \mu\text{m}$ while in z (along the beam direction) it is several millimetres long. The tracks which are then selected to determine the primary vertex per event have to pass certain quality criteria, including a rejection of tracks from long lived particle decays and interaction with detector material. In about 1% (LEP 1) of the events in which no such tracks are found the beam spot is taken as primary vertex.

This procedure yields average precisions for the primary vertex (PV) of simulated uds, c, b events of $\sigma_x = 36, 44, 60 \mu\text{m}$ and $\sigma_z = 43, 50, 70 \mu\text{m}$ [47]. The error of the IP is then given by

$$\sigma_{R\phi}^2 = \begin{cases} (\sigma_{R\phi}^{\text{trackfit}})^2 - (\sigma_{R\phi}^{\text{PV}})^2 & \text{if the track is included in the PV fit} \\ (\sigma_{R\phi}^{\text{trackfit}})^2 + (\sigma_{R\phi}^{\text{PV}})^2 & \text{otherwise} \end{cases} \quad (6.1)$$

and similar for σ_{Rz} .

Significance and track probability

The IP divided by its measurement error gives the track significance, $S_{R\phi} = \text{IP}_{R\phi}/\sigma_{R\phi}$. The long b-hadron lifetime in combination with the high transverse momentum leads to large positive significances for the b-hadron decay products. By contrast, the tracks originating from the primary vertex have significances of either sign, which peak around 0. The distribution $f(S)$ of the negative track significance is thus determined mainly by tracks from the primary vertex. It only receives a residual contribution from decay tracks of long-lived particles, which can be further reduced by an anti-b tag. Since this anti-b tag is constructed from only the tracks with positive significance, it does not bias the negative significance distribution. Hence, the distribution represents a detector resolution function and can be used to define a probability $P(S_i)$ that a track i with a measured significance S_i is compatible with the primary vertex,

$$P(S_i) = \begin{cases} \int_{-\infty}^{S_i} f(S) dS & , \text{ for } S_i < 0 \\ P(-S_i) & , \text{ for } S_i > 0 \end{cases} . \quad (6.2)$$

By definition, tracks from the primary vertex are expected to have a flat distribution of $P(S_i)$ between 0 and 1, while decay particles from long-lived hadrons and with large positive S_i values have small values of $P(S_i)$.

Resolution calibration and tuning

The transformation from significance to track probability is referred to as the *calibration* of the detector resolution, because the track probability can be obtained directly from the data and independently of any simulation. This takes into account possible differences in data and simulation. Such disagreements are clearly present already in the significance distributions, even after carefully simulating possible noise, inefficiency and misalignment effects in the Vertex Detector. To avoid large discrepancies in the resulting b-tagging description, an additional *tuning procedure* is applied to the simulated IPs [49]. It involves correcting $(\sigma_{R\phi}^{\text{trackfit}})^2$ and $(\sigma_{Rz}^{\text{trackfit}})^2$ by means of the negative IP distribution and smearing the simulated $R\phi$ and Rz IPs in order to reproduce the observed real data distributions. In both, calibration and tuning, each year of data taking is treated separately to allow for the changes in the detector performance. The remaining differences between data and simulation can mainly be explained by uncertainties in the modelling of the decays of b- and c-hadrons.

Lifetime probability

The track probabilities are used to define a more general probability for any group

absolute charge	$ q > 0$
absolute value of momentum	$0.05 \text{ GeV}/c < \vec{p} < 1.1 \cdot E_{\text{beam}}$
length of tracks measured only with TPC (years 1992-1995 only)	$l_{\text{track}} > 30 \text{ cm}$
relative error on momentum	$\Delta \vec{p} / \vec{p} < 1$
3-d distance to B path (see text)	$D/\sigma_D < 2.5, < 10$
number of VD hits	$N_{\text{layer}} \geq 1$
$\chi^2/n.d.o.f.$ for the VD hits of a track	$\chi^2_{\text{VD}} < 4$

Table 6.1: The conditions applied to tracks that are used for lifetime tagging.

of N tracks with their observed significances S_i to originate from the primary vertex.

$$P_N \equiv \Pi \cdot \sum_{j=0}^{N_{R\phi}+N_{Rz}-1} \frac{(-\ln \Pi)^j}{j!}, \quad \text{where } \Pi \equiv \prod_{i=1}^{N_{R\phi}} P_{R\phi}(\sigma_i^{R\phi}) \cdot \prod_{i=1}^{N_{Rz}} P_{Rz}(\sigma_i^{Rz}) \quad . \quad (6.3)$$

This group of tracks can be a jet, a hemisphere or the whole event. If one restricts the sum to the tracks in the group that have positive significances, the lifetime probability P_N^+ provides a variable to tag b events, because those tracks contain the lifetime information from the B decay. In contrast, only the negative IP tracks are utilised for calibration and tuning, so that the samples used in the calibration and in the analysis do not overlap. In addition, selection cuts are applied to the tracks entering the lifetime probability. Track candidates have to have at least one measurement in the Vertex Detector, and the distance D of closest approach in three dimensions between the track and the estimated B flight path has to stay below a certain limit. This limit for D with respect to its expected precision σ_D is set to 2.5 for accepting both $R\phi$ and Rz IP measurements, and to 10.0 for accepting only $R\phi$ measurements. This rejects wrong IP measurements, which occur more likely in Rz . The detailed list of track cuts is given in Table 6.1. Finally, tracks coming from reconstructed K^0 and Λ decays are excluded.

6.2 Combined Tagging

In the combined tagging algorithm, the tagging power of the lifetime probability is enhanced by adding more discriminating variables that are sensitive to other physical properties of b -hadrons. The extra variables are more sophisticated in the way that signal and background are not as clearly separated as in the lifetime probability, and the number of available variables depends e.g. on the presence of a secondary vertex. As a powerful and at the same time simple way to combine all available information into a single tagging variable, a likelihood ratio method was chosen in DELPHI [46, 50]. Care was taken to pick a set of variables with reduced correlations among them because likelihood ratio methods provide the optimal tagging performance, i.e. background suppression at a given signal efficiency, only for independent variables. A cross-check based on a Neural Network approach, which is supposed to treat also

correlated variables in an optimal way, showed no significant improvement in the performance [51].

Secondary vertex reconstruction

Some of the additional discriminating variables require the presence of a reconstructed B decay vertex. A secondary vertex is therefore searched for in each jet of the event in an iterative procedure. Candidates for secondary vertices are accepted only if the distance to the primary vertex divided by its error is more than 4, and at least two tracks in the secondary vertex candidate have VD measurements in both $R\phi$ and Rz . Tracks from a subsequent D meson decay, which are otherwise incompatible with the reconstructed B decay vertex, are identified by their close distance to the B direction of flight. Although not included in the secondary vertex fit, such tracks are included in the computation of quantities like the b-hadron mass. By setting additional quality constraints on the impact parameter of the b-hadron momentum, on the lifetime probability of the tracks included in the secondary vertex candidate and on the maximal decay length, the background of light quarks among the jets with secondary vertices is suppressed further. At large distances between secondary and primary vertex, the rate of K^0 decays and false secondary vertices becomes relatively high, so that the cut on a maximal decay length prevents pure background from generating strong b-tagging signals. This procedure yields a reconstructed secondary vertex in about 44 % of the b-jets (in 4π , so disregarding the VD acceptance).

The discriminating variables

The requirement for a secondary vertex (SV) increases the b-purity, $p_b = N_b/(N_b + N_{\text{udsc}})$, from the initial 22 % in hadronic Z boson decays to about 85 %. Furthermore, it classifies all jets into three categories, $\mathcal{K}_1 - \mathcal{K}_3$. The first category, \mathcal{K}_1 , comprises all jets with one or more reconstructed secondary vertices and allows the calculation of all extra discriminating variables in the combined b-tagging. If a secondary vertex is not reconstructed, but at least two tracks are found with a track significance probability, $P(S_i)$ (Eq. 6.2), below 0.05, the jet is assigned to the second category, \mathcal{K}_2 . The remaining jets are included in the third category, and in this case the combined tag is reduced to an inclusive set of discriminating variables, like the lifetime probability. An overview of the discriminating variables in use and the flavour fractions in the three categories can be found in Table 6.2.

criterion		variables	fractions		
			b	c	uds
\mathcal{K}_1	SV tracks	all	44 %	8 %	0.6 %
\mathcal{K}_2	b-tagged tracks	a), b), c)	14 %	8 %	2.8 %
\mathcal{K}_3	rest	a), c)	42 %	84 %	96.6 %

Table 6.2: The three different jet categories for tracks entering the combined b-tagging algorithm. The fractions are taken from [47].

The discriminating variables used in the combined b-tagging are:

- a) The *jet lifetime probability*, P_J^+ , is constructed using Eq. 6.3 from the positive IPs of all tracks included in the jet. Fig. 6.3(a) shows the distribution of the transformed variable $-\log_{10}(P_J^+)$ for simulated jets with a reconstructed secondary vertex.

While uds-jets are well separated from b-jets, the separation between b- and c-jets is less clear because long-lived D mesons produce a lifetime probability similar to the one of B mesons. This variable is calculated for all three jet categories, $\mathcal{K}_1 - \mathcal{K}_3$.

- b) The *effective mass of particles from the secondary vertex*, M_{SV} , helps in distinguishing between b and c events. As can be clearly seen in Fig. 6.3(b), the mass distribution for jets in c-events is limited by the mass of the D meson, which is about $1.8 \text{ GeV}/c^2$ (see also Table 2.2). By contrast, the mass in a b-jet can go up to $5 \text{ GeV}/c^2$. The mass from the secondary vertex is calculated for the jet categories \mathcal{K}_1 and \mathcal{K}_2 .
- c) The *rapidity of each track*, $R_{(SV)}^{\text{trk}}$, possibly restricted to the set of tracks included in the secondary vertex, is also a very strong separating variable. In general, the rapidity with respect to a given reference axis is

$$R^{\text{trk}} = \frac{1}{2} \ln \left(\frac{E + p_{\parallel}}{E - p_{\parallel}} \right) , \quad (6.4)$$

yielding a maximal rapidity $R^{\text{trk}, \text{max}} = \ln(2E_{\text{beam}}/m_q)$ for the initial quarks. Hence c quarks have a higher rapidity than b quarks. Because the mean rapidity is conserved in decays, the tracks entering the combined b-tagging show the same tendency in Fig. 6.3(c). Light quarks do not show the leading particle effect so strongly, so that the rapidity spectrum in light quark events is wider. The track rapidities are used in $\mathcal{K}_1 - \mathcal{K}_3$.

- d) The *fraction of the charged jet energy included in the secondary vertex*, X_{SV}^{ch} , reflects the differences in the fragmentation properties of different quark flavours. The transfer of energy in the fragmentation process is modelled by the fragmentation functions, which were discussed in Section 2.7.2 and Fig. 2.8(b) therein. All other flavours have softer fragmentation functions than b-quarks, so that b quarks accumulate at high values of X_{SV}^{ch} in Fig. 6.3(d). This and the last variable are only employed in \mathcal{K}_1 .
- e) The *transverse momentum at the secondary vertex*, P_{SV}^{\perp} , takes into account missing particles not included in the secondary vertex definition. It is defined as the resultant transverse momentum of all charged particles in the secondary vertex and computed with respect to the estimated flight direction of the b hadron. As can be seen from Fig. 6.3(e), the value of P_{SV}^{\perp} is higher for b-jets due to the high b-hadron mass. For this tendency it does not matter if the missing particle is a neutrino in a semileptonic B decay or a neutral particle or a charged track that could not be reconstructed.

A possible sixth variable, the *transverse momentum of an identified energetic lepton*, provides special sensitivity to semileptonic b-hadron decays independent of any track IPs. However, in order to keep the correlation low with the dedicated measurement of A_{FB}^b based on a semi-inclusive lepton reconstruction [52], this variable is not included in the combined b-tagging used in this analysis.

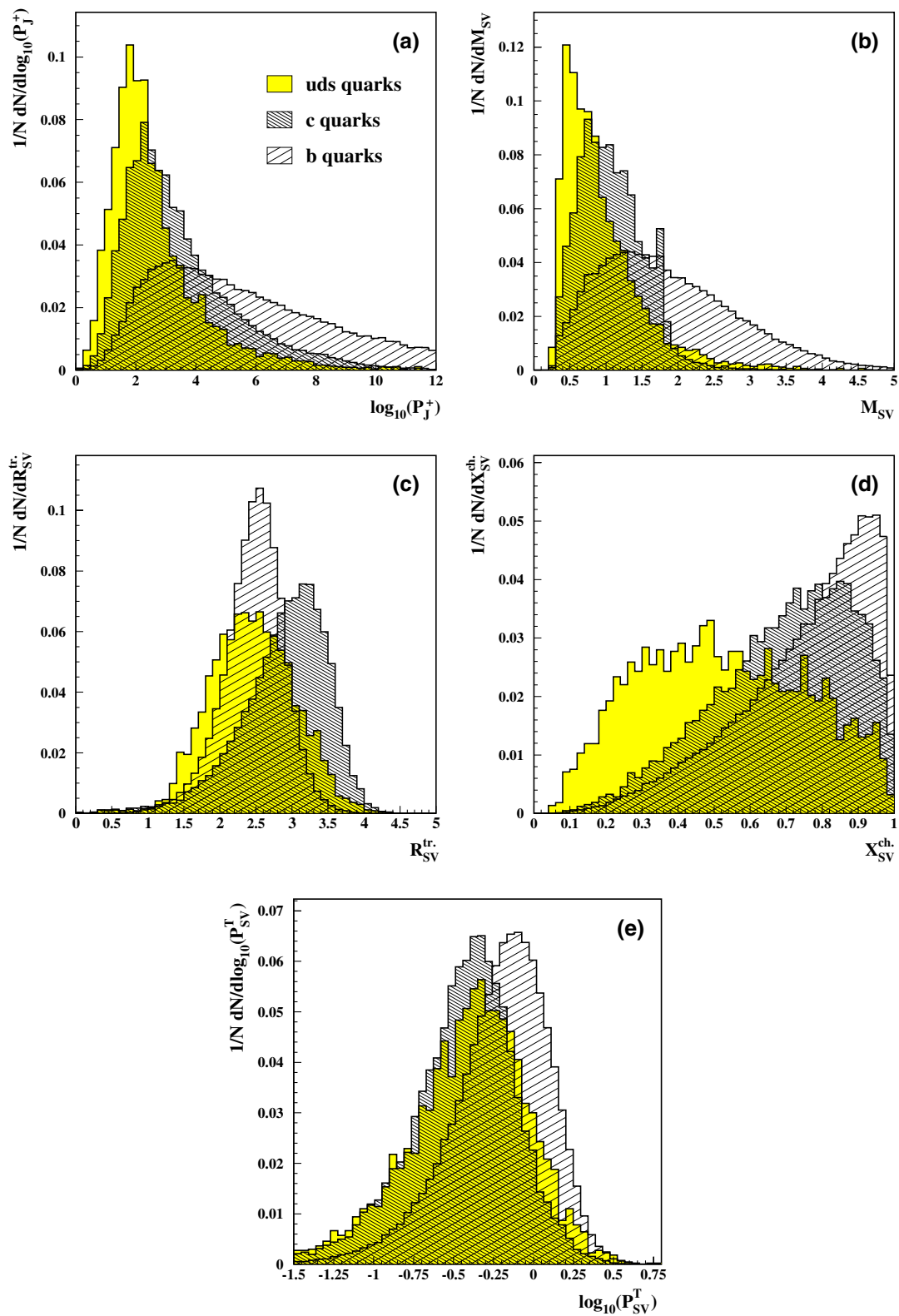


Figure 6.3: The discriminating variables used in the combined b-tagging algorithm. The distributions are shown for simulated jets with a reconstructed secondary vertex (category \mathcal{K}_1).

The likelihood ratio and the final b-tagging variable

In the likelihood ratio method, a set of discriminating variables x_1, \dots, x_n is combined into a single tagging variable y , which is defined as

$$y = \frac{f^{\text{bgd}}(x_1, \dots, x_n)}{f^{\text{sig}}(x_1, \dots, x_n)} . \quad (6.5)$$

Here, $f^{\text{bgd}}(x_1, \dots, x_n)$ and $f^{\text{sig}}(x_1, \dots, x_n)$ are the probability density functions of the discriminating variables for the background and the signal respectively. Because the ratio of the probability density functions has a monotonous dependence on y , any selection $y < y_0$ gives an optimal tagging of the signal. In the case of discriminating variables having reduced correlations among them, expression 6.5 factorises to

$$y = \prod_{i=1}^n \frac{f_i^{\text{bgd}}(x_i)}{f_i^{\text{sig}}(x_i)} =: \prod_{i=1}^n y_i , \quad (6.6)$$

thus simplifying greatly the probability density functions, which then can be determined from simulation for each variable x_i .

This scheme is implemented in the DELPHI combined b-tagging, which computes every value $y_i = f_i^{\text{bgd}}(x_i) / f_i^{\text{sig}}(x_i)$ for the index i running over the four jet variables a), b), d), e) and the set of selected tracks for the track rapidities $R_{(\text{SV})}^{\text{rk}}$. By the construction of the discriminating variables, independent probability density functions can be computed for jets from c and uds background events as well as from the three categories $\mathcal{K}_1 - \mathcal{K}_3$. Consequently, the tagging variable y_α for a jet of category α is defined as:

$$y_\alpha = \frac{n_\alpha^{\text{c}}}{n_\alpha^{\text{b}}} \prod_i \frac{f_{i,\alpha}^{\text{c}}(x_i)}{f_{i,\alpha}^{\text{b}}(x_i)} + \frac{n_\alpha^{\text{uds}}}{n_\alpha^{\text{b}}} \prod_i \frac{f_{i,\alpha}^{\text{uds}}(x_i)}{f_{i,\alpha}^{\text{b}}(x_i)} . \quad (6.7)$$

The factors n_α^{q} are the normalised rates for each flavour $q = \text{uds}, \text{c}$ or b , so that $\sum_{\mathcal{K}_1}^{\mathcal{K}_3} n_\alpha^{\text{q}}$ equals R_{q} . Implemented like this, the classification into different jet categories effectively acts like an additional discriminating variable with the discrete probabilities given by n_α^{q} . The jet tagging variable is transformed to a more convenient range of values by defining $X_{\text{jet}} = -\log_{10} y_\alpha$. The tagging performance of this variable in terms of efficiency and purity is displayed in Fig. 6.4 for different sets of discriminating variables. Compared to the pure lifetime probability, $-\log_{10}(P_{\text{J}}^+)$, a significantly better background suppression is visible for the combined tagging variables. Even including an extra discriminating variable like $X_{\text{SV}}^{\text{ch}}$, which by itself shows a very poor tagging performance, improves the background suppression further due to its small correlation with the other variables.

A hemisphere tagging variable as needed in this analysis, $b\text{-tag}_{\text{hem}}$, is simply obtained by picking the jet with the largest value of X_{jet} , regardless to which jet category α it belongs. Because the primary b quarks move in opposite directions in Z boson decays at LEP 1, only one signal jet is expected per hemisphere. Hence the choice of the largest X_{jet} value maintains the optimal tagging of the signal. Here it should be noted that this analysis does not require a secondary vertex to be reconstructed within the b-tagging algorithm. Unlike the measurement of R_b at LEP 1, b-tagged jets from all three categories are used. It is the algorithm for separating b quarks from anti-b quarks, the charge tag, which is later restricted to events having at least one hemisphere with a reconstructed secondary vertex. The charge tag, however, uses

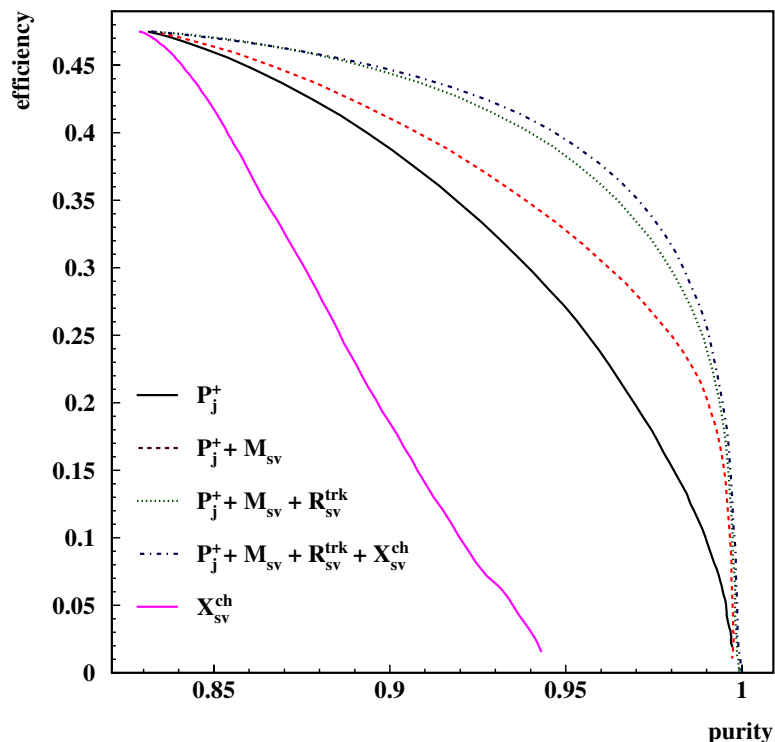


Figure 6.4: Comparison of the tagging performance of single discriminating variables and their combination in the likelihood ratio. A secondary vertex has been required for all jets entering the efficiency and purity computation.

a slightly different algorithm to reconstruct secondary vertices, which is adapted to its needs, as described in Section 7.4.

The event b -tagging variable is made of the sum of the two hemisphere discriminators:

$$b\text{-tag} = \sum_{\text{hem}=1}^2 b\text{-tag}_{\text{hem}} + 0.5 \quad . \quad (6.8)$$

The offset of 0.5 is only used to maintain compatibility with older, preliminary publications of this analysis [53, 54, 55]. Decays to b quarks tend to have higher b -tag values whereas decays to other quarks are peaked at smaller values as can be seen in Fig. 6.5, separately for the combined years 1992 + 93, 1994 + 95 and 1996-2000. High purity samples are selected by cutting on $b\text{-tag} > -0.2$ for 1992 + 93 and $b\text{-tag} > 0.0$ for 1994 to 2000. This guarantees a working point at constant b purity over the years regardless of the change in tagging performance due to the differences in the VD set-up.

In previous steps, the simulation has been tuned to the data by event reweighting (Chapter 5) and by accurate tuning of the resolution function in the track probability (page 49). Still, the discriminating variables in the combined b -tagging depend on detector resolution (mainly via the secondary vertex reconstruction efficiency) as well as on b and c hadron decay properties and lifetimes. Their limited knowledge can lead to an improper description of the tagging performance in the simulation.

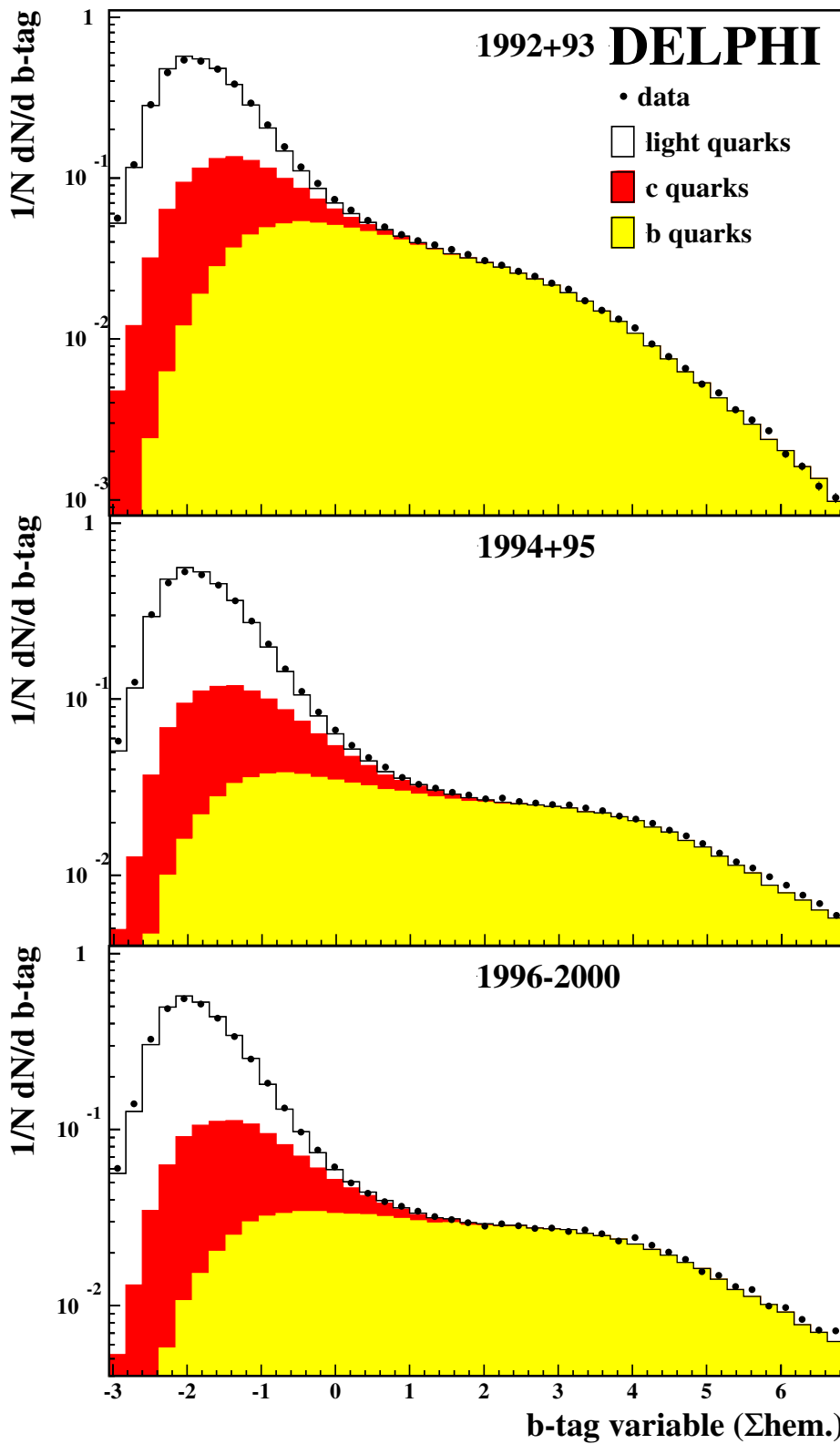


Figure 6.5: Comparison between data and simulation of the normalised number of events versus the b -tag variable for 1992+93 (upper plot), 1994+95 (middle) and 1996-2000 (lower plot). The b , c and light quark composition of the simulation has been reweighted according to the measured branching fractions [24]. The b and c quark simulation correction from Section 6.4 is not applied at this stage.

6.3 The b Tagging Efficiency in b and c Events

To avoid a resulting bias in the background estimates, the b and c efficiencies on the b -enriched samples are calibrated by means of a double tagging method similar to the one which has been used in the R_b measurement to derive the b efficiency simultaneously with R_b [46]. A special application of the double tagging method to this analysis [56] corrects the fractions of b and c quarks and is described in the following. The efficiencies and flavour fractions relevant for extracting A_{FB}^b on the b -enriched charge tagged samples then are calculated using the so-corrected simulation.

The selection efficiencies ε_i modify the fractions of b , c and uds events, which are initially the fractions of b and c events produced in hadronic Z decays, R_b and R_c . This applies likewise to hemispheres, where the fraction with $b\text{-tag}_{\text{hem}}$ variable X larger than some cut value X_0 can be written as,

$$\frac{N^{X>X_0}}{N^{\text{tot}}} = \mathcal{F}^{X>X_0} = R_b \cdot \varepsilon_b^{\text{hem}} + R_c \cdot \varepsilon_c^{\text{hem}} + (1 - R_c - R_b) \cdot \varepsilon_{\text{uds}}^{\text{hem}} \quad (6.9)$$

where N^{tot} is the initial number of hemispheres and $\varepsilon_j^{\text{hem}}$ the selection efficiency for each flavour. In detail, $\varepsilon_c^{\text{hem}}$ is the efficiency to tag a real c event hemisphere as a “ b ”. For R_c and R_b — here as well as throughout the whole analysis — the LEP+SLD average values of $R_c^0 = 0.1719 \pm 0.0031$ and $R_b^0 = 0.21644 \pm 0.00065$ are used [24].

Since each event has 2 hemispheres, such a selection defines three different kinds of event: **double** b -tagged events where both hemispheres have a $b\text{-tag}_{\text{hem}}$ value bigger than the selection-cut, **single** b -tagged events where only one hemisphere is larger than the cut and **no** b -tagged events where both hemispheres are below the selection cut. The fraction of double, single and no-tagged are therefore,

$$\mathcal{F}^d = R_b \cdot \varepsilon_b^d + R_c \cdot \varepsilon_c^d + (1 - R_c - R_b) \cdot \varepsilon_{\text{uds}}^d \quad (6.10)$$

$$\mathcal{F}^s = R_b \cdot \varepsilon_b^s + R_c \cdot \varepsilon_c^s + (1 - R_c - R_b) \cdot \varepsilon_{\text{uds}}^s \quad (6.11)$$

$$\mathcal{F}^n = R_b \cdot \varepsilon_b^n + R_c \cdot \varepsilon_c^n + (1 - R_c - R_b) \cdot \varepsilon_{\text{uds}}^n \quad , \quad (6.12)$$

By definition $\sum_j \mathcal{F}^j = 1$, and so only two of these equations are independent. The selection efficiencies of the three different kinds of event depend on the product of the two hemisphere selection efficiencies and the correlation that exists between them.

events	without correlation	with correlation	
		in λ	in k
ε^d	$\varepsilon \cdot \varepsilon$	$\varepsilon^2(1 + \lambda)$	$\varepsilon k + \varepsilon^2(1 - k)$
ε^s	$2 \cdot [\varepsilon \cdot (1 - \varepsilon)]$	$2\varepsilon - 2\varepsilon^2(1 + \lambda)$	$2\varepsilon(1 - k) - 2\varepsilon^2(1 - k)$
ε^n	$(1 - \varepsilon) \cdot (1 - \varepsilon)$	$1 - 2\varepsilon + \varepsilon^2(1 + \lambda)$	$1 - \varepsilon(2 - k) + \varepsilon^2(1 - k)$
$\sum \varepsilon^i$	1	1	1

Table 6.3: The event-efficiencies for correlated hemispheres: $k = 0$ implies the hemispheres are uncorrelated whereas $k = 1$ means that the hemispheres are fully correlated.

This correlation is assumed to be linear and parameterised by the factor $(1 + \lambda)$, like in the mid column of Table 6.3. In this approach, the hemispheres are fully

correlated for $\lambda = 1/\varepsilon$ – the correlation appears as a function of the hemisphere selection efficiency. In order to remove the dependence on the efficiency, the correlation is rescaled to k where $k = \frac{\varepsilon \cdot \lambda}{(1-\varepsilon)}$. The limit $k = 0$ implies the hemispheres are uncorrelated whereas $k = 1$ means that the hemispheres are fully correlated. Table 6.3 lists the dependence of the event efficiencies on the single hemisphere selection efficiency for different parameterisations of the hemisphere correlation. The expressions in terms of k are summarised below where index j runs over the three flavour classes: b , c and uds ,

$$\varepsilon_j^d = \varepsilon_j^{\text{hem.}} k_j + (\varepsilon_j^{\text{hem.}})^2 (1 - k_j) \quad (6.13)$$

$$\varepsilon_j^s = 2\varepsilon_j^{\text{hem.}} (1 - k_j) - 2(\varepsilon_j^{\text{hem.}})^2 (1 - k_j) \quad (6.14)$$

$$\varepsilon_j^n = 1 - \varepsilon_j^{\text{hem.}} (2 - k_j) + (\varepsilon_j^{\text{hem.}})^2 (1 - k_j) \quad (6.15)$$

The method involves solving Eqs. (6.10)-(6.12) for $\varepsilon_b^{\text{hem}}$ and $\varepsilon_c^{\text{hem}}$ with the replacement of the modified efficiencies of Eqs. (6.13)-(6.15). A detailed derivation and presentation of the analytical solution can be found in [56]. The solution obtained on simulated data yields the correlations k_j by solving Eqs. (6.13)-(6.15). For real data, the fractions of double-, single- and no-tagged events are measured, but the efficiency for uds events and the k_j are taken from simulation. This method measures the selection efficiency for b and c hemispheres directly in the data. The resulting efficiencies can then be compared with the corresponding quantities in the simulation and a correction function formed from any difference seen. This function is then used to bring the simulated b and c selection efficiencies into agreement with those measured in real data. The correction is formed and applied separately for b and c hemispheres.

The range of $b\text{-tag}_{\text{hem}}$ values, to which these corrections can be safely applied, has been studied in detail in [56]. At $b\text{-tag}_{\text{hem}}$ less than -1.0 , the light quark fraction is no longer a small correction, but forms a more important contribution than the b or c quark samples, which the method was originally designed for to treat as signal. This was reflected in a systematic error larger than the b and c efficiency corrections when assuming a preliminary uncertainty on the uds efficiency. In the regime of low $b\text{-tag}_{\text{hem}}$ values, the solution also ran into technical problems in solving the quadratical equation, which were found to be related to statistical fluctuations and the assumed values for ϵ_{uds} and the correlations. If a solution could still be obtained, it was an unphysical result like $\epsilon_b \gtrsim 1.0$ in some cases. This range of limited applicability is well below the $b\text{-tag}_{\text{hem}}$ cuts used to construct the measurement samples to extract A_{FB}^b .

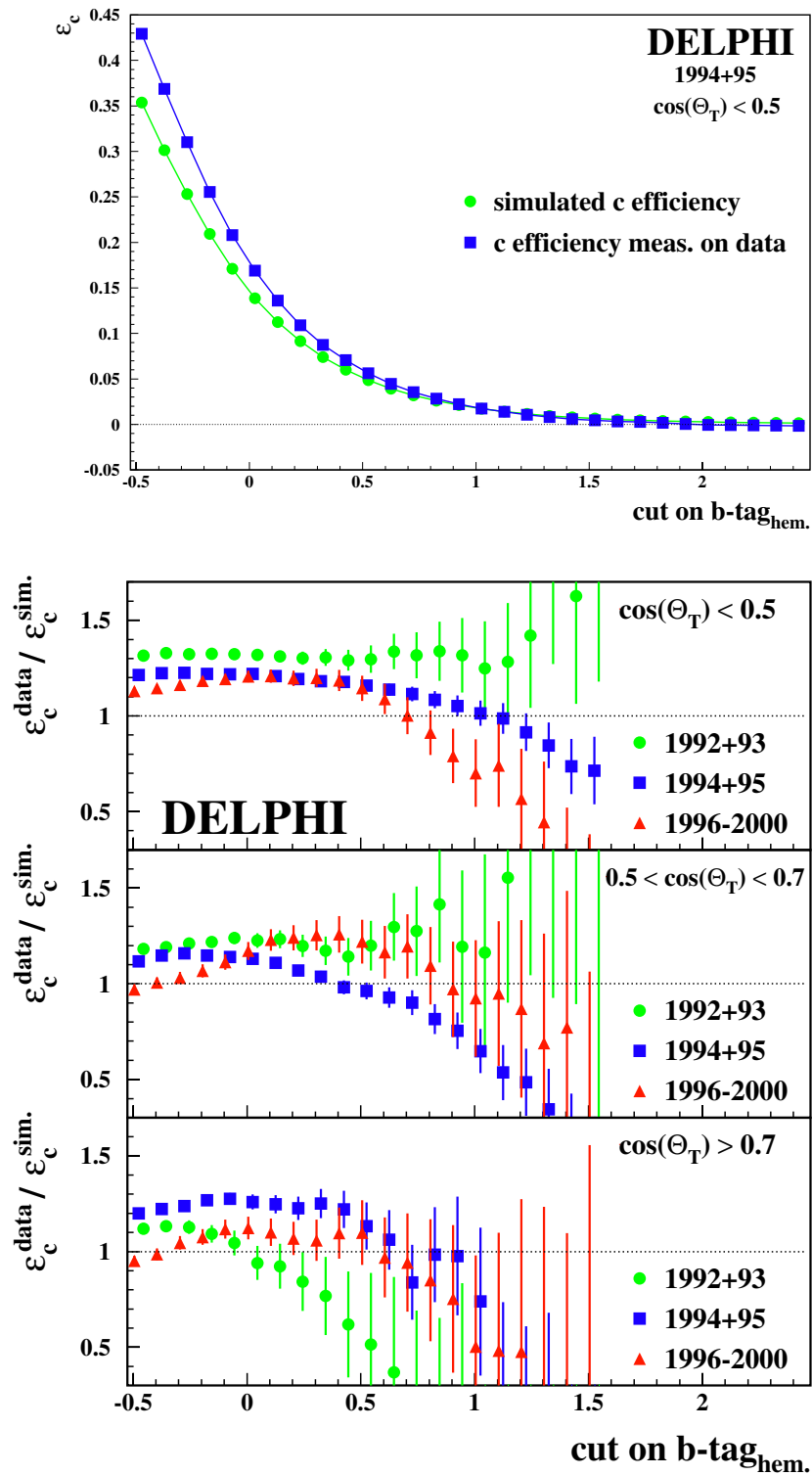


Figure 6.6: The measured efficiency of c -quark hemispheres, as a function of the cut on $b\text{-tag}_{\text{hem}}$, in simulation compared to real data following the procedure outlined in the text. The upper plot details the situation in the central region for the 1994+95 data, while the triple plot below summarises the agreement found in all three VD set-ups and polar angle ranges.

6.4 The Correction Function

Among the different steps to calibrate and measure the b selection efficiency, only the previously introduced double b tag method gives access to the c efficiency on real data. The measured c selection efficiencies in simulation and real data are shown in the upper part of Fig. 6.6 for the example of the 1994+95 central region at $\cos\theta_{\vec{T}} < 0.5$. The displayed range for the cut on the $b\text{-tag}_{\text{hem}}$ variable represents the interval where c quarks are the dominant background contribution for this analysis and where the efficiency calibration for b and c events is performed. It is found that in a low $b\text{-tag}_{\text{hem}}$ region where the c background forms an important contribution, the simulation underestimates the amount of c quarks entering the sample. This observation is expected to vary between the different set-ups for the vertex detector and its angular acceptance. In the lower part of Fig. 6.6 the ratio of real to simulated c efficiency is shown for 1992+93, 1994+95 and 1996-2000 as well as for the angular regions of $\cos\theta_{\vec{T}} < 0.5$, $\cos\theta_{\vec{T}} \in [0.5, 0.7)$ and $\cos\theta_{\vec{T}} \geq 0.7$.

The correction function used to calibrate the simulated b and c efficiencies is constructed individually on those set-ups and regions studied in Fig. 6.6, thus taking the slightly different data to simulation ratios into account. Its construction is illustrated in the sketch in Fig. 6.7, which mirrors the situation found in Fig. 6.6. For each bin in $b\text{-tag}_{\text{hem}}$, a correction is applied to the $b\text{-tag}_{\text{hem}}$ value in simulated b and c hemispheres in order to force the data and simulation efficiency curves into agreement.

The correction at the level of the whole event is then accounted for by simply adding together the corrected $b\text{-tag}_{\text{hem}}$ values of the two event hemispheres.

The result of applying such a correction function is shown in Fig. 6.8 which plots the data to simulation ratio for the integrated $b\text{-tag}$ at event level. The simulation is found to agree with data within $\pm 1\%$. Uncertainties of the remaining modelling input to the correction function, such as hemisphere correlations and residual uds background, are taken into account in the study of systematic uncertainties.

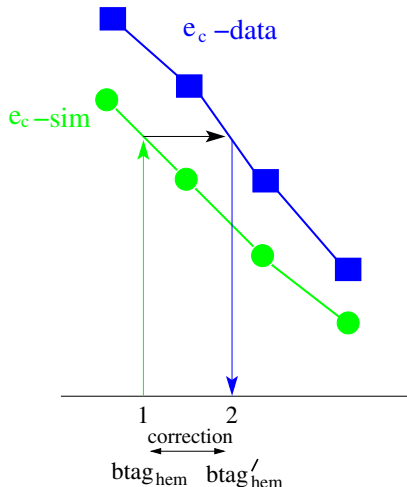


Figure 6.7: Construction of the correction function for each bin

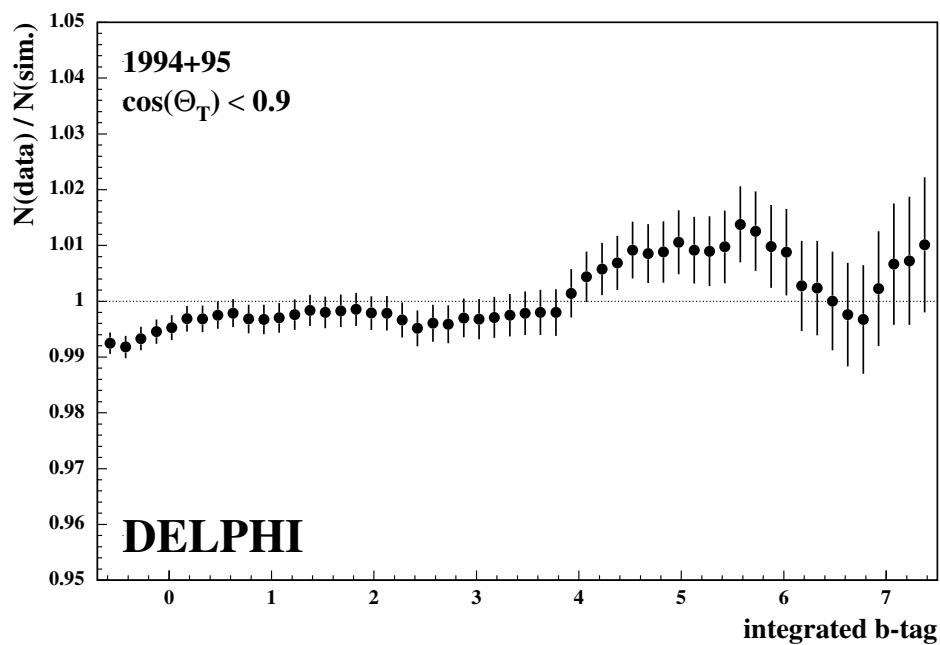


Figure 6.8: The (integrated) b -tag ratio of real to simulated events after the application of the correction functions to simulated b and c quark events. The data are from the 1994+95 DELPHI data set. Different correction functions for the $\cos \theta_{\bar{T}}$ intervals of $[0.0, 0.5]$, $[0.5, 0.7]$ and ≥ 0.7 were applied before integrating over the full polar angle.

Chapter 7

Inclusive Charge Reconstruction by BSAURUS

This chapter explains the novel high precision method for inclusive b charge tagging. This method uses the full available experimental charge information from b jets which is combined into one tagging variable using a Neural Network technique. The tagging method is part of a DELPHI analysis package for b physics called BSAURUS¹. In the following sections its main tools and features are explained with respect to the inclusive charge tag. Full technical details are given in reference [57].

The hemisphere charge tagging Neural Network is designed to distinguish between hemispheres originating from the b quark or anti-quark in $Z \rightarrow b\bar{b}$ decays and thus to provide the essential information to measure the asymmetry. For b jets with a reconstructed secondary vertex it combines jet charge and vertex charge information² with so-called b-hadron flavour tags, quantities that reconstruct the b quark charge at the time of production and, if possible, also at the time of decay for any given b-hadron hypothesis. The chapter begins with a general introduction into artificial Neural Networks. Before the ingredients for the final hemisphere charge tagging Network are described in Section 7.6.3 the basic requirements such as particle identification, secondary B or D decay vertex finding and other auxiliary Neural Networks are outlined.

7.1 Neural Network Techniques

With sophisticated tasks, sequentially working computers and algorithms can rapidly reach their performance limit. Such tasks comprise pattern recognition in speech, images or any other data as well as extensive optimisation or control problems, but they can also be the evaluation of event topologies in high energy physics, where the observed final states reflect an interplay of the various underlying physical properties. In many cases it is better to parallelise the task, hereby simulating the way the human brain works: like an extremely parallel computer with some 10 billion highly interconnected processors, which is able to cope with steady and frequent failures at the level of single elements. Artificial Neural Networks follow this approach by emu-

¹The authors advertise it as BSAURUS - B Spectroscopy And Useful Routines from US

²For definitions see Equations 7.5 and 7.6 below.

lating the behaviour of a natural nerve cell, a *neuron*, and connecting the simulated neurons to form a network adapted to the type of task under consideration.

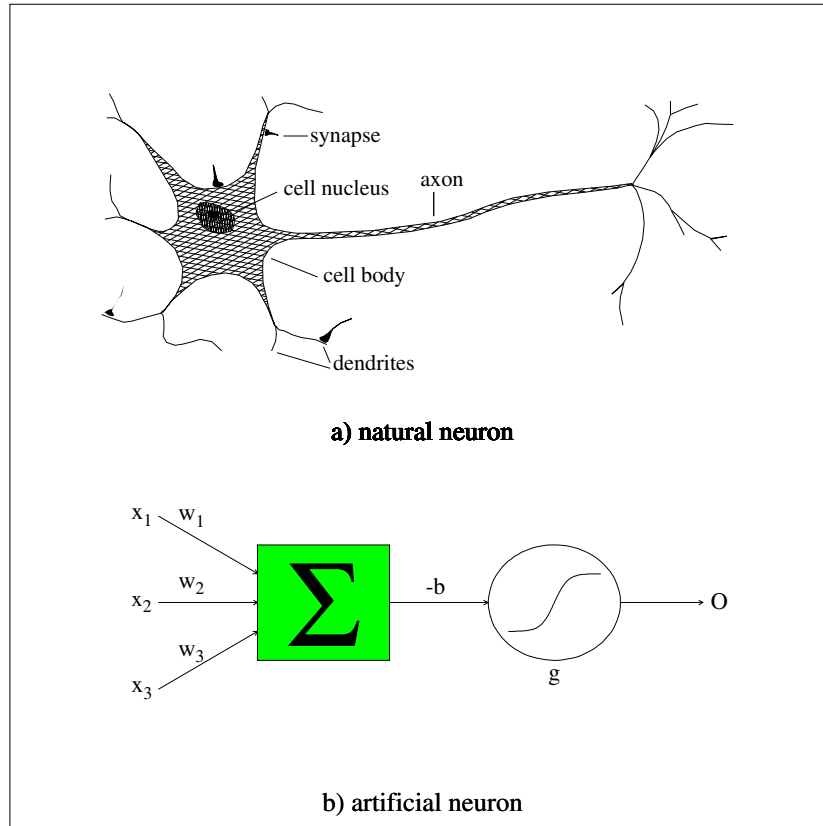


Figure 7.1: Comparison of a natural and an artificial neuron. In this very basic neuron, the dendrites receive the inputs that are to be processed in the cell body (soma). Its output is sent by the axon to the synapses, the electro-chemical connections to other cells. The artificial neuron emulates this principle. Drawing from [58].

The basic concept from W.S. McCulloch and W.H. Pitts [59] is illustrated in Fig. 7.1, which compares an artificial neuron to a natural one. The behaviour of the natural neuron is simulated by assigning to each incoming signal connection x_i a weight $w_i \in [-1, +1]$, which controls by how much the signal is inhibited or amplified. If the sum of the weighted inputs, $\sum_i w_i x_i$, passes a certain level, b , the axon fires off, i.e. the artificial neuron yields $O = 1$. This procedure is parameterised as

$$O = g \left(\sum_i w_i x_i - b \right) \quad (7.1)$$

where the activation function, $g(y)$, approximates the threshold behaviour of the axon. The most interesting types of g -function are *differentiable* sigmoid functions (see Fig. 7.1b) like

$$g(y) = \tanh\left(\frac{y}{T}\right) \quad \text{or} \quad g(y) = \frac{1}{1 + \exp\left(-\frac{y}{T}\right)}, \quad (7.2)$$

because they allow of modern learning algorithms like the Gradient Descent Rule. The internal parameter T is termed *temperature* or *turn-on gradient* and can be

used to control the response behaviour of the whole artificial neuron. Its output is then continuous, $O \in [-1, +1]$ or $[0, +1]$, a property that can be further exploited in physics applications such as conditional probabilities. Such an artificial neuron is often called *node* and forms the basic element of a Neural Network.

Similar to natural brains, artificial Neural Networks first need to undergo a training phase before they can be employed. During this training phase, they are presented with a set of learning patterns, so that the synaptic weights can be adapted, following a certain learning algorithm. The choice of an efficient learning algorithm and a related end-point of the training procedure is non-trivial. When this end-point is reached and the training finished, the weights stay fixed and the Network can be employed in processing new patterns. The great advantage of using Neural Networks lies in their ability to still provide a proper result for patterns with slightly modified features or with flawed or missing inputs. In addition, they automatically allow for correlations among the input variables and effectively provide selection criteria in the high-dimensional input parameter space.

Feed-forward Networks

The type of Network implemented in BSAURUS is a feed-forward Network, which typically processes information in a single direction from a layer of input nodes to a single output or a layer of output nodes. In between there are one or more *hidden layers*, which are used only internally. To achieve a good and stable performance of the Network, the input nodes should be given discriminating variables with reduced correlations among them and high sensitivity to the output. As a basic rule, the number of nodes in the hidden layer is somewhat related to the complexity of the problem. Additional hidden layers might be useful if the process being modelled is separable into multiple stages or if the number of weights must be kept low, while they otherwise hold the danger of purely memorising the training patterns. If memorisation happens then no generalisation of the data trends will occur, making the network useless on new data sets. Every node in one layer is connected to every node in the subsequent layer, just like in Fig. 7.8, which displays the structure of the final charge tag Network. It is a feed-forward Network with 9 input nodes, 10 hidden nodes in one layer and a single output node.

The training algorithm used for most feed-forward Networks, and in particular for the Networks within BSAURUS, is the *backpropagation* algorithm (BPA) [60], whose current form was developed by D.E. Rumelhart et al. [61]. During the BPA learning process, one or several training input sets are fed forward through the Network and the output of each element is computed layer by layer. The squared difference between the outputs of the final layer and the desired outputs is back-propagated to the previous layer(s), usually modified by the derivative of the activation function. The connection weights to the previous layer are normally adjusted using the Gradient Descent Rule, which appends to the derivative an additional proportional constant tied to the learning rate. This process proceeds for the previous layer(s) until the input layer is reached. The BPA effectively approximates unknown functions, i.e. it determines in the high-dimensional space spanned by the inputs those hyperplanes that yield an optimal separation between the different output classes. Usually such an approach performs much better than a sequence of linear cuts, and can handle a much more sophisticated set of input variables than the likelihood ratio method, which is implemented e.g. in the b-tagging algorithm.

Neural Networks in BSAURUS

Finally it should be stressed again that Neural Networks use the same computers and code as “normal” programmes, but they differ in the way the information is mapped from the physical variables to the classification or prediction output. This mapping is extremely non-linear and high-dimensional.

BSAURUS basically uses the feed-forward Neural Network software from the JETNET package [62]. The BSAURUS Networks employ a sigmoid activation function and are nearly always set up with three layers, i.e. one hidden layer containing one more node than there are input nodes. In the training, two statistically independent samples are used; the training sample (usually with a 50-50 mix of signal and background) and the performance sample. The training is usually stopped when the network output error obtained on the *performance sample* does not improve further. The network output error is determined from the difference between desired and actual output value, added in quadrature for the number of existing output nodes. Variables used as inputs are often pre-processed, that is transformed internally so that the Network sees (ideally) a linear, continuous variation in the ratio of signal to background across the full range of the transformed input variable.

7.2 Particle Identification

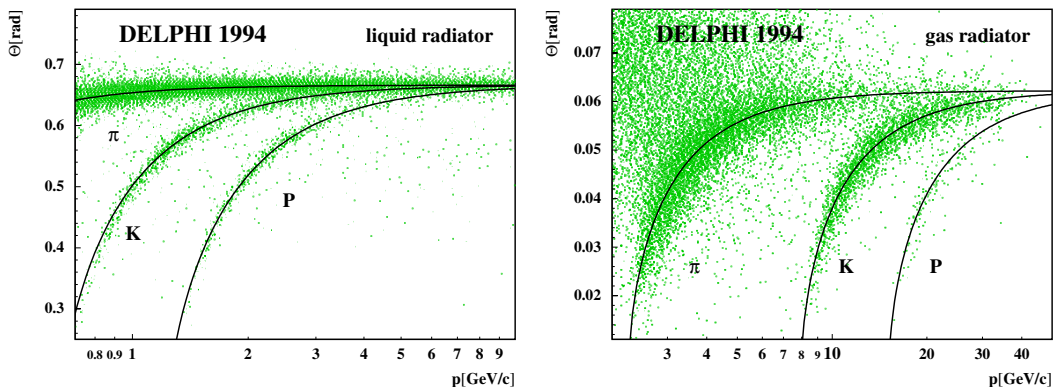


Figure 7.2: The Cherenkov angle versus the particle momentum as measured by the liquid (left) and gas radiators (right) in the DELPHI barrel RICH. The lines represent the expectation for pions, kaons and protons. From [41].

Particle identification in the RICH detectors

By using the combination of two different Cherenkov radiators as outlined in Section 3.2.3, the DELPHI RICH system is able to provide charged particle identification for protons, pions and kaons in a momentum range from 0.7 GeV/c up to 25 GeV/c. The mean Cherenkov angle and the number of photons are reconstructed by the RIBMEAN package [63], which performs an iterative clustering algorithm searching for peaks in the θ_c -distribution of a given track. For each of the five particle hypotheses (e , μ , π , K, p), a cluster candidate is formed from the set of photons. Hereby the photons are weighted according to their signal-like property, i.e. photons

in a region of overlap receive lower weights than isolated ones, thereby avoiding ambiguities. The mean Cherenkov angle is then obtained from the cluster candidate with the highest number of weighted photons, yielding a precision of 13.3 mrad for the liquid radiator and 4.3 mrad for the gas radiator [29]. The mean Cherenkov angle is plotted against the measured momentum in Fig. 7.2 for a subset of the data of 1994 and for both liquid and gas radiators. On the basis of these distributions, the software package NEWTAG transforms the RIBMEAN information into particle identification and quality variables. It combines data from both radiators, possibly adding veto information (Eq. 3.4) for a given particle hypothesis [64].

Combined hadron identification

Additional particle identification information is obtained in DELPHI from the measurement of the specific energy loss by ionisation, dE/dx , which depends on the particle mass and momentum via the Bethe-Bloch formula. Particles crossing the DELPHI TPC transfer energy to the ionised electrons, which drift to the TPC end plates where they are detected by sense wires. Their pulse height information provides the sensitivity to the dE/dx of different kinds of particles. It is analysed taking into account its statistical distribution, additional quality information and a careful calibration. The resulting resolution in the dE/dx allows to separate pions, kaons and protons at low momenta, adding to the particle identification capability of the liquid RICH and extending it down to $p > 0.2 \text{ GeV}/c$.

The various sources of particle identification information are combined using the MACRIB package, a tool with separate Neural Networks to tag kaons and protons [65]. It tags for example K^\pm with an efficiency of 90 % (70 %) with a background contamination of 15 % (30 %) for the range $p < 0.7 \text{ GeV}/c$ ($p > 0.7 \text{ GeV}/c$).

Lepton identification

An electron identification is performed using a Neural Network combining spatial and energy information from the HPC, tracking info, the dE/dx from the TPC, and searches for kinks in the track in known layers of material and for photons radiated tangentially in them. The most important inputs are in detail:

- Contrary to pions and other hadrons, electrons deposit nearly their entire energy in the electromagnetic calorimeter. The quotient of energy (measured by the HPC after correcting for photon radiation outside and other effects inside the HPC) and momentum (determined by the tracking system) is hence expected to be close to one, $E/p \simeq 1$.
- The three-dimensional shape of the shower is different for electrons and for pions. By construction, the HPC is able to reconstruct spatial parameters of the shower. The differences $\Delta\phi$ and Δz to the shower location predicted by the track extrapolation as well as the longitudinal shower evolution are provided as separation variables.
- The dE/dx measurement from the TPC provides an additional means of separating pions and electrons. The two kinds of particles can be separated with a significance of around 3σ at energies below 4.5 GeV and 2σ at energies of 20 GeV.

The electron identification Neural Network is a part of the ELEPHANT package [66]. It is set up as a feed-forward Network with one hidden layer, providing an output variable that is expected to be zero for pions and +1 for electrons.

Muons are identified by extrapolating tracks from the tracking chambers and associating them to possible hits in the muon chambers. The $\chi^2/n.d.o.f.$ of the fit of this association procedure [67] is used as a variable to separate real muons from background, e.g. from hadrons penetrating the iron of the HCAL. Different quality levels (from “very loose” via “standard” to “tight”) can be required for a track to be identified as muon, resulting in tightened criteria for hits used in the association fit procedure and for the χ^2 . A “standard” cut identifies $(86.1 \pm 0.2)\%$ of the muons with a hadron impurity of $(0.7 \pm 0.1)\%$ [29].

In addition, both electron and muon candidates in BSAURUS are required to have an energy larger than 3 GeV.

7.3 The Reference Axis

Each hemisphere in BSAURUS has associated with it two axes: the thrust axis and the reference axis. As detailed in Chapter 5, events are split into two hemispheres by the plane perpendicular to the *thrust axis*. Mainly due to the presence of gluon radiation, however, the thrust axis is not necessarily a good first approximation of the B direction of flight. Therefore, a *reference axis* is defined in each hemisphere along a jet reconstructed via the routine LUCLUS [15]. According to simulation studies, using LUCLUS with p_{\perp} as the distance measure and with the cutoff parameter $d_{\text{join}} = 5.0 \text{ GeV}$ gave the best reconstruction of the initial b-hadron direction. For the 16% of all cases when two or more jets are reconstructed per hemisphere, the situation is more complicated:

- If one of the two or more jets is the highest energy jet in the entire event, it is selected as the b-jet.
- Otherwise, the B-TAG’s lifetime probability at the jet level (Eq. 6.3) is used to discriminate the b-jet from the gluon jet.
- If no jet in the hemisphere is b-tagged ($P_{\text{J}}^+ < 0.05$), the one with the higher energy provides the reference axis.

With this scheme, the probability of correctly selecting the two b-jets in a three-jet event is about 70% [68].

This reference axis is then used to define the longitudinal momentum component and compute the track rapidities as already defined in Eq. 6.4. In the computation, identified particles were assigned their respective masses while all other charged particles were assigned a pion mass. Similar to its application in the combined b-tagging, the rapidity distinguishes B decay tracks by their high mean value from fragmentation tracks. It is therefore used at a stage before the more sophisticated Neural Networks are applied and by itself serves as a useful input to the auxiliary Networks operating on the level of tracks, such as the TrackNet (see Section 7.5).

7.4 Secondary Vertex Finding

Obtaining a charge tag in the hemisphere under consideration requires the presence of a secondary vertex, which is reconstructed in a two-stage iterative method. The first stage selects tracks with quality criteria similar to those in Table 6.1 and discriminates the tracks originating from the secondary vertex from fragmentation tracks by using lifetime and kinematic information as well as particle identification. Starting from this track list, the secondary and primary vertex positions are simultaneously fitted in three dimensions, using the event primary vertex as a starting point and constrained to the flight direction of the b-hadron. Hereby the flight direction is obtained via the “rapidity algorithm”, which sums up the particle four-momenta, (\vec{p}_i, E_i) , for tracks with rapidity $y > y_{\text{cut}}$. If the fit has not passed certain convergence criteria, the track making the largest χ^2 contribution is ignored and the fit repeated in an iterative procedure. Once a convergent fit has been attained, the second stage involves an attempt to rebuild and extend the lists of tracks in the fit using as discriminator the output of an interim version of the TrackNet. Tracks that have not passed the initial selection criteria, but are nevertheless consistent with originating from one of the vertices, are iteratively included in this stage, and retained if the new fit converges.

7.5 Auxiliary Neural Networks

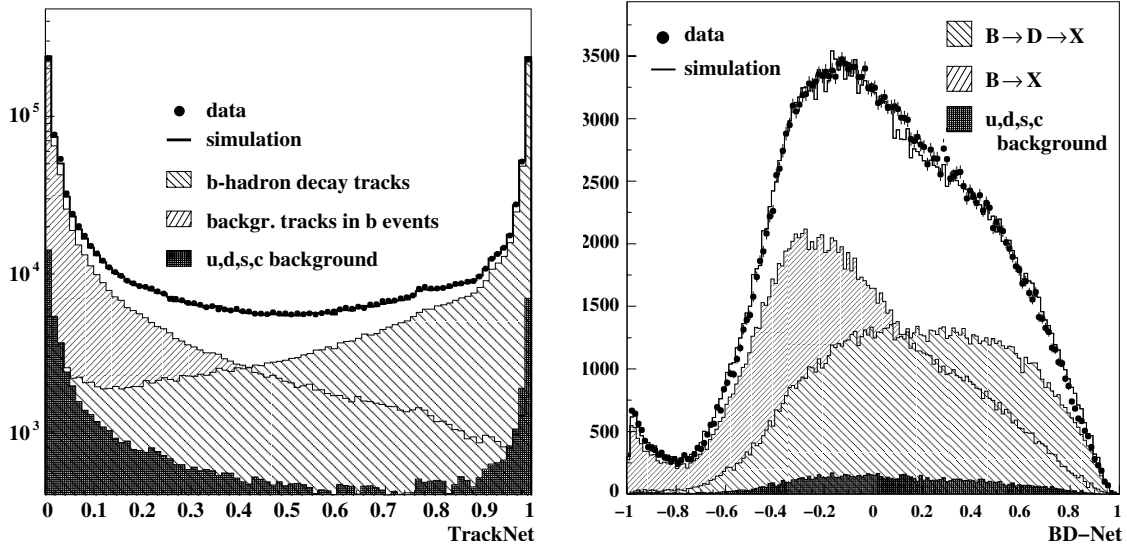
TrackNet

A Neural Network called TrackNet provides a probability for each track in a hemisphere to originate from a weakly decaying b-hadron. The Network needs a reconstructed secondary vertex to be present and uses the b-hadron four-vector supplied by the rapidity algorithm. The separation from tracks originating from the event PV relies on a variety of inputs like particle rapidity, lifetime probabilities for primary and secondary vertices and additional kinematic information.

Fig. 7.3(a) shows the TrackNet output distribution for real compared to simulated tracks after a strong b event selection cut has been applied (combined tag $X_{\text{ev.}} > 0.3$ and $|\cos \theta_{\vec{F}}| < 0.65$, from [68]). Charged particles produced in the b-hadron weak decay chain form the signal class (output +1) during the training of the network, while the background (output 0) consists of everything else in b events, such as fragmentation tracks and decay products of excited b-hadrons. As emphasised by Fig. 7.3(a), the TrackNet supplies a very powerful identification of b-hadron decay products. The shape of the output is well predicted by simulation. Like all plots in this chapter, the distributions for data and simulation have been normalised to the same number of entries. The signal-like spike in the u, d, s, c background is produced by D decay products in charm events, which represent $\sim 80\%$ of the background events after the b-tagging cut.

BD-Net

In addition to the direct decay products of the b-hadron, the TrackNet inevitably also selects tracks originating from the subsequent D cascade decay point. When such tracks are present, the reconstructed B decay point is biased in the direction of the D vertex and has a worse resolution. Therefore, a dedicated Neural Network



(a) The TrackNet. It identifies B decay products with high purity and efficiency.

(b) On the set of identified B decay products, the BD-Net separates B \rightarrow D \rightarrow X cascade decays tracks from direct B tracks.

Figure 7.3: Some auxiliary Neural Networks in BSAURUS; from [57].

called BD-Net uses mainly decay vertex and kinematic information in a given jet to separate particles from the weak B decay from those from the subsequent cascade D decay. By design it acts on tracks with a TrackNet output value larger than 0.5. The target value for particles from B decay is -1 , while for particles from the following D decay it is $+1$. Fig. 7.3(b) shows the BD-Net variable for data compared to the simulation for the same configuration as the TrackNet in Fig. 7.3(a). It is evident that the agreement between data and simulation is not as good as it is e.g. with the TrackNet. This is assumed to be related to the greater sensitivity to b- and c-hadron physics modelling [68]. The BD-Net is used for ordering tracks that enter secondary vertexing algorithms or in the form of a ratio of BD-Net variables, but not as a variable that is explicitly cut on.

EB-Net

Even the energy of the weakly decaying b-hadron is reconstructed via a Neural Network, whose output nodes represent discretised B energy thresholds. Each output O_i separates hemispheres with E larger than a threshold value $E_B(O_i)$ from those with $E < E_B(O_i)$. Non-aequidistant threshold values are chosen, which maintain a constant number of hemispheres between adjacent thresholds. In addition, the entire Network is constructed in a way that a Bayesian interpretation can be applied to its output vector, effectively yielding a probability density function for the energy on a hemisphere-by-hemisphere basis. Different kinematic estimators of the B energy together with measures of the estimated quality of these estimators form the inputs to the EB-Net, which yields a B energy resolution of 2.5 GeV in the best case. Further information on the EB-Net and its performance is given in reference [68]. The reconstructed B energy supplies hemisphere quality information to various Networks in BSAURUS.

7.6 The Hemisphere Charge Tagging Neural Network

7.6.1 The Construction of the b-Hadron Flavour Tags

The approach to forming the b-hadron flavour tags works by constructing first a conditional probability on the track level: the probability $P^{time}(same\ Q|B)$ for a given charged particle to have the *same* sign as the b quark charge in a given b-hadron type (B^0 , B^+ , B_s and b-baryon). It is defined for both the *time* of fragmentation (i.e. production) and the time of decay.

This goal is achieved by training dedicated Neural Networks for each of the four b-hadron types. In addition, two sets of Networks are produced, one trained only on tracks originating from the fragmentation process, and the other trained only on tracks originating from the weak b-hadron decay. The Networks are defined in a way that the target output value is +1 (−1) if the charge of a particle is correlated (anti-correlated) to the b quark charge. A set of predefined input variables is used to distinguish between them:

- The output from the TrackNet, which selects particles from secondary vertices.
- The particle identification network output variables from MACRIB as described in Section 7.2.
- B-D separation.

From the BD-Net output, a second variable:

$$\frac{\text{BD-Net} - \text{BD-Net}^{min}}{\Delta\text{BD-Net}} \quad (7.3)$$

is constructed to isolate particles from D decays further. BD-Net^{min} is the minimum BD-Net value of all charged particles in the hemisphere above a TrackNet value of 0.5. $\Delta\text{BD-Net}$ is the difference between the maximum and minimum value of BD-Net for all charged particles in the hemisphere.

- Particle variables.

Further variables separate particles from the primary interaction from B decays. The energy of the particle and any ambiguities in the track reconstruction are input to the Networks. In addition, particles are boosted into the estimated B candidate rest frame. In this frame the momentum and the angle of the particle with respect to the B direction of flight are calculated, providing sensitivity to the characteristically large p_{\perp} of B decay products.

- Hemisphere quality variables.

For each hemisphere a set of additional variables characterise the quality of the B candidate:

- the ratio of the reconstructed B candidate energy (from the EB-Net) to the LEP beam energy,
- the invariant mass of the particles at the reconstructed B vertex,
- the χ^2 probability of the fit for the B decay vertex,
- the uncertainty on the vertex charge measurement,

- the number of charged particles assigned to secondary vertices in the hemisphere with TrackNet above 0.5,
- the hemisphere rapidity gap between the particles of highest rapidity below a TrackNet cut at 0.5 and that of smallest rapidity above this cut;
- and the number of particles in the hemisphere with ambiguities in reconstruction.

Only the Networks for distinguishing the decay flavour use all input variables described above. The lepton flavour identification and B-D separation variables do not depend on the flavour state at the time of fragmentation and are therefore not used in the training of the fragmentation flavour networks.

The particle correlation conditional probabilities, $P^{time}(same\ Q\ |B)$, for the fragmentation and the decay flavour are then combined using a likelihood ratio to obtain a flavour tag for a given hemisphere:

$$F_B^{time} = \sum_{\text{particles}} \ln \left(\frac{1 + P^{time}(same\ Q\ |B)}{1 - P^{time}(same\ Q\ |B)} \right) \cdot Q \quad . \quad (7.4)$$

Here B is either a B^+ , B^0 , B_s or b-baryon and *time* stands for *fragmentation* or *decay*. Q is the particle charge. Depending on the hypothesis considered, a different selection is applied for particles entering the summation. For the fragmentation flavour all tracks with TrackNet < 0.5 are considered, while for the decay flavour a particle must satisfy TrackNet ≥ 0.5 . The output of the b-hadron flavour tags is shown in Fig. 7.4 for the different fragmentation and decay tags.

7.6.2 The Jet Charge

The most simple approach to measuring the quark charge is to sum up the charges of all particles in a jet. Due to charge conservation in the fragmentation and subsequent decays, ideally, this would yield the quark charge on average. The limited detector acceptance and effects from fragmentation and decays however introduce strong fluctuations and biases, rendering this idea impossible. R.D. Field and R.P. Feynman [17] therefore suggested a momentum-weighted charge sum, which exploits the *leading particle effect*, the observation that the particle with the highest momentum is likely to carry the initial quark while soft particles from fragmentation are nearly irrelevant. After further studies it turned out that the momentum fraction $|\vec{p}_i \cdot \vec{T}|$ longitudinal to the thrust axis used as a weight provided the best results [17]. This idea has led to the *jet charge*, which is defined as:

$$Q_J = \frac{\sum_{\text{particles}} |\vec{p}_i \cdot \vec{T}|^\kappa \cdot Q}{\sum_{\text{particles}} |\vec{p}_i \cdot \vec{T}|^\kappa} \quad , \quad (7.5)$$

where the sum is over all charged particles in a hemisphere. Although the jet definitions in this analysis are the hemispheres, it is called jet charge to avoid confusion with the hemisphere charge tagging network and to some extent also for historical reasons. The internal parameter κ fine-tunes the relative weights of fast and slow tracks. A boundary value of $\kappa=0$ produces an unweighted mean charge, while for the limit $\kappa \rightarrow \infty$ only the charge of the track with the highest longitudinal momentum

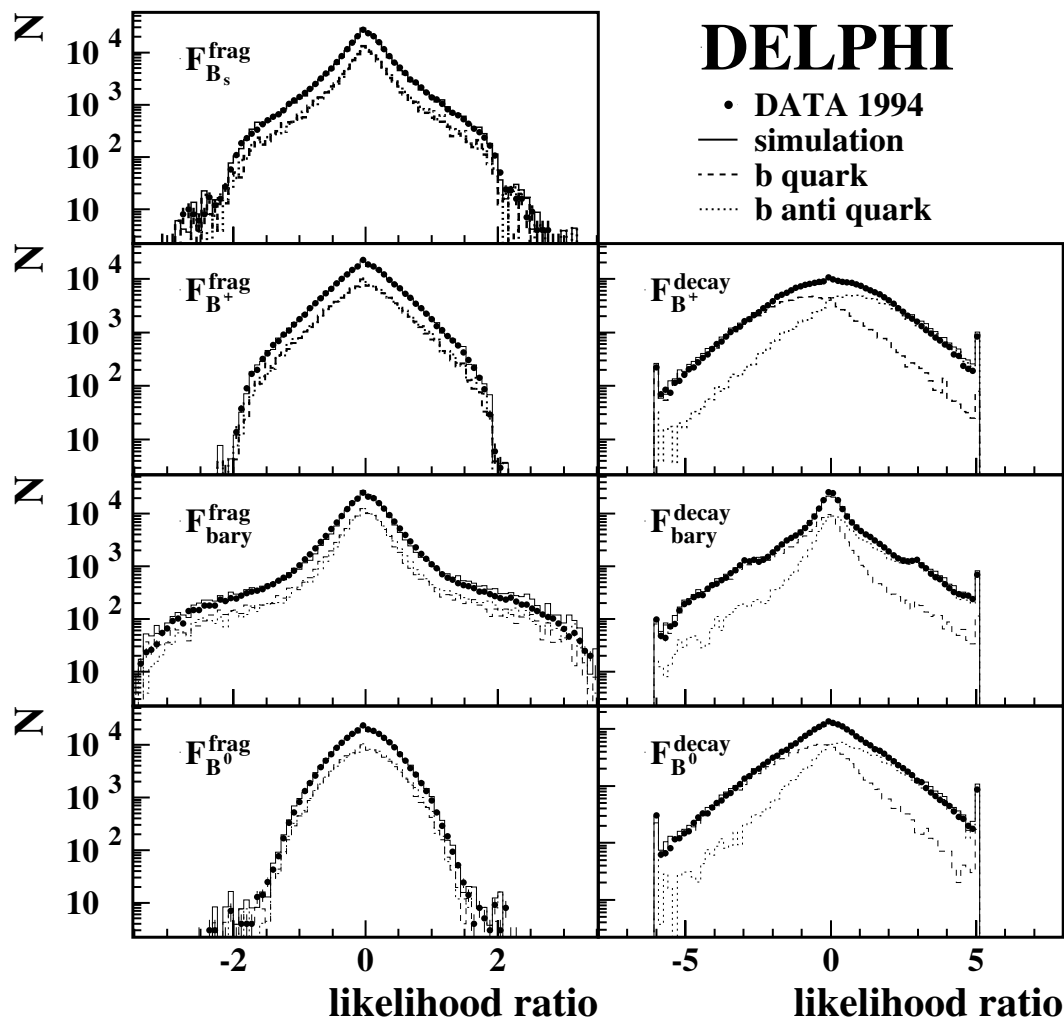


Figure 7.4: The b-hadron flavour tag for the time of the fragmentation for the B^+ , B^0 , B_s and b-baryon hypothesis and for the time of the decay for the B^+ , B^0 and b-baryon hypothesis. Shown is the comparison between data and simulation for the data of 1994.

is taken into account. A weight of $\kappa \lesssim 1$ usually provides the best sensitivity to the quark charge, slightly depending on the quark type and the B hadron hypothesis. The distributions of the jet charge for two different values of the internal parameter, $\kappa = 0.3$ and $\kappa = 0.6$, are displayed in the upper part of Fig. 7.5. Clearly visible is the good capability of separating quark from anti-quark, suffering however from a long tail of jet charges with a negative correlation to the quark charge. The jet charge has been the basic ingredient to earlier measurements of the forward-backward asymmetry like [69], because it provides a sufficient and universal charge reconstruction, which requires neither a reconstructed secondary vertex nor Neural Network techniques.

Although the combination with the vertex charge and other variables in BSAURUS, like the b-hadron flavour tags, leads to a much better performance than the jet charge alone, the jet charge still provides charge information in the case of neutral mesons, for which the vertex charge usually fails to do so. An example is given by the

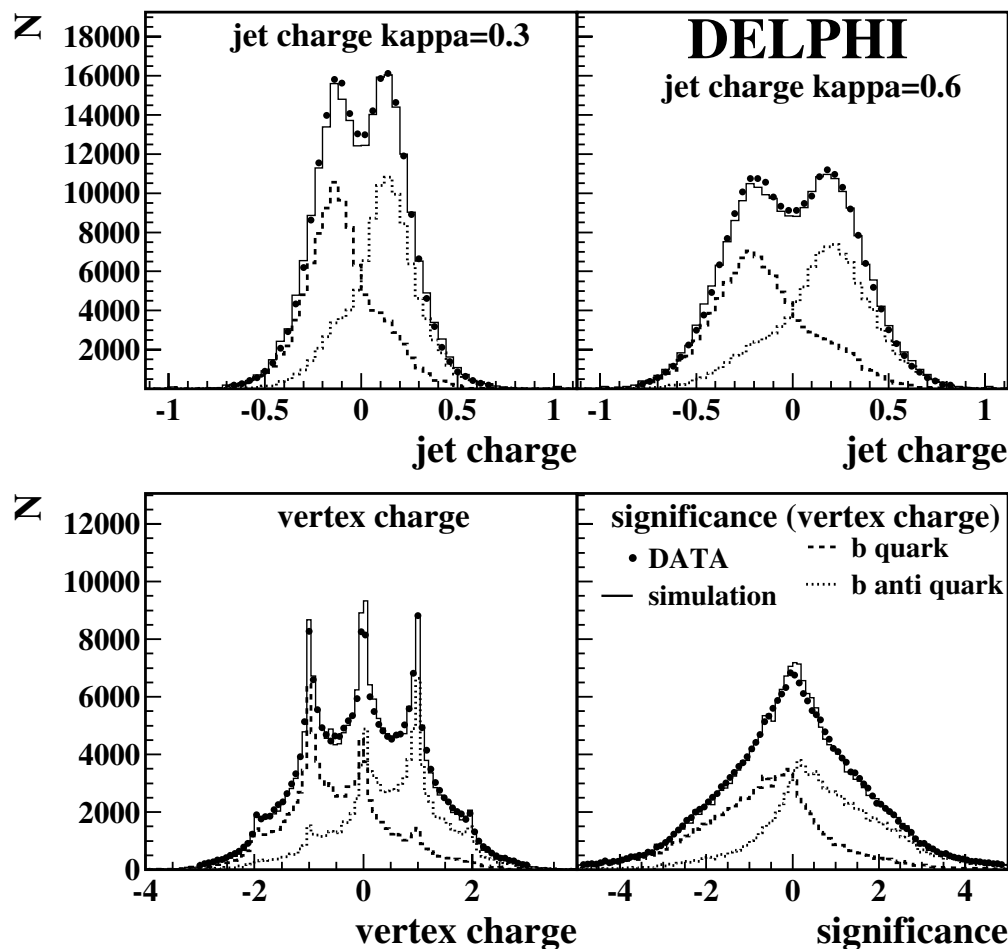


Figure 7.5: The jet charge information for $\kappa = 0.3$ and 0.6 (upper plots) and the vertex charge and its significance (lower plot). Shown is the comparison between 1994 data and simulation for all hemispheres that are both b and charge tagged.

inclusive decay of B_d^0 to $K^-\pi^+$. The b in the B_d^0 has a negative charge sign, which is transferred to the kaon. The system of $K^-\pi^+$ is neutral, so that the charge sum at a possibly reconstructed secondary vertex would not give any clue. Back in the lab frame, where the jet charge is measured, the high boost of the B hadron leads to a higher momentum for the heavier particle, the K^- . As a consequence, the jet charge shows a residual sensitivity to the correct b charge. By contrast, the leading particle effect is not present any more for the B_s^0 meson. Here the corresponding decay leads to a system of two kaons, K^-K^+ , with on average equal momenta in the lab system.

In general, the jet charge for signal b quarks as well as for background light flavours is effected by processes in the hadronisation and decay phases and therefore very sensitive to their modelling in the simulation.

- The radiation of gluons during the parton shower shifts a possibly large fraction of the quark momentum to a set of particles with zero total charge. In addition, it distorts the orientation of the quark jets with respect to the thrust axis, affecting the longitudinal momentum weight in the jet charge. Both effects reduce the correlation to the primary quark charge.

- The question whether the leading particle is produced as charged or neutral particle is decided in the individual fragmentation process, when a newly created quark (pair) forms a colour-neutral state with the primary quark. On average, however, differences between u-type and d-type primary quarks become visible. For example, the possibility to create s quarks in the fragmentation leads to a stronger correlation for u-type quarks, while it reduces the chance to produce charged mesons out of primary d-type quarks.
- Finally the decay into stable hadrons can have an impact on the leading particle effect. While in the case of B_d^0 mesons the decay chain can end in a leading particle with the correct charge information, the leading particle effect is lost or even reversed in the decay of excited D mesons. An example is the quite likely decay chain

$$D^{*+} \rightarrow D^0 \pi_{\text{slow}}^+ \rightarrow (K^- \pi^+) \pi_{\text{slow}}^+$$

where the leading particle would be the K^- , and the slow π^+ carries away the charge information. As a result, the mean correlation to the quark charge is expected to be relatively poor for primary c quarks. Similar mechanisms occur in the production and decay of baryons.

The above list gives some examples of a wide range of physical properties that determine the charge information contained in the jet charge. Even a complete misidentification of the quark charge sign as observed in the overlapping tails of the jet charge distribution in Fig. 7.5 can happen at a stage where additional effects from the detector acceptance were not yet taken into account. The list also stresses the importance to model these properties with high accuracy in the simulation. The comparison to the simulated jet charge in Fig. 7.5 shows that the simulation predicts the shape well, also while evolving with the internal parameter κ . However, small discrepancies remain in the width of the distributions.

7.6.3 The final hemisphere charge tagging Neural Network $flav_{\text{hem}}$

Nine different inputs for the final hemisphere charge tagging Neural Network³ are constructed. The first set of inputs is a combination of the fragmentation and decay b-hadron flavour tags multiplied by the probabilities for that b-hadron type:

- (1) $F_{B_s}^{\text{frag.}} \cdot P(B_s)$
- (2) $\left(F_{B^+}^{\text{decay}} - F_{B^+}^{\text{frag.}}\right) \cdot P(B^+)$
- (3) $\left(F_{\text{baryon}}^{\text{decay}} - F_{\text{baryon}}^{\text{frag.}}\right) \cdot P(\text{baryon})$
- (4) $\left(F_{B^0}^{\text{decay}} \cdot \left(1 - 2 \sin^2 \left(\frac{\Delta m_d}{2} \cdot \tau_{\text{rec}}\right)\right) - F_{B^0}^{\text{frag.}}\right) \cdot P(B^0)$

Here τ_{rec} is the reconstructed proper B lifetime in the hemisphere under consideration. The construction takes the effective B^0 oscillation frequency into account which affects the charge information in the hemisphere. It is assumed to be $\Delta m_d = 0.474/\text{ps}$. This is not possible for the case of B_s , where the oscillations are so fast that at the time of decay a 50-50 mix of B_s and \bar{B}_s remains.

³In Ref. [57] this Network is described under the name ‘‘Same Hemisphere Production Flavour Network’’

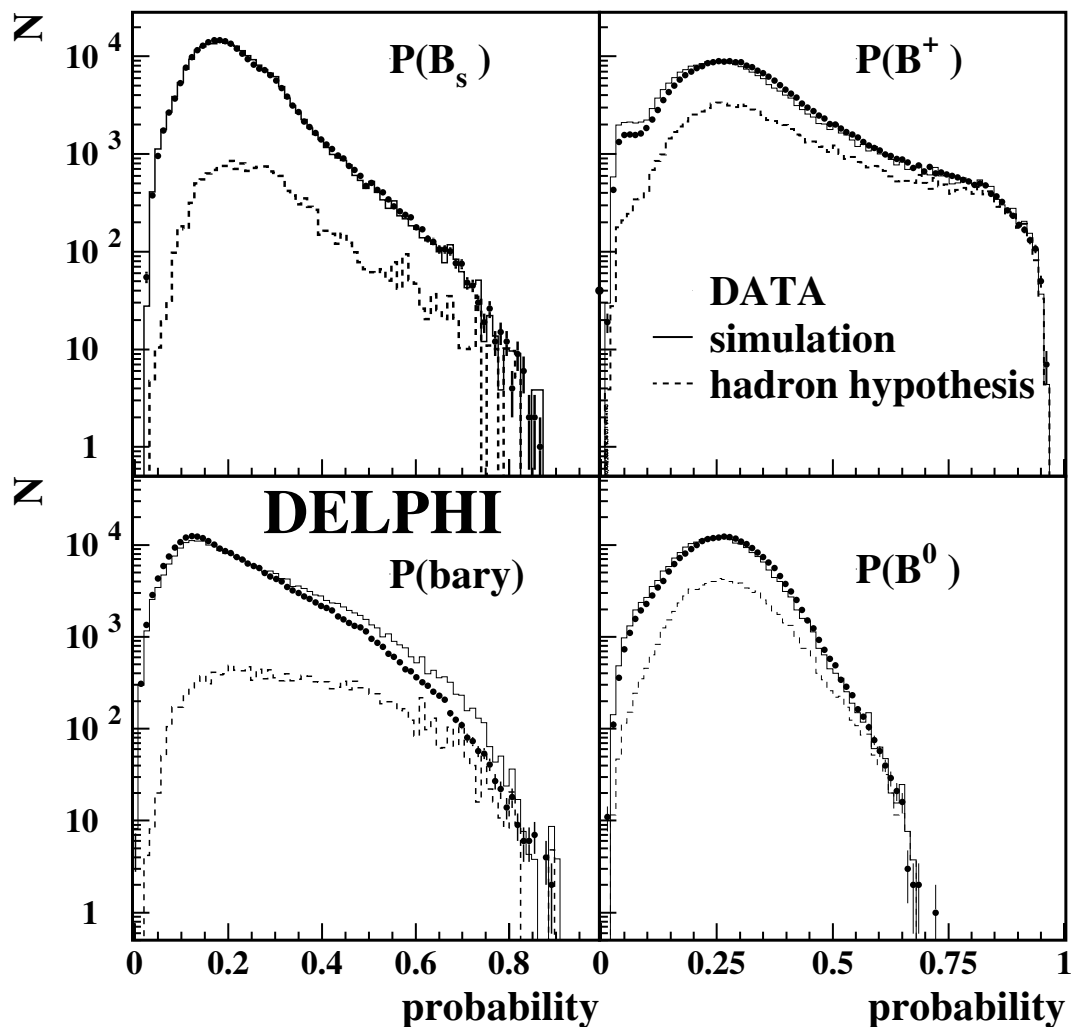


Figure 7.6: The hemisphere constructed probabilities for the different b hadron types B^+ , B^0 , B_s and b-baryon obtained from the BSAURUS B species identification Network. Shown is the comparison between data and simulation for the data of 1994.

The $P(B)$ factors are the outputs of a dedicated B species identification Network and represent probabilities that the hemisphere in question contains a weakly decaying b-hadron of a particular type B. They are constructed such that on the average their sum is 1, but as they are used to form a new Network input this constraint is not applied on a single measurement. The B species probabilities are shown in Fig. 7.6. The input variables 1-4 are shown in Fig. 7.7.

The remaining inputs are:

- (5-7) The jet charge as described in Section 7.6.2. The optimal choice of the free parameter κ depends on the type of b-hadron under consideration. Therefore a range of values ($\kappa = 0.3, 0.6, \infty$) is used, where the last one corresponds to taking the charge of the highest momentum particle in the hemisphere.
- (8) The vertex charge is constructed using the TrackNet value as a probability for

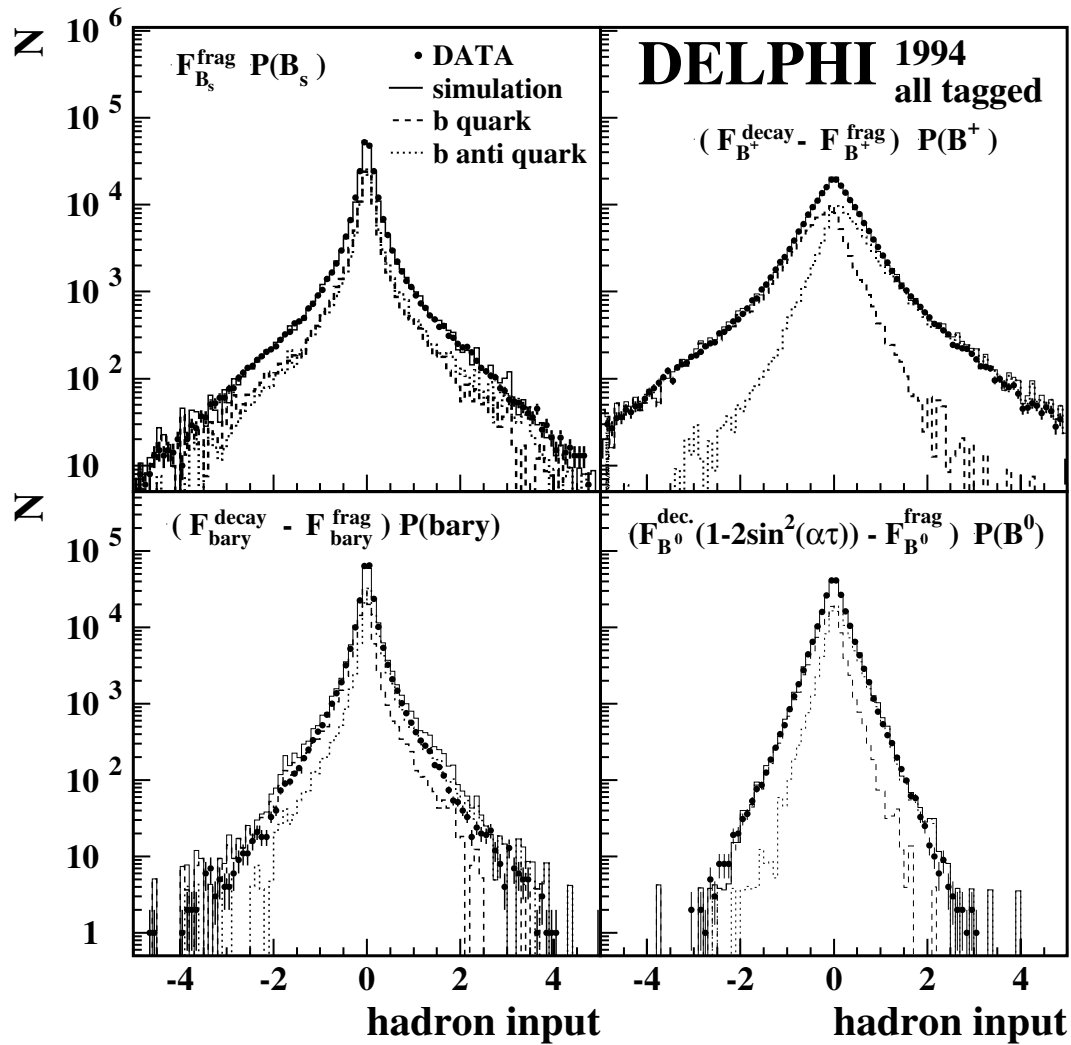


Figure 7.7: The four combined hemisphere charge probabilities for the B^+ , B^0 , B_s and b-baryon hypothesis. Shown is the comparison between data and simulation for the data of 1994.

each track to originate from the b-hadron decay vertex. The weighted vertex charge is formed by:

$$Q_V = \sum_{\text{particles}} \text{TrackNet} \cdot Q \quad . \quad (7.6)$$

- (9) The significance $Q_V/\sigma(Q_V)$ of the vertex charge calculated using a binomial error estimator:

$$\sigma(Q_V) = \sqrt{\sum_{\text{particles}} \text{TrackNet} \cdot (1 - \text{TrackNet})} \quad . \quad (7.7)$$

As an example the distributions of the jet charge for $\kappa = 0.3$ and 0.6 and of the vertex charge and its significance are shown in Fig. 7.5 for data and simulation.

In addition to the charge discriminating variables described above, use is made of ‘quality’ variables, e.g. the reconstructed energy of the B candidate in the hemi-

sphere. These inputs supply the network during the training process with information regarding the likely quality of the discriminating variables, and are implemented in the form of weights to the turn-on gradient (or ‘temperature’) of the sigmoid function used as the network node transfer function. A possible dependence of the above inputs on the detector configuration in the barrel and the forward region has been investigated in [55]. Differences in the width of the distributions and in the predicted capability of separating positive from negative charge were observed, reflecting the better momentum resolution and secondary vertex reconstruction in the central part of the detector. By contrast, the agreement between data and simulation turned out to be of the same good quality in the central and the forward part.

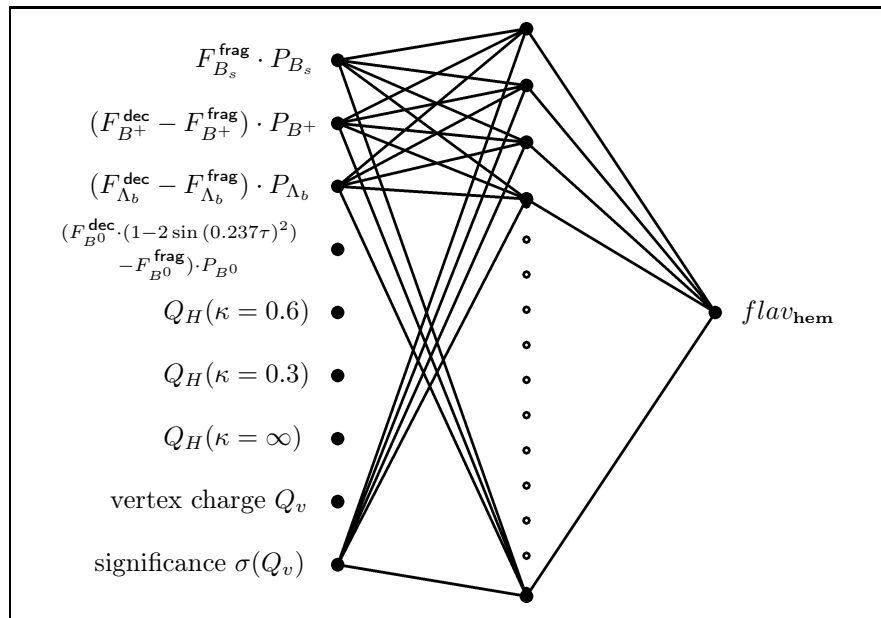


Figure 7.8: Structure of the hemisphere charge tagging Neural Network, $flav_{\text{hem}}$. The hidden layer has ten nodes, which are fully connected to each input and the output nodes. For simplicity, only a part of the connections is shown.

The architecture of the final hemisphere charge tagging Neural Network, $flav_{\text{hem}}$, is illustrated in Fig. 7.8. It consists of a standard feed-forward algorithm with nine input nodes, one for each of the variables defined above, a hidden layer containing 10 nodes and one output node. During the training, the target values at the output node for one hemisphere were -1 for a b quark or $+1$ for a b anti-quark.

The output distribution of the hemisphere charge Neural Network is discussed in detail in the following two Figures, 7.9 and 7.10. The first shows the $flav_{\text{hem}}$ distribution for the data of 1994 split into the four event samples with increasing b purity, as used in the fit to A_{FB}^b . The data points are compared to the simulation. The contributions from hemispheres containing b quarks and anti-quarks are shown separately for the simulation to illustrate the excellent charge tagging power, i.e. the capability of separating quark from anti-quark. Apart from the increasing b event fraction, an increase of the tagging power with growing purity is also clearly visible. The small discrepancy between data and simulation in the width of the distribution is pronounced most strongly at highest b purities, indicating a small difference

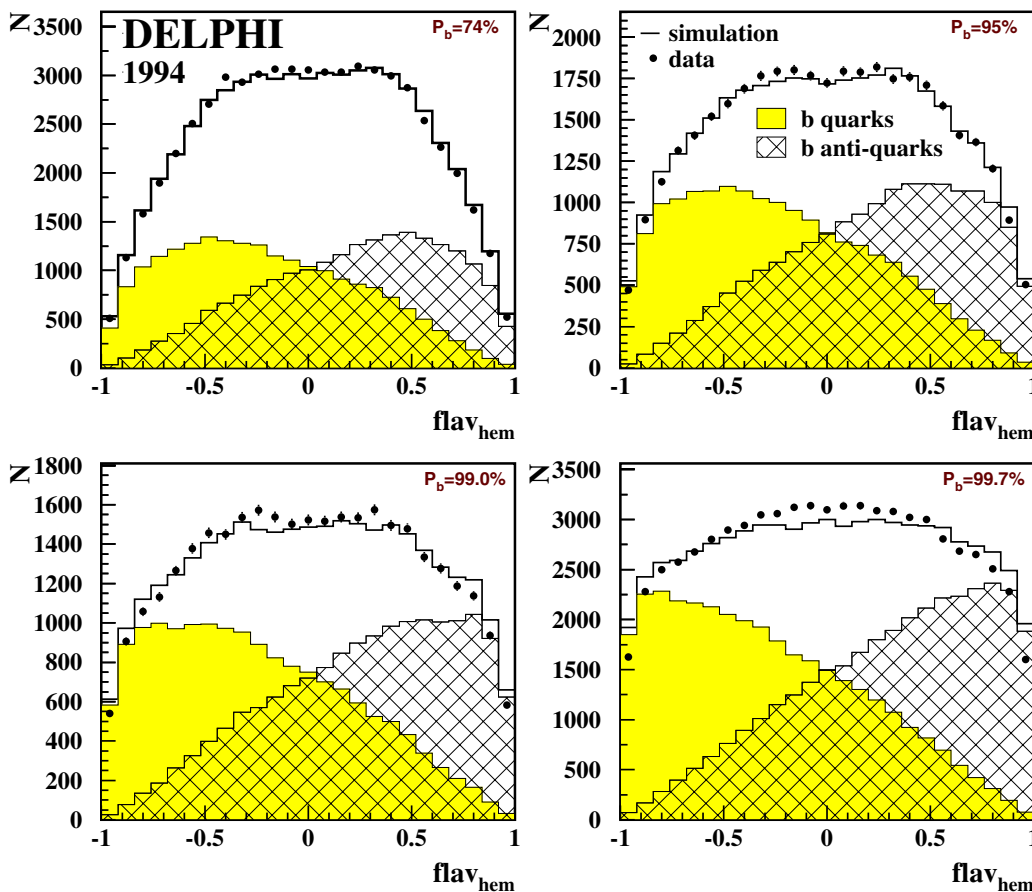


Figure 7.9: Comparison between data and simulation for the hemisphere charge tagging Network output, $flav_{hem}$, for the data of 1994. The distribution is shown for each of the four b-purity enhanced samples. The b/\bar{b} contributions are normalised to the b purity.

in the charge tagging power. This will be discussed in detail under the topic of self-calibration in the A_{FB}^b measurement in Sections 8.3.1 and 8.3.3.

The second set of plots in Fig. 7.10 shows the $flav_{hem}$ output distribution for every year 1992, 1993, 1994, 1995 and “1996-2000”, this time integrated over the four b-tagged samples. It reveals that the tagging power is also a function of the Vertex Detector set-up, as outlined in Section 3.2.1 and observed in a similar way during the b-tagging calibration in Section 6.4. The agreement between data and simulation in the early years 1992 and 1993 suffers mainly from the absence of $B^0 - \bar{B}^0$ oscillation modelling in the corresponding simulation. Again, the year-by-year differences in the agreement are fully taken into account in the analysis by performing the self-calibration independently on every single year and b-purity sample.

In the analysis, a hemisphere is defined as charge tagged if a secondary vertex is sufficiently well reconstructed to produce a Neural Network output $flav_{hem}$ and if the absolute value $|flav_{hem}|$ exceeds the working point cut of 0.35 (0.30 in case of 1992+93 data). This working point is indicated in Fig. 7.10 and was chosen to minimise the total relative error of the measured b asymmetry on simulated data.

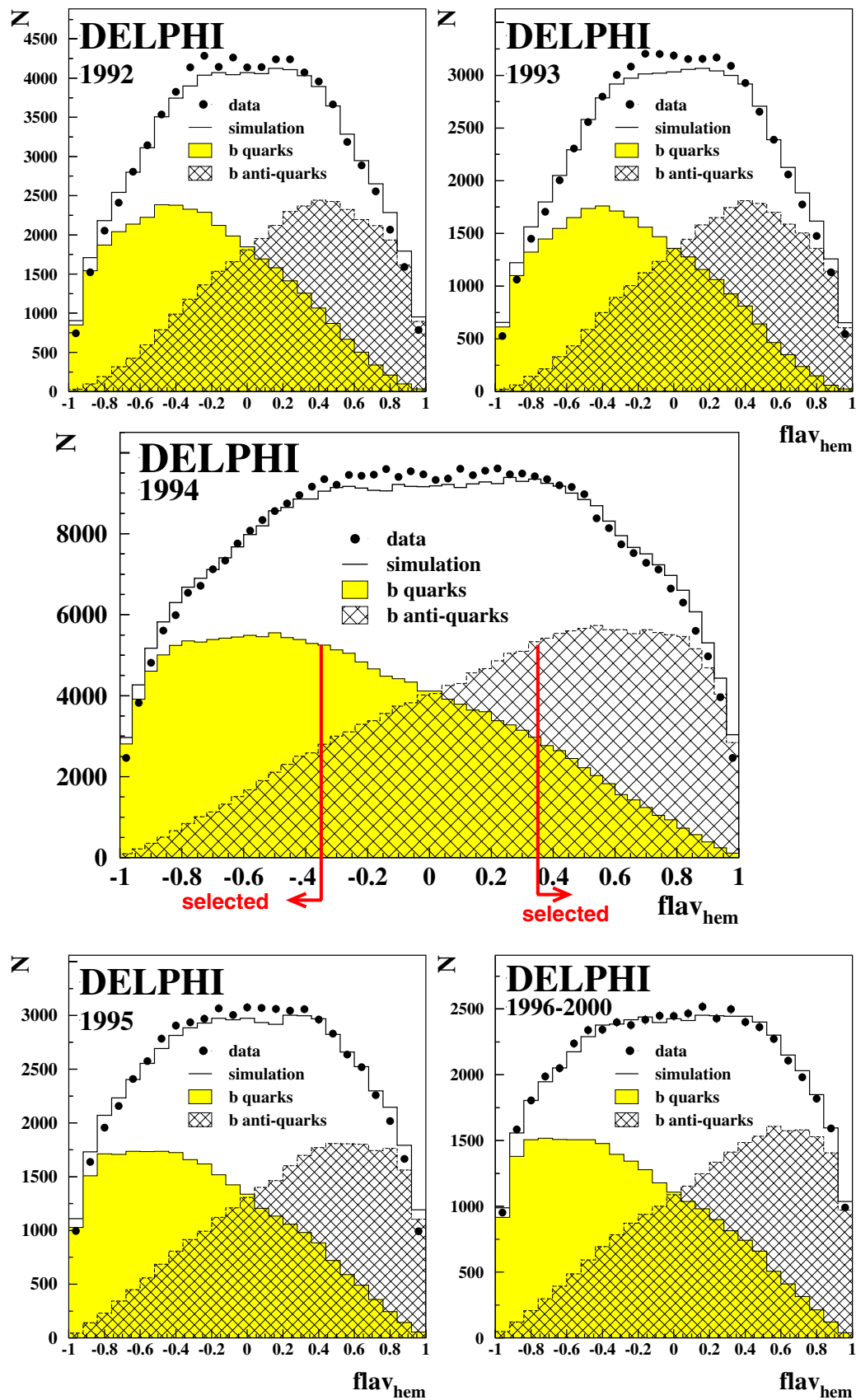


Figure 7.10: Comparison between data and simulation for the hemisphere charge tagging Neural Network output, $flav_{hem}$, for the years 1992 to 2000. Hemispheres from all b-enhanced samples were integrated, resulting in a b purity of 90%.

Chapter 8

The Measurement of the b Quark Forward-Backward Asymmetry

In this chapter the self-calibrating method to extract the b quark forward-backward asymmetry will be explained. It includes the technique to determine the tagging probabilities for b quark events as well as for the main background of c quark events. In this context, charge correlations between the two event hemispheres are examined. QCD radiative corrections to the measured asymmetry are discussed and technical details on the fit method given before the final results for A_{FB}^{b} are presented.

8.1 The method to extract the b asymmetry

Single and double charge tagged events

The Neural Network charge tag is used to reconstruct the charge sign of the primary b quark on a hemisphere-by-hemisphere basis. Different categories are distinguished according to the configuration of the two charge-signed hemispheres in an event.

In *single charge tagged* events the orientation of the primary quark axis is obtained from the sign of the tagged hemisphere's Neural Network output. The quark axis is forward oriented ($\cos \theta_{\vec{T}} > 0$) if a forward hemisphere is tagged to contain a b quark or a backward hemisphere is tagged to contain a b anti-quark. Otherwise the quark axis is backward ($\cos \theta_{\vec{T}} < 0$) oriented.

One needs to distinguish two categories of events if both hemispheres are charge tagged. Events with one hemisphere tagged as quark and the other as anti-quark belong to the category of *unlike-sign double* charge tagged. Here the event orientation is determined by either hemisphere. The situation is similar to single hemisphere events, but the additional second hemisphere charge tag increases the probability to identify the sign of the quark charge correctly. By contrast, events for which both hemispheres are tagged to contain quarks (or both anti-quarks) do not have a preferred orientation. As the quark final state is known to be $\text{b}\bar{\text{b}}$, one of the two hemispheres must be mis-tagged. These *like-sign* events are used to measure the charge tagging probability.

The observed asymmetry

The difference between the number of forward and backward events normalised to the sum is the forward-backward asymmetry. It is for single hemisphere tag events:

$$A_{\text{FB}}^{\text{obs}} = \frac{N - \bar{N}}{N + \bar{N}} = \sum_{f=d,u,s,c,b} (2 \cdot w_f - 1) \cdot A_{\text{FB}}^f \cdot p_f \cdot \eta_f \quad , \quad (8.1)$$

where

$$\begin{aligned} N &= \text{number of single charge tagged forward events,} \\ \bar{N} &= \text{number of single charge tagged backward events.} \end{aligned}$$

Similarly for the double charge tagged events:

$$A_{\text{FB}}^{\text{D,obs}} = \frac{N^D - \bar{N}^D}{N^D + \bar{N}^D} = \sum_{f=d,u,s,c,b} (2 \cdot w_f^D - 1) \cdot A_{\text{FB}}^f \cdot p_f^D \cdot \eta_f \quad , \quad (8.2)$$

where

$$\begin{aligned} N^D &= \text{number of double charge tagged forward events,} \\ \bar{N}^D &= \text{number of double charge tagged backward events.} \end{aligned}$$

The observed asymmetry is the sum of the contributions from b events and from c and uds background events. A_{FB}^f is the forward-backward asymmetry, p_f and p_f^D are the fractions for each flavour in the single and double unlike-sign tagged event categories. The η -term accounts for the differently signed charge asymmetries, $\eta_f = -1$ for up-type quarks and $\eta_f = 1$ for down-type quarks. The quantities w_f and w_f^D are the probabilities to identify the sign of the quark charge correctly in single and double tagged events.

The differential asymmetry

The differential asymmetry is insensitive to changes in the detector efficiency between different bins in polar angle, as long as the detector efficiency is charge-symmetric. Hence the measurement of the b asymmetry is done in consecutive intervals of $\cos \theta_{\vec{T}}$. According to the different VD set-ups, eight bins covering $\cos \theta_{\vec{T}} \in [0.0, 0.825]$ were chosen for 1992 and 1993, and nine bins covering $\cos \theta_{\vec{T}} \in [0.0, 0.925]$ for 1994 to 2000. The bins have a constant width of 0.1; only the highest bin has a width of 0.125. In each bin the observed asymmetry is given by replacing the forward-backward asymmetry A_{FB}^f in Eq. 8.1 and 8.2 by the differential asymmetry:

$$A_{\text{FB}}^{\text{f,diff}}(\cos \theta_{\vec{T}}) = \frac{8}{3} \cdot A_{\text{FB}}^f \cdot \frac{\cos \theta}{1 + \cos^2 \theta} \quad . \quad (8.3)$$

To extract A_{FB}^b all parameters of Equations 8.1 and 8.2 need to be determined bin by bin. The rates N , \bar{N} , N^D , \bar{N}^D are obtained from the data. The b purity, p_b , and the probability to correctly identify the b quark charge can also be extracted directly from data with only minimal input from simulation. This includes corrections due to the hemisphere correlations and light quark background for each bin. The determination of p_b and the measurement of $w_b^{(D)}$ and $w_c^{(D)}$ are discussed in the next sections.

The c quark background $w_c^{(D)}$ is calibrated by means of exclusively reconstructed D hemispheres as described in Section 8.3.3. The probability of identifying the quark charge on the small amount of light quark background is estimated from simulation using Eq. 8.6 for the single tagged and Eq. 8.7 for the double tagged events. The background forward-backward asymmetries for d , u and s quark events are set to the Standard Model values, and for c events the forward-backward asymmetry is set to its measured LEP value, $A_{\text{FB}}^c(91.260 \text{ GeV}) = 0.0641 \pm 0.0036$ [24]. It is extrapolated by means of ZFITTER to the DELPHI centre-of-mass energies, giving $A_{\text{FB}}^c = -0.0338$, 0.0627 and 0.1241 for peak-2, peak and peak+2 [9].

8.2 Calculation of the b Efficiency and Flavour Fractions

The selection of events in single and double charge tagged categories modifies the meaning of the selection efficiencies and flavour fractions calibrated in Section 6.3. The final selection efficiencies take into account the complete selection that requires both b -tag and charge tag in a given bin in $\cos\theta_{\bar{T}}$. The fraction of events selected in a given sample, \mathcal{F} , can be used to extract the b efficiency and purity directly from the data themselves, using

$$\epsilon_b(\text{cut}) = \frac{\mathcal{F}(\text{cut}) - R_c \times \epsilon_c(\text{cut}) - (1 - R_c - R_b) \times \epsilon_{\text{uds}}(\text{cut})}{R_b} \quad (8.4)$$

Here, ϵ_{uds} is the simulated selection efficiency for the light flavours while ϵ_c for charm events is obtained from the simulation which has been calibrated using the correction function from Section 6.4. The fractions of c and b events produced in hadronic Z decays, R_c and R_b , are set to the LEP+SLD average values of $R_c^0 = 0.1719 \pm 0.0031$ and $R_b^0 = 0.21644 \pm 0.00065$ (cf. Section 6.3). For the off-peak energy points the LEP+SLD on-peak R_q values are likewise extrapolated using ZFITTER.

The corresponding fractions, p_f , are then calculated for b , c and light flavours via:

$$p_f(\text{cut}) = \epsilon_f(\text{cut}) \times \frac{R_f}{\mathcal{F}(\text{cut})} \quad (8.5)$$

The combined data sample of single and unlike-sign double charge tagged events contains an average b fraction p_b of close to 90% after the complete selection. An overview of the b fractions in each year and bin in b -tag is given in Table 8.1.

	$-0.2 < x < 0.8$	$0.8 < x < 1.9$	$1.9 < x < 3.0$	$3.0 < x < \infty$
1992	0.787 ± 0.009	0.960 ± 0.012	0.992 ± 0.014	0.998 ± 0.014
1993	0.773 ± 0.011	0.956 ± 0.014	0.990 ± 0.016	0.998 ± 0.016
	$0.0 < x < 1.2$	$1.2 < x < 2.3$	$2.3 < x < 3.4$	$3.4 < x < \infty$
1994	0.712 ± 0.006	0.952 ± 0.009	0.989 ± 0.009	0.997 ± 0.006
1995	0.729 ± 0.011	0.952 ± 0.015	0.988 ± 0.016	0.997 ± 0.011
1996-2000	0.756 ± 0.013	0.964 ± 0.017	0.993 ± 0.017	0.998 ± 0.012

Table 8.1: The measured b purities, or fractions, for the different years and intervals in $x := b$ -tag. The purities found for the off-peak data match the corresponding peak values well within errors.

In Fig. 8.1 the $\cos\theta_{\bar{f}}$ dependence of the b efficiencies ϵ_b and ϵ_b^D and b purities p_b and p_b^D is shown. The b purity p_b^{same} of the like-sign double tagged events is also included, as it is important for the self calibration method Eq. 8.10. Both efficiency and purity are stable in the central region of the detector. At large $\cos\theta_{\bar{f}}$ the purity increases slowly for both categories of single and double tagged events. At the same time the b efficiency decreases with a fast drop for $\cos\theta_{\bar{f}} > 0.7$. This effect is due to a decreasing detector performance for the b tagging causing only events with a clear b signature to be tagged. For single tag events, the measured efficiency and purity agree well with the simulation especially in the central region of the detector. The b-fraction of unlike-sign double tagged events, p_b^D , is predicted by $\simeq 1\%$ too high in the simulation, while the rate of b events with one mis-tagged hemisphere, p_b^{same} , is underestimated by an even tinier amount. As will be discussed in detail in the self-calibration, Section 8.3.1, the measured rates of like- and unlike-sign double tagged events provide sensitivity to $w_b^{(D)}$ on the data themselves. The small deviation in the mis-tagging rate is therefore expected to cause a slightly too optimistic prediction of the probability to identify the b quark charge correctly, and indeed this is visible in Fig. 8.2.

8.3 Calculation of the Charge Identification Probability

For simulated events the probabilities to identify the sign of the quark charge correctly can be determined directly by exploiting the truth information, whether the sign of the underlying quark charge is correctly reconstructed by the charge tag. For single tagged events:

$$w_f = \frac{\hat{N}_f + \hat{N}_{\bar{f}}}{N_f + N_{\bar{f}}} \quad , \quad (8.6)$$

where N_f ($N_{\bar{f}}$) is the number of events tagged as quark (anti-quark) by the single hemisphere providing the $flav_{\text{hem}}$ output. \hat{N}_f ($\hat{N}_{\bar{f}}$) is the number of events in which the quark (anti-quark) has been correctly identified.

For unlike-sign events the fraction of events, in which both quark and anti-quark charges are correctly identified, is defined analogously to the single charge tagged events as the ratio of correctly tagged (\hat{N}_f^D , $\hat{N}_{\bar{f}}^D$) over all double-tagged unlike-sign (N_f^D , $N_{\bar{f}}^D$) events:

$$w_f^D = \frac{\hat{N}_f^D + \hat{N}_{\bar{f}}^D}{N_f^D + N_{\bar{f}}^D} \quad . \quad (8.7)$$

8.3.1 The probabilities to identify the b quark charge correctly

For the case of b quarks the probabilities, $w_b^{(D)}$, to identify the charge correctly can be measured directly from the data leading to a self-calibration of the analysis. The principle idea of the method is that the unlike-sign and like-sign double tagged events are proportional to:

$$N^D + \overline{N^D} \propto [w_b^2 + (1 - w_b)^2] \quad , \quad (8.8)$$

$$N^{same} \propto 2 \cdot w_b \cdot (1 - w_b) \quad , \quad (8.9)$$

with N^{same} denoting the number of double tagged like-sign events.

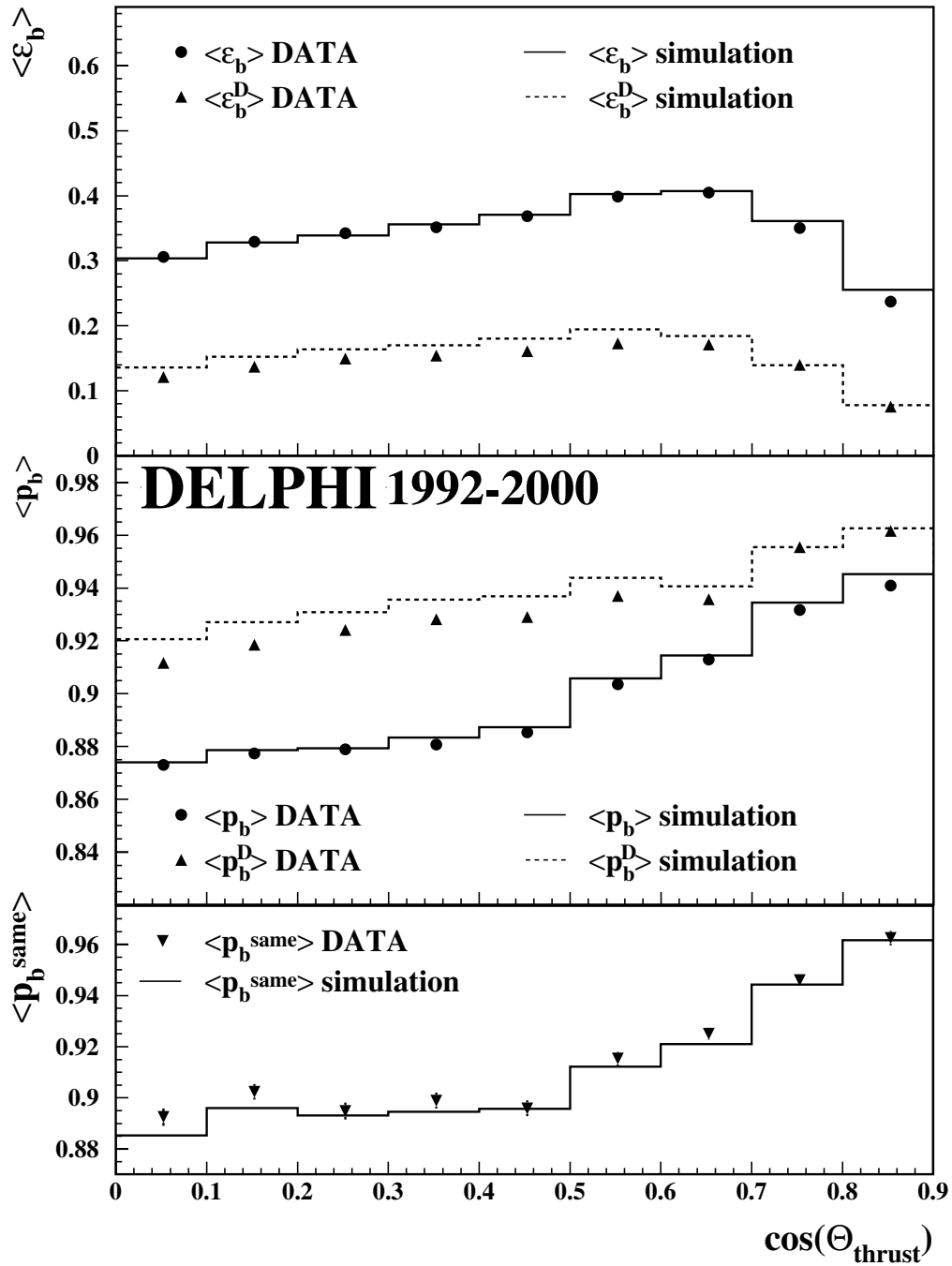


Figure 8.1: The b efficiencies ϵ_b and ϵ_b^D and the purities p_b and p_b^D for single and double unlike-sign tagged events as a function of the polar angle. The purity p_b^{same} for double like-sign tagged events is relevant for measuring the charge tagging probability, $w_b^{(D)}$.

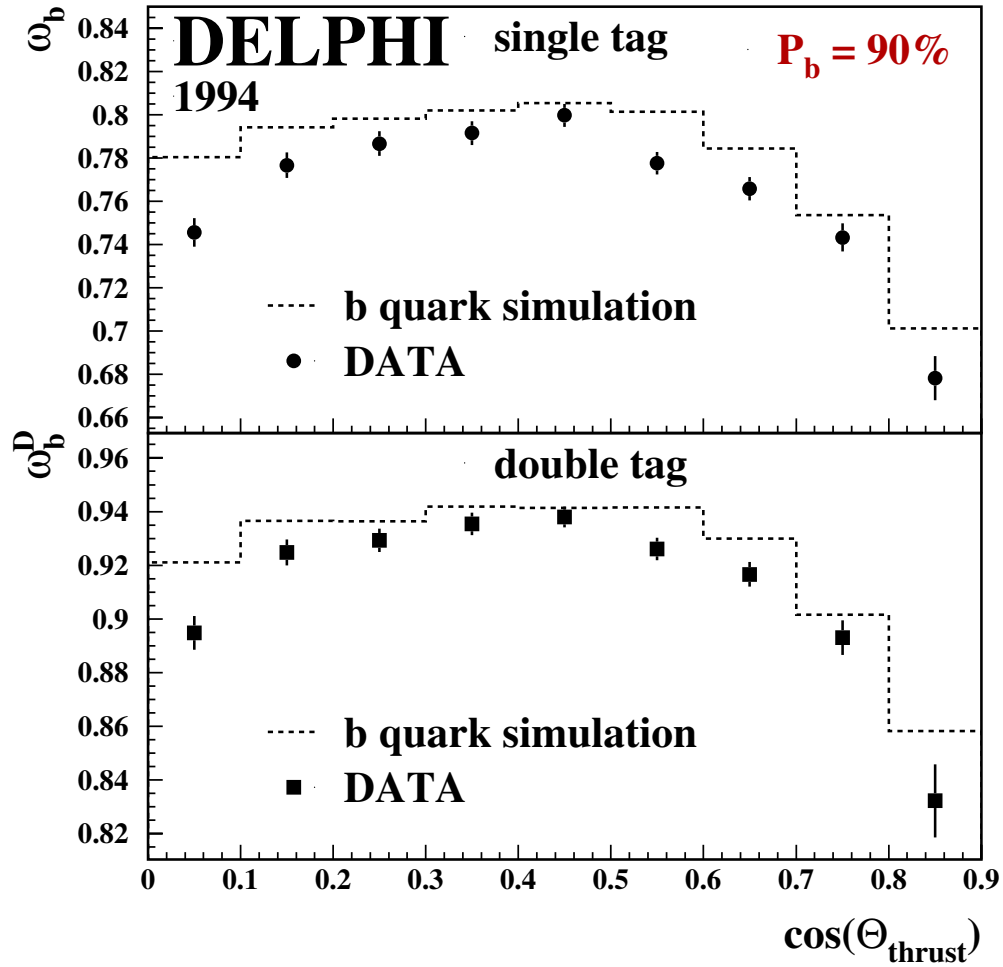


Figure 8.2: The measured probabilities to identify b quarks correctly for data and simulation for the year 1994. The upper plot shows the result for single tagged, the lower for double tagged events.

Solving the quadratic equations and taking into account background events leads to:

$$w_b \cdot \sqrt{1 + \delta} = \frac{1}{2} + \sqrt{\frac{1}{4} - \frac{1}{2} \cdot \frac{N^{\text{same}} \cdot p_b^{\text{same}}}{[N^D + \overline{N^D}] \cdot p_b^D + N^{\text{same}} \cdot p_b^{\text{same}}}} \quad , \quad (8.10)$$

$$w_b^D \cdot \sqrt{1 + \beta} = \frac{w_b^2 \cdot (1 + \delta)}{w_b^2 \cdot (1 + \delta) + (1 - w_b \cdot \sqrt{1 + \delta})^2} \quad . \quad (8.11)$$

A detailed derivation of these equations can be found in the Appendix A. p_b^D and p_b^{same} are the b purities determined individually for the unlike-sign and like-sign categories using equations 8.4 and 8.5. The additional terms $\sqrt{1 + \delta}$ and $\sqrt{1 + \beta}$ allow for hemisphere charge correlations and are discussed in section 8.3.2.

In Fig. 8.2 the measured probabilities for single and double tagged events are shown as a function of the polar angle for the year 1994. The results on data are corrected for background contributions and are compared to the prediction from simulation.

In double tagged events w_b^D rises to be above 90 % and drops to 83 % for large $\cos\theta_{\overline{T}}$ near the edge of the detector acceptance. A similar shape with a maximum of 80 % is found for the single tagged events. The plot shows that the relative discrepancy between simulated and measured $w_b^{(D)}$ is at the percent level, slightly varying with polar angle. This overall tendency to predict the real charge tagging power a little too high was observed regardless of b purity working point or year.

8.3.2 The correlations δ and β

The probabilities to identify the quark charge correctly are deduced from double charge tagged like-sign and unlike-sign events. Correlations between the two hemisphere charge tags affect the measurement and need to be taken into account. The term $\sqrt{1+\delta}$ in Eq. 8.10 allows for such correlations when calculating the single tagged probability, w_b , using the double tagged events. The probability to identify the quark charge in double tagged unlike-sign events, w_b^D , is obtained from w_b using Eq. 8.11. Here the additional term $\sqrt{1+\beta}$ allows for the different correlations in double tagged unlike-sign events. One possible effect causing this different or additional correlation is the charge conservation in the event, acting mainly on unlike-sign, i.e. charge-conserved events. The charge conservation and other physical origins for hemisphere correlations are discussed in detail later in this section.

In the double b -tagging method, used to calibrate ε_b and ε_c from Section 6.3, a simple linear parameterisation was assumed for the b -tagging hemisphere correlation. The same linear approach is used here when the factors $(1+\delta)$ and $(1+\beta)$ are applied to the quadratic Equations A.9 and A.11. The analytic solution for w_b and w_b^D then leads to the square root expression. It should be noted that the correlation in the double b -tagging method could be described by a single variable k . This is directly related to the fact that the b -tagging is insensitive to the charge sign, while the charge tagging provides two different kinds of tagged hemisphere, leading to the two categories of double tagged events.

The correlation terms $\sqrt{1+\delta}$ and $\sqrt{1+\beta}$ are obtained from simulation using b quark events. For that purpose, the result of the right hand side of Eq. 8.10 is compared to the true tagging probability for single tagged events calculated using the simulation truth. The ratio of both results is given by the term $\sqrt{1+\delta}$. Similarly the term $\sqrt{1+\beta}$ is deduced from the ratio of the result from the right hand side of Eq. 8.11 and the truth in double tagged unlike-sign events.

In Fig. 8.3 the correlations δ (upper plot) and β (lower plot) are shown as a function of the polar angle $\cos\theta_{\overline{T}}$ for the different years of data taking. Within errors the correlations are stable as a function of the polar angle. Some of the values for δ fluctuate by more than what would be expected of statistical fluctuations around a mean value: the $\chi^2/n.d.o.f.$ is $79.6/(43-1)$ for the slightly conservative test of fitting a single constant average $\langle\delta\rangle$ to all values displayed in Fig. 8.3. The corresponding probability of finding a set of δ values with at least this level of discrepancy to the mean value is 0.4%. The structure of the outliers and the underlying simulated probabilities w_b have been investigated, but the effect could not be attributed to a particular sample in b purity or year. Additional tests on the stability of the analysis have therefore been performed. They are described in combination with the systematic uncertainty related to the hemisphere correlations in Chapter 9. The

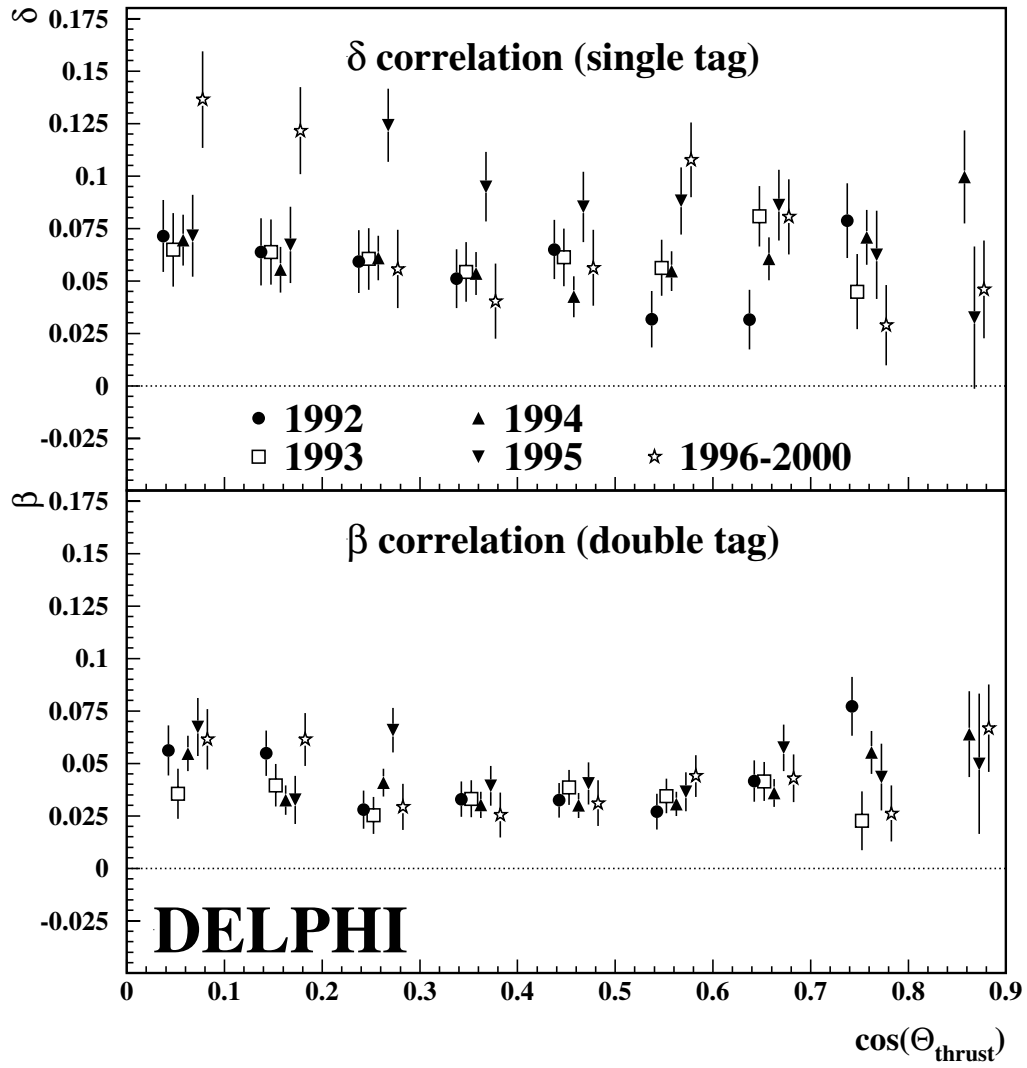


Figure 8.3: Correlation of single and double tagged simulated events for the years 1992 to 2000.

mean correlations $\langle\delta\rangle$ and $\langle\beta\rangle$ averaged over years and bins in $\cos\theta_{\vec{T}}$ are listed in Table 8.2 for the event samples with increasing b purities.

Possible sources of the hemisphere charge correlations have been investigated in detail. In order to understand the origin of the correlations, experimental input variables were consecutively discarded from the charge tagging Neural Network. With the charge tagging modified in this way, the measurement was repeated. Only for the charge network for which the jet charge for $\kappa = 0.3$ was omitted was a significant variation in the correlation observed. The mean of the correlations $\langle\delta\rangle$ and $\langle\beta\rangle$ calculated with this version of the charge tag is shown as dashed lines in Fig. 8.4. This can be compared to the dependence of the correlations for the full Neural Network as a function of the cut on the charge tag output $|flav_{\text{hem}}|$, which is shown as points. Almost no correlations for $\langle\delta\rangle$ and $\langle\beta\rangle$ remain after removing the jet charge information with the lowest κ parameter.

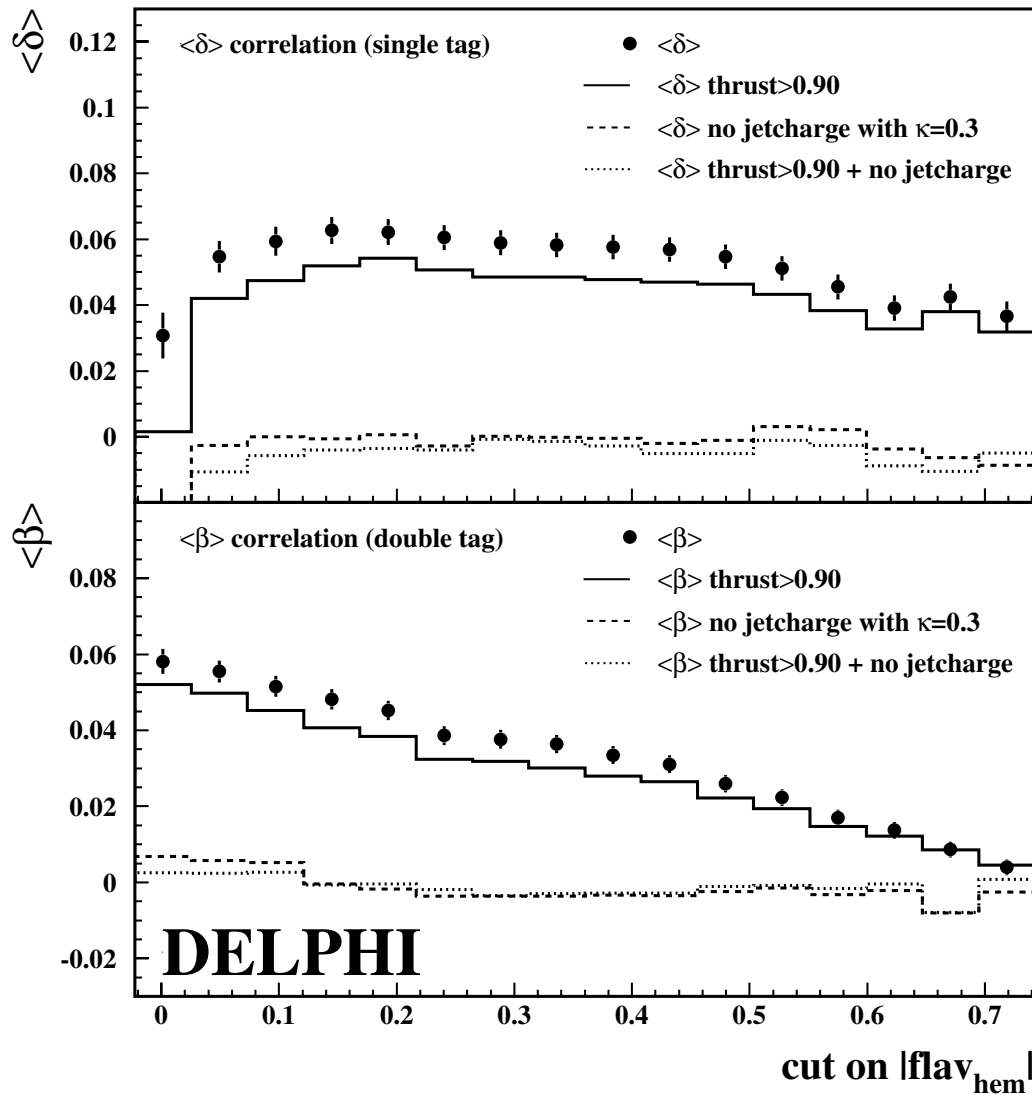


Figure 8.4: The mean of the correlations δ and β of 1994 simulation as a function of the cut on the charge tag output $|flav_{hem}|$. Besides the full hemisphere charge network (points), results using modified networks without the jet charge input for $\kappa = 0.3$ are shown. The whole study is repeated with an additional cut on the thrust value, $|\vec{T}| > 0.9$. The statistical uncertainties on the quantities represented by lines are not drawn, but they are slightly larger than those shown by the points.

	$p_b = 0.74$	$p_b = 0.95$	$p_b = 0.99$	$p_b = 0.997$
$\langle\delta\rangle$	0.085 ± 0.005	0.064 ± 0.005	0.050 ± 0.005	0.038 ± 0.004
$\langle\beta\rangle$	0.059 ± 0.004	0.045 ± 0.004	0.030 ± 0.003	0.025 ± 0.002

Table 8.2: The mean hemisphere correlations $\langle\delta\rangle$ and $\langle\beta\rangle$ for the different b purity samples and for the simulation 1992-2000.

The source of hemisphere charge correlations for the jet charge analysis has been studied in the references [69, 70]. The result of the studies is summarised in Fig. 8.5. It was found that the dominant sources of correlations are charge conservation in the event and QCD effects introduced by gluon radiation. High values for the correlation MC_{cor} appear for the lowest setting of the internal weight parameter, $\kappa = 0.3$, in the jet charge (Eq.7.5 on p. 71). This setting gives a high weight to soft tracks and renders the jet charge sensitive to charge conservation effects. The same behaviour of a significantly smaller hemisphere correlation is found for the charge tagging Neural Network when this jet charge variable is removed from the network input.

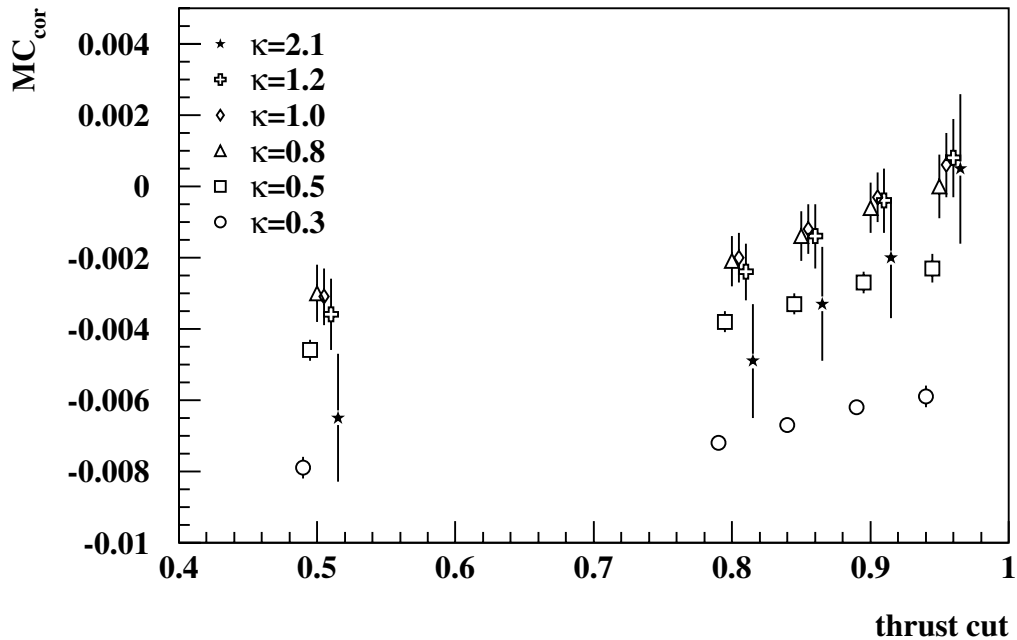


Figure 8.5: The hemisphere correlations for the A_{FB}^b measurement using only the jet charge [69]. The correlation is displayed for different values of the internal weight parameter κ and as a function of the cut on the thrust value. From [70].

The hemisphere charge correlations δ and β are also sensitive to gluon radiation. This behaviour is illustrated in Fig. 8.4 by applying a cut on the thrust value of $|\vec{T}| > 0.9$ to the events before entering both versions of the Network. Again, this mirrors the behaviour visible in Fig. 8.5.

Further possible sources of correlations have been investigated. The beam spot is shifted with respect to the centre of the DELPHI detector. Furthermore its di-

mension differs in x and y by more than one order of magnitude (see Section 6.1). A possible ϕ structure in the mean correlations $\langle\delta\rangle$ and $\langle\beta\rangle$ has been investigated by comparing results for different intervals of the thrust azimuthal angle, $\phi_{\vec{T}}$. No significant variation has been found at the working point cut in $flav_{\text{hem}}$.

8.3.3 The probabilities to identify the c quark charge correctly

The charge separation for the background of charm events directly determines the background asymmetry correction. Because the c asymmetry enters the measurement with opposite sign with respect to the b asymmetry, it is a potentially important source of systematic error. Therefore the charge identification probability is measured directly from data using a set of exclusively reconstructed D meson events. Fig. 8.6 illustrates the sensitivity to the charm charge tagging probability. It shows the product of the hemisphere charge tag $flav_{\text{hem}}$ multiplied with the charge sign of the D^* reconstructed in the opposite hemisphere, for the four fully reconstructed decay modes

$$\begin{aligned} D^{*+} &\rightarrow (K^-\pi^+)\pi^+ \quad , \\ D^{*+} &\rightarrow (K^-\pi^+\gamma\gamma)\pi^+ \quad , \\ D^{*+} &\rightarrow (K^-\pi^+(\pi^0))\pi^+ \quad \text{and} \\ D^{*+} &\rightarrow (K^-\pi^+\pi^-\pi^+)\pi^+ \quad . \end{aligned}$$

Additional selection criteria are applied to the scaled D energy, $X_E = 2E_{D^*}/\sqrt{s}$, and the event b -tag to reject $b \rightarrow c \rightarrow D$ further. An anti-correlation between the contributions from c and b quarks is indicated by the corresponding shapes of the simulated events in Fig. 8.6.

From the rates of hemispheres with correctly ($-Q(D) \cdot \text{sign}(flav_{\text{hem}}) > 0$) and incorrectly (< 0) reconstructed D charge, an asymmetry A is constructed:

$$A = \frac{N(-Q(D) \cdot \text{sign}(flav_{\text{hem}}) > 0) - N(-Q(D) \cdot \text{sign}(flav_{\text{hem}}) < 0)}{N(-Q(D) \cdot \text{sign}(flav_{\text{hem}}) > 0) + N(-Q(D) \cdot \text{sign}(flav_{\text{hem}}) < 0)} \quad . \quad (8.12)$$

This asymmetry is a function of the probability to identify the quark charge correctly:

$$A = \sum_{q=d,u,s,c,b} f_q \cdot cor_q \cdot (2w_q - 1) \quad . \quad (8.13)$$

The fractions f_q of the involved quark flavours and the correlation cor_q between the D meson and the primary quark have to be taken from simulation. To separate the contributions from c and b events on the data themselves, a two dimensional fit to A is performed using the D energy and the b tagging information in the D hemisphere as separating variables. The latter avoids a possible correlation between the hemisphere b tagging and the hemisphere charge tagging in the hemisphere opposite to the D in which w_c is to be measured. To allow for a sensitive measurement, the analysis to determine the c quark charge tagging probability is performed on the full set of 9 different exclusive D decay modes used by DELPHI to measure the charm asymmetry [41, 71]. In addition, the requirements for a charge tag as used in the rest of this paper are slightly modified, in that the b -tag cut is relaxed to $b\text{-tag} > -0.7$ for the purpose of preserving enough charm events in the fitted sample. It has been checked that there is no significant change in w_c while moving the b -tag working point from $p_b = 90\%$ to a p_b of about 75%. Combining the individual results from all nine

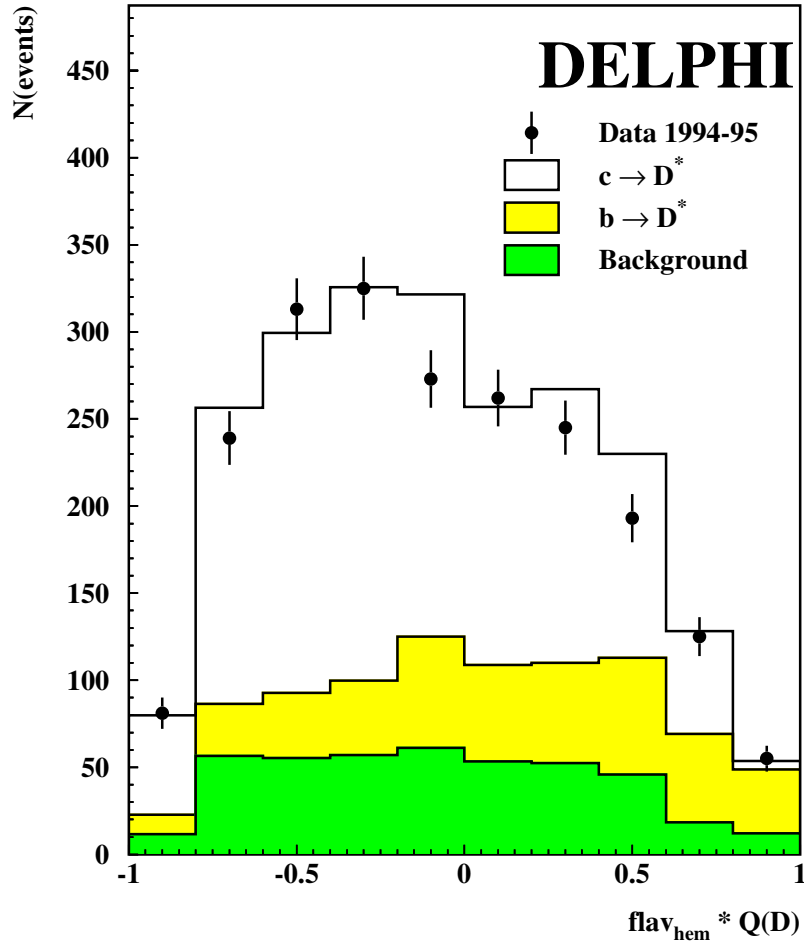


Figure 8.6: The product of the charge tagging Neural Network output times the charge of a reconstructed D^* in the opposite hemisphere. Only a subset of the full samples is shown here for illustration purposes: The data comprise the four decay channels $D^{*+} \rightarrow (X)\pi^+$, where X can be $K^-\pi^+$, $K^-\pi^+\gamma\gamma$, $K^-\pi^+\pi^-\pi^+$ or $K^-\pi^+(\pi^0)$, for the years 1994-95. The $c \rightarrow D^*$ fraction was increased by requiring $X_E > 0.45$ and the event b -tag in the range -0.7 to 1.0 . The b quark and combinatorial background is corrected using the measured distribution from a c depleted selection on the same data samples.

decay modes and all four years 1992-95, the charm charge tagging probability is found to be different from the simulated one by a factor 0.944 ± 0.030 as shown in Fig. 8.7. This means that the charm charge tagging is in fact weaker than predicted in simulation.

In the fit to A_{FB}^b , Eq. 8.1 and 8.2, w_c enters via the dilution factor $2w_c - 1$. The simulated dilution factor is then scaled by the data to simulation ratio obtained for $2w_c - 1$ from the set of reconstructed D events, namely 0.71 ± 0.15 .

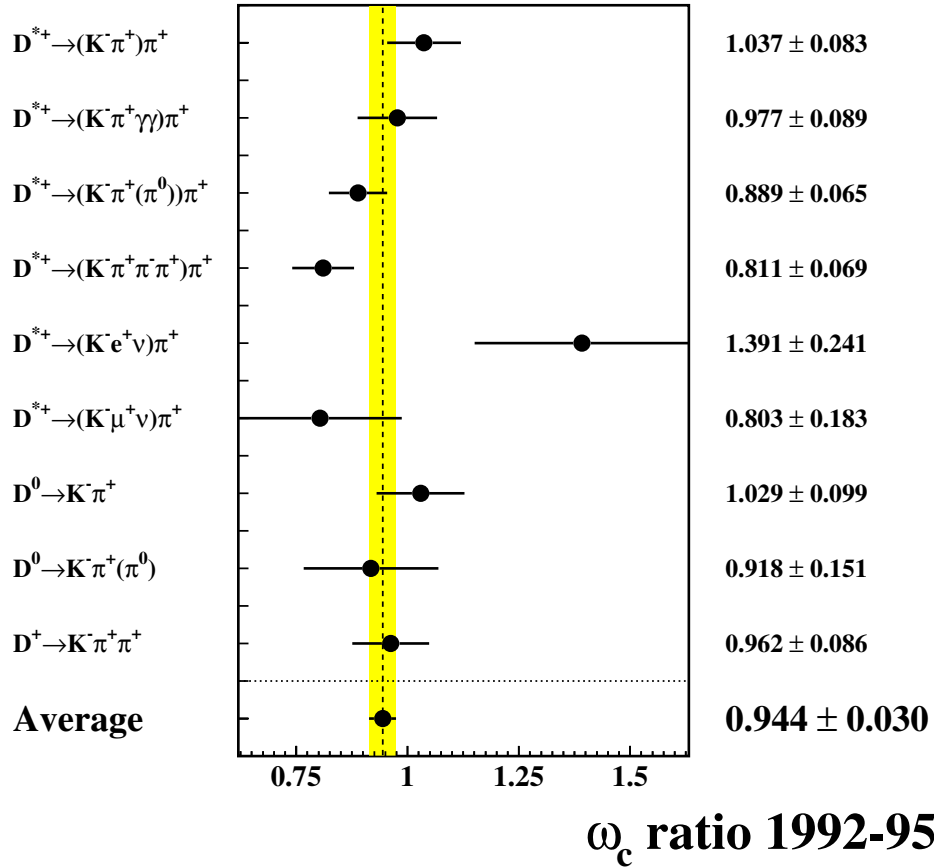


Figure 8.7: The ratio of real data to simulation in the c quark charge identification w_c provided by a $flav_{\text{hem}}$ tag in a hemisphere opposite a reconstructed D . The final result is decomposed into the 9 different decay channels used in [41, 71].

8.4 The QCD correction

The measurement of the b quark forward-backward asymmetry is sensitive to QCD corrections to the quark final state. The correction takes into account gluon radiation from the primary quark pair and the approximation of the initial quark direction by the experimentally measured thrust axis. The first part, the effect of gluon radiation, has been calculated to second order in α_s for an asymmetry based on the parton level thrust axis, $(A_{\text{FB}}^q)_{\text{parton}}$. The first-order coefficient, c_1 , in the expansion in orders of α_s ,

$$(A_{\text{FB}}^q)_{\text{parton}} = (A_{\text{FB}}^q)_{\text{noQCD}} \left(1 - c_1 \frac{\alpha_s(m_Z^2)}{\pi} + c_2 \left(\frac{\alpha_s(m_Z^2)}{\pi} \right)^2 \right), \quad (8.14)$$

has been calculated in [72] for the pole quark masses, $m_b = 4.5 \text{ GeV}/c^2$ and $m_c = 1.5 \text{ GeV}/c^2$, giving the values quoted in Table 8.3. The size of the second order contribution, c_2 , has been re-estimated in [73] and confirmed by a numerical calculation in [74]. It is also shown in Table 8.3.

	b\bar{b} events	c\bar{c} events
c_1	0.77	0.86
c_2	5.93	8.5

Table 8.3: Calculated values for the QCD correction coefficients for b and c quark events. The value for c_1 is from [72] while c_2 is from the more recent work described in [73, 74].

A theoretical calculation is only possible for a thrust axis computed on the parton level. Therefore the second part of the correction needs to cover the difference between the parton level thrust axis and the experimentally measured hadron level thrust axis. This remaining correction is much smaller and has been determined by means of hadronisation models in Monte Carlo simulation. The full QCD correction to the b quark asymmetry is then parameterised by

$$(A_{\text{FB}}^b)_{\text{QCD}} = \left(1 - C_{\text{QCD}}^{\text{b, est.}} \right) (A_{\text{FB}}^b)_{\text{noQCD}}. \quad (8.15)$$

Here $(A_{\text{FB}}^b)_{\text{noQCD}}$ is the asymmetry of the initial b quarks without gluon radiation, which can be calculated from the measured asymmetry $(A_{\text{FB}}^b)_{\text{QCD}}$ through the correction coefficient $C_{\text{QCD}}^{\text{b, est.}}$. Its value $C_{\text{QCD}}^{\text{b, est.}} = (3.54 \pm 0.63)\%$ is derived in [75] from the above steps. The different contributions to its theoretical uncertainty of 0.63% are listed in [72] and [75]. The dominating source of uncertainty are mass-dependent terms at higher orders, which either had to be neglected or were of unknown form. This uncertainty has been estimated by varying the quark pole mass to the running mass in the \overline{MS} scheme ($m_b \simeq 3 \text{ GeV}/c^2$) and by allowing logarithmically enhanced leading mass terms in the second order calculation.

The QCD correction is of special importance because it commonly affects all LEP asymmetry measurements: S. Catani and M.H. Seymour [74] estimate that for each permille that the corrected value of the quark asymmetries is increased, a percent decrease of the central value of the higgs mass (and its upper bound) is obtained. Great care is therefore taken not only in the theoretical calculations but also in applying the QCD correction to the analysis and the resulting systematic uncertainties.

A realistic measurement has a reduced experimental sensitivity to the QCD effects because of biases in the analysis. In this analysis the charge tagging and also the b tagging introduce a bias against events with hard gluon radiation and towards more two-jet-like events. The remaining effects from events with gluon radiation were observed partly responsible for the hemisphere charge correlations, which are corrected for internally in the determination of w_b in Section 8.3.2. The parameterisation for the correlations therefore hides a part of the QCD effects and possibly reduces the effective QCD correction further. Eq 8.15 has to be modified:

$$(A_{\text{FB}}^b)_{\text{QCD}} = (1 - C_b)(A_{\text{FB}}^b)_{\text{noQCD}} = (1 - s_b C_{\text{QCD}}^{b,\text{est.}})(A_{\text{FB}}^b)_{\text{noQCD}} \quad (8.16)$$

to take into account a reduced effective QCD correction coefficient, C_b . This coefficient can be decomposed into a product of the full QCD correction $C_{\text{QCD}}^{b,\text{est.}}$ to the b quark asymmetry measured, using the thrust direction and the sensitivity s_b of the individual analysis to $C_{\text{QCD}}^{b,\text{est.}}$.

The experimental bias needs to be studied on simulation. It is obtained by fitting the differential asymmetry of the b simulation after setting the generated asymmetry of the initial b quarks before gluon radiation to the maximum of 75 % (Eq. 8.3). By modifying the generated A_{FB}^b in such a way, the numerical precision of the s_b factors is increased without affecting the topology of events and their weight in the measurement samples. The observed relative differences of the asymmetries are studied separately for each $\cos\theta_{\vec{T}}$ interval and bin in b -tag. In Fig. 8.8 the coefficient C_b is shown for single and double tagged events for the different years. At small $\cos\theta_{\vec{T}}$ values the sensitivity to the asymmetry is small and hence C_b receives a larger statistical uncertainty. It should be noted that no systematic variation of C_b with $\cos\theta_{\vec{T}}$ is seen at large polar angles. From the coefficient C_b the experimental bias factor s_b is deduced, using a value [72] of $C_{\text{QCD}}^{b,\text{sim.}} = (3.06 \pm 0.03)\%$ that is specific to the physics and detector modelling in the DELPHI simulation. The uncertainty quoted for $C_{\text{QCD}}^{b,\text{sim.}}$ is the statistical error obtained with the generator and is negligible compared to the modelling uncertainty. The values of s_b averaged over bins in b -tag and polar angle are shown in Table 8.4 for the different years of data taking.

year	s_b [%]
1992	27 ± 7
1993	21 ± 8
1994	13 ± 5
1995	13 ± 9
1996-2000	14 ± 9

Table 8.4: Summary of bias factors s_b with their statistical uncertainty.

On real data the theoretical calculation discussed above is applied, $C_{\text{QCD}}^{b,\text{est.}} = (3.54 \pm 0.63)\%$, as the calculation is expected to be more reliable than the simulation. In the following fits the correction coefficients $s_b \cdot C_{\text{QCD}}^{b,\text{est.}}$ are taken into account for each bin in polar angle separately and hence all asymmetries quoted are corrected for QCD effects.

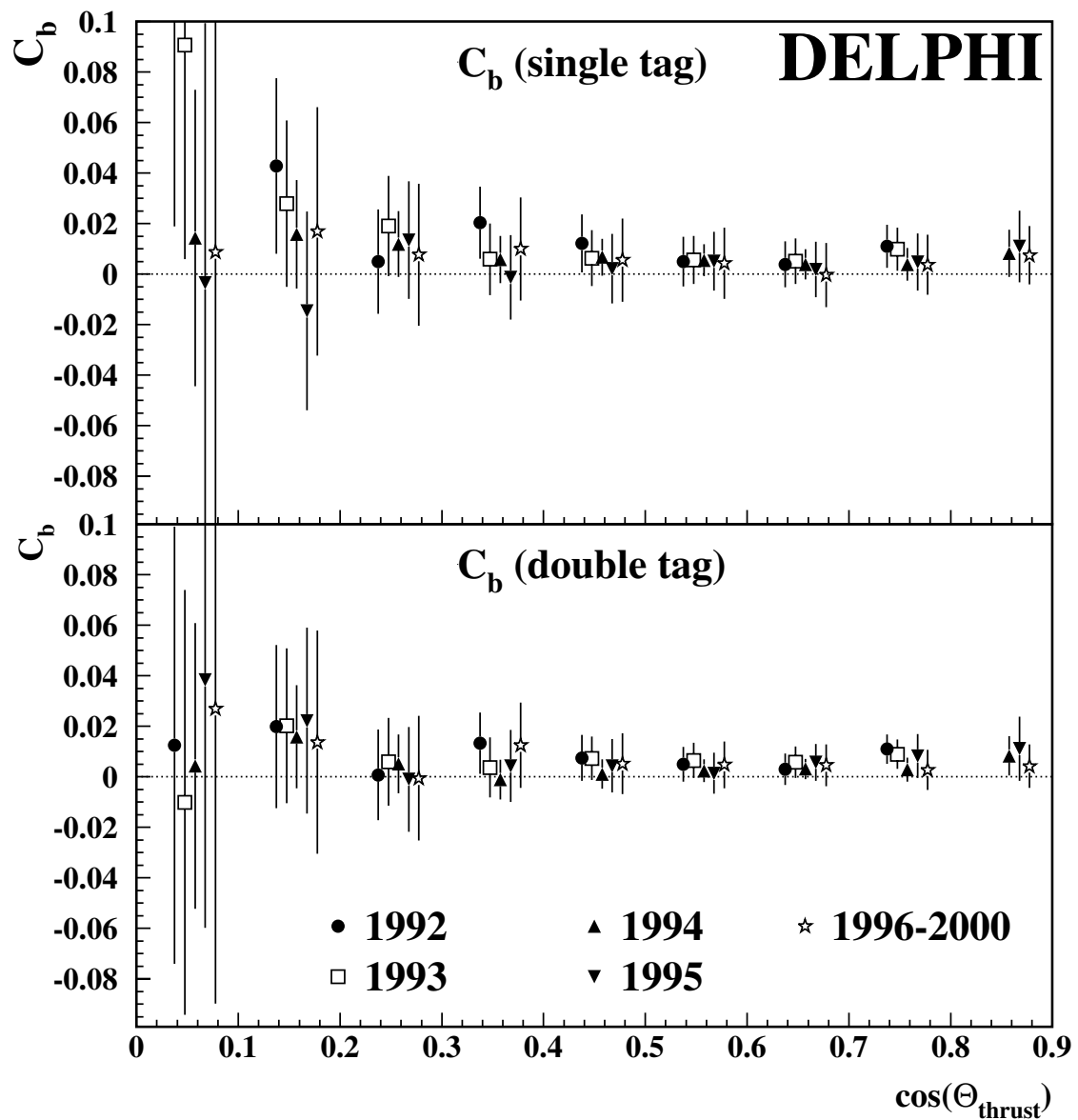


Figure 8.8: The size of the QCD correction coefficient $C_b = s_b C_{\text{QCD}}^{\text{b, sim.}}$ including experimental biases as a function of the polar angle of the thrust axis. In the upper plot the correction is shown for single charge tagged events from the different years. In the lower plot the corresponding corrections are shown for double charge tagged events.

8.5 The Fit of the b Quark Forward-Backward Asymmetry

The b quark forward-backward asymmetry is extracted from a χ^2 -fit dividing the data of each year in 4 intervals of b -tag. This allows for the change in b purity (Table 8.1) and in the size of the hemisphere correlations as a function of b -tag (Table 8.2). In addition, it reduces the dependence on the charm asymmetry from ± 0.00023 for a single cut on b -tag to the value of ± 0.00014 as quoted in Table 9.1. Technically A_{FB}^b is extracted in each interval from a χ^2 -fit to the event rates in the five independent categories, N , \bar{N} , N^D , \bar{N}^D and N^{same} , in bins of polar angle. The full fit functions for the event rates and the terms that finally form the χ^2 are given in Appendix B.

The double charge tagged unlike-sign events are sensitive to the asymmetry, but the rates also enter into the determination of the charge tagging probabilities w_b and w_b^D , as can be seen in Equations 8.10 and 8.11. This leads to correlations between the probabilities and the measured asymmetry in each bin. In the combined χ^2 -fit to the five event rates N , \bar{N} , N^D , \bar{N}^D and N^{same} these correlations are taken into account. As detailed in the appendix, the rates can be expressed as a function of the b quark forward-backward asymmetry A_{FB}^b , the probability w_b and two arbitrary normalisation factors, which absorb the overall efficiency corrections. These normalisations are set to their proper values for each bin in the fit. The number of degrees of freedom (*n.d.o.f.*) is 15 for 1992+93 and 17 for 1994-2000. The χ^2 probabilities for the altogether 36 fits in the different intervals in b -tag, years and energy points have been verified. Fig. 8.9 shows the distribution of the $\chi^2/n.d.o.f.$ values, giving an average of 1.07 with an r.m.s. of 0.38. A few additional cross-checks, which are detailed in Section 9.1, have been carried out on simulation to verify if there is any bias present in the analysis method. No such bias has been found.

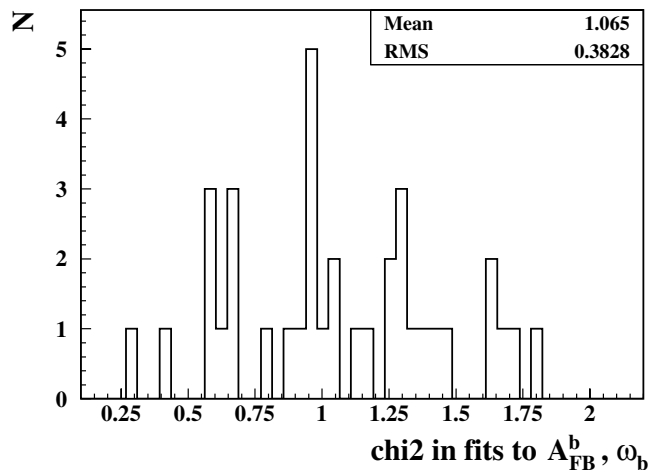


Figure 8.9: Distribution of the $\chi^2/n.d.o.f.$ of the fits to A_{FB}^b from the four different samples in b purity times the nine different years, respectively energy points.

In Fig. 8.10 the measured asymmetries with their statistical errors are shown in intervals of b -tag for the different years. The band represents the overall result with its statistical uncertainty.

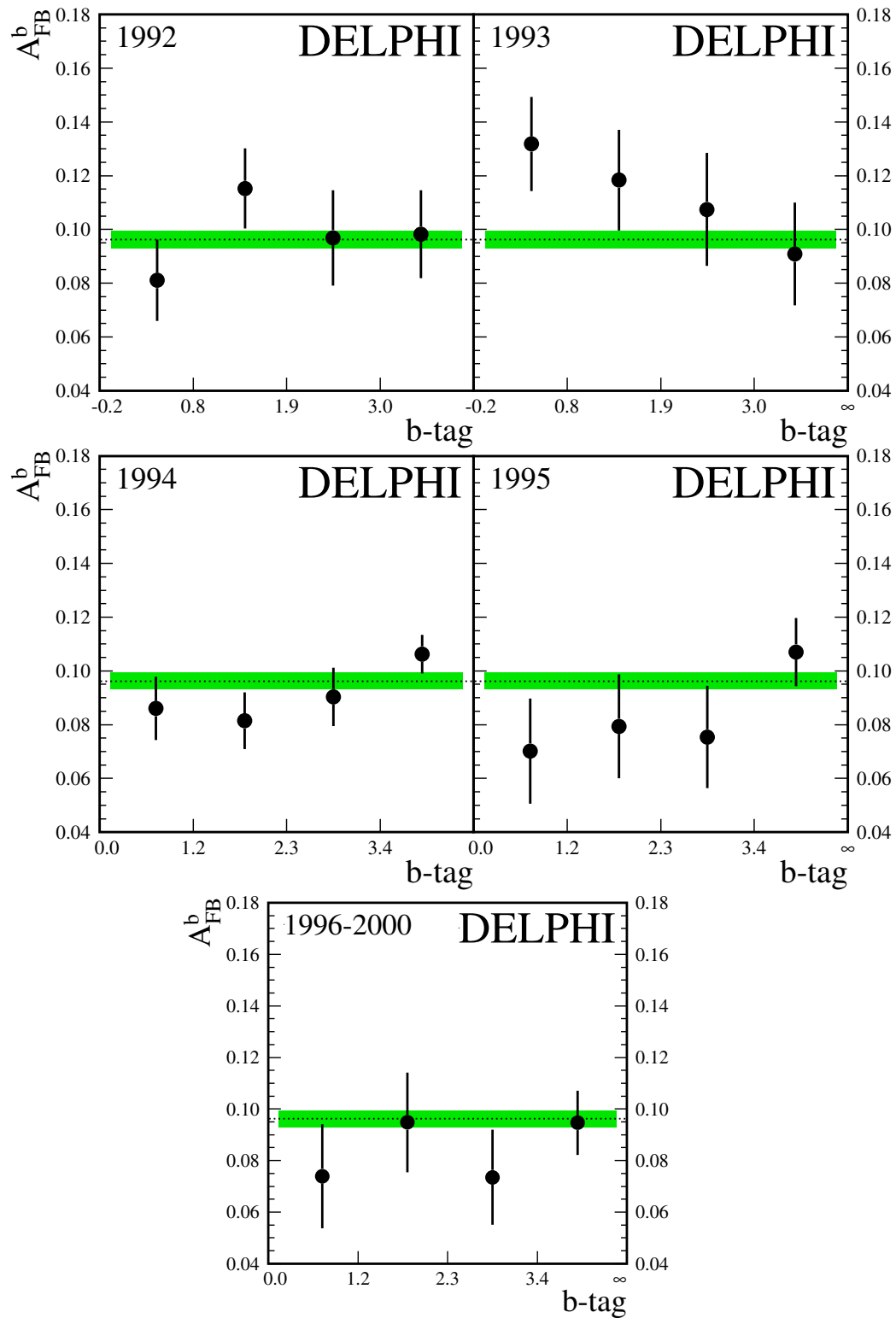


Figure 8.10: The A_{FB}^b results for each year and each interval in b -tag with their statistical errors. The 20 individual measurements enter into the final fit taking into account statistical and systematic errors. The line is the average from the χ^2 -fit at $\sqrt{s} = 91.231$ GeV with its statistical uncertainty shown as the band.

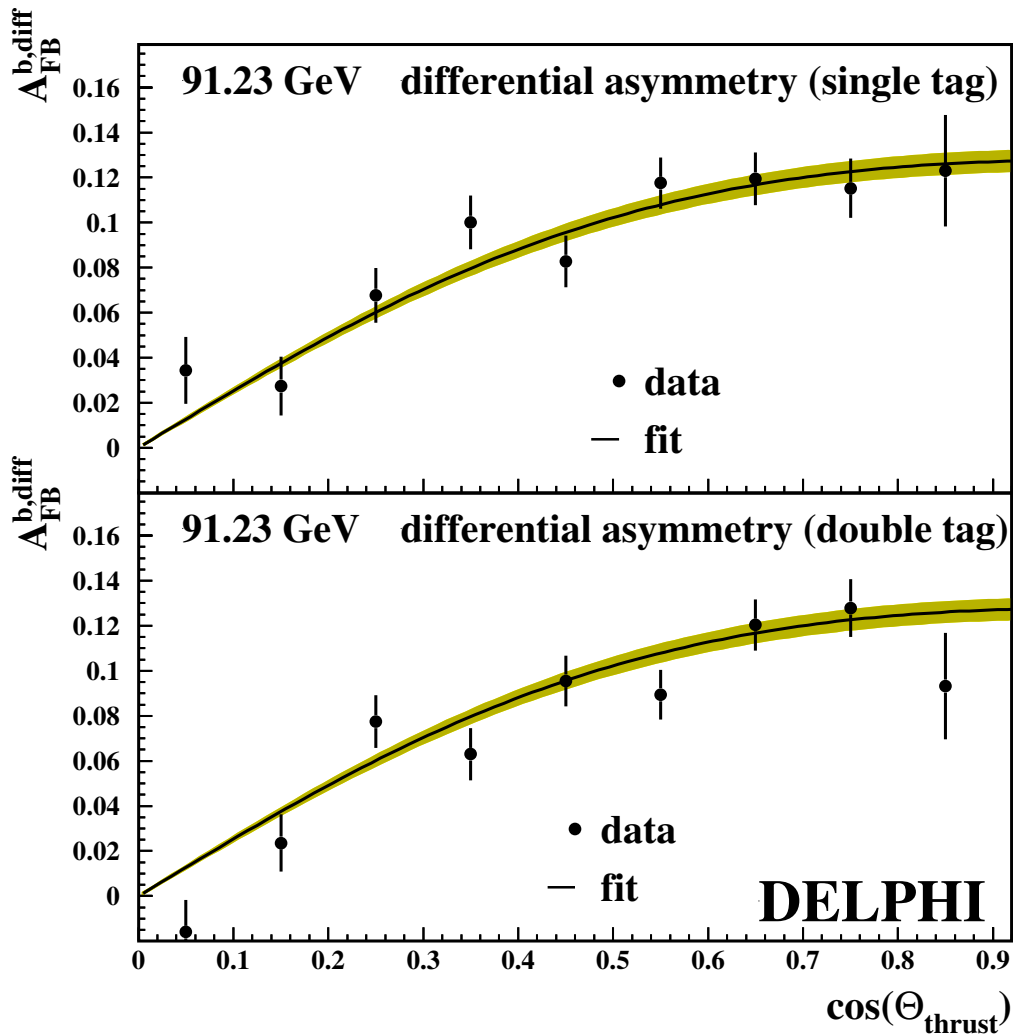


Figure 8.11: The differential b quark forward-backward asymmetry of the years 1992 to 2000 at a centre-of-mass energy of 91.231 GeV. It is shown separately for the two classes of single and double charge tagged events. The curve is the result of the common χ^2 -fit with its statistical error shown as the band.

Fig. 8.11 shows the measured differential asymmetry for single and double tagged events as a function of $\cos \theta_{\vec{T}}$ averaged over all years of data taking and over all b -tag intervals. Again, only statistical uncertainties are shown and the band represents the overall result.

8.5.1 The off-peak data sets

The data sets at 2 GeV above and below the Z-pole each have about a factor five less events than the corresponding on-peak data. They are analysed using the same method as the 91.231 GeV data, but with a few adaptations:

- For the off-peak data taken intermittently between the Z peak running, no extra $\varepsilon_b/\varepsilon_c$ calibration was done, but the peak correction functions were applied.
- The energy dependence of the charge tagging performance is negligible over this small range of centre-of-mass energies. So the peak quantities related to the charge tagging for the two years in question are transferred to the off-peak analysis. These quantities comprise the w_b and w_c measurements on data, as well as the simulated charge tagging input to the fit, w_{uds} , the correlations δ and β and the QCD correction C_b .
- The number of $\cos\theta_{F^{\pm}}$ bins is reduced. For 1993 from 8 to 4 and for 1995 from 9 to 5, always covering the same range. The corresponding χ^2 -fits to the event numbers have 11 degrees of freedom for 1993 and 14 for 1995.

Fig. 8.12 shows the results in intervals of b -tag separated for each year. The measured differential asymmetry in Fig. 8.13 displays the averaged results from both years combining single and double tagged events for all three centre-of-mass energies.

8.5.2 Combined results

For each year of data-taking, the measurements for A_{FB}^b in the four bins are averaged by means of another χ^2 fit that takes into account not only statistical errors but also systematic uncertainties as a function of b-purity. The averaging procedure is based on the method of Best Linear Unbiased Estimate (BLUE) [76] and is the same as the one used by the LEP Electroweak Working Group for averaging the full set of electroweak observables [77]. The systematic uncertainties will be discussed in detail in the next Chapter. The summary of the individual A_{FB}^b results for the different years with their statistical uncertainties is given in Table 8.5. The χ^2 probabilities for each year state the probability of observing A_{FB}^b results in bins of b -tag as compatible or less with the fitted common result.

For the combination of these measurements, the year-by-year variation in the centre-of-mass energy at the level of ~ 50 MeV was taken into account by translating all A_{FB}^b measurements to a common energy of 91.231 GeV (resp. 89.449 and 89.449 GeV). Combining the measurements from the different years again taking common uncertainties into account yields the final result:

$$\begin{aligned} A_{FB}^b(89.449 \text{ GeV}) &= 0.0637 \pm 0.0143(\text{stat.}) , \\ A_{FB}^b(91.231 \text{ GeV}) &= 0.0958 \pm 0.0032(\text{stat.}) , \\ A_{FB}^b(92.990 \text{ GeV}) &= 0.1041 \pm 0.0115(\text{stat.}) . \end{aligned}$$

These results are displayed as a function of the centre-of-mass energy in Fig. 8.14 where they are also compared to the Standard Model expectation. The latter is obtained from ZFITTER version 6.36, using as input parameters the central values of the following quantities [24]:

$$\begin{aligned} m_Z &= 91.1875 \pm 0.0021 \text{ GeV}/c^2 & m_t &= 174.3 \pm 5.1 \text{ GeV}/c^2 \\ m_h &= 150 \pm 100 \text{ GeV}/c^2 & \Delta\alpha_5^{\text{had.}} &= 0.02761 \pm 0.000035 \\ \alpha_s &= 0.118 \pm 0.002 \end{aligned}$$

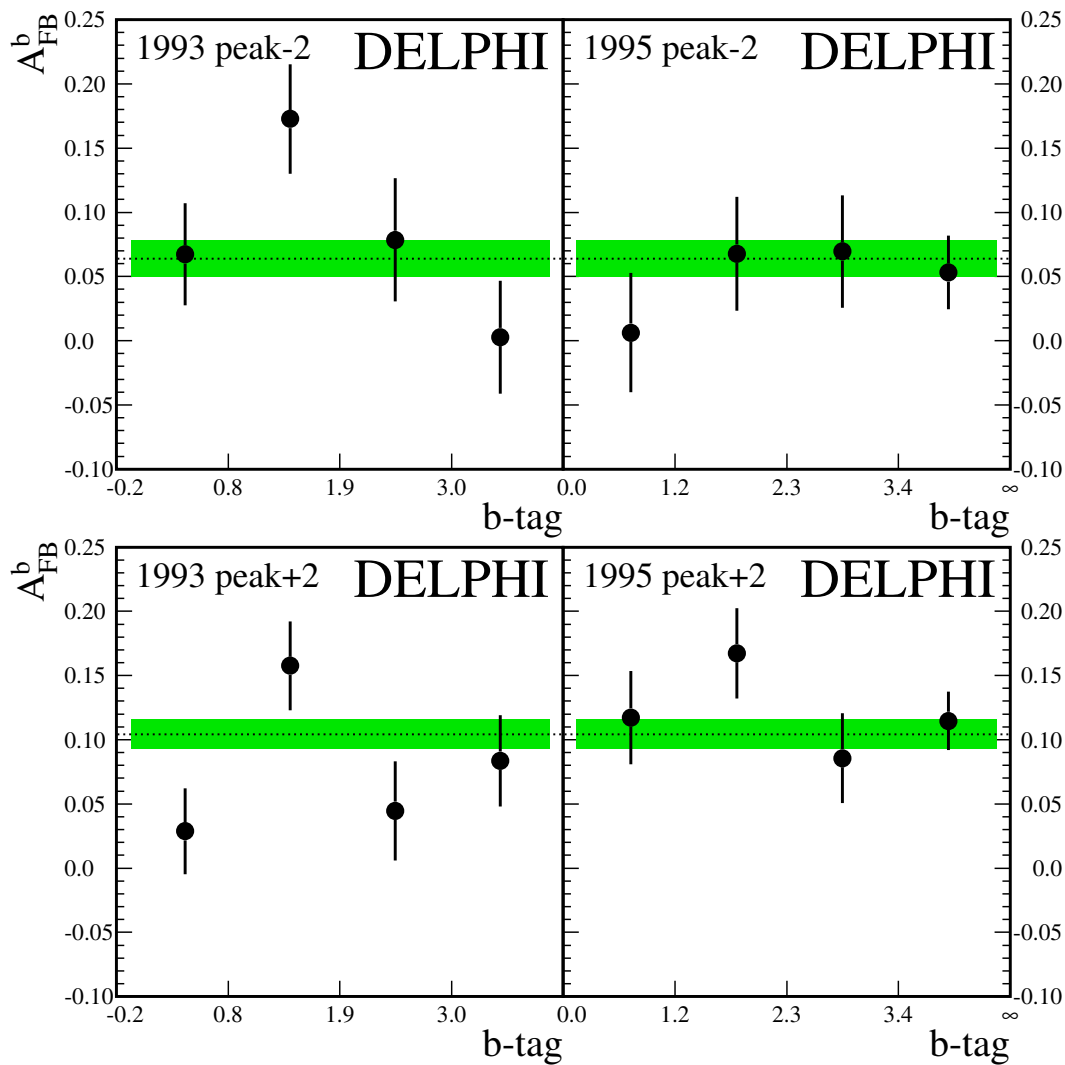


Figure 8.12: The A_{FB}^b results for the 1993 and 1995 off-peak runs and each interval in b -tag with their statistical errors. The lines in the upper and lower plots are the results of χ^2 -fits that were run separately at $\sqrt{s} = 89.449$ and 92.990 GeV. The band shows again the statistical uncertainty.

QED initial state radiation is fully considered in the simulation and taken into account by ZFITTER in Fig. 8.14 and when the Z pole asymmetry is computed. This is particularly important for the peak+2 measurements. It has been checked in the simulation that the event selection, including the charge tag, does not introduce a bias on the $\sqrt{s'}$ distribution assumed by ZFITTER.

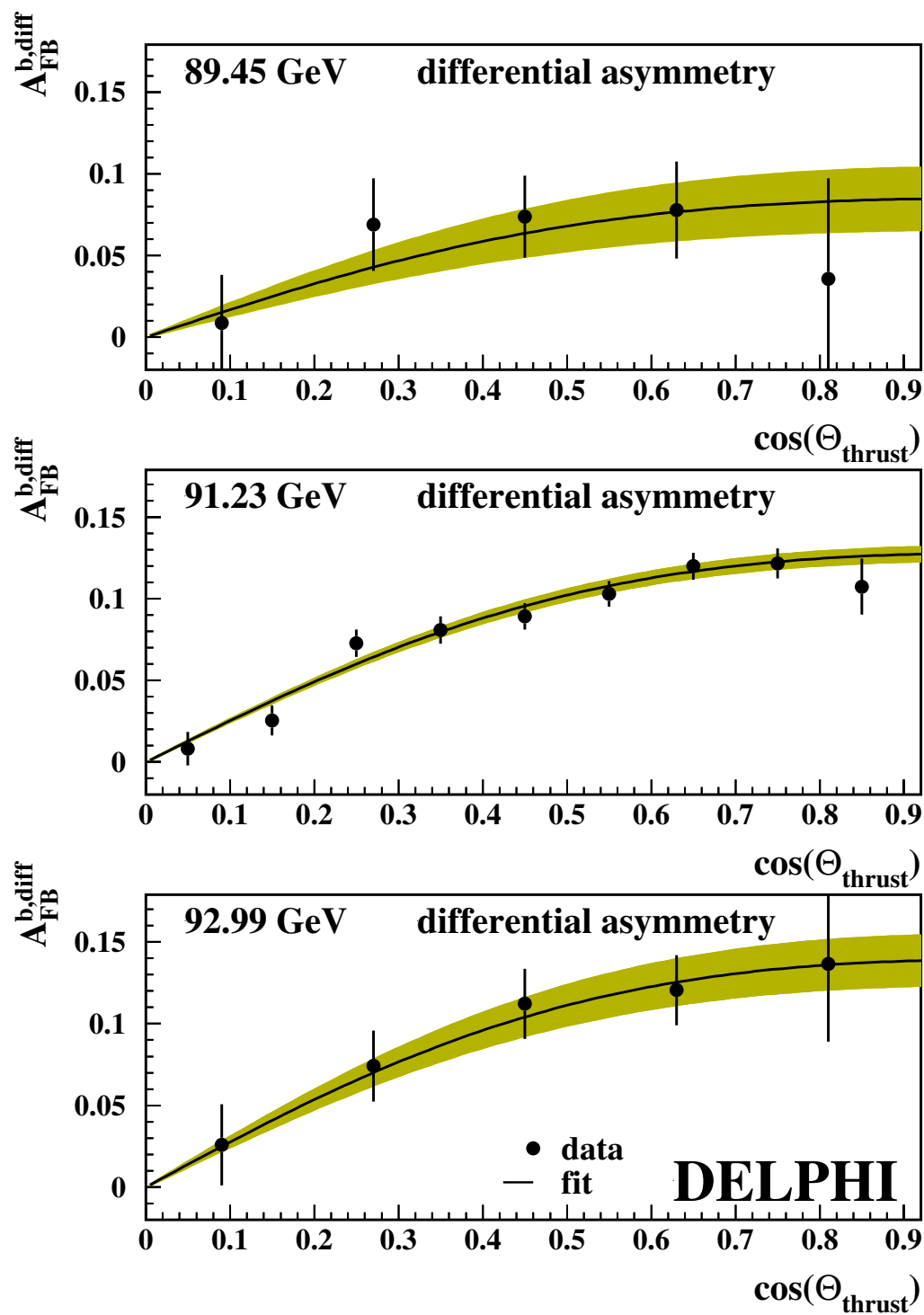


Figure 8.13: The differential b quark forward-backward asymmetry (single and double tag) at the three centre-of-mass energies of 89.449, 91.231 and 92.990 GeV. The curve is the result of the common χ^2 -fit with its statistical error shown as the band.

Year	\sqrt{s} [GeV]	A_{FB}^b	prob(χ^2)
1992	91.280	0.0984 ± 0.0079	0.47
1993	91.225	0.1130 ± 0.0095	0.46
1994	91.202	0.0952 ± 0.0048	0.19
1995	91.288	0.0895 ± 0.0084	0.30
1996-2000	91.260	0.0870 ± 0.0083	0.69
1993 peak-2	89.431	0.0803 ± 0.0216	0.05
1993 peak+2	93.015	0.0817 ± 0.0177	0.06
1995 peak-2	89.468	0.0506 ± 0.0191	0.71
1995 peak+2	92.965	0.1213 ± 0.0152	0.40

Table 8.5: Summary of the A_{FB}^b results for the different years with their statistical uncertainty. The number of degrees of freedom is $(4-1)$ for the fit of each year of data taking, as shown in Figures 8.10 and 8.12.

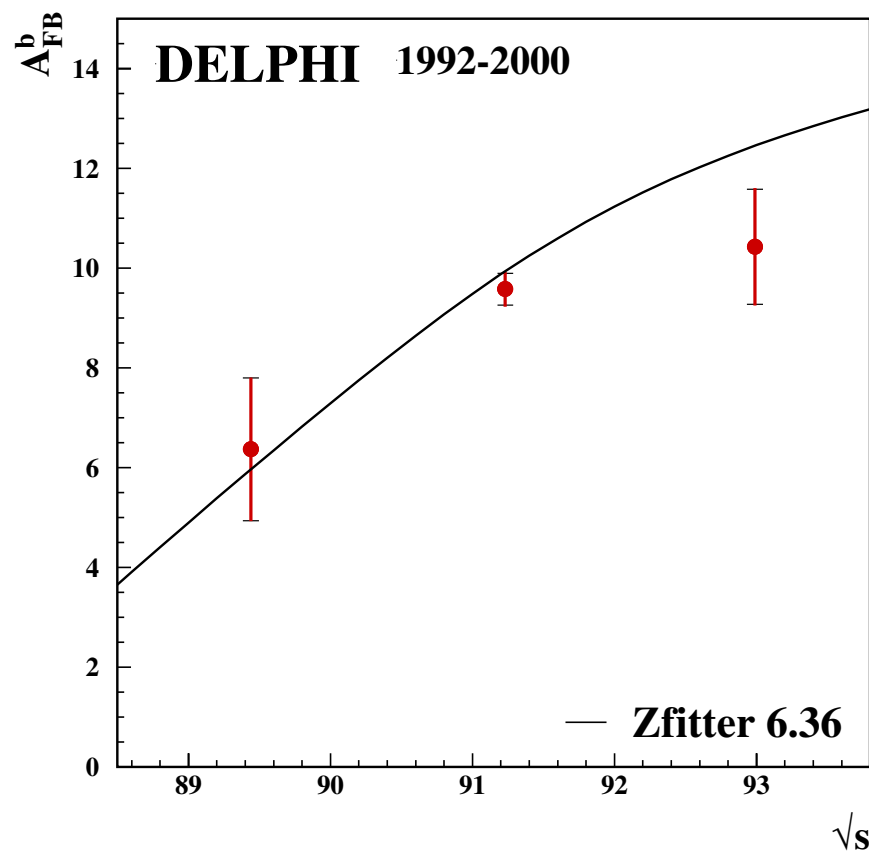


Figure 8.14: The A_{FB}^b results versus the centre-of-mass energy. The total errors (bars) are only slightly larger than the statistical (flags). The curve represents the Standard Model prediction obtained from ZFITTER (see text for details).

Chapter 9

Discussion of Systematic Uncertainties

The two main components of the analysis are the enhanced impact parameter b tagging and the Neural Network charge tagging. Both components are sensitive to detector resolution effects as well as to the modelling of light quark and c events in the simulation. Therefore both careful tuning of the simulation and measuring all possible input parameters directly were applied as described before. Remaining uncertainties are studied and changes in the result are propagated through the whole analysis chain. The variation of systematic errors as a function of the b -tag intervals is taken into account.

The systematic error sources affecting the measurement are:

- In the measurement the LEP+SLD average values [24] for the **electroweak parameters** $R_b^0 = 0.21644 \pm 0.00065$, $R_c^0 = 0.1719 \pm 0.0031$ and $A_{\text{FB}}^c = 0.0641 \pm 0.0036$ are used. They enter the determination of the b -tag correction function and the flavour fractions in the selected data sets, and they form the main background asymmetry in the measurement. Variations of $\pm 1\sigma$ with respect to the LEP+SLD averages are included in the systematic error.

The dependencies on $R_{b,c}^0$ and A_{FB}^c are not so much a systematic uncertainty, but provide valuable information to the LEP Electroweak Working Group when the combined fit is performed to the electroweak parameters in the heavy flavour sector and correlations between the measured parameters have to be taken into account. The dependencies in this combined fit procedure are treated individually at each of the three LEP centre-of-mass energies close to the Z peak. Therefore the resulting uncertainties on A_{FB}^b — respectively the dependency of A_{FB}^b on the $\pm 1\sigma$ variation of each parameter — are given in Table 9.1 separately for each energy point.

- The **detector resolution** on the measured impact parameter affects both the b tagging and the charge tagging in a similar fashion, because both tagging packages exploit the lifetime information in the events. A bad description of the resolution in the simulation may lead to a wrong estimation of remaining background in the sample. In the analysis a careful year by year tuning of these resolutions and of the vertex detector efficiency has been used [49] for both tagging packages.

contribution	variation	$\Delta A_{\text{FB}}^b \times 10^2$		
		$\sqrt{s} = 89.449$	$\sqrt{s} = 91.231$	$\sqrt{s} = 92.990$
R_b	0.21644 ± 0.00065	∓ 0.010	∓ 0.011	∓ 0.016
R_c	0.1719 ± 0.0031	∓ 0.010	∓ 0.014	∓ 0.021
A_{FB}^c	0.0641 ± 0.0036	± 0.019	± 0.014	± 0.018

Table 9.1: Dependencies of A_{FB}^b on the electroweak parameters. The effect of the $\pm 1\sigma$ variation contributes to the systematic uncertainty. The measured value of A_{FB}^c from [24] is extrapolated to DELPHI centre-of-mass energies by means of ZFITTER, giving -0.0338, 0.0627 and 0.1241 for peak-2, peak and peak+2.

For the systematic error estimation the recipe from the DELPHI R_b measurement [46] was followed. First the calibration of the impact parameter significance for the simulation was replaced by the corresponding one for the real data to test residual differences between data and simulation. Second the VD efficiency correction was removed from the simulation. Finally the resolution of the impact parameter distribution was changed by $\pm 1\sigma$ with respect to the measured resolution in a real data sample depleted in b events. The b tagging correction functions used to calibrate ε_c and ε_b have been re-calculated for every change, and each time the effect has been propagated through the full analysis. Thus the detector description variation affects both b and charge tagging in a consistent way. The systematic uncertainty quoted was chosen conservatively as the linear sum of all three contributions, for which the last one gives the dominant uncertainty.

- The **efficiency for tagging charm** in the b tagging procedure enters the background subtraction via the flavour fractions. The double tagging technique described in Section 6.3 measures the charm efficiency directly on the data while taking the uds efficiency and the b tagging correlations from simulation. This leads to a residual uncertainty on the charm efficiency which is estimated from a set of correction functions with varied simulation inputs. The uds efficiency is closely related to the detector resolution of which the consistent variation has already been discussed.

The b tagging hemisphere correlations k_j were measured in the DELPHI R_b measurement [46] and their uncertainties studied in detail. It was found that angular effects, gluon radiation and to a lesser extent also B physics modelling had a total effect of $\pm 20\%$ on the correlation. In this analysis the correlations k_j were varied by $\pm 20\%$ and the effect of this variation on the calculated flavour efficiencies and fractions was propagated through the A_{FB}^b analysis.

The calibration functions that are applied to simulated charm events in the barrel and forward regions are displayed in Fig. 9.1 for the working point correction and for the re-calculated correction with varied correlations, varied detector resolution and varied LEP/SLD inputs. Different detector conditions in the years 1992+93 and 1994+95 as well as the barrel and forward range result in slightly different correction functions. At low $b\text{-tag}_{\text{hem}}$ values where charm is an important background, the variation of the resolution modelling

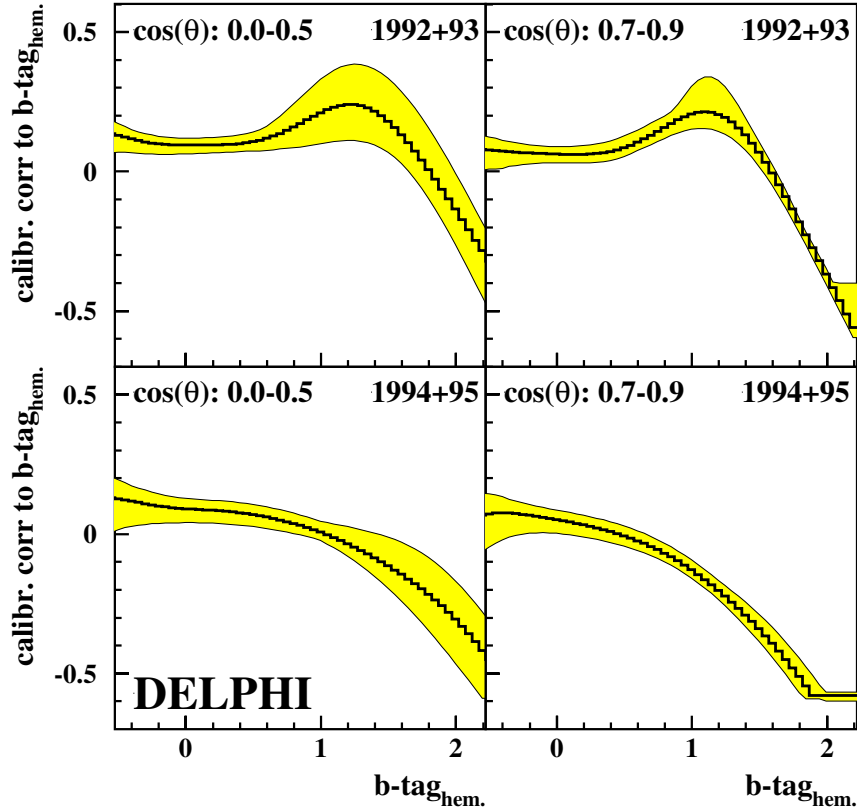


Figure 9.1: The values of the c efficiency correction function applied to the $b\text{-tag}_{\text{hem}}$ variable on simulated c events. They are shown for the two most important year periods and for events in the central and forward regions of the detector. For each systematic variation that affects the b tagging calibration the functions were re-calculated, leading to slightly shifted shapes. The maximal and minimal correction found for any variation span the error band, namely the resolution variation at $b\text{-tag}_{\text{hem}}$ below 0.5 and the correlation variation elsewhere.

has the largest impact on the calibration correction. At higher $b\text{-tag}_{\text{hem}}$ values the variation of the b tagging hemisphere correlation becomes dominant. However there the charm background is already so much reduced that the total impact on the analysis remains low, leading to a small contribution to the systematic uncertainty on A_{FB}^b .

- The **b quark charge identification probability** is measured directly from data using the double tagging technique described above. Small correlations between the probability in each $\cos\theta_{\bar{f}}$ bin and A_{FB}^b via the double tagged opposite sign events are therefore automatically taken into account. The statistical uncertainties of the charge identification probabilities w_b and w_b^D are determined in the χ^2 -fit and are included in the statistical error on A_{FB}^b .
- The probability for **identifying the quark charge in background events** determines directly the background asymmetry correction. This correction is dominated by the c quark asymmetry correction, which itself enters with

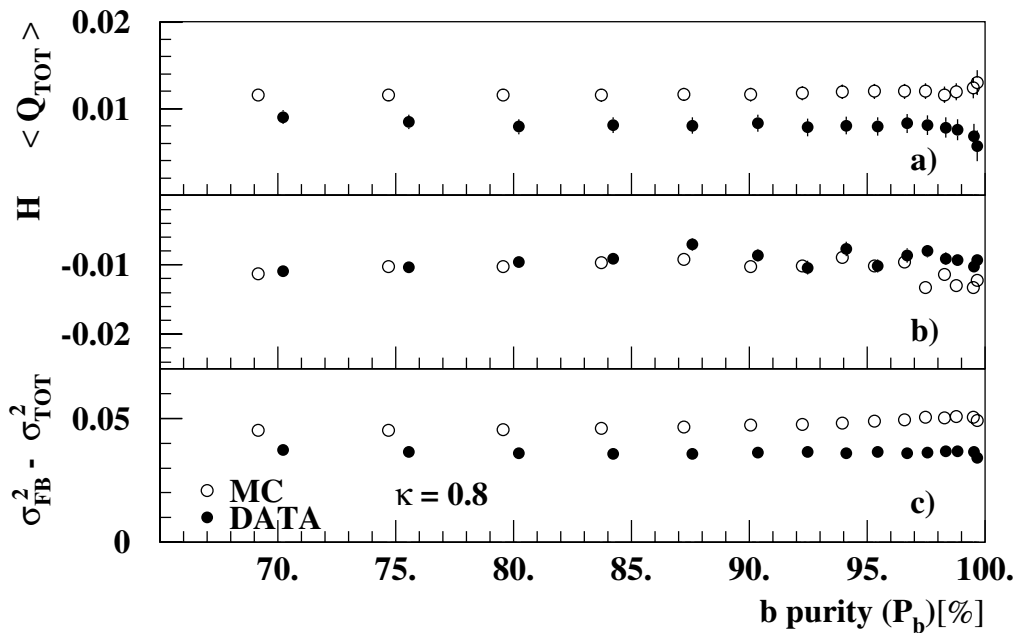


Figure 9.2: A comparison of data and simulation for observables that enter the determination of the hemisphere correlations in the A_{FB}^b measurement based on a single jet charge variable [69].

opposite sign, while the effects of the light quark charge asymmetry partly compensate. Events with exclusively reconstructed D mesons have been used in Section 8.3.3 to correct the simulated $w_c^{(D)}$ on the data. The statistical uncertainty on the scaling factor to $2w_c - 1$, 0.71 ± 0.15 , from the measurement based on the exclusively reconstructed D mesons is used to determine the uncertainty on w_c in the asymmetry measurement.

The correction for light quarks has to be taken entirely from simulation. As a consequence, the Neural Network charge tag is sensitive to the details of vertexing in uds events. From the distributions of the Network inputs and the $flav_{hem}$ output variable at different b purities there is no indication that the light quark charge tagging is not correctly simulated. Nevertheless the full uds correction is chosen as a conservative error.

- The **charge tagging hemisphere correlations** are an important source of systematic uncertainty. The hemisphere charge correlations δ and β for this measurement are introduced by the jet charge as discussed in section 8.3.2. In reference [69] the hemisphere correlation for the jet charge at different values of κ have been studied on the data themselves. They entered the determination of the b charge separation δ_b as a small correction, MC_{cor} , via

$$\sum_f p_f \delta_f = \sigma_{FB}^2 - \sigma_{TOT}^2 + \langle Q_{FB} \rangle^2 + MC_{cor} \quad (9.1)$$

Fig. 9.2 shows the observed difference in the widths of charge flow, σ_{FB}^2 , and total charge, σ_{TOT}^2 , as a function of b purity for data and simulation. A clear discrepancy between data and simulation is visible, which was attributed to the positive charge bias from secondary interactions with the detector material.

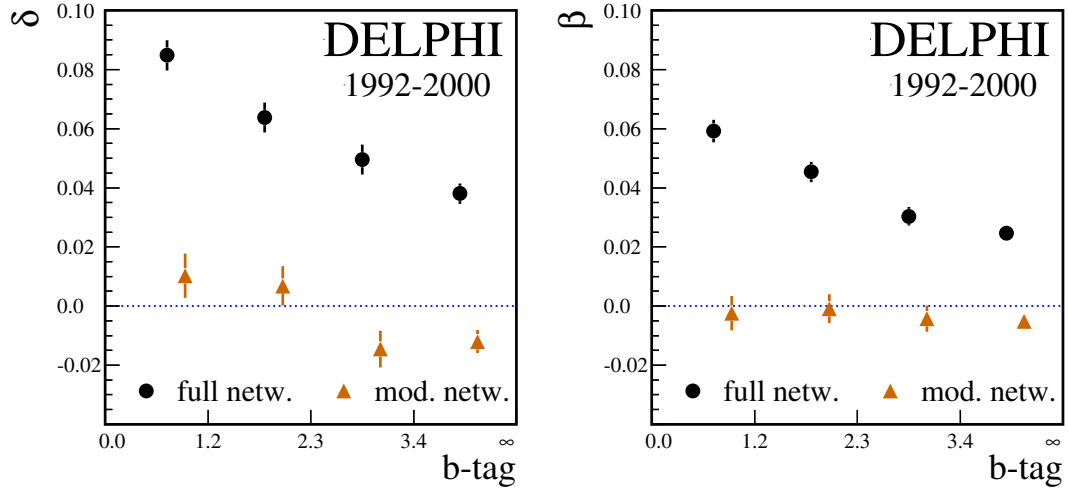


Figure 9.3: The hemisphere charge correlations for the on-peak data of 1992-2000 versus the interval in b -tag. The results using the full hemisphere charge tag (full dots) are compared to a modified version of the Neural Network (triangles) in which the jet charge with $\kappa = 0.3$ was taken out.

This charge bias is quantified by the mean sum of the two jet charges, $\langle Q_{\text{TOT}} \rangle$, which shows a similar discrepancy. On the other hand, the product of the jet charges, $\langle Q_{\text{F}} Q_{\text{B}} \rangle$ is related to the hemisphere correlation. In order to remove the charge bias and its poor description by simulation from this product, the modified observable

$$H = \langle Q_{\text{F}} Q_{\text{B}} \rangle - \frac{1}{4} \langle Q_{\text{TOT}} \rangle^2 \quad (9.2)$$

is constructed. It is very sensitive to the charge correlation between the jet charges and, as can be seen in Fig. 9.2, is sufficiently well modelled by the simulation. From the remaining differences between data and simulation, an uncertainty of $\pm 20\%$ was assigned to the correlation MC_{cor} . As the jet charge is the main source of hemisphere correlation, and the same simulated data used in both analyses, the uncertainty of $\pm 20\%$ was equally assumed for δ and β in this analysis. Additional checks, which will be discussed in the following, have confirmed that a variation of $\pm 20\%$ covers all effects related to the hemisphere charge correlations.

These checks comprised replacing the $\cos \theta_{\vec{T}}$ -dependent correlation values by the mean correlations from Table 8.2, once computed with the outliers and once without. The shifts in the measured asymmetry amounted to 0.2 and 0.4 times the systematic error due to the $\pm 20\%$ modelling uncertainty. Possible effects due to the outliers consequently are well covered by existing systematic uncertainties, and no additional error was assigned.

For the measurement discussed here the size of the hemisphere correlation is given by the relative weight of the jet charge and the vertex based charge information. This variation is explicitly allowed for using intervals in b -tag, as for high values of b -tag good vertexing information is present in the event and consequently the hemisphere correlations are small. The correlations δ and β as a function of the b -tag interval are shown as the full dots in Fig. 9.3.

As already mentioned before, the correlations arise mainly from charge conservation in the event and are introduced into the analysis mainly via the jet charge at $\kappa = 0.3$, which is sensitive to tracks with low momenta. The possibility used in Fig. 8.4 to remove the jet charge from the inputs to the Neural Network has also been exploited to test the stability of the central value directly. Fig. 9.3 displays the mean hemisphere correlations versus the intervals in b -tag once for the full Neural Network as used throughout the analysis and once for the modified Network (full triangles) with $Q_J(\kappa = 0.3)$ taken out. For the modified Neural Network the correlations are close to 0. When using the modified hemisphere charge Network, the $A_{\text{FB}}^b(91.231 \text{ GeV})$ result shifts by $+0.0011$. This is 0.6σ of the expected statistical variation comparing the data samples selected by the modified and the full charge tag. The shift corresponds to $+1\sigma$ in the systematic error quoted for the $\pm 20\%$ uncertainty related to the hemisphere correlation.

- In light quark events a **gluon splitting** into a $c\bar{c}$ pair or $b\bar{b}$ pair gives rise to lifetime information from the decays of the produced heavy quark hadrons. A variation of the splitting rates within the errors on the present world averages $g \rightarrow c\bar{c} = (2.96 \pm 0.38)\%$ and $g \rightarrow b\bar{b} = (0.254 \pm 0.051)\%$ [23] is included in the systematic error.
- Decays of **\mathbf{K}^0 and Λ** in flight lead to tracks with large impact parameters with respect to the primary vertex and consequently can lead to lifetime information in light quark events. The rate of such decays in light quark events was varied by $\pm 10\%$ to estimate the effect on the light quark efficiency ϵ_{uds} .
- The size of the **QCD correction** is theoretically known to be 0.0354 ± 0.0063 [75]. The experimental bias of the full analysis on the QCD correction has been discussed in section 8.4. Therefore the systematic uncertainty due to the QCD correction receives two contributions, one given by the statistical precision with which the QCD bias was estimated on simulation, the other one is given by the theoretical error multiplied by the experimental bias.

In Fig. 8.4 the hemisphere correlations β and δ are shown with and without applying a cut of thrust > 0.9 . The differences are due to effects from gluon radiation. Hence the correction for the hemisphere correlations includes an implicit QCD correction. The variation of the hemisphere correlation as a function of the thrust cut has been investigated in more detail, yielding the result shown in Fig. 9.4. From this observed thrust dependence the bias on the QCD correction within the hemisphere correlations is estimated to be 50%. This estimation was obtained as follows. Fig. 9.4 shows a $\simeq 30\%$ decrease in δ, β when going from the working point (no cut) to the maximal cut on the thrust value. The decrease represents 1.5 times the modelling uncertainty of $\pm 20\%$ and hence corresponds to a shift in A_{FB}^b of 0.0017. This number is half the QCD correction quoted above. The additional bias factor has to be taken into account for the systematic error due to the theoretical uncertainty, adding 0.00031 to the value obtained from the study that uses only the simulated QCD bias. This procedure provides a safe estimation of a type of systematic uncertainty which is common to all LEP A_{FB}^b measurements and therefore determined with great care.

- The contribution to the total error due the **limited simulated sample size** can be estimated by dropping from the χ^2 -fit the statistical uncertainties from

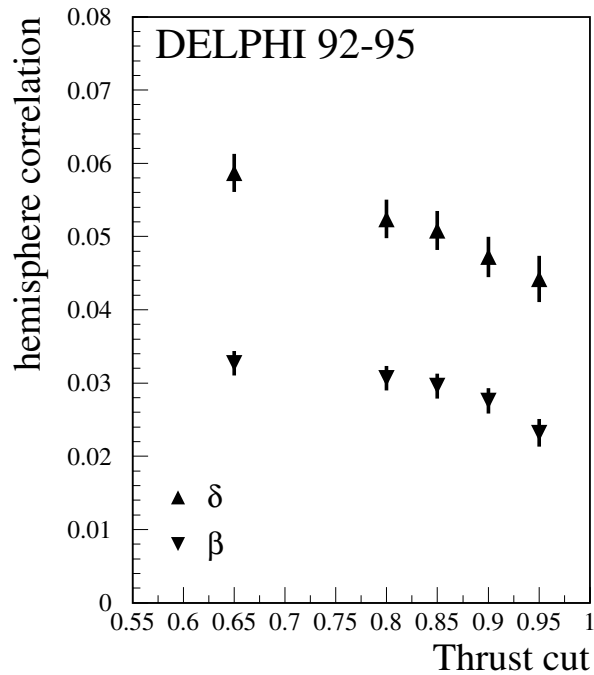


Figure 9.4: The mean hemisphere correlations versus cut on thrust.

the simulation. It is quoted separately from the pure statistical error of the data.

All contributions to the systematic error are summarised in Tables 9.1 and 9.2. They are quoted for the entire set of analysed events, i.e. averaged over years and bins in b -tag according to the weight of the A_{FB}^b result in the combined result. While the systematic uncertainties are relatively constant over the years, they clearly depend on the b purity. Six of the most significant contributions are displayed as a function of b purity together with the total systematic error in Fig. 9.5. The latter drops by a factor of $\simeq 4$ when going from 74% b purity to 99.7%. Using the p_b -dependent uncertainties in conjunction with the statistical error to obtain the combined A_{FB}^b result internally increases the weight of the highest purity bin and significantly contributes to the stability of the final result.

9.1 Additional Tests

The fit to A_{FB}^b is performed in four intervals in b -tag with averaged b purities ranging from 74% up to 99.7%. This takes into account a correlation between b and charge tagging by permitting a purity dependence in quantities related to the latter, such as $w_b^{(D)}$ and δ , β . Furthermore, a varying dependence on detector modelling, residual backgrounds and the hemisphere charge correlations (see Fig. 9.3) leads to a systematic error that decreases with increasing purity. Fig. 9.6 illustrates the stability of the 1992-2000 combined A_{FB}^b measurement as a function of b purity.

The QCD correction and light quark fragmentation modelling are dominant systematic uncertainties in the LEP average A_{FB}^b results [24]. Also this measurement is

contribution	variation	$\Delta A_{\text{FB}}^b \times 10^2$
		92-2000
detector resolution	see text	± 0.035
hemisphere b -tag correlations	$\pm 20\%$	± 0.011
c charge separation	see text	± 0.025
uds charge identification	full effect	∓ 0.048
hemisphere charge correlations	$\pm 20\%$	± 0.107
gluon splitting $g \rightarrow b\bar{b}$	0.00235 ± 0.00051	± 0.005
gluon splitting $g \rightarrow c\bar{c}$	0.0296 ± 0.0038	< 0.0001
rate of K^0/Λ	$\pm 10\%$	± 0.006
error on QCD bias	see text	± 0.022
uncertainty of QCD correction	see text	± 0.040
statistical error of simulation		± 0.016
total systematic error		± 0.14

Table 9.2: Systematic uncertainties and their influence on the determination of A_{FB}^b .

subject to gluon radiation entering via the hemisphere correlations and the sensitivity to the QCD correction. To test if this is correctly taken into account a cut on the thrust variable T was introduced and the full analysis was repeated with different settings of the cut value. Assuming the rejected events at a thrust cut $T > x$ to cause the loss in precision, the uncorrelated statistical error is obtained from the quadratic difference to the statistical precision of the full sample,

$$\sigma^2 \left(\Delta A_{\text{FB}}^b \right)_{\text{uncorr.}} = \sigma^2 \left(A_{\text{FB}}^{b, T > x} \right) - \sigma^2 \left(A_{\text{FB}}^{b, \text{no cut}} \right) . \quad (9.3)$$

The results of this check are displayed in Fig. 9.7 with both correlated and uncorrelated statistical errors. The full data-set of 1992 to 2000 at all three centre-of-mass energies was used to make the test as sensitive as possible. No dependency on the thrust cut could be found.

Another study covered the positive charge bias that is introduced by the presence of hadronic interactions with matter in the detector. In this analysis the sample of double like-sign events was split up into events with both hemispheres tagged positive, N_{++} , and both negative, N_{--} . A charge asymmetry

$$A_{++--}^{\text{obs.}} = \frac{N_{++} - N_{--}}{N_{++} + N_{--}} \quad (9.4)$$

was then formed which is displayed in Fig. 9.8 versus the bin in $\cos \theta_{\vec{T}}$ for the sum of all peak data-sets. Although tracks from secondary interactions are suppressed by both DELPHI track reconstruction and the analysis package for b physics, a residual charge bias can be seen. In simulation the charge bias is found to be significantly larger than in the real data. No dependence on $\cos \theta_{\vec{T}}$ was observed. Being constructed as the difference of two charges or count rates, the asymmetry is not sensitive to such a charge bias, as was verified on simulation.

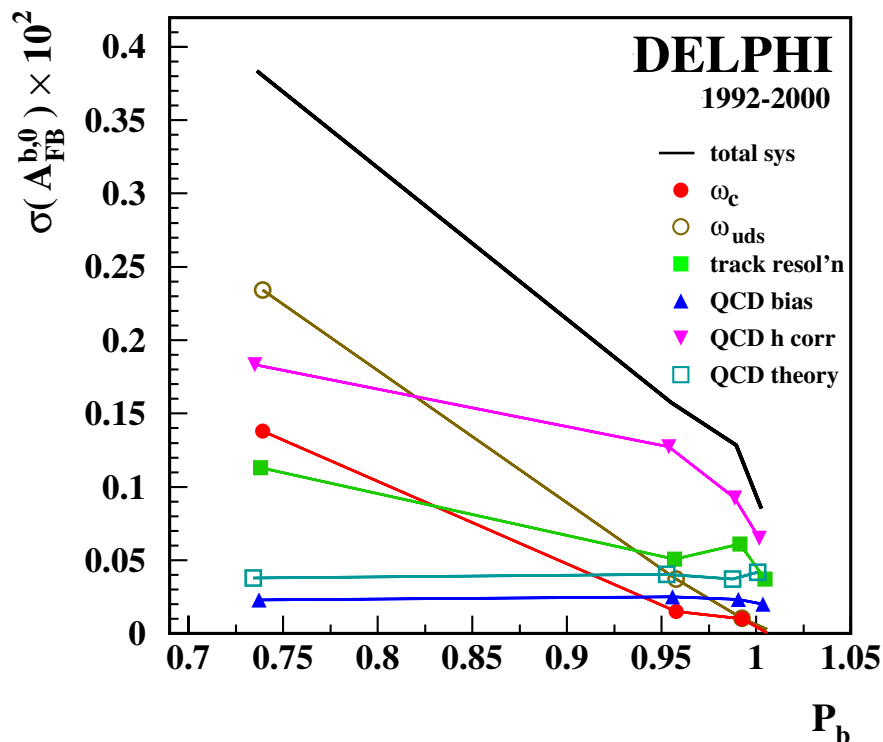


Figure 9.5: The most significant contributions to the systematic error as a function of b purity.

Three cross-checks have been performed on the simulation to verify if there is any bias remaining in the analysis method. The b quark asymmetry was measured on simulated data by feeding into the analysis the full set of simulated udsqb events instead of real data. External calibration corrections such as for ε_c and w_c were switched off for this test. The result of $A_{\text{FB}}^{b,\text{sim.}} = 0.1083 \pm 0.0017$ has to be compared with the true value¹ of $A_{\text{FB}}^{b,\text{truth}} = 0.11005 \pm 0.00105$ which was obtained by analysing the truth information about the b quark production angle in charge tagged events. The actual cross-check using the full simulation treated as real data receives additional uncorrelated information entering via the method, i.e. the calculation of the fractions, the double charge tagging, and the background subtraction using additional events (c and uds). Consequently the uncorrelated statistical error can be calculated via Eq. 9.3. This leads to the conclusion that the refitted and the true simulated asymmetry still agree within 1.3σ .

The second cross-check has investigated the influence of a bias due to small non-linear effects in double-tagging methods. Such effects were suspected in other analyses and are known to possess a $1/n$ dependence, where n is the number of events in the sample [78]. A $1/n$ -dependent bias becomes visible when, for example, the result from the method applied to the large 1994 simulated data-set is compared to the combined result from ten independently analysed, equal-sized subsets of the same data. This exercise was performed, and repeated ten times with differently formed subsets in order to achieve statistical precision on the bias. After translating to the actual event numbers in the independently analysed sets of real data using the $1/n$

¹It should be noted that the value of 0.11, which was implemented once into the event generator, obviously does not represent today's knowledge!

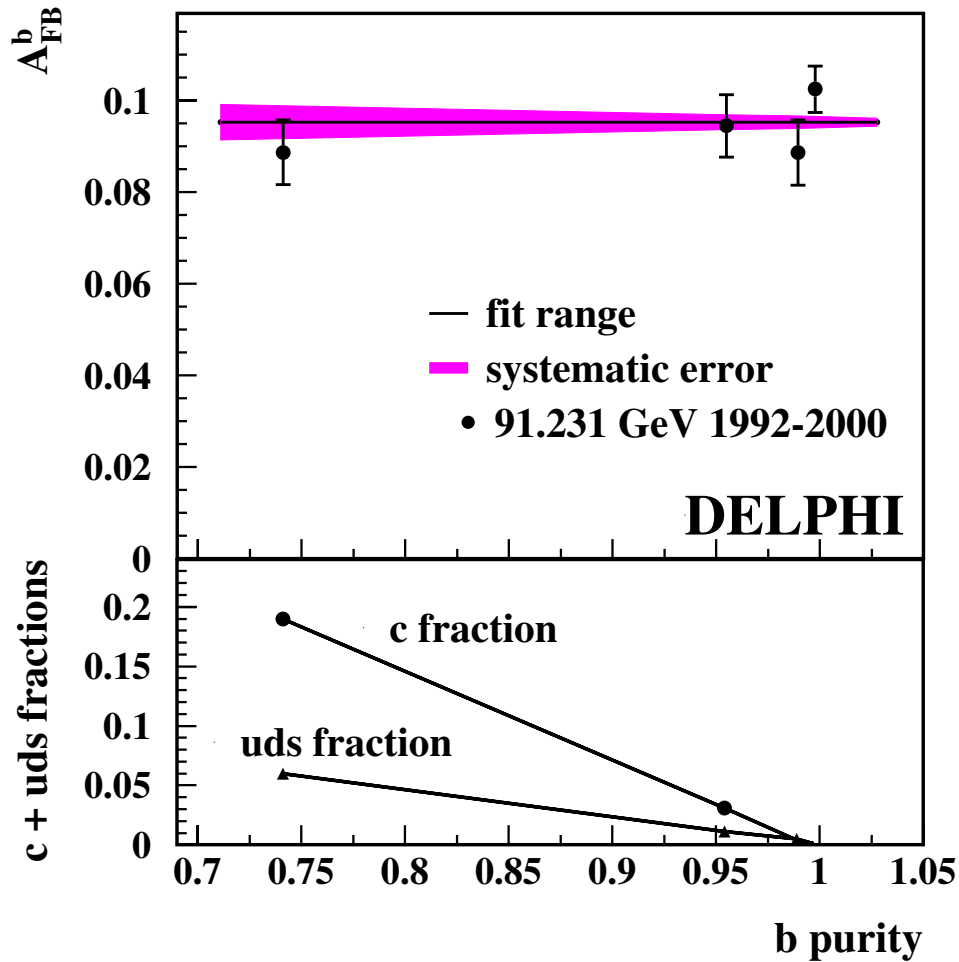


Figure 9.6: The peak asymmetry for the combined years 1992-2000 obtained on event samples with different b purity. The data points are the results from Fig. 8.10 in comparison with the 1992-2000 fit result. The band shows the systematic error as a function of the b purity. The lower plot illustrates how the background is composed of c and light quarks events.

dependence, the full result for A_{FB}^b is assumed to have a bias of $+0.00011 \pm 0.00004$. It amounts to less than a tenth of the systematic error and is thus neglected. Finally it has been verified that the number of bins into which the $\cos \theta_{\vec{r}}$ range is split has no influence on the central value of the result.

In the analyses that make use of only the jet charge as tagging variable it was found that exploiting the charge as a weight instead of a mere discriminator improves on the statistical precision. That approach has also been studied in this analysis by measuring A_{FB}^b on different classes defined by intervals in the absolute value $|flav_{hem}|$, thus taking into account varying sensitivities to the quark charge between each class. The gain in the statistical error of the modified analysis is negligible while losing the good control of calibration techniques and residual systematic uncertainties. So this approach was dropped.

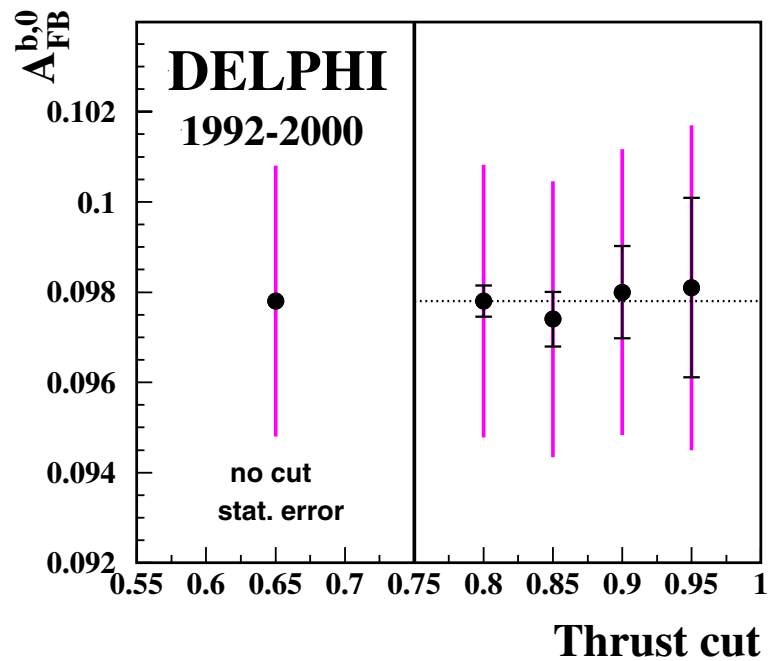


Figure 9.7: The b quark pole asymmetry for different cuts on the thrust value. It is compared to the final result from all three centre-of-mass energies which does not use any thrust cut (left hand side). The small error bars with the serifs show the uncorrelated statistical error estimated from the quadratic difference of the correlated errors.

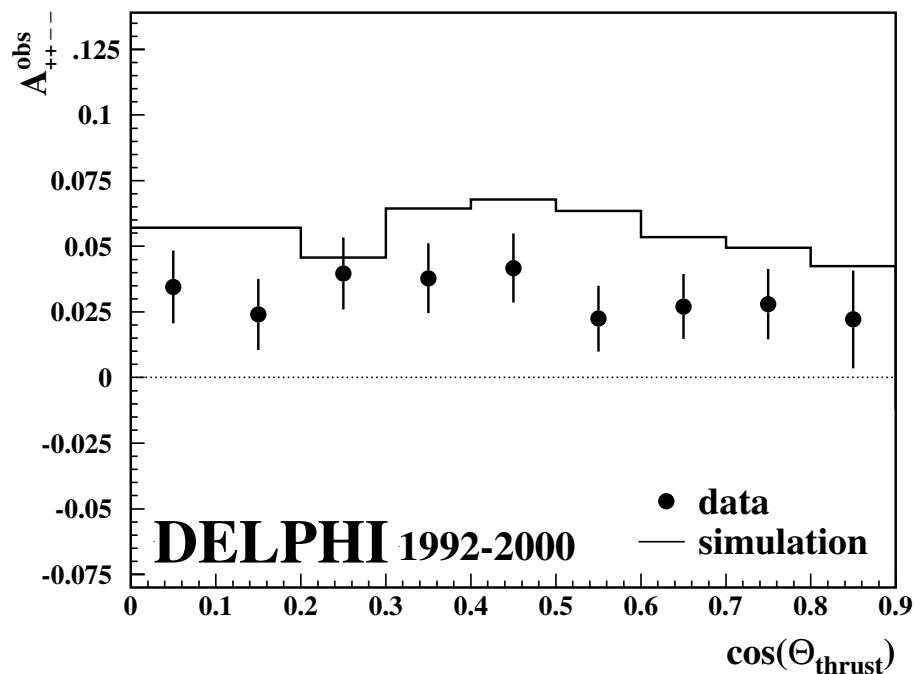


Figure 9.8: The asymmetry between double positive and double negative tagged events illustrates the charge bias observed in this analysis. The effect is less distinct in real data.

Chapter 10

Results and Their Interpretation

10.1 The Results for A_{FB}^{b}

This measurement of A_{FB}^{b} uses an enhanced impact parameter b tagging algorithm and an inclusive b quark charge tagging Neural Network. The analysis is based on the LEP 1 data collected with the DELPHI detector from 1992 up to 1995 and the LEP 2 calibration runs at the Z pole from 1996 to 2000. The measured b quark forward-backward asymmetries for the individual years of data taking are:

year	\sqrt{s} [GeV]	A_{FB}^{b} (\pm stat. \pm syst.)
1992	91.280	$0.0984 \pm 0.0079 \pm 0.0018$
1993 peak-2	89.431	$0.0803 \pm 0.0216 \pm 0.0022$
1993	91.225	$0.1130 \pm 0.0095 \pm 0.0021$
1993 peak+2	93.015	$0.0817 \pm 0.0177 \pm 0.0021$
1994	91.202	$0.0952 \pm 0.0048 \pm 0.0014$
1995 peak-2	89.468	$0.0506 \pm 0.0191 \pm 0.0020$
1995	91.288	$0.0895 \pm 0.0084 \pm 0.0020$
1995 peak+2	92.965	$0.1213 \pm 0.0152 \pm 0.0035$
1996-2000	91.260	$0.0870 \pm 0.0083 \pm 0.0018$

The 1995 peak+2 systematic error receives slightly increased contributions from the hemisphere correlation and the detector resolution variation. These measurements are QCD corrected. The final result is obtained taking correlated systematic errors into account:

$$\begin{aligned}
 A_{\text{FB}}^{\text{b}}(89.449 \text{ GeV}) &= 0.0637 \pm 0.0143(\text{stat.}) \pm 0.0017(\text{syst.}) , \\
 A_{\text{FB}}^{\text{b}}(91.231 \text{ GeV}) &= 0.0958 \pm 0.0032(\text{stat.}) \pm 0.0014(\text{syst.}) , \\
 A_{\text{FB}}^{\text{b}}(92.990 \text{ GeV}) &= 0.1041 \pm 0.0115(\text{stat.}) \pm 0.0024(\text{syst.}) .
 \end{aligned}$$

From this measurement the Z pole b quark asymmetry is extracted (for definition see Section 2.6). Two corrections for QED: photon exchange and Z/ γ interference amount to +0.0041 and -0.0003 , respectively [24]. A shift of -0.0008 is applied to correct for the energy dependence of the asymmetry when going from 91.231 GeV to $\sqrt{s} = m_Z$. This yields:

$$A_{\text{FB}}^{0,b} = 0.0988 \pm 0.0032(\text{stat.}) \pm 0.0014(\text{syst.}) .$$

Assuming a Standard Model like energy dependence, the results from the two energy points above and below the Z peak can be included in the pole asymmetry:

$$A_{\text{FB}}^{0,b} = 0.0978 \pm 0.0030(\text{stat.}) \pm 0.0014(\text{syst.}) .$$

A comparison with previous determinations of $A_{\text{FB}}^{0,b}$ from the DELPHI data and with the results from other LEP experiments will be given in the following Section. Using equations 2.33–2.35 for the effective electroweak mixing angle $\sin^2 \theta_{\text{eff}}^\ell$ yields:

$$\sin^2 \theta_{\text{eff}}^\ell = 0.23230 \pm 0.00054$$

Here it should be noted that, apart from the pure interest in quantities defined within the Standard Model, there is another important reason for transforming the measured b quark asymmetry into a result for the Z pole asymmetry and the related mixing angle. This reason is the wish, or even need, to combine the results from all available experiments in order to obtain a higher accuracy in $\sin^2 \theta_{\text{eff}}^\ell$ and hence make the test of the electroweak sector of the Standard Model much more stringent. Similar principles of combining measurements are applied when other electroweak quantities like the W and Z boson properties are determined. Such a combination requires a reduction of the many direct observables, which are measured by different experiments at different centre-of-mass energies in different processes, to a set of commonly defined electroweak precision observables. The latter are often denoted as *pseudo-observables* because their derivation involves applying corrections which are specific to each experiment and partly require a residual input from the Standard Model. The results of the combination procedure performed by the LEP Electroweak Working Group are presented and interpreted in Section 10.3.

10.2 The DELPHI Combined Results for $A_{\text{FB}}^{0,b}$ and $A_{\text{FB}}^{0,c}$

Precision measurements of the b quark forward-backward asymmetry are obtained in DELPHI from three independent methods, differing mainly in the way the b charge is reconstructed. They are based on the lepton charge in semileptonic B decays [52], on the jet charge [69] in b tagged events or on the Neural Network charge tag in the analysis presented here. The results for all three measurements are compared in Table 10.1, showing a good mutual agreement. The quality of the agreement and statistical correlations between the measurements will be discussed in the following.

The inclusive analysis, which uses Neural Networks to combine the full charge information, is an improved method with respect to the one that is based only on the jet charge. Both measurements yet are performed on a common data-set (1992-1995) and the jet charge variable also forms an important input to the Neural Network. A high statistical correlation therefore exists between the two results. By including additional discriminating variables in the b- and charge tag, on the other hand, the Neural Network method improves on the precision by a factor of 1.36. Events that predominantly have a signal in these additional and only loosely correlated variables therefore do not only add to the sensitivity of the entire measurement, but also enter

method	data sets	$A_{\text{FB}}^{0,b}$
lepton charge	1991-95	$0.1021 \pm 0.0052 \pm 0.0024$
jet charge	1992-95	$0.1012 \pm 0.0044 \pm 0.0015$
Neural Network	1992-2000	$0.0978 \pm 0.0030 \pm 0.0014$

Table 10.1: Results of the three most precise $A_{\text{FB}}^{0,b}$ measurements performed on the DELPHI data at the three centre-of-mass energies 89.449, 91.231 and 92.990 GeV.

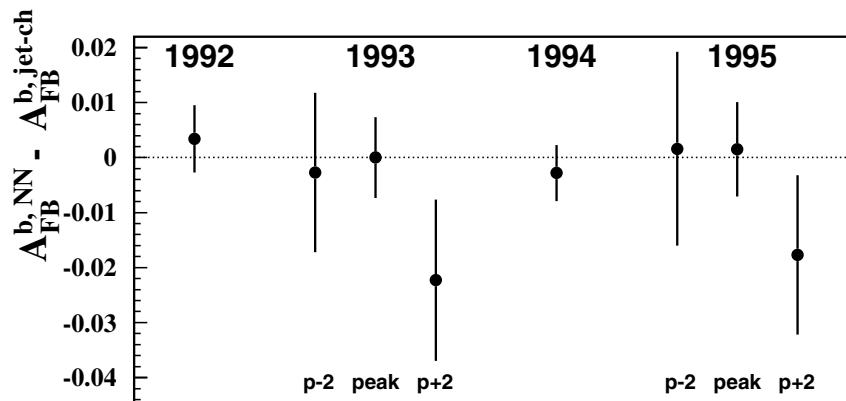


Figure 10.1: Direct comparison between the A_{FB}^b results from the jet-charge and from the Neural-Network based analyses. The uncorrelated components of the statistical errors are shown.

with different weight in the determination of the result, allowing it to differ from the previous result. The size of the possible deviation is limited by the fraction of this uncorrelated information in the measurement result. In a simple approximation, this fraction is assumed to be solely responsible for the gain in precision, so that it can be determined from the gain using the argument of Eq. 9.3. The difference between the jet-charge (JC) and Neural-Network (NN) based analyses is evaluated in this way in Fig. 10.1. Any observed differences are compatible with statistical fluctuations.

As mentioned above, the measurements analyse common data sets and employ similar basic techniques, such as the b tagging, the jet charge and the charge of identified leptons. Hence there are statistical correlations between the three analyses that need to be taken into account when the LEP data are combined and the electroweak observables determined. These correlations have been evaluated by monitoring common fluctuations on the large 1994 simulated data set, which was divided into $n = 100$ sub-samples for that purpose. For the example of the jet-charge and Neural-Network based analyses, the correlation coefficient, ρ , is determined by:

$$\rho = \frac{1}{n} \cdot \sum_{i=1}^n \frac{A_{\text{FB}}^{b,\text{NN}}(i) - \langle A_{\text{FB}}^{b,\text{NN}} \rangle}{\sigma(A_{\text{FB}}^{b,\text{NN}}(i))} \cdot \frac{A_{\text{FB}}^{b,\text{JC}}(i) - \langle A_{\text{FB}}^{b,\text{JC}} \rangle}{\sigma(A_{\text{FB}}^{b,\text{JC}}(i))} . \quad (10.1)$$

The $A_{\text{FB}}^{b,\text{JC/NN}}(i)$ are the results obtained on every sub-sample, i . They are displayed

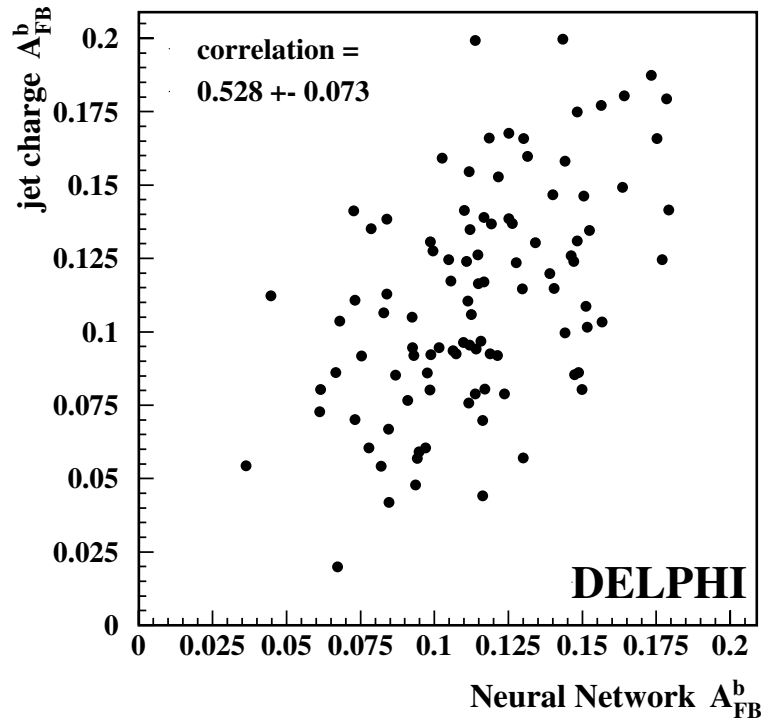


Figure 10.2: The mutual correlation between the DELPHI b quark asymmetry measurements is determined by analysing fluctuations on a set of 100 sub-samples, which the 1994 simulation was divided into. Here the results for the jet-charge and the Neural-Network based method are displayed.

in Fig. 10.2. During this procedure it was checked that the mean, $\langle A_{FB}^{b,*} \rangle$, and r.m.s. of the 100 measurements correspond to the result and its statistical error which were obtained on the whole, undivided simulated data sample. The $\chi^2/n.d.o.f.$ for the average over the 100 samples were 0.98, 1.07, 0.93 for the respective analyses using jet charge, Neural Network, or lepton charge. The precision of the estimated correlation is limited by the number of sub-samples the data could be divided into,

$$\sigma(\rho) = (1 - \rho^2)/\sqrt{n - 1} \quad . \quad (10.2)$$

The resulting values for the correlation are summarised in Table 10.2.

The analysis by means of the lepton charge in semileptonic B and D decays involves a correlation to charm, which is given in Table 10.2 as well. Therefore the combined DELPHI results for the b and c asymmetries are determined simultaneously, taking into account these statistical correlations as well as correlated systematic errors. The c and b asymmetry measurements from exclusively reconstructed D mesons [71] are also included in the combination. This combination gives the following values and their total errors

$$A_{FB}^{0,b} = 0.0990 \pm 0.0029, \quad A_{FB}^{0,c} = 0.0706 \pm 0.0068$$

with a χ^2/ndf of 11.2/(21 - 2) and a total correlation of -0.050 between them.

	A_{FB}^{b} N. N.	A_{FB}^{b} lepton	A_{FB}^{c} lepton
A_{FB}^{b} N. Netw.	1	0.29 ± 0.09	-0.05 ± 0.10
A_{FB}^{b} jet-ch.	0.53 ± 0.07	0.31 ± 0.09	-0.15 ± 0.10
A_{FB}^{b} leptons	0.29 ± 0.09	1	+0.22

Table 10.2: Correlations between the different methods used in DELPHI to determine the b asymmetry. The analysis using prompt leptons is optimised to measure both A_{FB}^{b} and A_{FB}^{c} at the same time, and hence determines the statistical correlation between the two observables internally [52].

10.3 Interpretation

The DELPHI inclusive measurement of A_{FB}^{b} , which has been presented in this thesis and published in reference [80], is included in the LEP combined result for the b quark pole asymmetry $A_{\text{FB}}^{0,\text{b}}$. The individual results for the lepton and inclusive analyses from each of the four LEP experiments are shown in Fig. 10.3. The results represent the status of summer 2003 and are very consistent with each other [81]. Separated according to the two types of analysis, the results are:

$$\begin{aligned} \text{inclusive} \quad A_{\text{FB}}^{0,\text{b}} &= 0.1000 \pm 0.0019 \\ \text{leptons} \quad A_{\text{FB}}^{0,\text{b}} &= 0.1000 \pm 0.0025 \end{aligned}$$

with an average statistical correlation between the inclusive and lepton analysis of $\simeq 25\%$. By taking into account statistical correlations and common systematic errors as well as off-peak measurements (Fig. 10.4) in cases where available one obtains the LEP combined result of

$$\langle A_{\text{FB}}^{0,\text{b}} \rangle = 0.0997 \pm 0.0016 \quad . \quad (10.3)$$

The correlated systematic error arises from mainly physics like the QCD correction and light quark fragmentation. Its value of 0.0004 is quoted in Fig. 10.3 and turns out to be very small.

The LEP result for peak+2, which is incorporated in the combined pole asymmetry result, is slightly low compared to the Standard Model expectation. The low result is not only caused by the DELPHI inclusive measurement based on Neural Networks, but is partly seen also by the other LEP experiments: the combined peak+2 result in Fig. 10.4 deviates by the same $\simeq 2\sigma$ as did the DELPHI result in Fig. 8.14. This tendency is also present with the high-energy data taken during the LEP 2 phase. At LEP 2 energies between 130 and 209 GeV, the forward-backward asymmetry is mainly caused by the quantum-mechanical interference between Z and photon exchange. Its measurement is generally performed using an inclusive jet charge technique on b-tagged events similar to the one applied at the Z pole. Additional corrections are necessary for the residual presence of initial state radiation and background of four-fermion final states. Full technical and experimental details are given in Appendix C for the case of the DELPHI measurement. Fig. 10.5 shows the LEP 2 combined result in comparison with the Standard Model prediction from ZFITTER. Above

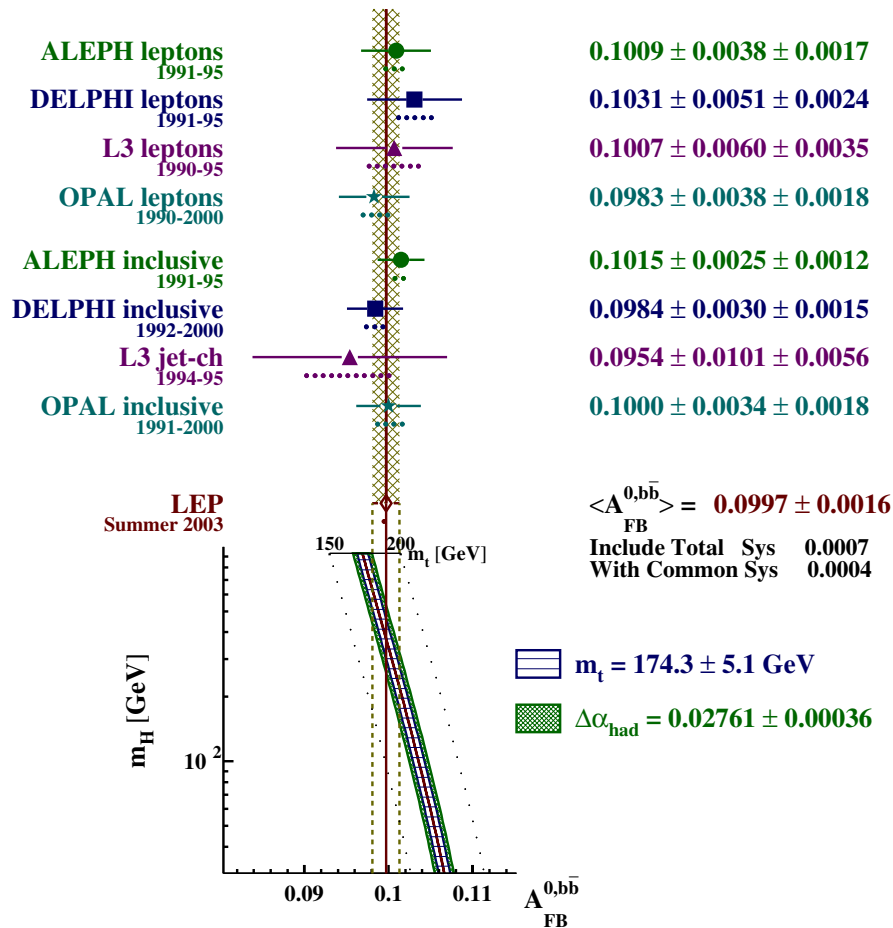


Figure 10.3: The b asymmetry measurements from the four LEP experiments. The contribution called “DELPHI inclusive” is the result from this thesis. The combined result is taken from the fit to all electroweak data obtained from heavy quark measurements, which was presented at the summer conferences of 2003 [81].

160 GeV the b -quark asymmetry is nearly independent of centre-of-mass energy. By taking into account the remaining small \sqrt{s} -dependence, an average asymmetry can be formed and the comparison made more stringent. The averaged discrepancy with respect to the Standard Model prediction is -1.56σ [82].

According to Section 2.6, the measurement of $A_{\text{FB}}^{0,b}$ can be used together with direct lepton A_{FB} measurements and A_{LR} from SLD [83] to determine the polarisation parameter \mathcal{A}_ℓ and consequently the *leptonic* electroweak mixing angle, $\sin^2 \theta_{\text{eff}}^\ell$. The quantity A_{LR} is the asymmetry between the Z boson cross-section produced by left and right longitudinally polarised electrons. At SLD this asymmetry can be measured due to the use of polarised electron beams in the SLC accelerator. The method to determine A_{LR} requires no detailed final state event identification and is insensitive to all detector acceptance and efficiency effects, consequently yielding a very high precision. The measurement of A_{LR} provides a direct determination of the polarisation parameter \mathcal{A}_e . In a similar way, the SLD measurement of the polarised forward-backward asymmetry, $A_{\text{FB,LR}}^b$, determines \mathcal{A}_b independently of other quan-

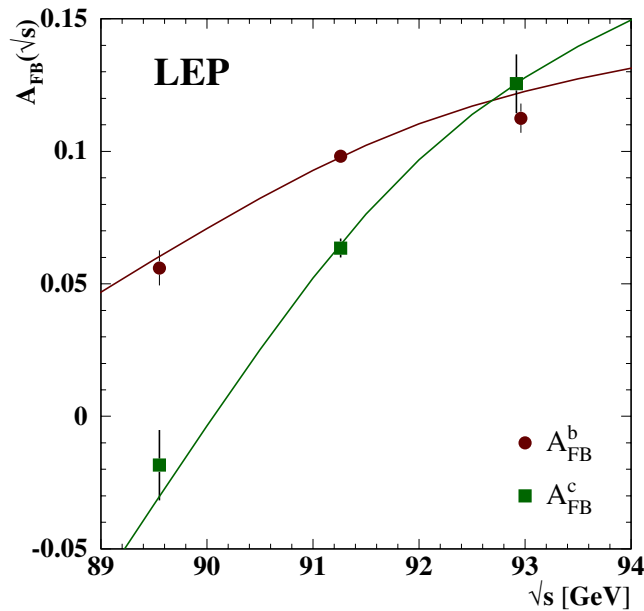


Figure 10.4: The LEP combined b and c quark asymmetries as a function of centre-of-mass energy \sqrt{s} .

tities [84]. Fig. 10.6 displays the combined LEP and SLD results for the lepton polarisation parameter, \mathcal{A}_ℓ , in comparison with \mathcal{A}_b from SLD. The results have a region of common overlap with the combined $A_{\text{FB}}^{0,b}$ from LEP if both \mathcal{A}_b and \mathcal{A}_ℓ are free parameters. Although the overlap region agrees poorly with the Standard Model expectation, the single results and especially $A_{\text{FB}}^{0,b}$ from LEP are well compatible with the expectation.

All of the above results for \mathcal{A}_ℓ and the product $\mathcal{A}_e \cdot \mathcal{A}_b$ can be turned into a determination of $\sin^2 \theta_{\text{eff}}^\ell$ with only minimal model-specific assumptions. These assumptions comprise lepton universality, which is already inherent in the definition of $\sin^2 \theta_{\text{eff}}^\ell$, and the difference between $\sin^2 \theta_{\text{eff}}^f$ for b quarks and leptons, which is taken from the Standard Model. The combination of the different measurements that determine $\sin^2 \theta_{\text{eff}}^\ell$ is illustrated in Fig. 10.7 and shows that the lepton and heavy quark results are not very consistent with each other; the current averages of the two groups of measurements are listed in Table 10.3. The averages differ by 3.1 standard deviations. This situation is mainly driven by a difference in the two most precise contributions,

“leptons” – $A_{\text{FB}}^{0,\ell}$, $\mathcal{A}_\ell(P_\tau)$, A_{LR}	0.23113 ± 0.00020
“hadrons” – $A_{\text{FB}}^{0,b}$, $A_{\text{FB}}^{0,c}$, $\langle Q_{\text{FB}} \rangle$	0.23215 ± 0.00027

Table 10.3: Results for $\sin^2 \theta_{\text{eff}}^\ell$ from different groups of measurements

the LEP b quark forward-backward asymmetry and A_{LR} from SLD. The difference has existed since the beginning of asymmetry measurements at LEP and SLC, and has stayed almost at the same level of significance. The history of the contributions to $\sin^2 \theta_{\text{eff}}^\ell$ from $A_{\text{FB}}^{0,b}$ and A_{LR} is illustrated in Fig. 10.8.

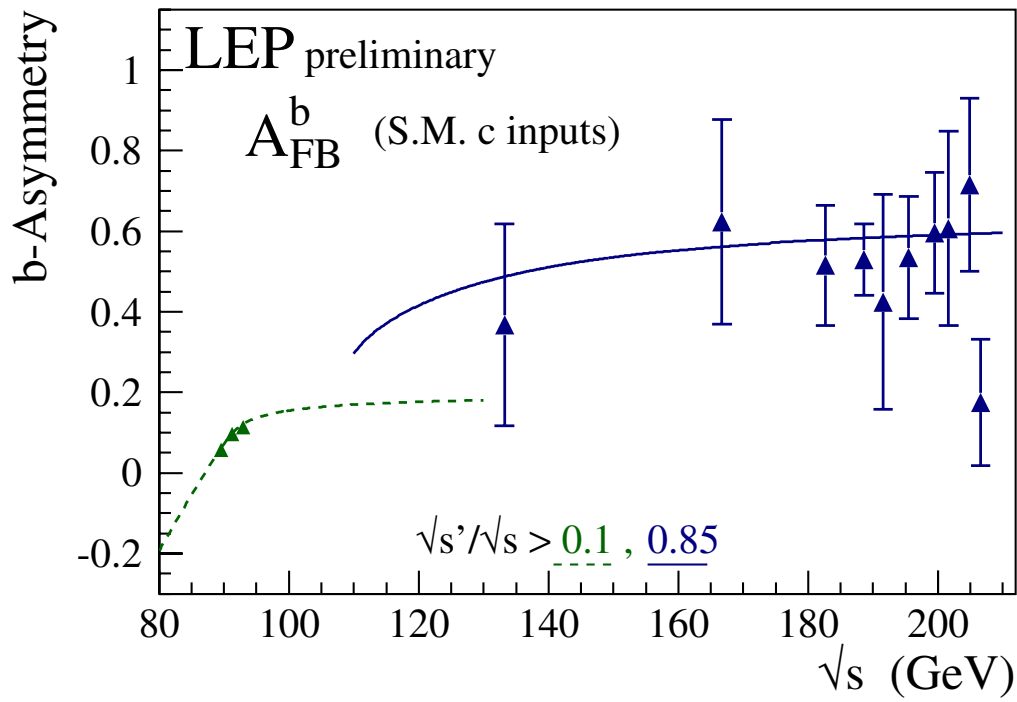


Figure 10.5: The LEP combined results for A_{FB}^b at the full range of LEP centre-of-mass energies.

Especially the $A_{\text{FB}}^{0,b}$ average has been stable over the time, while the precision has been continuously improved due to updated measurements using latest data reprocessings and new analysis techniques. While the precision was improved, the central values of the two contributions to $\sin^2 \theta_{\text{eff}}^\ell$ came closer so that the significance of their difference did not change much. In this way the effect is neither confirmed nor ruled out, and a statistical fluctuation as the cause cannot be excluded. All six measurements of $\sin^2 \theta_{\text{eff}}^\ell$ are therefore combined, giving a result of 0.23148 ± 0.00017 with a fit probability of 6.2%.

The leptonic electroweak mixing angle is especially interesting because it is one of the electroweak precision (pseudo-) observables that can be used to probe the Higgs sector of the Standard Model. Its sensitivity to the Higgs boson mass, m_h , via higher order effects has been discussed in Section 2.4 and provides an alternative, indirect way of gaining information on m_h . The resulting constraints are compared to the mass values which have been excluded by the direct search for the Higgs boson, which has not yet been successful.

The constraints on the Higgs boson mass from the measurements of the different electroweak precision observables are detailed in Fig. 10.9. It shows that $A_{\text{FB}}^{0,b}$ and A_{LR} are the two quantities that yield the highest sensitivity to m_h , followed by the W boson mass and the other determinations of $\sin^2 \theta_{\text{eff}}^\ell$. The current combined prediction for m_h is found to be $96_{-38}^{+60} \text{ GeV}/c^2$ (68 % C.L.) [85]. Interestingly, $A_{\text{FB}}^{0,b}$ is the only quantity that clearly prefers a high Higgs boson mass. The direct relation between the $A_{\text{FB}}^{0,b}$ result and m_h has already been displayed in the lower part of Fig. 10.3. As a matter of fact, the $A_{\text{FB}}^{0,b}$ result makes the electroweak fit more compatible with the exclusion limit on m_h from the direct search, $m_h < 114.4 \text{ GeV}/c^2$ [14].

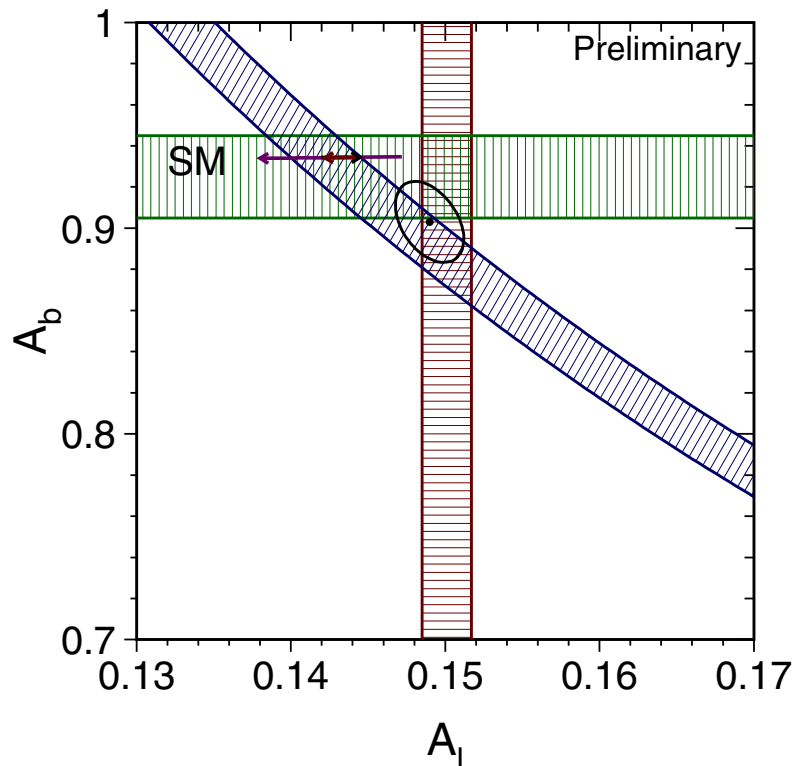


Figure 10.6: Interpretation of the A_{FB}^b results in terms of the polarisation parameters. The plot shows $\pm 1\sigma$ bands in the $(\mathcal{A}_\ell, \mathcal{A}_b)$ plane for \mathcal{A}_ℓ (from the A_{LR} , $A_{\text{FB}}^{0,\ell}$, and τ polarisation measurements), for \mathcal{A}_b (from the SLD polarised $A_{\text{FB,LR}}^b$) and for $A_{\text{FB}}^{0,b} = (3/4)\mathcal{A}_\ell\mathcal{A}_b$ (diagonal band). The ellipse denotes the 68% confidence level (C.L.) contour for the two polarisation parameter results from the joint analysis. The arrows represent the variation in the Standard Model prediction for the input parameters m_t , m_h and $\Delta\alpha_5^{\text{had}}$ varied by their uncertainties.

As mentioned above, also the determination of m_W contributes to the prediction of m_h . In the previous years [24, 75, 86], this contribution has shown, very similar to A_{LR} , a discrepancy to the one from $A_{\text{FB}}^{0,b}$, seemingly confirming the A_{LR} result. This discrepancy is now smaller with the updated result for m_W from summer 2003, which moved in the direction of high m_h [85]. The effect of the update is illustrated in Fig. 10.9 as well.

In the previous paragraph the data from the electroweak precision observables have been used to probe the Standard Model Higgs sector. The same principle can be applied to test the predictions of supersymmetric extensions of the Standard Model. S. Heinemeyer and G. Weiglein [87] have performed such a test by interpreting the electroweak precision data in the context of both Standard Model and Minimal Supersymmetric Standard Model (MSSM). For the purpose of greater model independence, the unconstrained MSSM has been studied which is free of specific assumptions on the underlying SUSY-breaking mechanism.

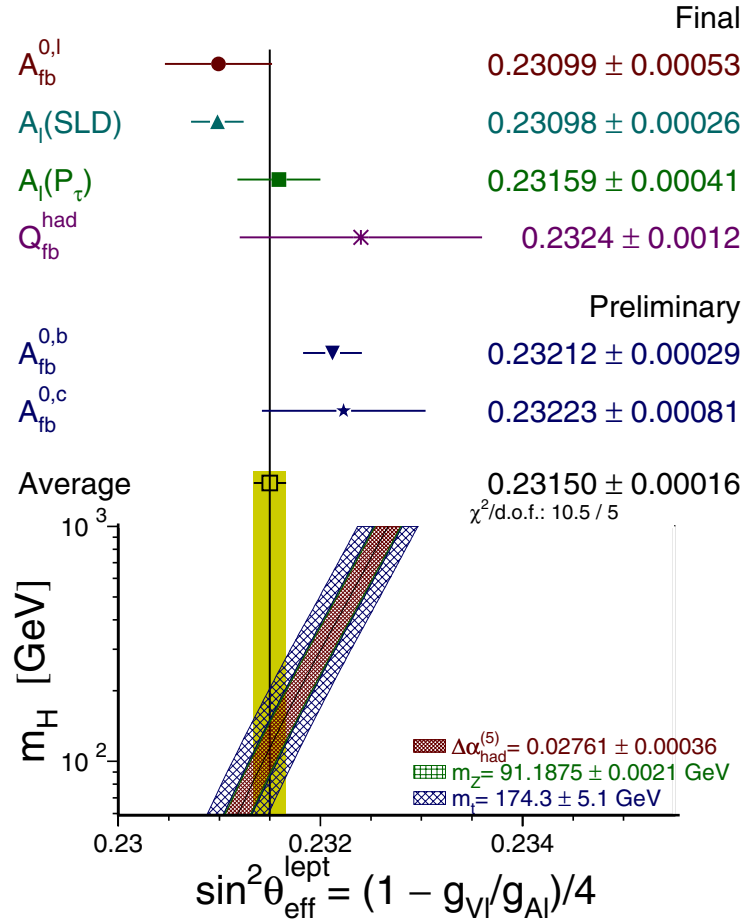


Figure 10.7: Interpretation of the A_{FB}^b results in terms of the leptonic effective electroweak mixing angle. The small sensitivity of A_b to $\sin^2 \theta_{\text{eff}}^b$ allows a direct comparison in terms of $\sin^2 \theta_{\text{eff}}^\ell$.

Fig. 10.10 shows the prediction in the plane of the two most precise electroweak observables, m_W and $\sin^2 \theta_{\text{eff}}^\ell$. For the Standard Model the prediction depends on the assumed values for the t quark mass and the mass of the Standard Model Higgs boson, which are varied within their experimental error, respectively theoretical limits. The light shaded band indicates the allowed region of the unconstrained MSSM. The upper edge, which forms the dark coloured overlap region with the Standard Model, corresponds to the decoupling limit, in which all superpartners are heavy, i.e. $m_{\text{particle}} \simeq \mathcal{O}(2 \text{ TeV}/c^2)$. By contrast, SUSY masses close to the lower experimental limit are assumed for the lower edge of the MSSM area. The current experimental data for the electroweak observables do not exclude either of the two models. Instead, they are well compatible with the region of a low-mass Standard Model Higgs boson, which could also be interpreted as the lightest SUSY higgs boson for which the MSSM predicts $m_h \lesssim 135 \text{ GeV}/c^2$ [87]. It should be noted that the prospective improvements in the accuracies of the electroweak observables for the future hadron and e^+e^- linear colliders will provide high sensitivities to any deviations from both MSSM and the Standard Model. The high sensitivity will not only be due to the increased precision of $\sin^2 \theta_{\text{eff}}^\ell$ and m_W , but also the theoretical prediction will become much more

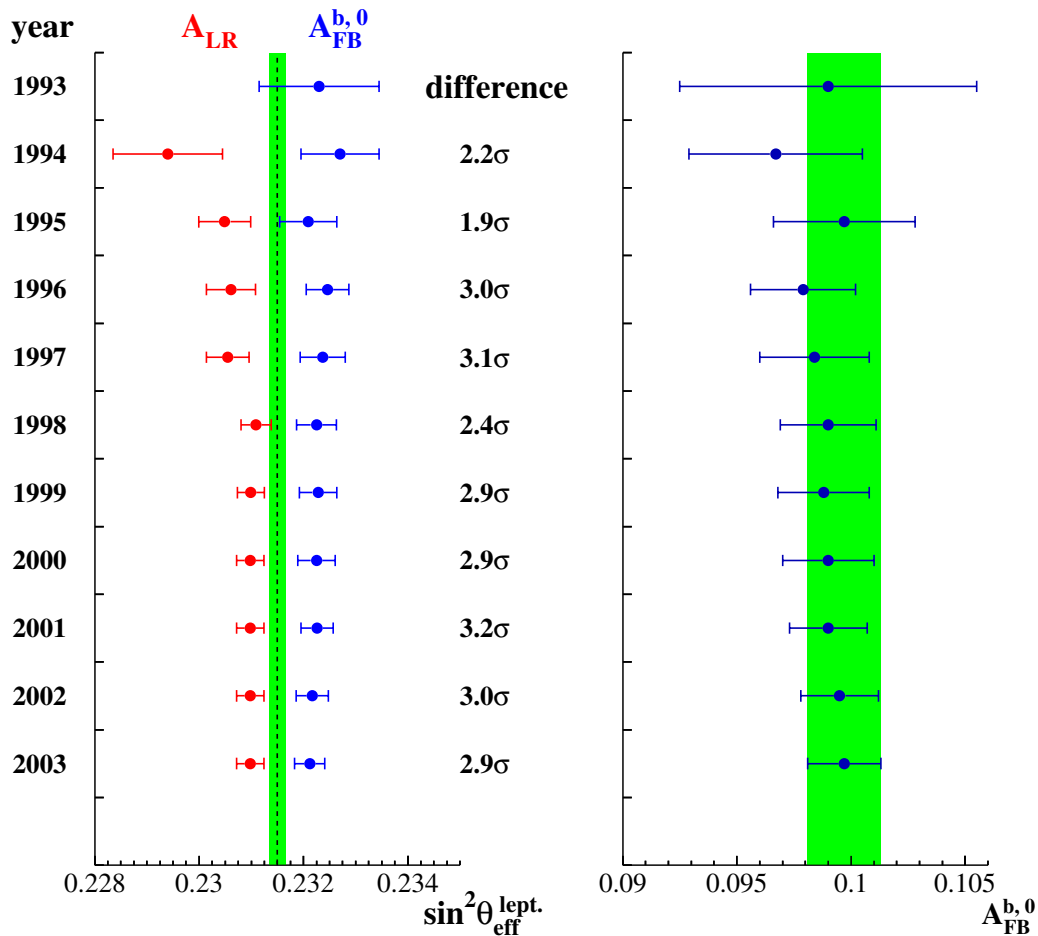


Figure 10.8: Time development of the $\sin^2 \theta_{\text{eff}}^{\ell}$ and A_{FB}^b results [24, 75, 81, 86].

accurate with decreasing uncertainty on the t quark mass. The recent re-analysis of the data taken by the D0 experiment has moved the principal D0 result for the direct m_t measurement from $m_t = 173.3 \pm 7.8 \text{ GeV}/c^2$ to $m_t = 180.1 \pm 5.4 \text{ GeV}/c^2$ [85]. If this is interpreted as a hint that the value of the t quark mass lies in fact higher than the current combined value of $m_t = 174.3 \pm 5.1 \text{ GeV}/c^2$, a further improvement in the agreement between prediction and data in Fig. 10.10 could be expected. In conjunction with the expected direct observation of the Higgs boson and possibly SUSY particles at the LHC, the electroweak observables provide a powerful consistency test of the (supersymmetric) Standard Model.

In addition to the electroweak observables, also the discrepancy between $A_{\text{FB}}^{0,b}$ and A_{LR} has created considerable attention in the literature, in particular among theorists. Loop-induced contributions from SUSY particles were investigated in the framework of the MSSM, but turned out to be too small to account for a sizable fraction of the $\simeq 3\sigma$ difference between the two observables [88].

Other studies have been performed which excluded the hadronic data from the global fit [88, 89]. Although the Standard Model global fit possesses a much higher fit probability in that case, the resulting upper bound on the Higgs boson mass is rather low and in poor agreement compared to the direct exclusion lower limit of

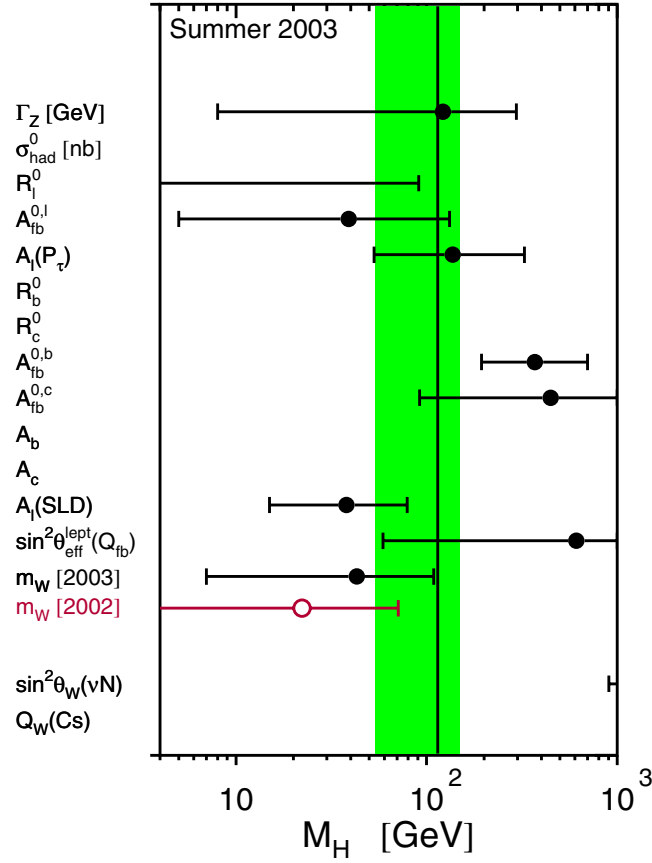


Figure 10.9: Constraints on the mass of the Higgs boson from each electroweak observable. The constraints were determined by setting the other free parameters in the electroweak fit, m_t , m_Z , $\Delta\alpha_5^{\text{had}}$ and α_s , to the values which were obtained in the combined fit to all data. This combined fit also yields the shaded band. In case of m_W , the current constraint (full dot) is compared with the one from summer 2002 (circle).

$m_h > 114.4 \text{ GeV}/c^2$ [14]. The value of $\sin^2\theta_{\text{eff}}^\ell$ obtained without the hadronic data is quoted in Table 10.3 to be 0.23113 ± 0.00020 . If this value was assumed, Fig. 10.10 shows that the MSSM would then provide a much better description of the data than the Standard Model, and the MSSM would clearly be favoured. This observation has caused additional analyses that study specific SUSY scenarios. However, in order to be put on solid ground, the whole idea completely lacks the argument why the hadronic data should be reduced in weight or totally disregarded. In the discussion at the beginning of this section it has been stressed that the results from the different analyses and independent experiments are very consistent with each other. The accuracy of the hadronic forward-backward asymmetries is limited by their statistical error, while common systematic uncertainties are much smaller. Therefore the presence of a common experimental problem or of other conceivable reasons for excluding the hadronic data is extremely unlikely.

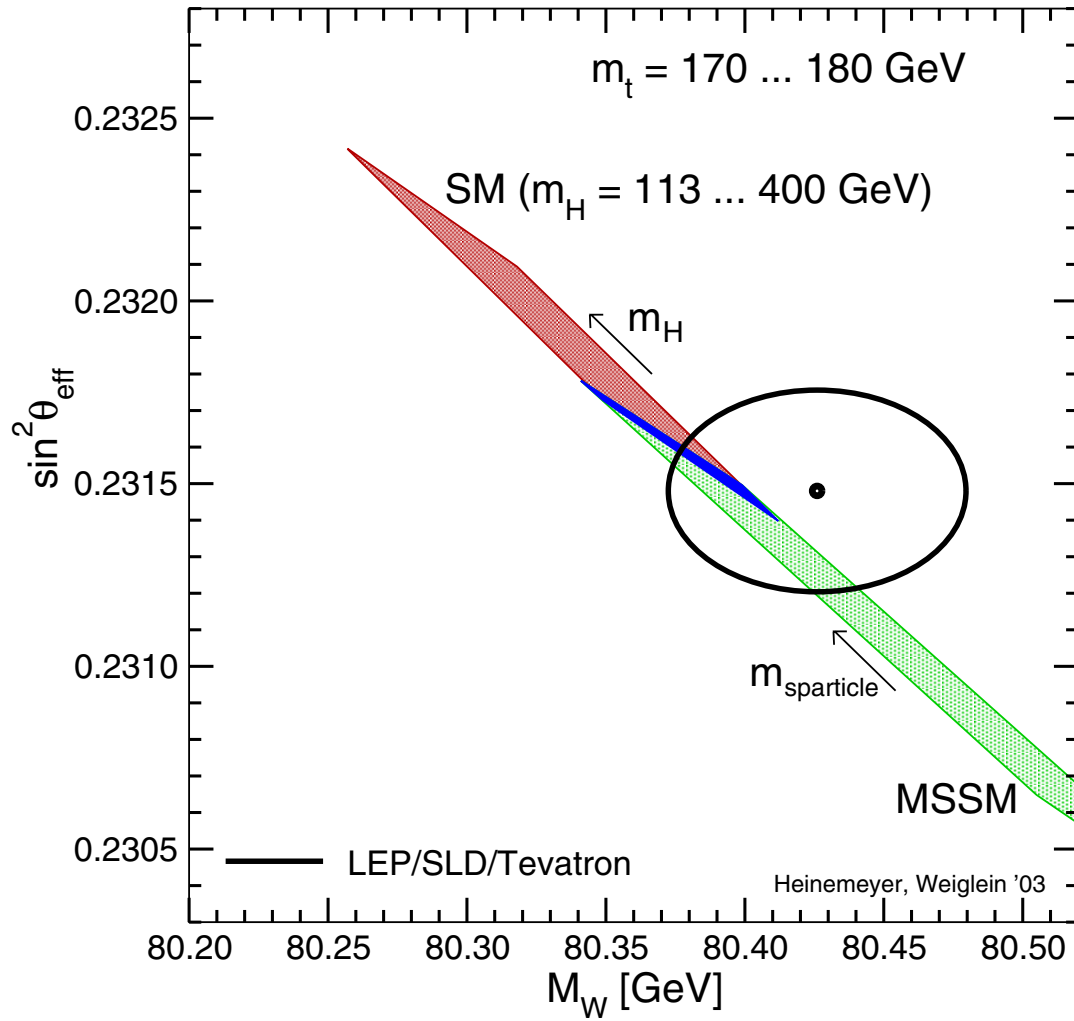


Figure 10.10: The current measurements for m_W and $\sin^2 \theta_{\text{eff}}^{\ell}$ at 68% C.L. (large ellipse) in comparison with the Standard Model prediction (dark, red band) and the MSSM prediction (light shaded, green band) from [87]. There is a common overlap region (blue band in the middle) for the special case of a light Standard Model Higgs boson, $m_h \lesssim 135 \text{ GeV}/c^2$, which in the context of the MSSM would be the lightest SUSY Higgs boson for the respective case of very heavy superpartners, $m_{\text{sparticle}} = \mathcal{O}(2 \text{ TeV}/c^2)$.

Chapter 11

Conclusions

The analysis presented in this thesis has measured the forward-backward asymmetry of b quarks from the DELPHI data taken in the years 1992 to 2000. It is based on an inclusive, self-calibrating method that exploits the characteristic properties of B hadrons for the selection of b quark events and the reconstruction of their charge. The enhanced impact parameter method to select b quark events provides data samples with b fractions ranging from 74% up to 99.7%. The fractions for both b quarks and the main background of c quarks are calibrated on the real data by means of a double hemisphere tagging method.

On these samples an inclusive hemisphere charge tag is obtained from a Neural Network, which combines different quark charge estimates like the jet charge, the vertex charge and the charge of specific B hadron hypotheses. Given the high b purity, this charge tag distinguishes the b quark from its anti-quark and hence makes the measurement of the b quark forward-backward asymmetry possible. The probability $w_b^{(D)}$ to identify the b charge correctly ranges between 0.78 and 0.93 and is calibrated on the data themselves by means of a second double tagging method, which is based on the ratio of like-sign and unlike-sign tagged hemisphere pairs. The hemisphere correlations, which appear in this procedure and have to be taken from simulation, represent the main systematic uncertainty entering the analysis. Their origin and effect on the analysis have consequently been studied in detail. Also the charge tagging probability for c quark events has been corrected using a set of exclusively reconstructed D meson decays. Changes between the different b purity samples and years of data-taking have been fully taken into account in the calibration and the determination of systematic uncertainties.

The results for the b quark forward-backward asymmetry at the three centre-of-mass energies on and around the Z pole are:

$$\begin{aligned} A_{\text{FB}}^b(89.449 \text{ GeV}) &= 0.0637 \pm 0.0143(\text{stat.}) \pm 0.0017(\text{syst.}) , \\ A_{\text{FB}}^b(91.231 \text{ GeV}) &= 0.0958 \pm 0.0032(\text{stat.}) \pm 0.0014(\text{syst.}) , \\ A_{\text{FB}}^b(92.990 \text{ GeV}) &= 0.1041 \pm 0.0115(\text{stat.}) \pm 0.0024(\text{syst.}) . \end{aligned}$$

Their precision is mainly limited by the statistical error. Various additional checks have been performed which are sensitive to the effects from hemisphere correlations, background corrections and gluon radiation. In all cases the full data set has been

used in order to make the test as sensitive as possible. The stability of the result observed during these tests confirms the chosen treatment of systematic uncertainties.

The measurement from this thesis is expected to be the final DELPHI result for the inclusive b quark asymmetry. It is therefore combined with the other three precise DELPHI heavy quark asymmetry measurements, giving

$$A_{\text{FB}}^{0,\text{b}} = 0.0990 \pm 0.0029, \quad A_{\text{FB}}^{0,\text{c}} = 0.0706 \pm 0.0068$$

for the b and c quark pole asymmetries. Statistical and systematic correlations are taken into account when calculating the combined result. The statistical correlations between the b asymmetries have been re-evaluated and were found to range between 0.29 and 0.53. The single result for A_{FB}^{b} as well as the DELPHI combined results are in good agreement with the LEP combined pole asymmetry. They confirm the existing situation in terms of the effective electroweak mixing angle.

Appendix A

The w_b Calibration Method

In this measurement events are sorted into five different categories. These categories are defined in Section 8.1:

N	=	number of single hemisphere tagged forward events,
\bar{N}	=	number of single hemisphere tagged backward events,
N^D	=	number of double hemisphere tagged forward events,
\bar{N}^D	=	number of double hemisphere tagged backward events,
N^{same}	=	number of double tagged like-sign events.

w_f and w_f^D are the probabilities to identify the quark charge correctly in single and double tagged events. For single tagged events it is defined as:

$$w_f = \frac{\hat{N}_f + \hat{N}_{\bar{f}}}{N_f + N_{\bar{f}}} \quad , \quad (\text{A.1})$$

where $N_f(N_{\bar{f}})$ is the number of events which contain a quark (anti-quark) in the forward hemisphere. $\hat{N}_f(\hat{N}_{\bar{f}})$ is the number of events in which the quark (anti-quark) has been correctly identified.

For unlike-sign events the fraction of events in which both quark and anti-quark charges are correctly identified is defined analogously to the single hemisphere tagged events as the ratio of correctly tagged ($\hat{N}_f^D, \hat{N}_{\bar{f}}^D$) over all double-tagged unlike-sign ($N_f^D, N_{\bar{f}}^D$) events:

$$w_f^D = \frac{\hat{N}_f^D + \hat{N}_{\bar{f}}^D}{N_f^D + N_{\bar{f}}^D} \quad . \quad (\text{A.2})$$

The single and double tagged unlike- and like-sign samples receive contributions from b events and from all other flavours. All categories also include events for which the quark charge was misidentified. Therefore the number of events entering in the different categories can be expressed as:

$$N = \sum_{f=d,s,b} [N_f \cdot w_f + N_{\bar{f}} \cdot (1 - w_f)] + \sum_{f=u,c} [N_{\bar{f}} \cdot w_f + N_f \cdot (1 - w_f)] \quad (\text{A.3})$$

$$\bar{N} = \sum_{f=d,s,b} [N_{\bar{f}} \cdot w_f + N_f \cdot (1 - w_f)] + \sum_{f=u,c} [N_f \cdot w_f + N_{\bar{f}} \cdot (1 - w_f)] \quad (\text{A.4})$$

$$N^D = \sum_{f=d,s,b} [N_f^D w_f^D + N_{\bar{f}}^D (1 - w_f^D)] + \sum_{f=u,c} [N_{\bar{f}}^D w_f^D + N_f^D (1 - w_f^D)] \quad (\text{A.5})$$

$$\bar{N}^D = \sum_{f=d,s,b} [N_{\bar{f}}^D w_f^D + N_f^D (1 - w_f^D)] + \sum_{f=u,c} [N_f^D w_f^D + N_{\bar{f}}^D (1 - w_f^D)] \quad (\text{A.6})$$

$$N^{same} = \sum_{f=d,u,s,c,b} N_f^{same} \quad . \quad (\text{A.7})$$

Here N_f ($N_{\bar{f}}$) denominates the number of single tagged events containing a quark (anti-quark) of flavour f in the forward hemisphere. Similarly N_f^D ($N_{\bar{f}}^D$) is the number of unlike-sign double tagged events containing a quark (anti-quark) of flavour f in the forward hemisphere. N_f^{same} is the number of like-sign double tagged events for each flavour.

Assuming a data sample which contains only b quark events, w_b can be extracted from the double tagged event samples via either one of the following two equations:

$$N^D + \bar{N}^D = \left(N^D + \bar{N}^D + N^{same} \right) \cdot [w_b^2 + (1 - w_b)^2] \quad (\text{A.8})$$

$$N^{same} = 2 \cdot \left(N^D + \bar{N}^D + N^{same} \right) \cdot w_b \cdot (1 - w_b) \quad . \quad (\text{A.9})$$

Both equations are linked through the total number of double tagged events and therefore contain the same information. Resolving the quadratic equation leads to the physical solution:

$$w_b = \frac{1}{2} + \sqrt{\frac{1}{4} - \frac{1}{2} \cdot \frac{N^{same}}{N^D + \bar{N}^D + N^{same}}} \quad . \quad (\text{A.10})$$

The second solution, with the minus sign, always leads to w_b values below 0.5.

The probability to identify a quark correctly for the single tag data sample can be used to calculate the probability to identify a quark or anti-quark correctly for the double tag data sample:

$$w_b^D = \frac{w_b^2}{w_b^2 + (1 - w_b)^2} \quad . \quad (\text{A.11})$$

Hemisphere charge correlations in the events entering the different categories need to be taken into account. For the probability w_b for single tagged events these correlations are given by a term $\sqrt{1 + \delta}$ which is introduced in Equation A.10:

$$w_b \cdot \sqrt{1 + \delta} = \frac{1}{2} + \sqrt{\frac{1}{4} - \frac{1}{2} \cdot \frac{N^{same}}{N^D + \bar{N}^D + N^{same}}} \quad . \quad (\text{A.12})$$

A similar correlation term, $\sqrt{1 + \beta}$, has to be applied for the probability of the double tagged sample, w_b^D :

$$w_b^D \cdot \sqrt{1 + \beta} = \frac{w_b^2 \cdot (1 + \delta)}{w_b^2 \cdot (1 + \delta) + (1 - w_b \cdot \sqrt{1 + \delta})^2} \quad . \quad (\text{A.13})$$

A last modification is needed because the selected double tagged data samples contain light and charm quark events in addition to the b quark events. The background events are taken into account by multiplying the different double tagged rates with the corresponding b purities:

$$w_b \cdot \sqrt{1 + \delta} = \frac{1}{2} + \sqrt{\frac{1}{4} - \frac{1}{2} \cdot \frac{N^{same} \cdot p_b^{same}}{[N^D + \overline{N^D}] \cdot p_b^D + N^{same} \cdot p_b^{same}}} . \quad (\text{A.14})$$

Equation A.13 is left unchanged. Equations A.14 and A.13 are used to extract the charge tagging probability to measure the b quark forward-backward asymmetry.

Appendix B

The χ^2 Fit to the Measured Event Rates

In the χ^2 minimisation to extract A_{FB}^{b} , the χ^2 is constructed from the differences between observed and predicted event numbers:

$$\begin{aligned} \chi^2 = \sum_{i=1}^{N_\theta} & \left(\frac{N_i - N(A_{\text{FB}}^{\text{b,fit}}, w_{\text{b},i}^{\text{fit}}, N_{0,i})}{\sigma(N_i)} \right)^2 + \left(\frac{\bar{N}_i - \bar{N}(A_{\text{FB}}^{\text{b,fit}}, w_{\text{b},i}^{\text{fit}}, N_{0,i})}{\sigma(\bar{N}_i)} \right)^2 + \\ & \left(\frac{N_i^D - N^D(A_{\text{FB}}^{\text{b,fit}}, w_{\text{b},i}^{\text{fit}}, N_{0,i}^D)}{\sigma(N_i^D)} \right)^2 + \left(\frac{\bar{N}_i^D - \bar{N}^D(A_{\text{FB}}^{\text{b,fit}}, w_{\text{b},i}^{\text{fit}}, N_{0,i}^D)}{\sigma(\bar{N}_i^D)} \right)^2 + \\ & \left(\frac{N_i^{\text{same}} - N^{\text{same}}(w_{\text{b},i}^{\text{fit}}, N_{0,i}^D)}{\sigma(N_i^{\text{same}})} \right)^2 . \end{aligned} \quad (\text{B.1})$$

The observed event numbers are the measured event rates in the five different categories of single and unlike-sign double tagged forward and backward events, N_i , \bar{N}_i , N_i^D , \bar{N}_i^D , and of the like-sign tagged events, N_i^{same} . This set of event rates is defined in each bin i of $\cos \theta_{\vec{T}}$, so that the χ^2 receives $5 \times N_\theta$ independent contributions giving just as many initial degrees of freedom. The predicted event rates $N(A_{\text{FB}}^{\text{b,fit}}, w_{\text{b},i}^{\text{fit}}, N_{0,i})$ etc. parameterise the expectation for a given event category and bin as a function of the forward-backward asymmetry, $A_{\text{FB}}^{\text{b}} = A_{\text{FB}}^{\text{b,fit}}$, and the probabilities to identify the b quark charge correctly, $w_{\text{b},i}$. The $\cos \theta_{\vec{T}}$ dependence of the asymmetry is given by Eq. 8.3 while the probabilities are allowed to vary independently in each bin. This means that the self-calibration of the probabilities w_{b} is performed in the same step as the determination of A_{FB}^{b} . Such a construction is necessary because the two parameters are correlated via the rates of unlike-sign double tagged events, which also enter the calibration via Eq. 8.10. The numbers $N_{0,i}$ and $N_{0,i}^D$ denote the total numbers of single and double tagged events in the i -th bin. Contrary to A_{FB}^{b} and $w_{\text{b},i}^{\text{fit}}$, they are not free parameters during the minimisation process but supplied as external constants to the fit in order to maintain its stability.

The expressions for the observed asymmetries, Eq. 8.1 and 8.2, directly yield the

predicted event rates for single and unlike-sign double tagged events.

$$N(A_{\text{FB}}^{\text{b,fit}}, w_{\text{b},i}^{\text{fit}}, N_{0,i}) = \frac{N_{0,i}}{2} \left(1 + \sum_{\substack{f= \\ \text{d,u,s,c,b}}} (2w_{f,i} - 1) \cdot A_{\text{FB}}^f \cdot r_{\text{diff.}}(i) \cdot p_{f,i} \cdot \eta_f \right) \quad (\text{B.2})$$

$$\bar{N}(A_{\text{FB}}^{\text{b,fit}}, w_{\text{b},i}^{\text{fit}}, N_{0,i}) = \frac{N_{0,i}}{2} \left(1 - \sum_{\substack{f= \\ \text{d,u,s,c,b}}} (2w_{f,i} - 1) \cdot A_{\text{FB}}^f \cdot r_{\text{diff.}}(i) \cdot p_{f,i} \cdot \eta_f \right) \quad (\text{B.3})$$

$$N^D(A_{\text{FB}}^{\text{b,fit}}, w_{\text{b},i}^{\text{fit}}, N_{0,i}^D) = \frac{N_{0,i}^D}{2} \left(1 + \sum_{\substack{f= \\ \text{d,u,s,c,b}}} (2w_{f,i}^D - 1) \cdot A_{\text{FB}}^f \cdot r_{\text{diff.}}(i) \cdot p_{f,i}^D \cdot \eta_f \right) \quad (\text{B.4})$$

$$\bar{N}^D(A_{\text{FB}}^{\text{b,fit}}, w_{\text{b},i}^{\text{fit}}, N_{0,i}^D) = \frac{N_{0,i}^D}{2} \left(1 - \sum_{\substack{f= \\ \text{d,u,s,c,b}}} (2w_{f,i}^D - 1) \cdot A_{\text{FB}}^f \cdot r_{\text{diff.}}(i) \cdot p_{f,i}^D \cdot \eta_f \right). \quad (\text{B.5})$$

The factor $r_{\text{diff.}}(i)$ absorbs the $\cos\theta_{\vec{T}}$ dependence of the differential asymmetry, Eq. 8.3. For the case of light and c quarks, the probabilities to identify the charge correctly are obtained via Eq. 8.6 f. from simulation. For b quarks it is given by the fit parameter, taking into account the hemisphere correlations and the relation 8.11 between w_{b} and w_{b}^D .

$$w_{\text{b},i} = w_{\text{b},i}^{\text{fit}} / \sqrt{1 + \delta_i} \quad (\text{B.6})$$

$$w_{\text{b},i}^D = \frac{(w_{\text{b},i}^{\text{fit}})^2}{(w_{\text{b},i}^{\text{fit}})^2 + (1 - w_{\text{b},i}^{\text{fit}})^2} \cdot \frac{1}{\sqrt{1 + \beta_i}} \quad (\text{B.7})$$

Finally, Eq. 8.10 is used to obtain the rate of like-sign tagged events,

$$N^{\text{same}}(w_{\text{b},i}^{\text{fit}}, N_{0,i}^D) = \frac{X_i \cdot N_{0,i}^D \cdot p_{f,i}^D}{1 - X_i} + N_{\text{had.}} \cdot (R_{\text{c}} \epsilon_{\text{c},i}^{\text{same}} + (1 - r_{\text{c}} - R_{\text{b}}) \epsilon_{\text{uds},i}^{\text{same}}) \quad (\text{B.8})$$

$$\text{with } X_i = 2w_{\text{b},i}^{\text{fit}} - 2(w_{\text{b},i}^{\text{fit}})^2 \quad (\text{B.9})$$

The final number of degrees of freedom (*n.d.o.f.*) in the χ^2 fit depends on the actual number of bins in $\cos\theta_{\vec{T}}$. The full number $5 \times N_{\theta}$ is reduced by the $2 \times N_{\theta}$ external normalisations and the $N_{\theta} + 1$ free parameters, $w_{\text{b},i}^{\text{fit}}$ and A_{FB}^{b} , giving

$$n.d.o.f. = 2N_{\theta} - 1 \quad (\text{B.10})$$

Appendix C

The DELPHI measurement of A_{FB}^b and R_b at LEP 2



A Measurement of the Cross-Section Ratio R_b and the Forward-Backward Asymmetry A_{FB}^b for $b\bar{b}$ Events with the DELPHI Detector at LEP 2.

E. Brodet¹, P. Brückman^{2,3}, P. Collins⁴, M. Elsing⁴, T. Lesiak^{2,3}, W. Liebig⁵, G. Wilkinson¹

Abstract

Measurements of the cross-section ratio $R_b = \sigma_{b\bar{b}}/\sigma_{\text{had}}$ and the b quark forward-backward asymmetry A_{FB}^b have been performed in $e^+e^- \rightarrow Z/\gamma$ events with the DELPHI detector using data delivered by LEP from 1997 to 2000. They correspond to centre-of-mass energies ranging from 183 to 209 GeV and comprise a total integrated luminosity of 650 pb^{-1} . For the identification of $b\bar{b}$ events a tagging variable was used which combines the information coming from B lifetime, the mass found in secondary vertices and the rapidity of tracks coming from a secondary vertex.

The asymmetry measurement uses the charged tracks to distinguish between the b and \bar{b} hemispheres. A_{FB}^b is extracted from the charge-signed polar angle distribution using an unbinned log likelihood fit.

Contributed Paper for EPS HEP 2001 (Budapest) and LP01 (Rome)

¹Department of Physics, University of Oxford, Keble Road, Oxford OX1 3RH, UK

²Institute of Nuclear Physics and University of Mining and Metallurgy, Ul. Kawiorów 26a, PL-30055 Kraków, Poland

³partially supported by the KBN grant 2 P03B 111 16 and SPUB-M/CERN/P-03/DZ 297/2000

⁴CERN, CH-1211 Geneva 23, Switzerland

⁵Fachbereich Physik, University of Wuppertal, Postf. 100 127, D-42097 Wuppertal, Germany

C.1 Introduction

During the years 1996-2000 the LEP accelerator has delivered nearly 700 pb^{-1} to each of the four experiments at centre-of-mass energies ranging from 130 to 209 GeV. In this energy region above the Z resonance the photon exchange and its interference with the Z is no longer suppressed with respect to the Z exchange, resulting in a very different behaviour of the production characteristics of fermion pair events.

A measurement of the cross-section ratio R_b and the forward-backward asymmetry A_{FB}^b has been performed at energies between 183 and 209 GeV using data collected with the DELPHI detector [29]. Unlike at LEP 1, R_b is defined as $\frac{\sigma_{b\bar{b}}}{\sigma_{\text{had}}}$ rather than $\frac{\Gamma(Z \rightarrow b\bar{b})}{\Gamma(Z \rightarrow \text{had})}$. The $b\bar{b}$ events are isolated using well understood techniques developed at LEP1, with efficient b-tagging extended to a polar angle of 25° due to the LEP 2 silicon tracker upgrade. The b-tagging is cross-calibrated using data taken on the Z resonance in the same running periods as the high energy data. The good efficiency, together with the large amount of data accumulated, allows a test of the Standard Model prediction for $b\bar{b}$ production in two-fermion events. Previous results concerning the energy range 130–172 GeV can be found in ref. [90].

The paper starts with the presentation of the selection and b tagging techniques applicable to both the R_b and A_{FB}^b measurements, followed by a separate description of the measurements themselves.

C.2 Track Selection

The polar acceptance for charged tracks is limited by the geometry of the tracking system to a polar angle region between 11° and 169° . The track selection imposes additional constraints, selecting charged tracks only if :

- their momentum is between 0.1 GeV and $1.5 \cdot E_{\text{beam}}$,
- the relative error on the momentum measurement is less than 100 %,
- the distance of their closest approach to the beam-spot is less than 4 cm in the plane perpendicular to the beam axis and less than $4/\sin \theta$ cm along the beam axis.

For jet clustering and the computation of event cut variables, neutral particles are also used. They are accepted in a polar angle region between 3° and 177° , which gives a good rejection of off-momentum electrons. A minimum energy cut is applied on neutral tracks, which is 0.3 GeV for the barrel electromagnetic and small angle calorimeters, HPC and STIC, and 0.4 GeV for the electromagnetic calorimeter in the forward region, FEMC.

C.3 Event Selection

The signal coming from the process $e^+e^- \rightarrow q\bar{q}(\gamma)$ was selected using global event variables deduced from the set of selected tracks. The following set of cuts provides a selection of hadronic events while rejecting Bhabha and two-photon interaction background events:

- $N_{\text{charged}} \geq 7$,
- $E_{\text{FEMC}} := \sqrt{E_{\text{F}}^2 + E_{\text{B}}^2} \leq 85\% E_{\text{beam}}$,
- $\sum E_{\perp} \geq 20\% E_{\text{CMS}}$,
- $E_{\text{charged}} \geq 10\% E_{\text{CMS}}$.

E_{FEMC} is constructed from E_{F} and E_{B} , the sum of all showers found in the forward and backward arms of the forward electromagnetic calorimeter. Cutting on this quantity as a percentage of the beam energy rejects electrons from Bhabha events. The request for a minimum transverse energy, $\sum E_{\perp}$, rejects two-photon events better than a comparably high E_{charged} cut, thus allowing the latter to be reduced.

At energies well above the Z-resonance, not only two-fermion final states with an effective centre-of-mass energy $\sqrt{s'}$ near the initial energy \sqrt{s} contribute to the sample of measured events, but also radiative return events with $\sqrt{s'} \sim M_Z$ and several kinds of four-fermion events. To be able to study the values of R_b at $\sqrt{s'} \sim \sqrt{s}$, additional selection criteria are applied:

- Four-fermion events mainly coming from the process $e^+e^- \rightarrow \text{WW}/\text{ZZ} \rightarrow \text{qqqq}$ usually can be easily forced into a four-jet structure and lead to a high thrust $(1-T)$ value. Two-fermion events with a back-to-back topology have, if forced into four jets as well, at least one jet with considerably lower energy and smaller angle towards a neighbouring jet. An energy-dependent cut on $E_{\text{min}} \cdot \Theta_{\text{min}}$ ⁶ and a remaining soft cut on the Thrust, $(1-T) \leq 0.31$ (0.35 for 1997,1998), further reduce the contamination with four-fermion events. An $E_{\text{min}} \cdot \Theta_{\text{min}} \leq \sqrt{s} \cdot 0.083^\circ$ cut is chosen for the data of 1997, $E_{\text{min}} \cdot \Theta_{\text{min}} \leq \sqrt{s} \cdot 0.079^\circ$ for 1998 and $E_{\text{min}} \cdot \Theta_{\text{min}} \leq \sqrt{s} \cdot 0.075^\circ$ for 1999 and 2000.
- The acceptance is limited to the silicon tracker polar angle coverage by requiring the thrust axis to have a minimal polar angle of 25° .
- The high energy sample is defined by rejecting any event with a reconstructed centre-of-mass energy $\sqrt{s'}$ [91] lower than 85% of the initial centre-of-mass energy.

Furthermore, runs which do not fulfill the demands on the detector quality were rejected, along with very short fills, where the beamspot was not reliably reconstructed and the b tagging degraded.

The influence of remaining background events was estimated using full detector simulation data sets generated by the EXCALIBUR four-fermion generator in versions 0.91, 1.01, 1.08 and 2.01 for different years of data taking. High energy and radiative $q\bar{q}(\gamma)$ events were simulated using the PYHTIA generator, versions 5.72 and 6.125.

The data sets analysed and the number of selected events obtained via the above selection cuts are listed in Table C.1.

⁶ $E_{\text{min}}, \Theta_{\text{min}}$ are the smallest jet energy and the smallest angle between any two jets in an event after having forced it into a four-jet topology.

\sqrt{s}	$\int \mathcal{L} dt$	$N_{\text{had}}^{\text{RD}}$
182.65	53.20(8)	1428
188.63	157.5(2)	3642
191.58	25.11(7)	551
195.52	76.1(2)	1640
199.52	83.0(2)	1633
201.64	40.0(1)	792
204.85	81.4(2)	1565
206.54	133.4(2)	2593

Table C.1: Average energies, integrated luminosities and numbers of selected hadronic events for the analysed data sets

C.4 Detector Inefficiency during the 2000 Data-Taking

During the last third of data-taking in 2000 one twelfth of the main tracking detector TPC was missing due to a short between sense wires. As a consequence, although tracks in that angular region could still be reconstructed from hits in other tracking devices, the track finding efficiency and track resolution went down in that sector [92]. Special simulation was generated for that period, which started on the 1st of September and comprises 55.6 pb^{-1} . An extra sample of Z pole data was taken so that the same analysis chain could be run separately on the data before and after the loss of the chamber, using the corresponding Z^0 calibration runs and simulation data.

For the R_{b} and A_{FB}^{b} analyses the relevant distributions have been studied on both data sets separately, and no significant deterioration could be found in the agreement between data and simulation. Dedicated control plots such as the agreement in the number of b-jets reconstructed per sector show that the drop in efficiency is well described by simulation. The dilution factor needed to extract A_{FB}^{b} (see section C.7) was degraded by about 4%, again with good agreement between data and simulation.

C.5 Identification of b Quarks

The DELPHI silicon tracker [31] provides up to six three dimensional points per track from three layers at radii between 6 and 11 cm. The precise track extrapolations provide a means of distinguishing between tracks from the primary vertex and tracks coming from decays of short lived hadrons.

The characteristics of heavy quark production are expressed in three observables (variables a) to c) in Section 6.2):

- a lifetime variable constructed from the impact parameters in a jet,
- the mass of the secondary vertex if one is present,
- the rapidities of the tracks from the secondary vertex or jet.

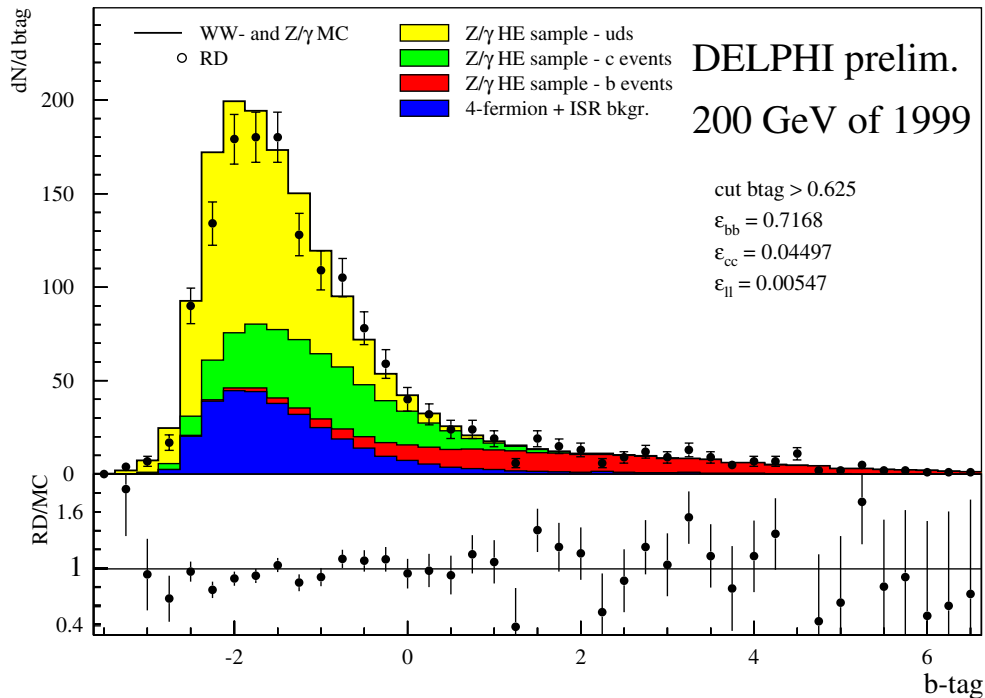


Figure C.1: Distribution of the event tagging variable in the 200 GeV data set. The simulation is divided into $b\bar{b}$, $c\bar{c}$, light quark and background events. The quality of the agreement between data and simulation is an ingredient of the systematic error estimation.

These variables are combined in an event probability variable ranging from -5 to $+10$. A detailed description of the observables and their combination can be found in Section 6.2.

High values of the tagging variable correspond to a high b purity, whereas light quark events are accumulated at low values. $c\bar{c}$ events are enriched in the intermediate region but are not clearly separated from the other flavour types. The distribution of the probability variable is displayed in Fig. C.1 for the selected events measured at $\sqrt{s} = 200$ GeV together with the simulation prediction consisting of Z/γ^* signal and different background types.

C.6 The R_b Measurement

By cutting on the event probability variable at $\mathcal{P}_b > 0.625$, a subsample ($N_{\text{tagged}}^{\text{RD}}$) is selected from the total number of selected events ($N_{\text{total}}^{\text{RD}}$) with a b purity between 88 % and 90 %, depending on the data set. When the background content is subtracted from the tagged and total selected events, the ratio of the two numbers can be expressed as a function of R_b using the tagging efficiencies for b , c and uds quarks (ε_b , ε_c , ε_{uds}):

$$\frac{N_{\text{tagged}}^{\text{RD}} - N_{\text{tagged}}^{\text{ISR}} - N_{\text{tagged}}^{\text{4f}}}{N_{\text{total}}^{\text{RD}} - N_{\text{total}}^{\text{ISR}} - N_{\text{total}}^{\text{4f}}} = R_b \varepsilon_b^{\text{meas.}} + R_c^{\text{SM}} \varepsilon_c^{\text{MC}} + (1 - R_b - R_c^{\text{SM}}) \varepsilon_{uds}^{\text{MC}} \quad . \quad (\text{C.1})$$

The constraint that the cross-section ratios add up to one requires that R_{uds} contains the measured R_b as well. The different coefficients are explained in the following.

Background estimation

The event selection reduces the remaining radiative return contamination to $\sim 8\%$ and four-fermion background to $\sim 18\%$, with the latter dropping to 3% in the WW-depleted b tagged sample.

The remaining backgrounds from selected four-fermion events (N_{tagged}^{4f} , N_{total}^{4f}) and from radiative events ($N_{\text{tagged}}^{\text{ISR}}$, $N_{\text{total}}^{\text{ISR}}$) contribute to the samples of selected and tagged events. They are estimated to be

$$N_{\text{tot/tag}}^{4f, \text{ISR}} = \left(\int \mathcal{L} \right) \cdot \sigma_{4f, Z/\gamma^*} \cdot \varepsilon_{\text{tot/tag}}^{4f \text{ISR}} \quad (\text{C.2})$$

and then subtracted from the number of measured events.

The cross-section for four-fermion background (σ_{4f}) was taken from the Monte Carlo generator, EXCALIBUR, whereas the $q\bar{q}(\gamma)$ cross-section (σ_{Z/γ^*}) is replaced by the semi-analytic ZFITTER [9] prediction. As ZFITTER and PYHTIA agree very well in the distribution of the true $\sqrt{s'}$, the fraction of radiative two-fermion events is taken from simulation. It is contained in $\varepsilon^{\text{ISR}, 4f}$, which is in both cases defined as the ratio of selected events to all events found in the simulated data set. Table C.2 shows the resulting estimated background contamination compared to the number of events in the data sample for the 200 GeV measurement.

	real data	ISR bg	4f bg
N_{total}	1633	102(2)	285(2)
N_{tagged}	206	14.3(5)	8.1(3)

Table C.2: Example of N^{ISR} , N^{4f} estimated based on Eq. C.2 for the 200 GeV data sample. The errors are related to the limited simulation statistics.

Efficiency determination

In order to minimise the dependence on the description of the b-modelling in the simulation, the b efficiency ε_b is calibrated by applying Eq. C.1 to the Z peak data of the corresponding LEP running period. The accurately measured cross-section ratio from the LEP 1 period is used [46], leading to a measured ε_b^0 which is then extrapolated to high energies. Thus only the relative change in efficiency needs to be taken from simulation. More precisely, the inefficiency $\bar{\varepsilon}$ is extrapolated, giving

$$\varepsilon_b^{\text{meas.}} = 1 - r \cdot (1 - \varepsilon_b^0) \quad \text{with the relative change } r = \frac{\bar{\varepsilon}^{\text{MC}}(E)}{\bar{\varepsilon}^{\text{MC}}(m_Z)}. \quad (\text{C.3})$$

ε_c and ε_{uds} are taken directly from high energy simulation.

R_c and acceptance correction

Standard Model predictions for R_c at high energies as well as on the peak are obtained from ZFITTER⁷ [9]. The values for R_b and R_c measured at LEP 1 and predicted by ZFITTER correspond to the full angular acceptance and a 100% hadronic selection efficiency. Hence these values are acceptance corrected before being used in Eq. C.1. The measured R_b results are corrected back to full acceptance.

⁷Version 6.22 with the FINR flag set to 0

Sources of systematic error

The following sources of systematic error are taken into account:

- Systematic errors can arise from uncertainties in the flavour tagging method, from the stability of the b-tagging for different data taking periods and the way the detector resolution enters the tagging.

They are determined by swapping the b-tagging calibration files for real data and simulation and by shifting the probability variable distributions for c and uds events to higher values, improving the agreement in the distribution on the Z. The second change is smaller than the first due to the high purity working point, away from the region where disagreements are generally observed.

For the 2000 data the detector alignment and consequently the b tagging calibration still shows problems with the current, not yet final data processing. The systematic error arising from this was estimated by switching between different b tagging calibrations from different data-taking periods. The result is that the preliminary systematic error given for detector and b tagging is about half the statistical error. It was assumed fully correlated while combining the results from the periods before and after the TPC sector loss.

- Imperfections in the b modelling do not enter the analysis method directly, because it calibrates itself on the Z data. However the statistical errors of the Z data sets, and also of the simulated samples used for extrapolation, result in an uncertainty in ε_b , which is of the same order of magnitude as the difference between calibrated and simulated ε_b . The corresponding effect on R_b is quoted as ε_b uncertainty.
- Uncertainties in the c and uds modelling have been studied for the LEP1 R_b measurement [46]. They arise mainly from the $c\bar{c} \rightarrow D^+$ fraction and the D decay multiplicity in case of ε_c , and from light hadron modelling and gluon splitting in case of ε_{uds} . Their size is scaled to the working point of this analysis and multiplied with a confidence factor of 2, taking into account the different working point and energy.
- Another source of systematic error originates from correcting the measured R_b to full acceptance. Its size is taken as one third of the correction.
- For the four-fermion background modelling, it has to be taken into account that very small contributions such as Zee and $llqq$ events have been neglected, and that the estimation relies on the correct knowledge of cross-sections and data luminosities. These effects are summarised in a variation of the four-fermion cross-section by $\pm 5\%$, which is larger than its theoretical error ($2 - 3\%$).
- The cut on the reconstructed centre-of-mass energy could introduce a bias due to ISR modelling or detector effects. Its size is estimated by varying the cut by $\pm 5\%$ and averaging the impact on R_b over all 6 energy points in order to minimise the influence of statistical fluctuations. A cross-check is performed by going back to a simpler form of the $\sqrt{s'}$ reconstruction algorithm which uses only topological information. Its effect is in agreement with the cut variation.
- A theoretical uncertainty in the modelling of the initial state / final state QED interference is quoted as well (“INTF modelling”). It is taken as half the change

Energy [GeV]	182.65	188.63	191.58	195.52	199.52	201.64	204.85	206.54
stat error MC	0.0006	0.0006	0.0022	0.0008	0.0008	0.0013	0.0008	0.0007
ε_b error	0.0023	0.0020	0.0033	0.0019	0.0020	0.0024	0.0047	0.0043
accept. corr.	0.0005	0.0007	0.0001	0.0004	0.0009	0.0009	0.0011	0.0008
4f BG modelling	0.0010	0.0013	0.0015	0.0015	0.0020	0.0019	0.0019	0.0017
ε_c uncertainty	-0.0019	-0.0023	-0.0022	-0.0024	-0.0024	-0.0025	-0.0020	-0.0021
ε_{uds} uncertainty	-0.0012	-0.0013	-0.0013	-0.0012	-0.0014	-0.0013	-0.0010	-0.0013
detector resolution	0.0018	0.0012	0.0015	0.0016	0.0016	0.0016	0.0088	0.0085
$\sqrt{s'}$ cut var.	-0.0008	-0.0005	-0.0013	-0.0007	-0.0008	-0.0011	-0.0009	-0.0009
INTF modelling	0.0009	0.0009	0.0009	0.0009	0.0009	0.0009	0.0009	0.0009
total	0.0041	0.0040	0.0055	0.0043	0.0047	0.0050	0.0106	0.0101
(stat. error RD)	0.0154	0.0103	0.0262	0.0150	0.0160	0.0229	0.0164	0.0120
R_c dependence (α)	-0.0473	-0.0557	-0.0540	-0.0594	-0.0581	-0.0617	-0.0484	-0.0492

Table C.3: List of systematic uncertainties affecting the measurement of R_b .

A negative sign denotes an anti-correlation with respect to variation. The total systematic error is computed as quadratic sum of all preceding contributions.

Energy [GeV]	R_{b} ($\pm\text{stat}$, $\pm\text{syst. error}$)	SM expectation
182.65	$0.1373 \pm 0.0154 \pm 0.0041$	0.1671
188.63	$0.1563 \pm 0.0103 \pm 0.0040$	0.1660
191.58	$0.1688 \pm 0.0262 \pm 0.0055$	0.1655
195.52	$0.1653 \pm 0.0150 \pm 0.0043$	0.1648
199.52	$0.1834 \pm 0.0160 \pm 0.0047$	0.1642
201.64	$0.1775 \pm 0.0229 \pm 0.0050$	0.1639
204.85	$0.1668 \pm 0.0164 \pm 0.0106$	0.1634
206.54	$0.1567 \pm 0.0120 \pm 0.0101$	0.1632

Table C.4: Preliminary results for R_{b} at energies between 183 and 207 GeV. Statistical and systematic errors are quoted separately. The Standard Model prediction has been computed with ZFITTER.

in the ZFITTER prediction when switching off the $\mathcal{O}(\alpha)$ interference correction, which is active by default.

An overview of the individual systematic error contributions for each of the six energy points is given in Table C.3. The total systematic error on R_{b} is obtained by quadratic summation and can be compared to the statistical error on real data.

The dependence on R_{c} is quoted in the systematic error breakdown in Table C.3 as well; it refers to the proportionality factor between R_{b} and the deviation from the Standard Model expectation: $R_{\text{b}} = R_{\text{b}}^{\text{meas.}} + \alpha \cdot (R_{\text{c}} - R_{\text{c}}^{\text{SM}})$.

Results

The measured results for R_{b} are summarised in Table C.4 and plotted in Fig. C.2 together with the prediction from ZFITTER. The plot also contains published measurements both on-peak and off-peak [46] and the 130-172 GeV results from [90]. Both the high energy ($\sqrt{s'}/\sqrt{s} > 0.85$) and the inclusive ($\sqrt{s'}/\sqrt{s} > 0.10$) theoretical prediction are included in the plot. The measured R_{b} values are consistent with the Standard Model prediction.

C.7 The A_{FB}^{b} Measurement

For events with a reconstructed centre-of-mass energy $\sqrt{s'}$ of close to 200 GeV, the forward-backward asymmetries, A_{FB} , of quarks are expected to be significantly higher than at the Z pole. The angular distribution of the b quarks as a function of their production angle θ can be described by

$$\frac{d\sigma}{d\cos\theta} = 1 + \cos^2\theta + \frac{8}{3}A_{\text{FB}}\cos\theta, \quad (\text{C.4})$$

where uncertainties due to the interference between initial and final state radiation have been neglected, as their impact on the measurement described here is small [93].

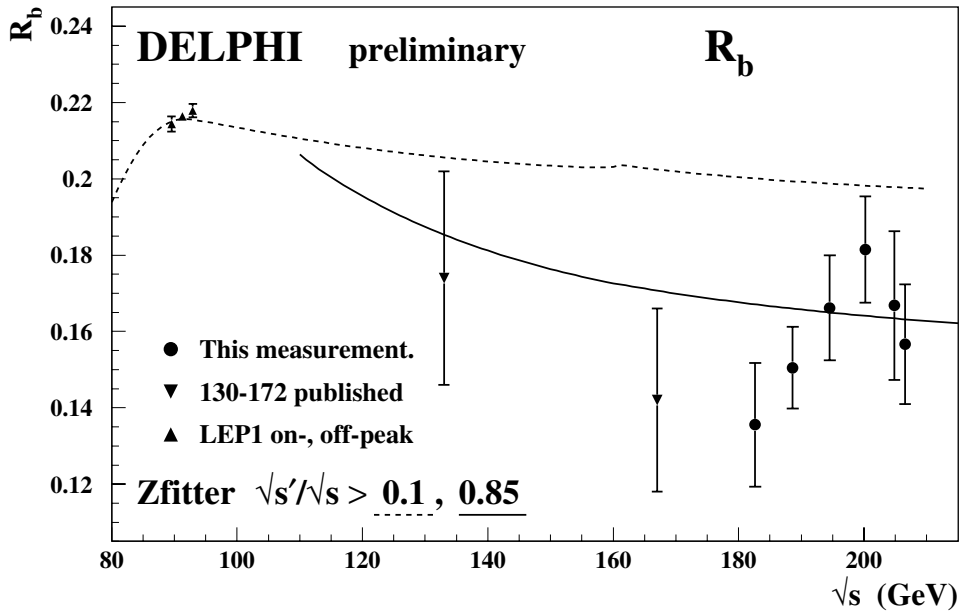


Figure C.2: The cross-section ratio R_b versus the LEP centre-of-mass energy \sqrt{s} . The data points show the preliminary results obtained with this analysis (closed circles) and previous results published in [90] and [46]. The LEP 2 results have to be compared with the high energy prediction ($\sqrt{s'}/\sqrt{s} > 0.85$) given by ZFITTER (full curve). In this plot the 192 and 196 GeV and the 200 and 202 GeV measurements have been combined.

Experimentally the quark charge can be estimated from the final state particles. In the regime $\sqrt{s'}/\sqrt{s} > 0.85$ the events are back-to-back, and the thrust axis of the event may be used to divide the event into forward and backward hemispheres, where the forward hemisphere is defined by the direction of the incoming electron. The momenta of the charged tracks are projected onto the forward unit thrust axis \vec{T} , and the charges of the forward (Q_F) and backward (Q_B) hemisphere are computed to be:

$$Q_{\text{F(B)}} = \frac{\sum_i q_i |\vec{p}_i \cdot \vec{T}|^\kappa}{\sum_i |\vec{p}_i \cdot \vec{T}|^\kappa} \quad (\text{C.5})$$

where q_i is the particle charge, p_i its momentum, and the exponent κ is set to a value of 0.6, chosen to optimise the discrimination. The sum runs over all charged tracks i , and all terms with $\vec{p}_i \cdot \vec{T} > 0$ contribute to Q_F , while all terms with $\vec{p}_i \cdot \vec{T} < 0$ contribute to Q_B . The information from the two hemispheres is combined in the charge flow variable Q_{FB} ,

$$Q_{\text{FB}} = Q_F - Q_B \quad (\text{C.6})$$

the sign of which is sensitive to whether the b quark is in the forward or backward hemisphere. The knowledge of the true quark charge is limited by the fragmentation, but improves for greater absolute values of Q_{FB} . If a cut is made requiring $|Q_{\text{FB}}| > 0.1$ the fraction of b events with an incorrect charge assignment, ω_q , is about 0.26 according to the Monte Carlo.

The variable x is defined to be the cosine of the event thrust axis signed by $-Q_{\text{FB}}$.

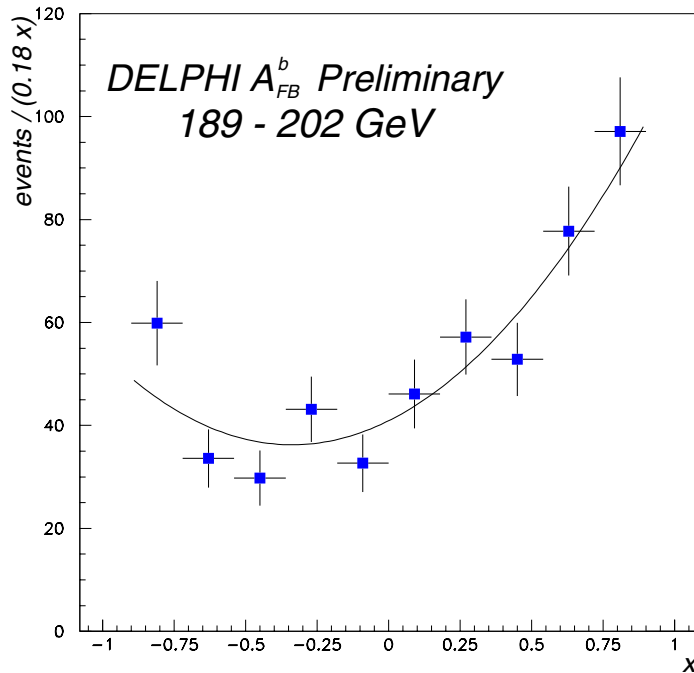


Figure C.3: The distribution of the variable x , the signed $\cos \theta$ of the event thrust axis, for the data sets from 189 GeV to 202 GeV inclusive. The data points have a symmetric $\cos \theta$ correction applied for the b tagging efficiency. The line shows the result of the maximum likelihood fit to $A_{\text{FB}}^{\text{obs}}$.

The observed asymmetry $A_{\text{FB}}^{\text{obs}}$ is fitted to the distribution of the events in x by maximising the likelihood

$$\ln \mathcal{L} = \sum_i \ln \left(1 + x_i^2 + \frac{8}{3} A_{\text{FB}}^{\text{obs}} x_i \right) \quad (\text{C.7})$$

where the sum runs over all events. The observed charge asymmetry contains contributions from the various backgrounds included in the sample. The WW background and the contamination from low $\sqrt{s'}$ are subtracted with asymmetries as measured on the Monte Carlo, giving corrections of about 3%. The remaining asymmetry can be expressed as

$$A_{\text{FB}}^{\text{obs}} = \sum_{q=\text{u,d,s,c,b}} s_q D_q A_{\text{FB}}^q F_q \quad (\text{C.8})$$

where the sum is over the quark species, A_{FB} is the asymmetry, F the relative abundance, D a dilution factor for each quark coming from charge misassignment, and the sign s is $+1$ for b , d and s quarks, and -1 for u and c quarks. The dilution factors are determined from the simulation by repeating the maximum likelihood fit on the simulated sample with and without use of the truth information to determine whether the b quark is in the forward or backward hemisphere. For the quarks other than the b quarks the Standard Model value for A_{FB}^q is taken. For this analysis, a high-purity working point is chosen with $F_b = 0.96$ and $F_c = 0.03$, minimising the corrections due to the non b quark contamination. This formula is used to extract A_{FB}^b . The fit to the distribution in the variable x is illustrated in Fig. C.3 for the data sets from 189 to 202 GeV.

Systematic Error Estimation

The principal contributions to the systematic error were as follows:

- **Knowledge of the dilution factors.** The dilution factors were cross-checked using the values of ω_q as measured on the Monte Carlo, and the relation $D_q = 1 - 2\omega_q$. The knowledge of the dilution factors was also checked by making the measurement on the Z^0 data accumulated in 1998, 1999 and 2000 and comparing to the LEP1 measured value of A_{FB}^b , and by looking at variations between the different years and energy points. Finally the exponent κ was varied between values of 0.3 and 0.9 and the dilution factors recomputed. The systematic error estimated from the variations between these methods was 7%.
- **Detector Effects.** The following detector effects were considered:
 - Variation of purity with $\cos\theta$
 - Changes of beamspot size and width between years and data samples
 - Estimated asymmetry in detector efficiency
 - Placement in z of the silicon tracker in data and simulation

A conservative error from these effects was estimated to be 5%.

- **Backgrounds.** The WW and ISR backgrounds were varied by 50%, leading to an uncertainty of less than 2%.
- **2000 TPC problems.** The data from the period with TPC problems was investigated separately. It was shown that the fluctuations seen with the problem sector removed lay well within those seen when removing an arbitrary sector.

The total systematic error was estimated at 9%. Note that the chosen working point means that the dependence of the result on the assumed branching fractions into $b\bar{b}$ and $c\bar{c}$ is negligible.

Results

Energy [GeV]	number of selected events	$A_{\text{FB}}^b \pm \text{stat.} \pm \text{syst. error}$
188.6	206	$0.50_{-0.14}^{+0.13} \pm 0.05$
191.6	44	$0.37_{-0.31}^{+0.30} \pm 0.03$
195.5	110	$0.72_{-0.19}^{+0.18} \pm 0.06$
199.5	117	$0.74_{-0.19}^{+0.18} \pm 0.07$
201.6	53	$0.59_{-0.29}^{+0.27} \pm 0.05$
204.8	79	$0.76 \pm 0.25 \pm 0.07$
206.6	157	$0.47 \pm 0.20 \pm 0.08$

Table C.5: Preliminary results for A_{FB}^b at energies between 189 and 207 GeV. Statistical and systematic errors are quoted separately.

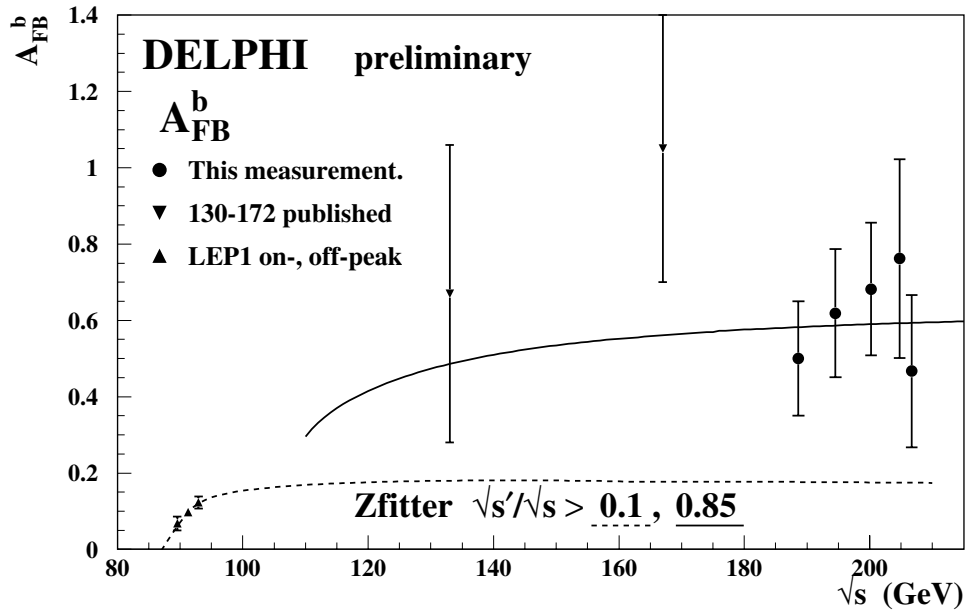


Figure C.4: The b quark asymmetries A_{FB}^b versus the LEP centre-of-mass energy \sqrt{s} . The data points show the preliminary results obtained with this analysis (closed circles) and previous results published in [90] and [69]. The solid line shows the high energy prediction ($\sqrt{s'}/\sqrt{s} > 0.85$) given by ZFITTER. Like the R_b results, the 192 and 196 GeV and the 200 and 202 GeV measurements have been combined.

The measured results for A_{FB}^b are summarised in Table C.5 and plotted in Fig. C.4 together with the prediction from ZFITTER, and the previously published values. The measurements are compatible with the Standard Model predictions.

C.8 Interpretation

Deviations from the Standard Model predictions for the process $e^+e^- \rightarrow b\bar{b}$ can be described model-independently in form of effective four-fermion contact interactions, giving access to new physics at higher energy scales. The heavy flavour production results have been used to obtain limits on such contact interaction scales.

Contact interactions are parametrised by an effective Lagrangian [94] of the form

$$\mathcal{L}_{\text{eff}} = \frac{g^2}{\Lambda^2} \sum_{i,j=L,R} \eta_{ij} (\bar{e}_i \gamma_\mu e_i) (\bar{f}_j \gamma^\mu f_j) \quad , \quad f \neq e, \quad (\text{C.9})$$

where e_i and f_j denote left or right-handed spinors, Λ is the scale of the contact interaction, and the coupling $g^2/4\pi$ is taken to be 1 by convention. Different helicity couplings $\eta_{ij} = \pm 1$ or 0 between initial and final state fermions can be assumed, defining a set of different models [95]. Each can have constructive (+) or destructive (−) interference with the Standard Model Lagrangian. Only the models explained in Table C.6 have been studied since they lead to large deviations in the $e^+e^- \rightarrow b\bar{b}$ production.

Model	η_{LL}	η_{RR}	η_{LR}	η_{RL}
LL^{\pm}	± 1	0	0	0
RR^{\pm}	0	± 1	0	0
VV^{\pm}	± 1	± 1	± 1	± 1
AA^{\pm}	± 1	± 1	∓ 1	∓ 1
LR^{\pm}	0	0	± 1	0
RL^{\pm}	0	0	0	± 1
V0^{\pm}	± 1	± 1	0	0
A0^{\pm}	0	0	± 1	± 1

Table C.6: Choices of η_{ij} for different contact interaction models.

All R_{b} and A_{FB}^{b} results above the Z° resonance are used as inputs, i.e. for 133 GeV, 167 GeV from [90] and for 183 (189 in case of A_{FB}^{b}) to 207 GeV from Tables C.4 and C.5. Hereby the R_{b} measurement has to be converted into a cross-section $\sigma_{\text{b}\bar{\text{b}}}$ using the DELPHI hadronic cross-section measurements published in [96]. The method of fitting each contact interaction model to the data works by fitting a parameter ϵ defined as $\epsilon = 1/\Lambda^2$. This parameter can take both positive and negative values in the fit and is 0 in the limit that no contact interactions exist. In the calculation of errors correlations between R_{b} and $\sigma_{\text{b}\bar{\text{b}}}$ were assumed negligible. However correlations between different energy points were taken into account by the fit.

The results for ϵ for each of the models are shown in Table C.7 together with their 68 % confidence level uncertainty. They are all compatible with the Standard Model expectation of $\epsilon = 0$. The lower limits on Λ are obtained by integrating the likelihood function over the physically allowed values, $\epsilon \geq 0$ for each Λ^+ limit and $\epsilon \leq 0$ for Λ^- limits. The resulting limits for a 95 % confidence level are also shown in Table C.7 and are displayed in Fig. C.5.

C.9 Conclusions

The cross-section ratio R_{b} and the forward-backward asymmetry A_{FB}^{b} have been measured for $\text{b}\bar{\text{b}}$ events observed with the DELPHI detector at LEP 2. The results are consistent with the Standard Model predictions. Exclusion limits have been set on the energy scale of new physics, assuming that it would interfere with the Standard Model $\text{b}\bar{\text{b}}$ production and can be parametrised by the general framework of contact interactions.

$e^+e^- \rightarrow b\bar{b}$			
Model	ϵ (TeV $^{-2}$)	Λ^- (TeV)	Λ^+ (TeV)
LL	$-0.0006^{+0.0074}_{-0.0078}$	7.9	8.4
RR	$-0.1626^{+0.1610}_{-0.0350}$	2.2	5.7
VV	$-0.0005^{+0.0041}_{-0.0043}$	8.6	9.5
AA	$-0.0006^{+0.0032}_{-0.0034}$	9.6	10.7
RL	$0.0459^{+0.1299}_{-0.0201}$	3.0	4.7
LR	$0.1274^{+0.0330}_{-0.1217}$	5.8	2.4
V0	$-0.0004^{+0.0053}_{-0.0056}$	9.3	9.9
A0	$0.0313^{+0.0272}_{-0.0381}$	5.4	3.7

Table C.7: Fitted values of ϵ and 95% confidence limits on the scale, Λ , for constructive (+) and destructive interference (−) with the Standard Model, for the contact interaction models discussed in the text. From $b\bar{b}$ results with centre of mass energies from 133 to 207 GeV.

$b\bar{b}$ – DELPHI preliminary

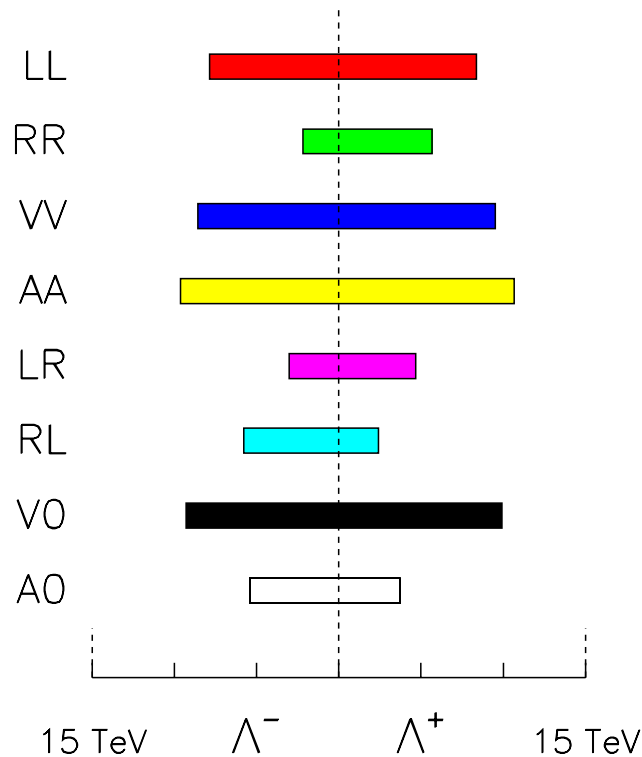


Figure C.5: Graphical display of the excluded values for the scale Λ for each model (95% CL). Positive (negative) values denote constructive (destructive) interference with the Standard Model.

List of Figures

2.1	Fundamental Feynman graphs of the electroweak theory	6
2.2	Fundamental Feynman graphs of QCD	7
2.3	Principal Feynman diagrams of the weak radiative corrections	11
2.4	Feynman diagrams for e^+e^- annihilation into fermions	13
2.5	The asymmetry as a function of the centre-of-mass energy	15
2.6	The relative contributions to the hadronic cross-section	16
2.7	The transition $e^+e^- \rightarrow hadrons \rightarrow stable\ particles$	18
2.8	The string fragmentation	19
2.9	The composition of the meson and baryon multiplets	21
2.10	Schematic view of heavy and light quark event topologies	23
2.11	Decay of b-hadrons in the spectator model	24
2.12	Feynman diagrams for the $B^0 - \bar{B}^0$ oscillation	24
3.1	Schematic view of the CERN accelerator complex	27
3.2	The Layout of the DELPHI detector	28
3.3	Picture of the DELPHI barrel and the collaboration	29
3.4	The DELPHI silicon tracker as installed in 1996-2000	30
3.5	Schematic layout of the DELPHI TPC	32
3.6	The polar angle acceptance of the tracking detectors	33
3.7	The operating principle of the DELPHI barrel RICH	34
6.1	An $e^+e^- \rightarrow b\bar{b}$ event measured by the Vertex Detector	47
6.2	The definition of positive and negative impact parameters	48
6.3	Discriminating variables used in the combined b-tagging	53
6.4	b-tagging efficiencies and purities for different discriminating variables	55
6.5	The measured and simulated distributions for the event b-tag variable	56

6.6	The measured efficiencies for tagging c quarks	59
6.7	Construction of the correction function for each bin	60
6.8	The integrated ratio of real to simulated events for the combined b-tag	61
7.1	Comparison of a natural and an artificial neuron	63
7.2	The measured Cherenkov angle for the liquid and gas RICH	65
7.3	Some auxiliary Neural Networks in BSAURUS	69
7.4	The b-hadron flavour tags	72
7.5	The jet and vertex charge inputs to the charge tagging	73
7.6	The b-hadron probabilities from the B-species ID network	75
7.7	The combined hemisphere charge probabilities for the four B-hypotheses	76
7.8	Architecture of the hemisphere charge tagging Neural Network	77
7.9	The output distribution of the hemisphere charge Neural Network	78
7.10	The hemisphere charge tag for the years 1992-2000	79
8.1	The measured b efficiencies and purities	84
8.2	The measured probability to identify b quarks correctly	85
8.3	Correlation of single and double tagged simulated events	87
8.4	A study of the mean correlations δ and β	88
8.5	Hemisphere correlations in the A_{FB}^{b} measurement with the jet charge	89
8.6	The charge tag in the hemisphere opposite a reconstructed D^* decay	91
8.7	The ratio of real data to simulation for w_c	92
8.8	The QCD correction including experimental biases	95
8.9	Distribution of the $\chi^2/n.d.o.f.$ in the fits to A_{FB}^{b}	96
8.10	The A_{FB}^{b} results for each year and each interval in $b\text{-tag}$	97
8.11	The differential b quark asymmetry of the years 1992 to 2000	98
8.12	The A_{FB}^{b} results for the 1993+95 off-peak runs and intervals in $b\text{-tag}$	100
8.13	The differential A_{FB}^{b} at the three centre-of-mass energies	101
8.14	The A_{FB}^{b} results versus the centre-of-mass energy	102
9.1	The c efficiency correction function applied to the $b\text{-tag}_{\text{hem}}$ variable	105
9.2	A study of observables in the jet charge hemisphere correlations	106
9.3	The hemisphere charge correlations vs. interval in $b\text{-tag}$	107
9.4	The mean hemisphere correlations versus cut on thrust	109

9.5	Systematic uncertainties as a function of b purity	111
9.6	The 1992-2000 asymmetry result vs. b purity	112
9.7	The b quark pole asymmetry for different cuts on the thrust value	113
9.8	The charge bias asymmetry observed in the analysis	113
10.1	Comparison between the jet-charge and Neural-Network based A_{FB}^{b}	116
10.2	Correlation between the jet-charge and Neural-Network based analyses	117
10.3	The LEP combined A_{FB}^{b} results	119
10.4	The LEP combined A_{FB}^{b} and A_{FB}^{c} results versus centre-of-mass energy	120
10.5	The LEP 1 and LEP 2 combined A_{FB}^{b} results versus centre-of-mass energy	121
10.6	Interpretation of the LEP combined A_{FB}^{b} results in terms of \mathcal{A}_{ℓ} , \mathcal{A}_{b}	122
10.7	The LEP combined A_{FB}^{b} results	123
10.8	Time development of $\sin^2 \theta_{\text{eff}}^{\ell}$ and A_{FB}^{b}	124
10.9	Constraints on the mass of the Higgs boson from each electroweak observable	125
10.10	Results for m_{W} and $\sin^2 \theta_{\text{eff}}^{\ell}$ compared with the SM and MSSM	126
C.1	Distribution of the event b-tagging variable in the 200 GeV data set	139
C.2	The cross-section ratio R_{b} versus the LEP centre-of-mass energy	144
C.3	Distribution of the signed $\cos \theta$ of the event thrust axis	145
C.4	The b quark asymmetries A_{FB}^{b} versus the LEP energy \sqrt{s}	147
C.5	Graphical display of the excluded values for the scale Λ	149

List of Tables

2.1	The 3 families of fermion fields and their quantum numbers	4
2.2	Properties of selected b- and c-hadrons	22
3.1	The polar angle acceptance for the different VD set-ups	31
3.2	Characteristics of the DELPHI calorimeters	36
5.1	Cuts to select particles. Impact parameters are defined relative to the primary vertex.	43
5.2	Selection cuts for Z decays to hadrons	44
5.3	Numbers of selected and simulated Z decays to hadrons	44
5.4	Topological D branching fractions used in the reweighting	45
6.1	The track conditions used for lifetime tagging	50
6.2	Jet categories for tracks entering the combined b-tagging	51
6.3	Event-efficiency for correlated hemispheres	57
8.1	The measured b purities for the different years and <i>b-tag</i> intervals . .	82
8.2	Mean hemisphere correlations for the different b purity samples . . .	89
8.3	Calculated values for the QCD correction coefficients c_1 and c_2 . . .	93
8.4	Summary of the QCD correction bias factors	94
8.5	Summary of the AFB results	102
9.1	Dependencies of A_{FB}^{b} on the electroweak parameters	104
9.2	Systematic uncertainties and their influence on A_{FB}^{b}	110
10.1	Results of the three most precise $A_{\text{FB}}^{0,\text{b}}$ measurements from DELPHI	116
10.2	Correlations between the different methods to determine A_{FB}	118
10.3	Results for $\sin^2 \theta_{\text{eff}}^{\ell}$ from different groups of asymmetry measurements	120

C.1	Characteristic numbers for the analysed LEP 2 data sets	138
C.2	Example of N^{ISR} , N^{4f} for the 200 GeV data sample.	140
C.3	List of systematic uncertainties affecting the measurement of R_b . . .	142
C.4	Preliminary results for R_b at energies between 183 and 207 GeV . . .	143
C.5	Preliminary results for A_{FB}^b at energies between 189 and 207 GeV. . .	146
C.6	Choices of η_{ij} for different contact interaction models	148
C.7	Limits on the scale for different contact interaction models	149

Bibliography

- [1] S.L. Glashow, Nucl. Phys. B 22 (1961) 579;
S. Weinberg, Phys. Rev. Lett. 19 (1967) 1264;
A. Salam, Phys. Lett. 13 (1964) 168.
- [2] S.L. Glashow, J. Iliopoulos and L. Maiani, Phys. Rev. D 2 (1970) 1285.
- [3] N. Cabibbo, Phys. Rev. Lett. 10 (1963) 531;
M. Kobayashi and K. Maskawa, Prog. Theor. Phys. 49 (1973) 652.
- [4] C.S. Wu, E. Ambler, R.W. Hayward, D.D. Hoppes and R.P. Hudson, Phys. Rev. 105 (1957) 1413.
- [5] M. Gell-Mann, Acta Physica Austriaca, Suppl. IX (1972) 733;
H. Fritzsch, M. Gell-Mann and H. Leutwyler, Phys. Lett. 47 B (1973) 365;
G. Zweig, Science 201 (1978) 973.
- [6] The Particle Data Group, K. Hagiwara et al, Phys. Rev. D 66 (2002) 1.
- [7] C. Giunti
Status of neutrino fits
Proc. of the XXXVIIIth Rencontres de Moriond, hep-ph/0305139.
- [8] G. Altarelli, R. Kleiss and C. Verzegnassi
Z Physics at LEP I – Vol. 1
CERN Yellowbook 89-08.
- [9] D. Bardin et al., Comp. Phys. Comm. **133** (2001) 229 and
arXiv:hep-ph/9908433.
- [10] G. Altarelli, T. Sjöstrand and F. Zwirner
Physics at LEP 2 – Vol. 1
CERN Yellowbook 96-01.
- [11] D.A. Ross and J.C. Taylor, Nucl. Phys. B 51 (1973) 25.
- [12] A. Sirlin, Phys. Rev. D 22 (1980) 971.
- [13] A. Djouadi, J.H. Kühn and P.M. Zerwas
b Jet Asymmetries in Z Decays
Z. Phys. C 46 (1990) 411.
- [14] The ALEPH, DELPHI, L3 and OPAL Coll., G. Abbiendi et al., Phys. Lett. B 565 (2003) 61.

- [15] T. Sjöstrand et al., *Comp. Phys. Commun.* 135 (2001) 238.
- [16] A. Krzywicki and B. Petersson, *Phys. Rev. D* 6 (1972) 924;
J. Finkelstein and R.D. Peccei, *Phys. Rev. D* 6 (1972) 2606;
F. Niedermayer, *Nucl. Phys. B* 79 (1974) 355;
A. Casher, J. Kogut and L. Susskind, *Phys. Rev. D* 10 (1974) 732.
- [17] R.D. Field and R.P. Feynman, *Nucl. Phys. B* 136 (1978) 1.
- [18] A. Heister et al., *Phys. Lett. B* 512 (2001) 30;
K. Abe et al., *Phys. Rev. Lett.* 84 (2000) 3400;
G. Abbiendi et al., [arXiv:hep-ex/0210031](http://arxiv.org/abs/hep-ex/0210031);
G. Barker et al., DELPHI note 2002-069 CONF 603.
- [19] R. Seuster
Spectroscopy and charm quark fragmentation at Belle
Parallel talk given at the EPS-HEP Aachen, Summer 2003.
- [20] C. Peterson et al., *Phys. Rev. D* 27 (1983) 105.
- [21] DELPHI Coll., P. Abreu et al,
Tuning and test of fragmentation models based on identified particles and precision event shape data
Z. Phys. C 73 (1996) 11.
- [22] The Particle Data Group, D.E. Groom et al., *Eur. Phys. J. C* 15 (2000) 1.
- [23] The LEP/SLD Heavy Flavour Working Group, D. Abbaneo et al.
Final input parameters for the LEP/SLD heavy flavour analyses
LEPHF/01-01, <http://www.cern.ch/LEPEWWG/heavy/lephf0101.ps.gz>
- [24] The LEP EWWG, D. Abbaneo et al.
A Combination of Prel. Electroweak Measurements and Constraints on the Standard Model
Contr. to the 2002 summer conferences, CERN-EP-2002-091 and [arXiv:hep-ex/0212036](http://arxiv.org/abs/hep-ex/0212036).
- [25] B. Richter, CERN/ISR-LTD/76-9, March 1976.
- [26] LEP Design Report, vol. 2, CERN-LEP/84-01 (1984).
- [27] See for example: R. Aßmann et al.
A brief history of the LEP collider
Nucl. Phys. B (Proc. Suppl.) 109B (2002) 17-31.
- [28] DELPHI Coll., P. Abreu et al.
The DELPHI detector at LEP
Nucl. Instr. and Meth. A 303 (1991) 233.
- [29] DELPHI Coll., P. Abreu et al.
Performance of the DELPHI detector
Nucl. Instr. and Meth. A 378 (1996) 57.
- [30] <http://delphiwww.cern.ch/photopit/>
Today the DELPHI barrel is on exhibition in the LHCb underground experimental area.

- [31] DELPHI Silicon Tracker Group, P. Chochula et al.
The DELPHI Silicon Tracker at LEP 2
Nucl. Instr. Meth. A 412 (1998) 304.
- [32] DELPHI Silicon Tracker Group, V. Chabaud et al.
The DELPHI Silicon Strip Microvertex Detector with Double Sided Readout
Nucl. Instr. Meth. A 368 (1996) 314.
- [33] Private communication with K. Österberg.
- [34] J.M. Heuser
Construction, Operation and Application of the DELPHI Pixel Detector at LEP 2
Ph.D. Thesis, Berg. Univ. Wuppertal, WUB-DIS 99-1, January 1999.
- [35] E.G. Anassontzis et al., Nucl. Instr. and Meth. A 323 (1992) 351.
W. Adam et al., Nucl. Instr. and Meth. A 343 (1994) 68.
DELPHI RICH Coll.
Contributions to the Second Workshop on RICH Detectors, Uppsala 1995
Nucl. Instr. and Meth. A 371 (1996).
- [36] W. Adam et al., Nucl. Instr. and Meth. A 338 (1994) 284.
- [37] DELPHI Coll., P. Aarnio et al.,
DELPHI Data Analysis Program (DELANA) User's Guide
DELPHI note 89-44 PROG-137.
- [38] F. Carena, G. Gopal
Cargo Data Base Management Systems Manual
DELPHI note 86-28 PROG 46.
- [39] D. Bertrand, L. Pape
TANAGRA: Track Analysis and Graphics Package
DELPHI note 86-75 PROG 55.
- [40] D. Wicke
A New Algorithm for Solving Track Ambiguities
DELPHI note 98-163 PROG 236 TRACK 92.
- [41] T. Brenke
Bestimmung des elektroschwachen Mischungswinkels $\sin^2 \theta_{\text{eff}}^\ell$ aus der Vorwärts-rückwärts-Asymmetrie von c - und b -Quarks
Ph.D. Thesis, BU Wuppertal, WUB-DIS 98-17, December 1999.
- [42] T. Spassoff
DELPHI Extended Short DST Content
DELPHI 97-147 PROG 222.
- [43] R. Brun and J. Zoll
ZEBRA User Guide
CERN program library 1994;
M. Goosens, O. Schaile, J. Shiers, J. Zoll
ZEBRA
CERN Prog. Lib. long writeup Q100/Q101 (1994).

- [44] DELSIM *User Manual*, DELPHI note 87-96 PROG 99;
 DELSIM *Reference Manual*, DELPHI note 87-98 PROG 100.
- [45] S. Brandt et al., *Phys. Lett.* 12 (1964) 57.
 E. Farhi, *Phys. Rev. Lett.* 39 (1977) 1587.
- [46] DELPHI Coll., P. Abreu et al., *Eur. Phys. J. C* 10 (1999) 415.
- [47] DELPHI Coll., J. Abdallah et al., *Eur. Phys. J. C* 32 (2004) 185.
- [48] ALEPH Coll., D. Buskulic et al., *Phys. Lett. B* 313 (1993) 535.
- [49] G. Borisov, C. Mariotti, *Nucl. Instr. Meth. A* 372 (1996) 181.
- [50] G. Borisov, *Nucl. Instr. Meth. A* 417 (1998) 384.
- [51] Private communication with H. Geenen.
- [52] DELPHI Coll., J. Abdallah et al., *Eur. Phys. J. C* 34 (2004) 109.
- [53] DELPHI Coll., K. Münich et al.
Det. of A_{FB}^b using inclusive charge reconstruction and lifetime tagging at LEP 1
 DELPHI note 2001-027 CONF 468.
- [54] DELPHI Coll., K. Münich et al.
Det. of A_{FB}^b using inclusive charge reconstruction and lifetime tagging at LEP 1
 DELPHI note 2001-048 CONF 476.
- [55] K. Münich
Präzisionsmessung der Vorwärts-Rückwärts-Asymmetrie von b-Quarks
 Ph.D. Thesis, Berg. Univ. Wuppertal, WUB-DIS 2001-2, June 2001.
- [56] T. Scheidle
*Bestimmung der b- und c-Quark Effizienz im DELPHI Detektor anhand einer
 "Double-Tag" Methode*
 Diploma thesis, IEKP-KA/2002-05, Karlsruhe.
- [57] T. Allmendinger, G. Barker, M. Feindt, C. Haag, M. Moch
BSAURUS – A package for inclusive B-reconstruction in DELPHI
 DELPHI note 2002-069 PHYS 868, arXiv:hep-ex/0102001.
- [58] P. Langefeld
*Identifikation von Zerfällen des Z Bosons in b-Quark-Paare — Multivariate
 Verfahren und neuronale Netzwerke im Vergleich*
 Diploma thesis, Berg. Univ. Wuppertal, WUD-93-42.
- [59] W.S. McCulloch and W.H. Pitts
A Logical Calculus of the Ideas Immanent in Nervous Activity
Bulletin of Math. Biophys. V (1943) 115.
- [60] F. Rosenblatt
Principles of Neurodynamics
 Spartan books, Wash. DC (1962) .
- [61] G.E. Hinton, D.E. Rumelhart and R.J. Williams
Learning Internal Representations by Error Propagation
Par. Distrib. Proc., MIT Press 1 (1986) 318.

- [62] L. Lönnblad, C. Peterson and T. Røgnvaldson
JETNET 3.0: A Versatile Artificial Neural Network Package
Comp. Phys. Commun. 81 (1994) 185.
- [63] M. Battaglia, P.M. Kluit
Particle identification using the RICH detectors based on RIBMEAN
DELPHI note 96-133 RICH 90.
- [64] E. Schyns
NEWTAG - π , K , p tagging for the DELPHI RICHes
DELPHI note 96-103 RICH 89.
- [65] Z. Albrecht, M. Feindt and M. Moch
MACRIB – High Efficiency, High Purity Hadron Identification for DELPHI
DELPHI internal note 99-150 RICH 95.
- [66] M. Feindt, C. Kreuter and O. Podobrin
ELEPHANT reference manual
DELPHI note 96-82 PROG 217;
C. Kreuter
Electron identification using a neural network
DELPHI note 96-169 PHYS 658.
- [67] N. Crosland, G. Wilkinson and P. Kluit, DELPHI note 92-17 PHYS 157;
H. De Boeck and G. Wilkinson, DELPHI note 93-14 PHYS 263;
G. Wilkinson and P. Collins, DELPHI note 93-13 PHYS 262;
F. Stichelbaut and G. Wilkinson, DELPHI note 95-140 PHYS 565.
- [68] DELPHI Coll., J. Abdallah et al.
A Precise Measurement of the B^+ , B^0 and Mean b -Hadron Lifetime with the DELPHI Detector at LEP I
Submitted to Eur. Phys. JC.
- [69] DELPHI Coll., P. Abreu et al., Eur. Phys. J. C9 (1999) 367.
- [70] B. Schwering
Messung der v.-r. Ladungsasymmetrie von b -Quarks bei Energien nahe der Z -Resonanz – Untersuchung von Ereignissen mit initialem b -Quark unter Verwendung der Jetladungstechnik mit dem DELPHI Detektor
Ph.D. Thesis, Berg. Univ. Wuppertal, WUB-DIS 99-06, June 1999.
- [71] DELPHI Coll., P. Abreu et al., Eur. Phys. J. C10 (1999) 219.
- [72] The LEP/SLD Heavy Flavour Working Group, D. Abbaneo et al., Eur. Phys. J. C4 (1998) 185.
- [73] V. Ravindran and W.L. van Neerven, Phys. Lett. B445 (1998) 206.
- [74] S. Catani and M.L. Seymour
Corrections of $\mathcal{O}(\alpha_s^2)$ to the forward-backward asymmetry
arXiv:hep-ph/9905424 and JHEP 9907 (1999) 23.
- [75] The LEP EWWG, D. Abbaneo et al., Contr. to the 1999 summer conferences, CERN-EP-2000-016.

- [76] See for example: L. Lyons et al, Nucl. Instr. Meth. A 270 (1988) 110.
- [77] The ALEPH, DELPHI, L3 and OPAL Coll., Nucl. Instr. Meth. A 378 (1996) 101.
- [78] Private communication with N. Kjaer.
- [79] ALEPH Coll., A. Heister et al., Eur. Phys. J. C 22 (2001) 201;
 ALEPH Coll., A. Heister et al., Eur. Phys. J. C 24 (2002) 177;
 L3 Coll., O. Adriani et al., Phys. Lett. B 292 (1992) 454;
 L3 Coll., M. Acciarri et al., Phys. Lett. B 448 (1999) 152;
 OPAL Coll., G. Alexander et al., Z. Phys. C 70 (1996) 357;
 OPAL Coll., G. Abbiendi et al., CERN-EP-2003-039, Submitted to Phys. Letts. B.
- [80] DELPHI Coll., J. Abdallah et al.
Determination of A_{FB}^b using inclusive charge reconstruction and lifetime tagging at the Z pole
 Contribution to EPS-HEP 2003 in Aachen and Lepton-Photon 2003 in Batavia
 DELPHI Note 2003-057 CONF 677
 (to be submitted to Eur. Phys. J. C).
- [81] M. Elsing
Heavy Flavour Results from LEP 1
 Parallel talk given at the EPS-HEP Aachen, Summer 2003.
- [82] The LEPEWWG \bar{b} Subgroup, C. Geweniger et al.
Combination of the LEP 2 \bar{b} Results
 Contr. to the 2001 summer conf., DELPHI note 2002-096 PHYS 926.
- [83] SLD Coll., K. Abe et al., Phys. Rev. Lett. 84 (2000) 5945.
- [84] SLD Coll., K. Abe et al., Phys. Rev. Lett. 88 (2002) 151801;
 SLD Coll., K. Abe et al., Phys. Rev. Lett. 81 (1998) 942;
 SLD Coll., K. Abe et al., Phys. Rev. Lett. 83 (1999) 1902;
 SLD Coll., K. Abe et al.
Direct measurement of A_b using charged kaons at SLD
 SLAC-PUB-8200, contr. paper to EPS-HEP 1999 in Tampere;
 SLD Coll., K. Abe et al.
Direct measurement of A_b using charged vertices at SLD
 SLAC-PUB-8542, contr. paper to ICHEP 2000 in Osaka.
- [85] P. Wells
Electroweak Review
 Plenary talk given at the EPS-HEP Aachen, Summer 2003.
- [86] The LEP EWWG, A. Blondel et al., Conf. contr. to EPS-HEP 1993 in Marseille and Lepton-Photon 1993 in Cornell, CERN-PPE/93-157;
 The LEP EWWG, D. Abbaneo et al., Conf. contr. to ICHEP 1994 in Glasgow, CERN-PPE/94-187;
 The LEP EWWG, P. Antilogus et al., Conf. contr. to EPS-HEP 1995 in Brussels and Lepton-Photon 1995 in Beijing, CERN-PPE/95-172;

The LEP EWWG, D. Abbaneo et al., Conf. contr. to ICHEP 1996 in Warsaw, CERN-PPE/96-183;
The LEP EWWG, D. Abbaneo et al., Conf. contr. to EPS-HEP 1997 in Jerusalem and Lepton-Photon 1997 in Hamburg, CERN-PPE/97-154;
The LEP EWWG, D. Abbaneo et al., Conf. contr. to ICHEP 1998 in Vancouver, CERN-EP/99-15;
The LEP EWWG, D. Abbaneo et al., Contr. to the 2000 summer conferences, CERN-EP-2001-021 and arXiv:hep-ex/0103048;
The LEP EWWG, D. Abbaneo et al., Contr. to the 2001 summer conferences, CERN-EP-2001-098 and arXiv:hep-ex/0112021.

- [87] S. Heinemeyer and G. Weiglein
The MSSM in the Light of Precision Data
arXiv:hep-ph/0307177.
- [88] G. Altarelli et al., JHEP 0106 (2001) 18 and arXiv:hep-ph/0106029.
- [89] M.S. Chanowitz
The direct limit on the higgs boson mass and the SM fit
proc. of the workshop on Electroweak Precision Data and the Higgs Mass, Zeuthen, February 2003, arXiv:hep-ph/0304199.
- [90] DELPHI Coll. – P.Abreu et al., Eur. Phys. J. C 11 (1999) 383.
- [91] P. Abreu et al.
SPRIME – A Package for Estimating the Effective $\sqrt{s'}$ Centre of Mass Energy in $q\bar{q}\gamma$ Events
DELPHI internal note 96-124 PHYS 632;
P. Abreu et al.
The Estimation of the Effective Centre of Mass Energy in $q\bar{q}\gamma$ Events from DELPHI
private communication.
- [92] M. Elsing et al.
Changes in the track reconstruction to recover from the TPC sector 6 failure
DELPHI note 2001-004 TRACK 95.
- [93] ALEPH Coll., Phys. Lett. B 399 (1997) 329;
DELPHI Coll., Z. Phys. C 72 (1996) 31.
- [94] E. Eichten, K. Lane and M. Peskin, Phys. Rev. Lett. 50 (1983) 811.
- [95] H. Kroha, Phys. Rev. D 46 (1992) 58.
- [96] DELPHI Coll. – P.Abreu et al., CERN-EP/2000-068;
DELPHI Coll., Contributed Paper 647 to ICHEP 2000, DELPHI note 2000-128 CONF 427;
A. Behrmann et al.
Results on Fermion-Pair Production at LEP running in 2000
DELPHI note 2001-022 CONF 463.

Acknowledgements

It is a pleasure to thank my supervisor, Prof. Dr. Jürgen Drees, for offering me the unique opportunity to undertake this research work on electroweak measurements with heavy flavours, and for his continuous support and interest in it. I am particularly grateful for the arrangement of my long-term stay at CERN and of my participation in several international conferences and meetings. The contacts established there and the experience gained while working directly at the laboratory seem invaluable. At the same time, it did not make a difference to be at CERN in order to benefit from the creative and constructive work atmosphere always present in Prof. Drees' group in Wuppertal.

I would also like to express my deep gratitude towards Dr. Markus Elsing from CERN for his advice and supervision, not only in matters of physics, and the excellent collaboration and fruitful discussions even at a later stage when CERN regarded his DELPHI engagement as pure “recreational activity”. Not so much recreation but nevertheless a very intriguing period was spring 2001 when the measurement of the asymmetry suddenly demanded a three-month long day-and-night effort to ensure its stability. Even more involved in that effort was Dr. Klaus München, whom I would like to thank greatly for having developed the novel high precision measurement technique in the course of his thesis, and for his help afterwards. In addition all three of us have shared in a sustainable training in marathon arguing with some of our “British guys” in DELPHI. Of course my thanks also go to the BSAURUS developers, to the DELPHI $A_{FB}^{b,c}$ team and to the whole DELPHI collaboration for their full support.

In addition I have appreciated to be member of the Wuppertal particle physics group. I would like to thank Dr. Klaus Hamacher for his advice on asymmetry measurements, and Patrick Buschmann, Dr. Frank Glege, Torsten Harenberg, Dr. Uwe Müller, Dr. Martin Siebel and Dr. Daniel Wicke for all kinds of computing assistance and for keeping me up to date what was going on back in Germany. To Dr. Uwe Müller I owe special thanks for improving the consistency and readability of this manuscript. When I came with administrative procedures to Dr. Helmut Wahlen, often at the last minute, his patience and help were very valuable.

It would fill far more than one paragraph to name the many people with whom I very much enjoyed the company and friendship at CERN and in Geneva. For example, colleagues and fellow students from Italy as well as those interested in Nordic Club events made it a pleasure to spend my free time in and around Geneva. I also appreciated that many of my friends back in Wuppertal helped keeping up the contact. With apologies to those not named here, I would like to mention also Dr. Ulrich and Maikki Parzefall, and Dr. Christian Weiser. Always at the core of a very entertaining dinner was the Karlsruhe gang, Dr. Jens Rehn, Dr. Ulrich

Schwickerath and Dr. Marcel Stanitzki, with whom I share memories of places where jeans stores were far away or the reception “not to be lost”!

Lastly I would like to thank my parents and my brother Christoph for their unfailing interest in my work and activities as well as for their support whilst I was in Wuppertal, and their thoughts whilst in Geneva. Also Shiri’s support and visits were a most welcome diversion in the period of finalising this thesis.

If not stated explicitly in the corresponding captions, all figures have been produced by the author, with the exception of 2.7–2.9 and 6.4 reproduced with kind permission by Dr. Thomas Brenke; and 6.1 with kind permission by Dr. Christian Weiser. Most of the machine and detector figures in Chapter 3 are reproduced from the WWW service of DELPHI and references therein. Figures 10.3, 10.4, 10.6, 10.7 and 10.9 (altered version) are reproduced from [85].